

ABSTRACT

MOATTI, ADELE, Control of Structural and Electrical Transitions in VO₂ Thin Film Heterostructures. (Under the direction of Dr. Jagdish Narayan).

In electron-correlated VO₂, the control over the occurrence of electrical and structural transitions which often accompany each other, are of immense scientific and technological importance with applications ranging from smart switching to sensing devices. The limiting factor for the switching speed and lifetime of such devices is the kinetically slower structural transition (10 picoseconds) in comparison with the electronic transition (0.1 picoseconds). As a result, a decoupling between structural and electrical transition is not avoidable in the presence of strain, dopants, and defects, which can directly affect the performance of these devices. The ideal solution then is to design and engineer the VO₂ structure with the isolated electrical transition, i.e. no accompanying structural transition. The energy of many interactions in the electron-correlated VO₂ to name a few electron-electron correlations, electron-lattice interactions, and spin-spin interactions are of the same order. That explains the reason behind the concurrent occurrence of the electrical transition with the structural transition. Thus, the interplay between these many degrees of freedom is critical in the manipulation of the transitions. This is achievable by using external stimuli to affect these interactions.

The primary objective of this dissertation is to develop practical methods for manipulation of the electrical and structural transitions through manipulating of the various interactions. This goal is achieved by exploitation of the misfit strain, point defects (oxygen vacancies), and spin engineering of an overlayer to control the lattice, charge, and spin degrees of freedom, respectively, which affect the orbital degree of freedom accordingly.

To systematically investigate the effect of strain on the electrical and structural transitions, VO₂/TiO₂/TiN/Si and VO₂/c-sapphire heterostructures have been investigated. These platforms

are designed to have two domains (in-plane rotation) with different misfit strains which are enforced by the selective buffer layer in VO₂ thin films. The behavior of different domains is studied separately by HAADF imaging and EELS spectroscopy to monitor the effect of strain on the structural and electrical transitions. The thermodynamics and kinetics models are also developed to study the effect of strain primarily on structural transition in VO₂.

By choosing the VO₂ to be below the critical thickness in VO₂/NiO/c-sapphire heterostructures, we are able to successfully eliminate the structural transition, and drive just the electrical transition. For VO₂ thicknesses below the critical thickness, it was possible to inhibit film relaxation and trap the misfit strain. This phenomenon is captured by *in-situ* techniques such as XRD and STEM microscopy. The DFT calculations are used to provide a full picture for the VO₂ isostructure.

The vacuum annealing is utilized to study the effect of oxygen vacancies on the electrical and structural transitions in VO₂/NiO/c-sapphire heterostructures, both below and above the critical thickness. The defects stabilize the M₂ phase of VO₂ and realize room-temperature metallic VO₂. The structural details are studied with atomic resolution techniques. A reversible on and off hysteresis behavior is observed. This design has a unique structure and property to be used in non-volatile memory devices.

Two unique heterostructures of Ni/VO₂/c-YSZ/Si were designed to control the coercive field of the Ni layer could be controlled via kinetics of growth, provide VO₂ with an external spin variable. Structural pinning is enforced by Ni island layer, which also induces an antiferromagnetic transition in the VO₂ layer leading to insulating behavior. This pinning occurs in a 200 nm thick VO₂ films where there is a continuous island growth on top of it. This heterostructure is integrated with Si and is an ultra-fast candidate for IR sensor-based devices.

© Copyright 2019 by Adele Moatti

All Rights Reserved

Control of Structural and Electrical Transitions in VO₂ Thin Film Heterostructures

by
Adele Moatti

A dissertation submitted to the Graduate Faculty of
North Carolina State University
in partial fulfillment of the
requirements for the degree of
Doctor of Philosophy

Materials Science and Engineering

Raleigh, North Carolina
2019

APPROVED BY:

Dr. Jagdish Narayan
Committee Chair

Dr. John Prater

Dr. Claude Reynolds Jr

Dr. Mohamed Bourham

DEDICATION

To,

My parents, this would have never been achieved without their sacrifices and support.

And all students who are affected by “Visa ban” and cannot see their families.

BIOGRAPHY

Adele Moatti was born in Arak, Iran. After completing her schooling in Farzanegan, a national organization for exceptional talents (NODET), she went to study Materials Science and Engineering at Iran University of Science and Technology in Tehran for her Bachelor of Science degree. Title of her thesis was “Optimization of mechanical properties of a novel glass-ceramic based dental composites.” She received a privileged admission to join M.Sc. program in Materials Science and Engineering at Iran University of Science and Technology. She graduated as a distinguished student and her work was on “Self-assembly of mesoporous alumina with the application for defluoridation of drinking water”. She joined Department of Materials Science and Engineering of NC State University in the fall of 2014 for her doctoral research, which involved control of structural and electrical transitions in epitaxial VO₂ thin-films, under the guidance of Dr. Jagdish Narayan.

ACKNOWLEDGMENTS

First and foremost, I would like to express my sincerest thanks to my research advisor Prof. Jagdish Narayan for his guidance, support and constant encouragement throughout this work. His commitment to research and passion for science has left a lasting impression on me. His expertise in the field and innovative ideas played a very important role in the completion of my work and my development as a researcher.

I also want to express my appreciation for my advisory committee member Prof. John. Prater. Prof. Lew Reynolds, and Prof. Mohamed Bourham for their contributions of time, guidance, and expertise, which can only improve the quality of my dissertation. I want to give a special thanks to my colleagues and friends: Marek Pulczynski, Dr. Gabrielle M Foley, Dr. Ritesh Sachan, Leila Khalili, Dr, Valentino Cooper, Siddharth Gupta, and Dr. M. Reza Bayati. Their help and support throughout my doctoral research at NC State has been invaluable and has made my stay a really enjoyable experience. Thanks to Edna Deas for her prompt help with the administrative work. Mentioning everyone who has in one way or the other helped me and supported me during my stay here is not possible, but, I want to thank from the bottom of my heart all my friends, who have made my stay at NC State worthwhile. Finally, I would like to say that I am indebted to my parents and siblings, Erfan Moatti, Fatima Moatti, and Marzieh (Sheyda) Rasooli. I also want to thank Marek for his kindness, love, and for always being there for me throughout difficult times. I owe my success and well-being to them and their unbridled support, love, and encouragement. I also thank the National Science Foundation for providing the funding for my work, DMR-1304607.

TABLE OF CONTENTS

LIST OF TABLES	ix
LIST OF FIGURES	x
Chapter 1: Introduction	1
References	7
Chapter 2: Background Knowledge	9
2.1. Vanadium dioxide.....	9
2.1.1. VO ₂ structural details.....	9
2.1.2. VO ₂ phase transition characteristics	10
2.1.3. Band structure across the metal-to-insulator transition	12
2.1.4. Control of transition through strain engineering (lattice and orbital degree of freedom).....	17
2.1.4.1. Peierls point of view	17
2.1.4.2. Mott point of view	17
2.1.5. Control of transition through defect engineering (charge degree of freedom).....	18
2.1.5.1. Peierls point of view	18
2.1.5.2. Mott point of view	19
2.1.6. Control of transition through spin engineering (spin degree of freedom)	19
2.2. Thin film epitaxy.....	20
2.2.1. Different growth modes	21
2.2.1.1. Frank-van der Merwe.....	21
2.2.1.2. Volmer-Weber	21
2.2.1.3. Stranski-Krastanov.....	22
2.2.2. The fundamental difference between lattice matching epitaxy (LME) and domain matching epitaxy (DME)	22
2.2.3. Misfit strain	23
2.2.3.1. Misfit strain in LME regime	23
2.2.3.2. Misfit strain in DME regime.....	23
2.2.4. Thermal mismatch strain	25
2.2.5. Defect strain	26
2.2.6. Stress-strain relationship.....	26
2.2.6.1. Stress-strain relationship in cubic thin films.....	26
2.2.6.2. Stress-strain relationship in hexagonal thin films.....	28
References.....	29
Chapter 3: Experimental techniques	32
3.1. Buffer layers and substrates	32
3.1.1. NiO structure.....	32
3.1.2. C-YSZ (cubic-yttria stabilized zirconia)	33
3.1.3. Nickel	33
3.1.4. TiN	34
3.1.5. TiO ₂	35
3.1.6. Silicon	36
3.1.7. Sapphire	37

3.2. Excimer lasers	37
3.2.1. Pulsed laser technique for thin-film deposition	38
3.2.2. Interaction of laser with material	39
3.2.3. Interaction of laser with formed plasma	40
3.2.4. Adiabatic plasma expansion	41
3.3. Characterization techniques	42
3.3.1. X-ray diffraction	42
3.3.1.1. θ -2 θ scan	43
3.3.1.2. Φ scan	44
3.3.2. Scanning electron microscopy (SEM)	45
3.3.2.1. Electron backscattered diffraction (EBSD)	47
3.3.2.1. Transmission Kikuchi diffraction (TKD)	48
3.3.3. Transmission electron microscopy (TEM)	48
3.3.3.1. Bright field imaging (BF)	49
3.3.3.2. Diffraction contrast-SAED	49
3.3.3.3. Electron energy loss spectroscopy (EELS).....	49
3.3.4. Scanning transmission electron microscopy (STEM).....	50
3.3.4.1. High-angle annular dark field image (HAADF).....	51
3.3.4.2. Electron energy loss spectroscopy (EELS).....	52
3.3.5. Electron transparent sample preparation.....	52
3.3.6. Electrical measurement.....	53
3.3.6.1. Van der Pauw measurement.....	53
3.3.6.2. Hall measurement	54
3.3.7. Magnetic measurement	55
3.3.8. Raman spectroscopy	55
References.....	57

Chapter 4: Strain engineering-VO₂ bi-epitaxy integrated with Si through TiO₂/TiN with a novel method of oxidation	61
4.1. Preparation of TiO ₂ /TiN/Si heterostructures as buffer layers for VO ₂ through a novel method of oxidation	61
4.1.1. Introduction	61
4.1.2. Experimental details	64
4.1.3. Results and discussion	65
4.1.3.1. Epitaxial relationship of TiO ₂ /TiN/Si(100) heterostructures	65
4.1.3.2. Oxidation mechanism	72
4.1.4. Conclusion	80
4.2. Thin film bi-epitaxy and transition characteristics of TiO ₂ /TiN buffered VO ₂ on Si(100) substrates.....	82
4.2.1. Introduction	82
4.2.2. Experimental details	83
4.2.3. Results and discussion	84
4.2.4. Conclusion	91
References.....	93

Chapter 5: Strain engineering-Effect of strain on thermodynamics and Kinetics of structural transitions in VO₂ thin films	100
5.1. Introduction	101
5.2. Experimental details	104
5.3. Results and discussion	105
5.3.1. Structural and microstructural analysis of VO ₂ thin films and interfaces	105
5.3.2. Electrical analysis and SMT characteristics	111
5.3.3. Temperature-dependent XRD measurements and SPT characteristics	113
5.3.4. Kinetic and thermodynamic models, SPT and SMT-strain correlation	116
5.4. Conclusion	122
References.....	123
Chapter 6: Strain engineering-Mechanism of strain relaxation and control of electrical transition in the VO₂ thin-films across the critical thickness	126
6.1. Introduction	127
6.2. Experimental details	128
6.3. Results and discussion	128
6.3.1. Critical thickness	128
6.3.2. DME	132
6.3.3. Surface energies	133
6.3.4. Interface analysis	134
6.3.5. Cryptographic description the interface between strained and relaxed grains ...	136
6.4. Conclusion	137
References.....	139
Chapter 7: Strain engineering-Removal of structural transition in VO₂ through strain engineering leading to the lattice pinning	142
7.1. An optimized sample preparation approach for atomic resolution <i>in-situ</i> studies of thin films	142
7.1.1. Introduction	143
7.1.2. Results	145
7.1.2.1. Sample deposition and wedge polishing procedure	145
7.1.2.2. Wedge fringes	147
7.1.2.3. FIB lift-out of thin lamella and carbon fiber attachment	148
7.1.2.4. Soft transfer of the sample to the S/TEM test stage.....	150
7.1.3. Conclusion	153
7.2. Electrical transition in isostructural VO ₂ thin-film heterostructures	154
7.2.1. Introduction	154
7.2.2. Experimental details	157
7.2.3. Results and discussion	159
7.2.4. Conclusion	172
References.....	174
Chapter 8: Defect engineering-Control of electronic and structural transitions through point defects	192

8.1. Vacancy-driven robust metallicity of structurally pinned monoclinic epitaxial VO ₂ thin films	192
8.1.1. Introduction	193
8.1.2. Experimental details	195
8.1.3. Results and discussion	197
8.1.4. Conclusion	208
8.2. Switching on/off metal-insulator transition in VO ₂ above the critical thickness through oxygen vacancies	209
8.2.1. Experimental details	209
8.2.2. Results and discussion	210
8.2.3. Conclusion	216
References.....	218
Chapter 9: Spin engineering-Magnetic tuning of structural phase transition in Ni/VO₂/c-YSZ/Si heterostructures (structural pinning of M₂ monoclinic induced by spin engineering in VO₂ thin-films)	224
9.1. Introduction	224
9.2. Experimental details	227
9.3. Results and discussion	228
9.4. Conclusion	242
References.....	244
Chapter 10: Conclusions	250

LIST OF TABLES

Table 4.1. Crystallographic parameters used to collect ϕ -patterns from (111) reflection of rutile TiO ₂ crystal and (220) reflections of TiN, and Si crystals.....	66
Table 5.1. Characteristics of the SMT (semiconductor to metal transition) of VO ₂ thin films grown on c-sapphire: the transition temperature (T _{smt}), the hysteresis (ΔH), the amplitude (ΔA), and the sharpness of the SMT	113
Table 7.1. Wedge polishing recipe with paper grade, depth, and the speed.....	146
Table 7.2. Ion milling condition with the angle, energy, and time required.....	147
Table 7.3. Lattice constants, V-V bond angles and lengths, and dimerization difference Δ_{V-V} for VO ₂ groundstate nonmagnetic (NM-M1) and ferromagnetic (FM-M0) phases. Comparisons to previous experiment and theory are included for validation purposes	167
Table 7.4. Lattice constants, V-V bond angles, and lengths, dimerization difference (Δ_{V-V}), and bandgap (E_{gap}) for VO ₂ structures used to explore the effects of dimerization on bandgap.....	168
Table 8.1. Carrier concentration values calculated for as-deposited and vacuum-annealed samples at room temperature and 100 °C	204
Table 9.1. Crystallographic parameters used to collect the XRD ϕ -patterns through the Si (202), cubic YSZ (202), M1-VO ₂ (011), M2-VO ₂ (20 $\bar{1}$), and Ni (200) reflections represented in Figure 9.1.....	230

LIST OF FIGURES

Figure 1.1. The decoupling between different degrees of freedom in electron-correlated VO ₂	2
Figure 2.1. Illustration of crystallographic unit-cells of rutile, monoclinic M ₁ , and M ₂ structures of VO ₂ including their oxygen octahedral surrounding vanadium cation with different V-V bond length	10
Figure 2.2. The metal-to-insulator hysteresis characteristics for single crystalline, textured (similar out-of-plane orientation, but in-plane rotation), and polycrystalline VO ₂ thin-films	11
Figure 2.3. Caption The crystal band structure, d-orbital splitting for rutile VO ₂ induced by edge-sharing octahedra.....	14
Figure 2.4. The band diagram belongs to VO ₂ metallic rutile phase depicting p-d orbitals overlap; two electrons take part in the covalent mixing between O and V (d _{xy} and d _{zx} and p _π orbitals) resulting in the formation of the narrow antibonding π* and a wider bonding π band. The remaining electron is nonbonding and goes into d (d _{z²-y²) which is directed parallel to the c-axis.}	14
Figure 2.5. The changes in V-V distance from rutile-tetragonal to monoclinic structure in VO ₂ . The vanadium atom moves away from the center of the octahedral in the transition from tetragonal to monoclinic	15
Figure 2.6. The Peierls transition (metal-to-insulator) in VO ₂ as the d band splits into a lower bonding d and upper antibonding d * due to homopolar V-V bonding formation	15
Figure 2.7. The Mott transition (metal-to-insulator) in VO ₂ . U is the Hubbard intra-atomic correlation energy. When U is bigger than the kinetic energy t, it can prevent electrons from hopping and delocalization and the insulator state dominates. The bandgap is defined by U which is a correlation gap.	16
Figure 2.8. The schematic depiction of orbital occupancy changes as c/a ratio in rutile VO ₂ varies (strain along the axes) from Peierls point of view.	17
Figure 2.9. Change in the bandwidth through strain engineering and its effect on electron hopping in VO ₂ from Mott point of view	18
Figure 2.10. Effect of addition of holes and electrons on d-orbital bands' level and electron occupancy in VO ₂ from Peierls point of view.....	19
Figure 2.11. Effect of introduction of holes and electrons in changing columbic interaction and thus VO ₂ metal-to-insulator transition.....	19

Figure 2.12. The spin ordering affects electron hopping due to Hund's rule coupling in VO ₂	20
Figure 2.13. Different growth modes of thin films depending on the free surface energy of the film σ_f , substrate σ_s , and the interfacial energy between film and substrate σ_{sf}	21
Figure 2.14. The systematic decrease of integral multiple with strain	24
Figure 3.1. The NiO unit cell including Ni cation surrounded by oxygen octahedron and its d-orbital band structure. NiO has an antiferromagnetic nature which is the cause of its insulating properties	32
Figure 3.2. The cubic yttria stabilized ZrO ₂ unit cell	33
Figure 3.3. The face-centered cubic lattice of nickel.....	34
Figure 3.4. The titanium nitride TiN unit cell following NaCl structure.....	34
Figure 3.5. The rutile and anatase phase of TiO ₂ unit cells. In rutile, Ti cations are surrounded by oxygen octahedra which rotate alternatively. While in anatase, there are distorted octahedra.....	35
Figure 3.6. The crystal band splitting in rutile vs anatase due to edge-sharing octahedra. In anatase, however, the distortion changes the bands' level and energy	36
Figure 3.7. The silicon unit cell including Si tetrahedra.....	36
Figure 3.8. The hexagonal lattice structure of sapphire including oxygen octahedral surrounding Al cations	37
Figure 3.9. The schematic of an excimer laser chamber including a discharge tube	38
Figure 3.10. The top diagram shows the initial shape of plasma after laser termination, and the lower diagram represents the shape of plasma before it hits the substrate and after adiabatic expansion	42
Figure 3.11. The X-ray generation through electron dislodges from the inner shell and transition of the outer shell electrons to the inner shell.....	43
Figure 3.12. Schematic illustration of Φ -scan geometry	45
Figure 3.13. Emission of secondary electrons (SE), backscattered electrons (BSE), and X-ray upon the incident of the electron beam.	46
Figure 3.14. The Scanning electron microscope schematic.....	47

Figure 3.15. Different phenomena upon electron beam incidence with a material (a), and detectors position to collect generated signals, HAADF detector angle > 50 mrad, ADF detector angle > 10 mrad, and BF detector < 10 mrad.....	50
Figure 3.16. Schematic depiction of critical optical elements in conventional TEM vs STEM	51
Figure 3.17. HAADF image of silicon dumbbells taken by STEM.....	52
Figure 3.18. The four probes placement for Van der Pauw measurement	53
Figure 3.19. Illustration of Hall Effect voltage, I, and B relationship	54
Figure 3.20. Diagram of SQUID.....	55
Figure 3.21. Energy level diagram before and after Raman scattering	56
Figure 4.1. XRD θ - 2θ pattern acquired from the TiO ₂ (110)/TiN(100)/Si(100) heterostructure	66
Figure 4.2. Results of XRD ϕ -scan performed on the TiO ₂ (110)/TiN(100)/Si(100) heterostructure: a) Si(220) reflection, b) TiN(220) reflection, and c) TiO ₂ (111) reflection	67
Figure 4.3. Schematic illustration of Real Space crystallographic alignment across TiO ₂ /TiN interface: a) Top view, b) Cross-section view along TiO ₂ [110] common axis, c) Cross-section view along TiO ₂ [001] common axis	68
Figure 4.4. High-resolution XRD θ - 2θ pattern performed through TiO ₂ (110), TiN(200) and Si(400) signals.....	71
Figure 4.5. Cross-section TEM micrograph and indexed SAED patterns from each interface. The patterns belong to Si [110], TiN [011], and TiO ₂ [100] zones, b) High-resolution TEM micrograph of the TiN/TiO ₂ interface, c) STEM micrograph of the TiN/TiO ₂ interface	72
Figure 4.6. Schematic illustration of Ti leaving nitrogen octahedron and weakening neighboring Ti atoms' bond.....	73
Figure 4.7. Cross-section Z-Contrast STEM micrograph of TiO ₂ ; illustrating faceted voids (cuboids) within TiO ₂ thin film, a) arrows pointing inside of the cuboid, b) high-resolution image of the interface of the cuboid/TiO ₂	73
Figure 4.8. EDS analysis a) Across TiO ₂ (110)/TiN(100)/Si(100) heterostructure, b) N distribution, c) O distribution, d) Ti distribution, and e) Elemental mapping.....	75
Figure 4.9. Rutile TiO ₂ structure sliced at different planes.....	77

Figure 4.10. Wulff construction belonging to [110] direction of rutile TiO ₂	78
Figure 4.11. Schematic illustration of TiO ₂ cuboid Surface transition from (111) to (110) and (001) during merging of the cuboids	78
Figure 4.12. EELS mapping analysis across TiN/TiO ₂ interface a) In the Ti L _{2,3} edges range, b) In the O K edge range, c) The location of the spots where the EELS data were collected. The numbers correspond to the numbers on figures a and b.....	79
Figure 4.13. XRD θ -2 θ pattern acquired from the VO ₂ (011)/TiO ₂ (110)/TiN(100)/Si (100) heterostructure	85
Figure 4.14. Results of XRD ϕ -scan performed on the VO ₂ (011)/TiO ₂ (110)/TiN(100)/Si(100) heterostructure: Si(220) reflection, TiN(220) reflection, TiO ₂ (111) reflection, and VO ₂ (101) reflection.....	86
Figure 4.15. TKD result of the FIB slice (a) Cross section electron image and the FIB made sample at the right corner, (b) Band contrast image, (c) Phase map image, and (d) Inverse pole figure map (IPF Y) of interfaces acquired from the VO ₂ (011)/TiO ₂ (110)/TiN(100)/Si (100) heterostructure	88
Figure 4.16. Kikuchi patterns of (a) Si, (b) TiN, (c) TiO ₂ , and (d, e) VO ₂ layers. (f) Poles belong to each layer of Si, TiN, TiO ₂ , and VO ₂ in the cross-section band contrast image, respectively from bottom to top.....	89
Figure 4.17. Resistance versus temperature in VO ₂ /TiO ₂ /TiN/Si heterostructure.....	90
Figure 4.18. Magnetic field dependent magnetization of VO ₂ (011) measurement at 4, 100, and 300 K with 200 Oe field cooling	91
Figure 5.1. a) XRD θ -2 θ pattern acquired from a VO ₂ (020)/ Sapphire (0006) heterostructure, b) XRD ϕ -scan on the VO ₂ (020)/ sapphire (0006) heterostructure: Sapphire (01 $\bar{1}$ 2) reflection, and VO ₂ (011) and VO ₂ (210) reflections, c) in-plane rotations of the (010) oriented t-VO ₂ unit cell on the c-sapphire basal plane with two possible in-plane orientations	107
Figure 5.2. a) The low mag HAADF image taken by STEM showing both orientations growing columnar along [10 $\bar{1}$ 0] sapphire zone axis, b) diffraction pattern belong to both crystallites of VO ₂ along [001] and [100] and [10 $\bar{1}$ 0] substrate, c) the associated inverse FFT images with respect to VO ₂ (200), sapphire (1210) and VO ₂ (022), sapphire (1216) are shown below HAADF images along [001], crystallite “a”, and [100], crystallite “b”, of VO ₂ , respectively, d) HAADF image taken along the [2 $\bar{1}$ $\bar{1}$ 0] sapphire zone axis	108

Figure 5.3. a) HAADF image showing two different orientations of VO ₂ on sapphire along [11 $\bar{2}$ 0] substrate, b, and c) selected spectrum collected across the interface in two different orientations as indicated by lines in Figure a, d and e) Peak fit amplitudes for V-L ₂ , V-L ₃ , O-K EELS edges along the XX' and YY' lines, respectively.....	111
Figure 5.4. a) Electrical resistance vs. temperature of VO ₂ thin films grown on sapphire (0001) substrates, b) derivatives of log ₁₀ R(T) for the cooling (black, circle) and heating (red, triangle) curves are shown. Symbols represent data points and the lines represent Gaussian fitting	113
Figure 5.5. a) Selected XRD θ -2 θ patterns before, during, and after transition during heating for VO ₂ (020)/ Sapphire (0006) heterostructures, b) temperature dependence of XRD data from VO ₂ thin films grown on c-sapphire measured during the heating and, c) cooling. The colors of contour plots represent the peak intensity. Evolution of (020) peaks belong to monoclinic and tetragonal phases has shown different intensity and slight changes in 2 theta position.....	114
Figure 5.6. Comparison of SMT (semiconductor to metal transition), through resistance measurement, and SPT (structural phase transition), through d-spacing measurement (using Boltzmann fitting), temperatures in a full heating-cooling cycle.....	115
Figure 5.7. a) Temperature dependence of in-plane and out-of-plane strains in VO ₂ thin films grown on c-sapphire, b) stress vs temperature during heating and cooling in VO ₂ (020)/ sapphire (0006) heterostructures	116
Figure 5.8. a) The energy level of tetragonal (stage I) and monoclinic, M ₁ and M ₂ (stage II); and the difference between these two stages, ΔG_a , b) changing the activation energy of transformation, ΔG_m , in the presence of compressive and tensile stre ..	120
Figure 5.9. Schematic energy band for the metal, insulator, and monoclinic metallic phase of VO ₂	122
Figure 6.1. a) The schematic illustration of VO ₂ /NiO/c-sapphire heterostructures where VO ₂ is grown above the critical thickness (h_c) of ~15 nm. b) The schematic illustration of VO ₂ /NiO/c-sapphire heterostructures where VO ₂ is grown in the vicinity of the critical thickness. The red area represents a relaxed area where the film is reached h_c value and dislocations glide using the slip plane. c) The schematic illustration of VO ₂ /NiO/c-sapphire heterostructures where VO ₂ is grown below the critical thickness	129

- Figure 6.2. a) The HAADF image of VO₂/NiO/c-sapphire heterostructures where VO₂ has grown above the critical thickness of ~15 nm. b) The HAADF image of VO₂/NiO/c-sapphire heterostructures where VO₂ is grown below the critical thickness. c, d) The atomic resolution HAADF image of VO₂ structure belongs to (a) and (b), respectively. e) The HAADF image taken by STEM showing both strained and relaxed state of VO₂ below and above the critical thickness along $[1\bar{2}1]$ NiO zone axis. The inset figure represents the low-mag image of the VO₂/NiO/c-sapphire heterostructure and their thicknesses. f) The HAADF image of the relaxed monoclinic VO₂ grain which is reached above the critical thickness 131
- Figure 6.3. a) The HAADF image taken by STEM showing the interface between the strained and relaxed state of VO₂. The periodic appearance of misfit dislocation at the interface is captured during the transition of strained to a relaxed state. The FFT pattern belongs to the relaxed monoclinic, strained monoclinic, and at the interface of both states is indicated by 1, 2, and 3, respectively. b) The formation of steps along low energy directions at the interface of a strained and relaxed state of VO₂ to minimize the total energy of the system 133
- Figure 6.4. a) The indication of two dislocation cores in the HAADF image of the interface, b) the image processing technique used to depict the atomic rearrangements around the dislocations' core. The dislocation loop and Burgers vector is illustrated for each dislocation. There is one atomic column missing, marked by a circle, in the vicinity of each dislocation core, marked by T, to compensate for the generated strain. c) Strain analysis along the relaxed and strained interface represents the strain centers. The red color is a positive strain going to black color for negative strains. The presence of periodic compressive and tensile strains around the dislocation cores also is an indication of atomic rearrangement to minimize the local strain 135
- Figure 6.5. a) HAADF image showing two different orientations of VO₂ belong to strained and relaxed states marked by squares x and y, respectively, on the NiO buffer layer along $[1\bar{2}1]$, b) selected spectrum collected from two different states marked as x and y belong to strained and relaxed VO₂, respectively 135
- Figure 6.6. a) Schematic illustration of the atomically sharp interface between the strained and relaxed state of VO₂ at high temperature. At high temperature, the relaxed state belongs to the tetragonal rutile VO₂ which is in contact with the strained monoclinic VO₂. b) The transition of the relaxed state from tetragonal to the monoclinic M₁ phase across the transition temperature of VO₂. c) Schematic illustration of the interface between the strained and relaxed state of VO₂ at low temperature. At low temperature (RT), the relaxed monoclinic is in contact with the strained monoclinic. The schematic illustration at low temperature follows our experimentally captured atomic images..... 138

Figure 7.1. The sample is placed on the TTS without nanotubes spacers before (a) and after (b) Pt deposition and shattering, respectively	145
Figure 7.2. Schematic illustration of making a sandwich of two samples with thin films facing each other	146
Figure 7.3. The optical images before (a) and after (b) ion milling with the schematic wedge polished sample at the inset.....	147
Figure 7.4. (a) Cutting the lamella off the sample with schematic image at the inset, (b) pulling some carbon nanotubes from a bunch of them, (c) attaching carbon nanotube to the needle, (e) attaching carbon nanotube to the lamella, and (f) schematic image of attaching carbon nanotubes to the lamella using Pt deposition	149
Figure 7.5. (a) The schematic depiction of the Protochips TTSs in which electric field is applied through W and sample is heated by SiC membrane, (b, c) the actual and schematic illustration of the needle carrying the sample by nanotubes to be placed on the TTS, (d, e), depiction of the sample being secured with Pt deposition on the TTS before cutting nanotubes by actual and schematic images, and (f, g) the final sample on the TTS actual and schematic illustratio....	150
Figure 7.6. The low (a) and high (b) magnification STEM micrographs of the VO ₂ /NiO/sapphire thin film heterostructures, respectively. The atomic resolution micrographs of VO ₂ structure on the heating chip (c) before, and (d) after heating.....	152
Figure 7.7. (a) The low magnification cross-sectional HAADF image of VO ₂ /NiO/(0001)sapphire heterostructures of 250 nm (thick) VO ₂ , (b) the atomic resolution HAADF image of NiO/VO ₂ the interface of thick VO ₂ films, (c) the Fourier transform of the VO ₂ thick films and the corresponding atomic model belong to the zone axis of [100] monoclinic phase (d) The low magnification HAADF micrograph of thin VO ₂ films, (e) the atomic resolution HAADF image of NiO/VO ₂ the interface of thin VO ₂ films, (f) the Fourier transform of the VO ₂ thin films and the corresponding atomic model belong to the zone axis of [010] monoclinic phase	160
Figure 7.8. In-situ XRD measurements as a function of temperature during heating and cooling cycles of (a) thick sample, and (b) thin sample of VO ₂	161

- Figure 7.9. The electrical resistivity as a function of temperature for a) thick, and b) thin samples. The derivative of electrical resistivity versus temperature of c) thick, and d) thin sample. The out-of-plane d-spacing (obtained from in-situ XRD measurements) measured as a function of the temperature of e) thin, and f) thick samples. In the inset of the image (e), the low and high-temperature HAADF images are provided in the case of the thick sample and in the inset of the image (f), the isostructural HAADF image of the thin sample is presented. The scale bars in HAADF images are 1 nm 163
- Figure 7.10. In-situ EELS spectra obtained for V-L_{2,3} and O-K₁ edges at high (150 °C) and low (20 °C) temperatures for thick and thin VO₂ films; the peaks at 513 eV and 521 eV correspond to V-L₃ and V-L₂ edges; the peak at 529 eV is indicative of O-K pre-peak constituting π^* and d^* orbitals. EELS spectra (a, b) at 150 °C and (c, d) at 20 °C are obtained from the thick VO₂ films. Spectra (e, f) at 150 °C and (g, h) at 20 °C represent thin VO₂ films. The atomic resolution HAADF images corresponding to low-temperature structures of thick and thin films with [100] and [010] zone axis, respectively, have shown in the center 166
- Figure 7.11. Bandgap (E_{gap}) as a function of the difference between short and long bonds (Δ_{V-V}) in VO₂. Black solid circles indicate data obtained from structures fixed to the epitaxially constrained experimental thin film values. Red hashed squares indicate the groundstate phases: NM-M1 (nonmagnetic M1 monoclinic phase) and FM-M0 (ferromagnetic M0 monoclinic phase). For FM phase's bandgaps were obtained from NM calculations of the FM groundstate atomic 169
- Figure 7.12. Schematic of VO₂ band structure in the metallic state for (a) thick and (b) thin samples, schematic of VO₂ band structure in the insulating state for (c) thick and (d) thin samples. The oxygen octahedron has shown in the center for the high-temperature structures of thick and thin films; the vanadium atom displacement is depicted from the center of the octahedron in the case of thin samples due to strain pinning 171
- Figure 8.1. The X-ray diffraction pattern of VO₂/NiO/sapphire thin film heterostructures below a critical thickness of ≈ 15 nm (a) as-deposited sample, and (b) after annealing in vacuum. (c) The schematic figure representing VO₂/NiO/sapphire heterostructures, (d, e) the HAADF images of the VO₂/NiO interface showing the formation of a thin NiO-VO₂ layer in the as-deposited and vacuum-annealed samples, respectively 198
- Figure 8.2. HAADF-STEM signal showing atomic resolution imaging produced from VO₂/NiO cross-sectional interface of (a) as-deposited sample with the zone axis of [010], and (b) the HAADF image of the annealed sample in a vacuum with the zone axis of [01 $\bar{2}$]. The inset figures in the (b) show the interface of VO₂/NiO with and without dislocation 199

Figure 8.3. (a) HAADF image of the VO ₂ thin film, (b) Ni, (c) V, and (d) O elemental maps corresponding to the marked region-of-interest (ROI) in (a) obtained from EELS. (e) The averaged intensity profile of V-L ₃₂ and Ni-L ₃₂ peaks along the ROI. (f) The representative EEL spectra from pure VO ₂ , VO ₂ +NiO and NiO regions from the as-deposited thin film sample	199
Figure 8.4. Contour plots of in-situ XRD measurements for (a) as-deposited epitaxial VO ₂ , and (b) annealed epitaxial VO ₂ in a vacuum atmosphere.....	201
Figure 8.5. The electrical resistivity of VO ₂ /NiO/sapphire thin film heterostructures, below the critical thickness of 10 nm for as-deposited and vacuum-annealed samples ...	204
Figure 8.6. (a) Raman spectra for bulk VO ₂ (above critical thickness), as-deposited thin film, and vacuum-annealed VO ₂ thin film. (b) Raman fitting for V-V ₁ and V-V ₂ bonds in as-deposited and vacuum-annealed VO ₂ thin films. (c) High-resolution Raman spectra for vacuum-annealed VO ₂ film, highlighting the absence of rutile-VO ₂ vibrational bonding characteristics	206
Figure 8.7. STEM-EELS measurements (a) core loss edges, and (b) low loss edges belong to VO ₂ thin films in bulk, as deposited, and vacuum annealed samples	208
Figure 8.8. The X-ray diffraction pattern of VO ₂ /NiO/sapphire thin film heterostructures above the critical thickness of ≈10 nm in the pristine, vacuum annealed at low and high temperatures (marked as VA-low T and VA-high T, respectively), and oxygen annealed samples. (b) The low-mag cross-sectional HAADF image of VO ₂ /NiO/sapphire heterostructures showing VO ₂ thickness above the critical thickness	211
Figure 8.9. The HAADF micrograph belongs to the pristine VO ₂ /NiO-VO ₂ thin film with [100] and [110] zone axis of M ₁ monoclinic VO ₂ and NiO, respectively. b) The atomic scale HAADF image of VO ₂ in (a). c) The HAADF micrograph belongs to the high-temperature vacuum annealed VO ₂ /NiO-VO ₂ thin film with [012] and [110] zone axis of M ₂ monoclinic VO ₂ and NiO, respectively. d) The atomic scale HAADF image of VO ₂ in (c). e) The HAADF micrograph belongs to the low-temperature vacuum annealed VO ₂ /NiO-VO ₂ thin film with [001] and [211] zone axis of M ₂ monoclinic VO ₂ and NiO, respectively. f) The atomic scale HAADF image of VO ₂ in (e). The inset figures provide the schematic of atomic structures for the corresponding micrograph.....	213
Figure 8.10. The electrical resistivity of VO ₂ /NiO/sapphire thin film heterostructures, above the critical thickness of 10 nm for pristine, low-temperature vacuum-annealed (VA-low T), and high-temperature vacuum-annealed (VA-high T) samples. The inset figure represents the resistivity vs temperature plot for VA-high T in the full temperature range of 100-370 K.....	214

Figure 8.11. The electrical resistivity of VO ₂ /NiO/sapphire thin film heterostructures before (marked as 1) and after high-temperature vacuum annealing (marked as 0) during four cycles (marked by 1C, 2C, 3C, and 4C).....	215
Figure 8.12. The HAADF image of high-temperature vacuum annealed VO ₂ /NiO/c-sapphire thin film heterostructure. The formation of twins in the vicinity of the step is illustrated at the interface of VO ₂ /NiO.....	216
Figure 9.1. The cross-sectional low magnification TEM micrographs of Ni/VO ₂ interface for (a) 2-D growth mode of Ni, and (b) 3-D growth mode of Ni. Θ -2 Θ XRD patterns of the VO ₂ /YSZ/Si thin film heterostructures before and after Ni deposition for (c) 2-D growth mode of Ni, and (d) 3-D growth mode of Ni. XRD ϕ -scans through the Si (202), cubic YSZ (202), M ₁ -VO ₂ (011), M ₂ -VO ₂ (20 $\bar{1}$), and Ni (200) reflections for (e) 2-D growth mode of Ni, and (f) 3-D growth mode of Ni.....	231
Figure 9.2. (a) The SAED pattern of 3D-Ni/M ₂ -VO ₂ /c-YSZ/Si heterostructures belongs to the zone axis of [110] Si, which showing the parallel alignment of ($\bar{2}$ 11)3D-Ni/(100)M ₂ -VO ₂ /(110)c-YSZ/(110)Si. The inset figure is a STEM-HAADF micrograph of Ni/VO ₂ interface and the schematic representation of M ₂ -VO ₂ belong to this zone-axis. (b) The STEM-HAADF micrograph of Ni/VO ₂ interfaces at the zone axis of [110]Ni. The 60° in-plane rotation is observed for M ₂ -VO ₂ . The inset figure is the schematic representations of M ₂ -VO ₂ belong to two zone-axes of [010] and [$\bar{1}$ 10]	232
Figure 9.3. a) Raman spectra for bulk VO ₂ film, 2D and 3D-Ni/VO ₂ films thin films. (b) Raman fitting for V-O bonding states in 2D and 3D-Ni/VO ₂ thin films. (c) High-resolution Raman spectra for 2D and 3D-Ni/VO ₂ films, highlighting the peak shift in V-V ₂ peak as a result of M ₂ phase formation	234
Figure 9.4. The in-situ XRD patterns as a function of temperature in (a) 2D-Ni/VO ₂ /c-YSZ/Si, and (b) 3D-Ni/VO ₂ /c-YSZ/Si heterostructures	235
Figure 9.5. a) Resistivity vs temperature plots for VO ₂ /c-YSZ/Si heterostructures before and after depositing a 6 nm 2D-Ni layer. b) The resistivity vs temperature plot for 3D-Ni/ VO ₂ /c-YSZ/Si heterostructure in the temperature range of 4-370 K. c) Resistivity vs temperature plots in the presence of -1T, 0T, and +1T magnetic field for 3D-Ni/ VO ₂ /c-YSZ/Si heterostructure	238

Figure 9.6. a, b) The zero fields-cooled (ZFC) magnetic moment measurements as a function of temperature for 2D-Ni/VO₂ and 3D-Ni/VO₂ films, respectively. c, d) The field-cooled (FC) magnetic moment measurements as a function of temperature for 2D-Ni/VO₂ and 3D-Ni/VO₂ films, respectively. e) The coercivity vs temperature plot for 2D-Ni/VO₂ and 3D-Ni/VO₂ films. The inset figure represents the exchange bias (H_{EB}) for 2D-Ni/VO₂ and 3D-Ni/VO₂ film. f) The H_{EB} and its second derivative with temperature for 3D-Ni/VO₂ films depict a peak around 350 K..... 239

Figure 9.7. a) The Magnetic moment vs temperature plots at for zero fields cooled (ZFC) and different field-cooled (FC) condition. The inset represents the field magnitude in Oe. b) The derivative of difference between FC and ZFC magnetization vs temperature illustrating a peak around 348K. c, d) The $-\Delta S_m$ (magnetization entropy) vs temperature for 2D-Ni/VO₂ and 3D-Ni/VO₂ films, respectively..... 242

CHAPTER 1

1. Introduction

VO₂ (in the form of freestanding bulk single crystals) can exhibit an extremely sharp and ultrafast (sub-picosecond regime) first-order phase transformation from monoclinic (low-temperature, semiconductor phase) into tetragonal or rutile (high-temperature, metallic phase) structure at 68⁰C in the absence of any internal and external stresses. This semiconductor to metal transition (SMT) in single crystals normally has a large amplitude about 4-5 orders of magnitude change in resistivity and infrared transmission. The SMT is characterized by sharpness (ΔT), amplitude (ΔA), and hysteresis (ΔH). In strain-free crystals, this transition from high-temperature Rutile (R) phase occurs directly into the low-temperature monoclinic M₁ phase. However, in the presence of internal and external stresses, the formation of a transient monoclinic phase which is an intermediate of M₁ and R phases often broadens the transition characteristics. The SMT, known as electrical transition, in a bulk strain-free VO₂ occurs concurrently with monoclinic to tetragonal phase transition, known as a structural phase transition (SPT).

The SMT and SPT characteristics in VO₂ films are found to be extremely sensitive to strain, magnetic alignment, and defects (point defects and clusters, dislocations, and grain boundaries). It is envisaged that the nucleation of rutile and monoclinic phases (M₁ and M₂) is initiated by strain centers, magnetic inhomogeneity, and defects; therefore, SMT and SPT characteristics can be controlled by strain, magnetic tuning, and defect engineering. The schematic Figure 1.1. The coupling between different degrees of freedom in electron-correlated VO₂. shows the coupling between different degrees of freedom in electron-correlated VO₂. The inner circle shows the coupling between spin, charge, lattice, and orbital. The middle ring depicts different ways of controlling the phase transition. The outer ring represents the physical properties which are

affected by inner and middle rings factors. In some cases, the concurrent changes in the physical properties, as traditionally happen in bulk VO₂, can be decoupled or prevented, if one of the four factors of charge, spin, orbital, and the lattice is being locked. The SPT and SMT are described as the changes in physical properties of crystal structure and electrical properties, respectively.

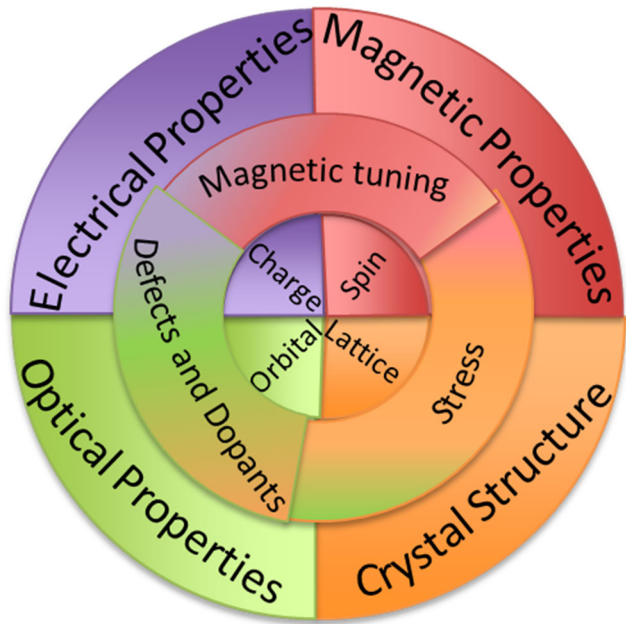


Figure 1.1. The coupling between different degrees of freedom in electron-correlated VO₂. Modified from Ref 1.

Strain can be controlled by adjusting misfit strain using different buffer layer. Defects can be introduced precisely by ion and laser irradiations or vacuum annealing, and their concentrations controlled by annealing in oxygen. Magnetic tuning is achievable through buffer layer choice.

Stress can modify the transition temperature which means it can enhance/degrade nucleation of monoclinic M₁ and M₂ phases. Stress can also remove the structural transition, altogether. The stress and strain in VO₂ thin films can be tuned using different buffer layer in order to have tensile/compressive stress or near-bulk behavior.

The hysteresis (ΔH) increases with the introduction of defects, which may indicate easier nucleation of the M_2 phase and subsequent delay in the transformation to the M_1 phase. The three methods to control defects in VO_2 can be explained as:

1) Swift heavy ion (SHI) irradiation: The ion energies to be used should have energies 100-200MeV for Au and Ag ions. The electronic stopping should dominate over nuclear stopping. Since most of the electronic losses are quickly dissipated into phonons (heating), these experiments provide a unique opportunity to compare these changes with those produced by nanosecond pulsed laser irradiation. The SMT characteristics change from first-order to mixed phase second order phase transformation ².

2) Pulsed laser irradiation: By using nanosecond pulsed laser irradiation (such as KrF EXCIMER, $\lambda = 248$ nm, pulse duration of 25 ns) at energy densities below the threshold for melting ($E = 0.25$ Jcm⁻²), we are able to introduce defects such as vacancies in a controlled way by varying the number of pulses.

3) Vacuum annealing: By annealing in a vacuum of 10^{-6} Torr or lower at high temperature (500⁰C or higher), we can produce vacancy-type defects in a controlled way by varying the time of annealing. Systematic changes in electrical, optical and magnetic properties are produced, which can be reversed by annealing in an oxygen ambient. The property changes produced will be correlated directly with oxygen diffusion distances ($2\sqrt{D\tau}$) where D is the diffusion coefficient and τ is the time of annealing.

The magnetic tuning is achievable by inducing spin alignment across the interface of the buffer layer and VO_2 thin film. VO_2 films can be made ferromagnetic under certain processing conditions, and these magnetic properties, which are quite stable at room temperature, can be further enhanced by inserting an antiferromagnetic layer in between the substrate and VO_2 layer.

Thus magnetic properties can be integrated with electrical and optical properties to enhance functionalities.

The fundamental understanding and control over electrical and structural transitions in VO₂, which occur often simultaneously, are of immense scientific and technological importance with applications ranging from smart switching to sensing devices. In the last decade, abundant efforts have been made focusing on the manipulation of these transitions using defect/dopants and interface engineering³⁻⁷. However, the switching speed and lifetime of such devices are often restricted by the complexities that emanate from the kinetically slower nature of structural transitions (10 picoseconds) in comparison with the electrical transition (0.1 picoseconds)⁸⁻¹¹. This leads to the decoupling between SMT and SPT in the presence of strain, dopants, and defects and detrimentally affects the performance of these devices^{4,6,10}. The contemporaneous of SMT and SPT leaves practical challenges in solid-state VO₂-based device fabricating⁵. On this matter, an ideal solution would be to design a material which displays an isolated electrical transition without accompanying the structural transition. This is achievable by strain-engineering in VO₂ thin films¹²⁻¹⁶.

To systematically investigate the effect of strain on the SMT and SPT, VO₂/TiO₂/TiN/Si and VO₂/c-sapphire heterostructures have been developed and integrated with the two most common substrates for microelectronic industries. These platforms are designed to have two different-orientated domains with different misfit strains enforced by the selected buffer layer in VO₂ thin films. Different domains are studied separately to monitor the effect of strain on the SMT and SPT.

In an effort to remove SPT and obtain isolated occurrence of SMT, VO₂/NiO/c-sapphire was designed, where VO₂ thickness was varied below and above the critical thickness in order to

trap the misfit strain below the critical thickness. VO₂/NiO thin films provide near-bulk behavior for VO₂ when it is grown above the critical thickness since VO₂ is fully relaxed through domain matching epitaxy. While, below the critical thickness, VO₂ undergoes isolated SMT with ferromagnetic behavior.

The vacuum annealing has been employed to study the effect of the defect on the SMT and SPT in VO₂/NiO/c-sapphire heterostructures, below and above the critical thickness. It is shown that it is possible to make room-temperature metallic VO₂ due to a strong defect effect and changing the interaction between the charge, orbital, spin, and lattice degrees of freedom. This design has a unique structure and property to be used as non-volatile memory devices.

The heterostructure of Ni/VO₂/c-YSZ/Si was designed to study the SPT pinning through the spin and lattice degrees of freedom locking enforced by Ni magnetic layer. This heterostructure is integrated with Si and is the ultra-fast candidate for IR sensors devices.

The rest of the dissertation is organized into the following chapters:

Chapter 2. Background knowledge pertinent to this dissertation is presented.

Chapter 3. A brief description of the experimental techniques used for the present work is given.

Chapter 4, 5, 6, and 7 are related to the strain engineering in VO₂ thin films. In chapter 8 and 9 defect engineering and spin engineering of VO₂ thin films are discussed, respectively.

Chapter 4. A detailed study on the integration of bi-epitaxial VO₂ with Si through a novel buffer layer of TiO₂/TiN/Si which is prepared by oxidation of TiN to TiO₂ is reported.

Chapter 5. This chapter discusses the effect of strain on the thermodynamics and kinetics of structural transition in VO₂. A unique bi-epitaxial VO₂ is designed in VO₂/NiO/c-sapphire

heterostructures where two different domains consisting of the different amount of strains. The lag between the electronic and structural transition of VO₂ is reported due to the in-plane strain.

Chapter 6. In this chapter, a method is provided to control the strain uniformly in VO₂ structure. This chapter discusses the critical thickness limit for VO₂/NiO/c-sapphire thin film heterostructures where below that limit the thin film is uniformly strained. This is an introduction to the next chapter.

Chapter 7. This chapter reports a successful removal of structural transition through strain engineering in VO₂ (VO₂/NiO/c-sapphire) when it is grown below the critical thickness.

Chapter 8. This chapter provides a different tool to control the electronic transition in VO₂ by the introduction of point defects (oxygen vacancies). A successful reversible switching behavior in VO₂ is reported where the hysteresis can be turned off and turn into a full metal and vice versa.

Chapter 9. In this chapter, the removal of structural transition is reported through magnetic tuning in VO₂ integrated with Si (Ni/VO₂/c-YSZ/Si). A high coercive field Ni layer provides robust spin to pin the M₂ monoclinic phase in VO₂ which goes through electronic and magnetic transitions. The coercivity in Ni was controlled by the kinetics of growth to have flat film vs islands.

Chapter 10. A summary of different methods for the manipulation of electronic and structural transitions in VO₂ is provided.

REFERENCES

1. Zhou, Y., Ramanathan, S. Mott memory and neuromorphic devices. *P. IEEE*. **103**, 1289-1310 (2015).
2. Gupta, A., Singhal, R., Narayan, J., Avasthi, D. Electronic excitation induced controlled modifications of semiconductor-to-metal transition in epitaxial VO₂ thin films. *J. Mater. Res.* **26** (23), 2901-2906 (2011).
3. Aetukuri, N. B. et al. Control of the metal-insulator transition in vanadium dioxide by modifying orbital occupancy. *Nat. Phys.* **9**, 661 (2013).
4. Théry, V. et al. Role of thermal strain in the metal-insulator and structural phase transition of epitaxial VO₂ films. *Phys. Rev. B*. **93**, 184106 (2016).
5. Mizokawa, T. Metal-insulator transitions: Orbital control. *Nat. Phys.* **9**, 612 (2013).
6. Molaei, R., Bayati, R., Wu, F. & Narayan, J. A microstructural approach toward the effect of thickness on semiconductor-to-metal transition characteristics of VO₂ epilayers. *J. Appl. Phys.* **115**, 164311 (2014).
7. Bayati, R., Molaei, R., Wu, F., Narayan, J. & Yarmolenko, S. Dependence of Semiconductor to Metal Transition of VO₂ (011)/NiO {100}/MgO {100}/TiN {100}/Si {100} Heterostructures on Thin Film Epitaxy and Nature of Strain. *J. Am. Ceram. Soc.* **98**, 1201-1208 (2015).
8. Eames, C. et al. Ionic transport in hybrid lead iodide perovskite solar cells. *Nat. Commun.* **6**, 7497 (2015).
9. Viswanath, B. & Ramanathan, S. Direct in situ observation of structural transition driven actuation in VO₂ utilizing electron transparent cantilevers. *Nanoscale* **5**, 7484–7492 (2013).
10. Tao, Z. et al. Decoupling of Structural and Electronic Phase Transitions in VO₂. *Phys. Rev. Lett.* **109**, 166406 (2012).

11. Cavalleri, A. et al. Picosecond soft x-ray absorption measurement of the photoinduced insulator-to-metal transition in VO₂. *Phys. Rev. B.* **69**, 153106 (2004).
12. Yang, M. et al. Suppression of Structural Phase Transition in VO₂ by Epitaxial Strain in the Vicinity of Metal-insulator Transition. *Sci. Rep.* **6**, 23119 (2016).
13. Gao, X. et al. Nanoscale self-templating for oxide epitaxy with large symmetry mismatch. *Sci. Rep.* **6**, 38168 (2016).
14. Liao, F. et al. Tuning the metal-insulator transition of vanadium dioxide thin films using a stretchable structure. *J. Alloys Compd.* **705**, 468–474 (2017).
15. Yang, M. et al. Surface-growth-mode-induced strain effects on the metal-insulator transition in epitaxial vanadium dioxide thin films. *RSC Adv.* **5**, 80122–80128 (2015).
16. Milani, A. A., Khan, M. T. A., Chakraborty, A. & Husain, I. Equilibrium Point Analysis and Power Sharing Methods for Distribution Systems Driven by Solid-State Transformers. *IEEE Trans. Power Syst.* **33**, 1473–1483 (2018).

CHAPTER 2

2. Background Knowledge

2.1. Vanadium dioxide

2.1.1. VO₂ structural details

VO₂ (in the form of freestanding bulk single crystals) can exhibit an extremely sharp and ultrafast (subpicosecond regime) first-order phase transformation from monoclinic (low-temperature, semiconductor phase) into tetragonal or rutile (high-temperature, metallic phase) structure at 68°C in the absence of any internal and external stresses (Figure 2.1). This semiconductor to metal transition (SMT) in single crystals normally has a large amplitude (about 4-5 orders of magnitude) change in resistivity and infrared transmission. The high-temperature VO₂ phase has a tetragonal (P4₂/mmm) rutile structure, and the low-temperature phase has a monoclinic (P2₁/c) structure (M₁ phase). A remarkable feature of this monoclinic structure is the presence of V-V pairs along its a-axis, where a-mono = 2c-rut alter transformation to the rutile structure. During the phase transformation, the regular V-V separation of 0.287nm in the tetragonal rutile structure transforms to alternate V-V separations of 0.265nm and 0.312nm leading to a doubling of the unit cell^{1,2}. In view of these phase transformation characteristics, we envisage that this transformation results from a single coordinated jump of V cations along a-mono or c-rut. The semiconductor to metal transition (SMT) is influenced greatly by the strain along a-mono or c-rut, which needs to be controlled for reliable device fabrication^{1,2}. In strain-free crystals, this transition from high-temperature rutile (R) phase (a = b = 0.455nm and c = 0.285nm) occurs directly into low-temperature monoclinic M₁ phase (a = 0.575nm; b = 0.453nm; c = 0.538nm, β = 122.60). However, in the presence of internal and external stresses, the formation of a transient

monoclinic ($C2/m$) phase M_2 ($a = 0.906\text{nm}$, $b = 0.580\text{nm}$, $c = 0.425\text{nm}$, $\beta = 91.80$) which is an intermediate of M_1 and R phases, often broadens the transition characteristics (Figure 2.1). The formation of the M_2 phase in thin film heterostructures is caused by internal stresses and constraints imposed by the substrates, which can be controlled by epitaxial growth orientations and relaxation of stresses and strains. The conversion matrix between the lattice parameter of phases can be described with equation 2.1 and 2.2.

$$\begin{pmatrix} a \\ b \\ c \end{pmatrix}_{M_1} = \begin{pmatrix} 0 & 0 & 2 \\ 1 & 0 & 0 \\ 0 & 1 & -1 \end{pmatrix} \begin{pmatrix} a \\ b \\ c \end{pmatrix}_R \quad \text{Equation (2.1)}$$

$$\begin{pmatrix} a \\ b \\ c \end{pmatrix}_{M_2} = \begin{pmatrix} 2 & 0 & 0 \\ 0 & 0 & 2 \\ 0 & -1 & 0 \end{pmatrix} \begin{pmatrix} a \\ b \\ c \end{pmatrix}_R \quad \text{Equation (2.2)}$$

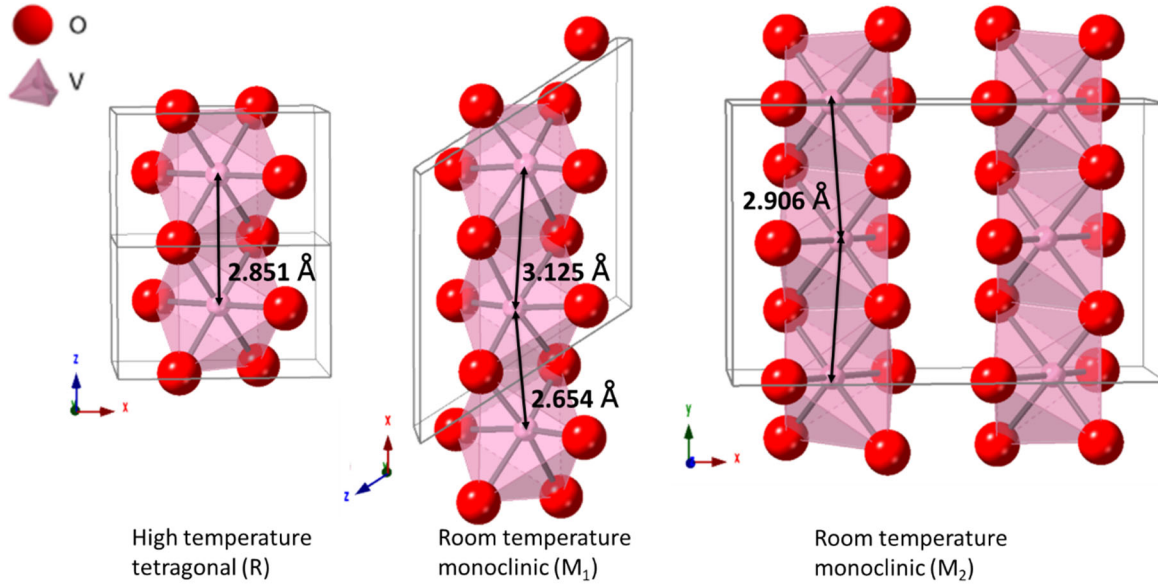


Figure 2.1. Illustration of crystallographic unit-cells of rutile, monoclinic M_1 , and M_2 structures of VO_2 including their oxygen octahedral surrounding vanadium cation with different V-V bond length.

2.1.2. VO_2 phase transition characteristics

The SMT is characterized by sharpness (ΔT), amplitude (ΔA), and width (ΔH) of the hysteresis. These SMT characteristics are critically determined by the details of strains, defects,

interfaces chemistry, and magnetic properties, which are controlled by processing and substrate/buffer-layer parameters. Characteristics of grain boundaries and relative orientation, grain size distribution and defects within the grains play a critical role in determining the characteristics of the hysteresis and the nature of the SMT transition³⁻⁶. The SMT is influenced significantly by residual strain, specifically, the tensile strain in the c-direction increases the transition temperature and the compressive strain decreases the transition temperature from the bulk value⁷⁻⁹. The control over microstructure and defects gives us a tool to design the hysteresis properties and consequently the application for that heterostructures. The hysteresis characteristics, microstructure, and application correlations are shown in Figure 2.2.

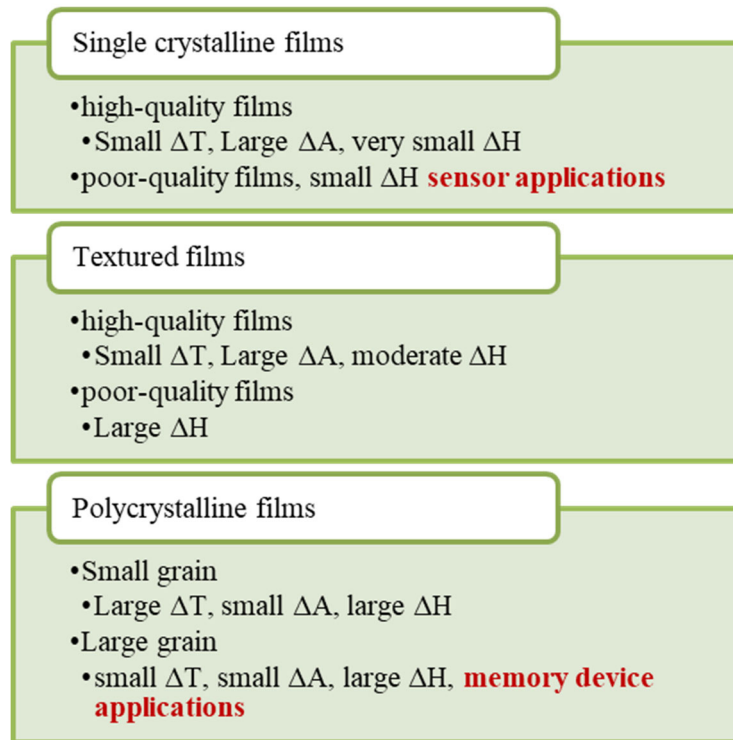


Figure 2.2. The metal-to-insulator hysteresis characteristics for single crystalline, textured (similar out-of-plane orientation, but in-plane rotation), and polycrystalline VO₂ thin-films.

The critical issues, which have not been addressed in any detail so far, include the role of specific defects on the SMT characteristics, and the role of strains on SPT prevention. More importantly, control of these defects to enable one to tune SMT characteristics for intended applications remains largely unexplored. By controlled introduction of defects by laser, vacuum annealing, and ion irradiation ¹⁰, room-temperature ferromagnetism (RTFM) in VO₂/c-sapphire thin film heterostructures can be achieved. The origin of the RTFM in VO₂ films is related to the presence of process-induced intrinsic defects. The ferromagnetic properties such as saturation magnetization and coercivity are expected to be enhanced in VO₂ films by inserting the Ni layer in the Ni/VO₂ heterostructures. The Ni is a ferromagnetic layer which can pin the spin moments of the ferromagnetic VO₂, and more importantly pin the SPT in addition to providing an epitaxial template. Some recent studies have shown evidence of phase coexistence with the coupling of electronic motion and ionic displacements ¹¹. Nanoscale imaging studies, on another hand, show a decoupling between structural and electronic transitions ^{12,13} Thus, further systematic studies on well-characterized samples are needed to resolve the details of SMT and SPT characteristics, which are hindering the potential of VO₂ for nanoelectronics applications.

2.1.3. Band structure across the metal-to-insulator transition

During the metal-to-insulator transition, the V⁴⁺ cation moves away from the center of the oxygen octahedron toward the edges and form V-V pairs whereupon the conductivity decreases sharply. At the high-temperature tetragonal state, V⁴⁺ in the octahedra obstructs the free rotation of the electrons and quenches the orbital angular momentum giving rise to the splitting of the 3d¹ energies into e_g (d_{3x²-r²}, d_{yz}) and t_{2g} (d_{z²-y²}, d_{xy}, d_{zx}) orbitals (Figure 2.3) ¹⁴. The e_g wave functions are pointing toward O²⁻, thus having higher energies, while t_{2g} points between them ¹⁵. Covalent mixing between the two electrons in d_{xy} and d_{zx} and p_π orbitals of the anion results in the formation

of the narrow antibonding π^* and a wider bonding π band. The remaining electron is nonbonding and goes into $d_z^2-y^2$ which is directed parallel to the c-axis as shown in Figure 2.4. This electron is not involved in the V-O bonding and provides V-V bonding along the c-axis, also partially fills the $d_z^2-y^2$, which is the reason for rutile phase being metallic, and reduces the c/a ratio. The relative energies and stabilities of the $d_z^2-y^2$ and d_{xy} , d_{zx} orbitals depend upon the c/a ratio as proposed by Goodenough¹, discussed by Hearn¹⁶, and experimentally shown by Aetukuri¹⁷. According to this theory, the requirement for the insulating band structure is i) destabilizing the π^* orbital and/or stabilizing the bottom half of the $d_z^2-y^2$ orbital by raising the π^* orbital energy above the Fermi level, and ii) splitting of the $d_z^2-y^2$ orbital. Goodenough proposed that the distortion of the structure by displacement of V ions perpendicular to c-axis (Figure 2.5) destabilizes the π^* orbital (the antiferroelectric distortion) and a decrease in the c/a ratio stabilizes the bottom half of the $d_z^2-y^2$ orbital which fulfills the first requirement, and a homopolar V-V bonding along the c-axis split the $d_z^2-y^2$ and defines the energy gap (Figure 2.6)^{1,17}. However, Zylbersztein and Mott believed the role of distortion is to destabilize the π^* orbital and to induce the transition and not to determine the electrical gap¹⁸. They proposed that each V^{4+} has a moment and that the energy to form a carrier (defined as band gap) is equal to $U-1/2(B_1+B_2)-J_H$, where U is the Hubbard intra-atomic correlation energy, B_1 and B_2 are the bandwidth of upper and lower Hubbard bands here for the motion of electron (V^{3+}) and hole (V^{5+}), and J_H is the coupling energy (Figure 2.7). Thus, the bandgap is mainly a correlation gap. At room temperature, U for an electron to jump is bigger than kT, as shown in Figure 2.4. That is, if U (Coulombic repulsion between electrons) is stronger than the kinetic energy t, it can prevent electrons from hopping and delocalization, and as a result, the insulating state is stable in this condition.

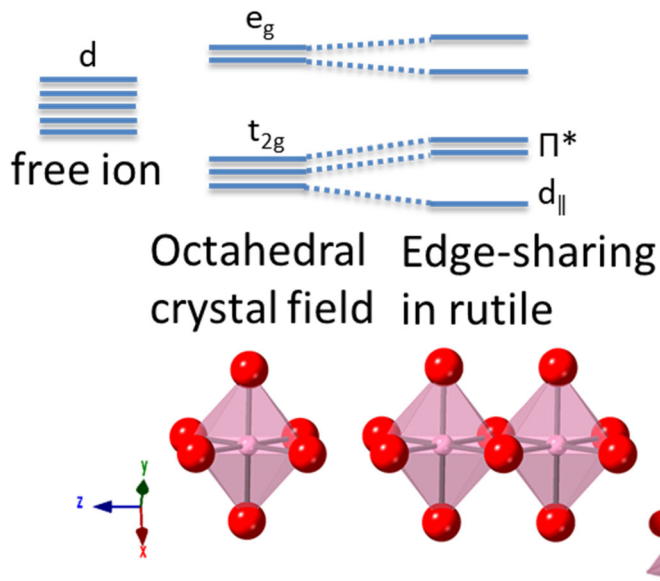


Figure 2.3. The crystal band structure, d-orbital splitting for rutile VO_2 induced by edge-sharing octahedra.

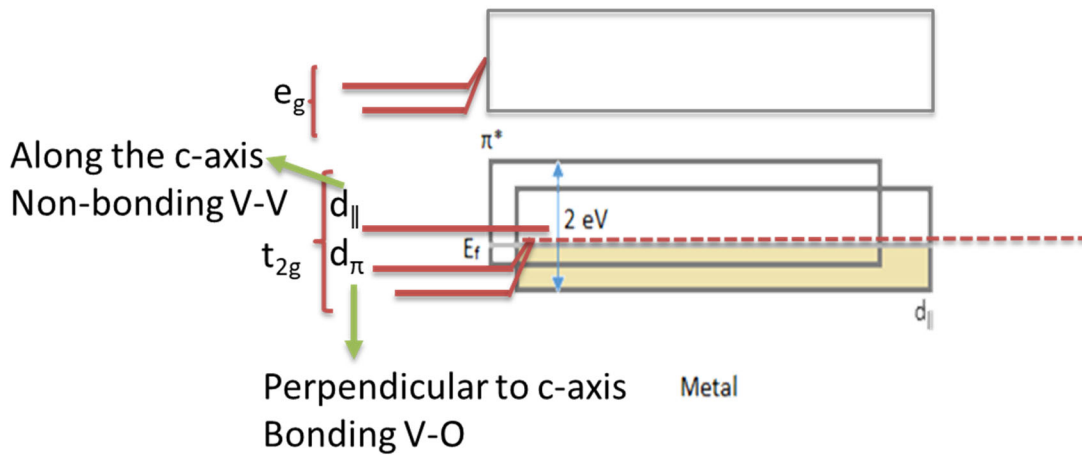


Figure 2.4. The band diagram belongs to VO_2 metallic rutile phase depicting p-d orbitals overlap; two electrons take part in the covalent mixing between O and V (d_{xy} and d_{zx} and p_{π} orbitals) resulting in the formation of the narrow antibonding π^* and a wider bonding π band. The remaining electron is nonbonding and goes into $d_{||}$ ($d_{z^2-y^2}$) which is directed parallel to the c-axis.

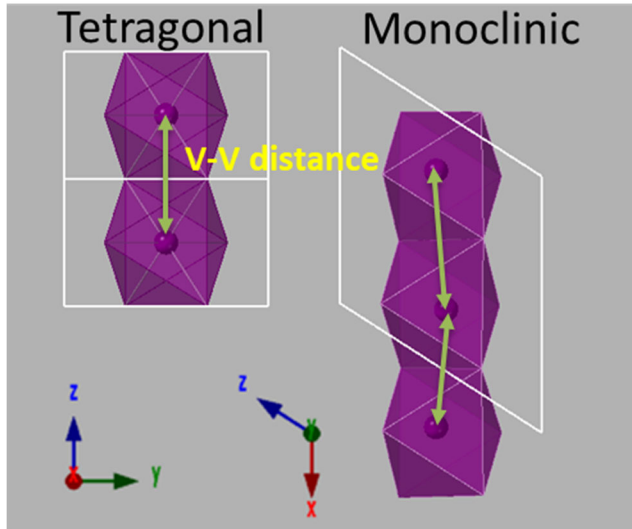


Figure 2.5. The changes in V-V distance from rutile-tetragonal to monoclinic structure in VO_2 . The vanadium atom moves away from the center of the octahedron in the transition from tetragonal to monoclinic.

Peierls Insulator

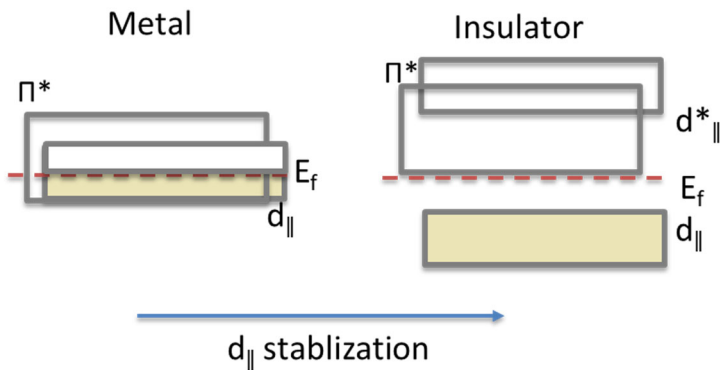


Figure 2.6. The Peierls transition (metal-to-insulator) in VO_2 as the d_{\parallel} band splits into a lower bonding d_{\parallel} and upper antibonding d_{\parallel}^* due to homopolar V-V bonding formation.

Mott Insulator

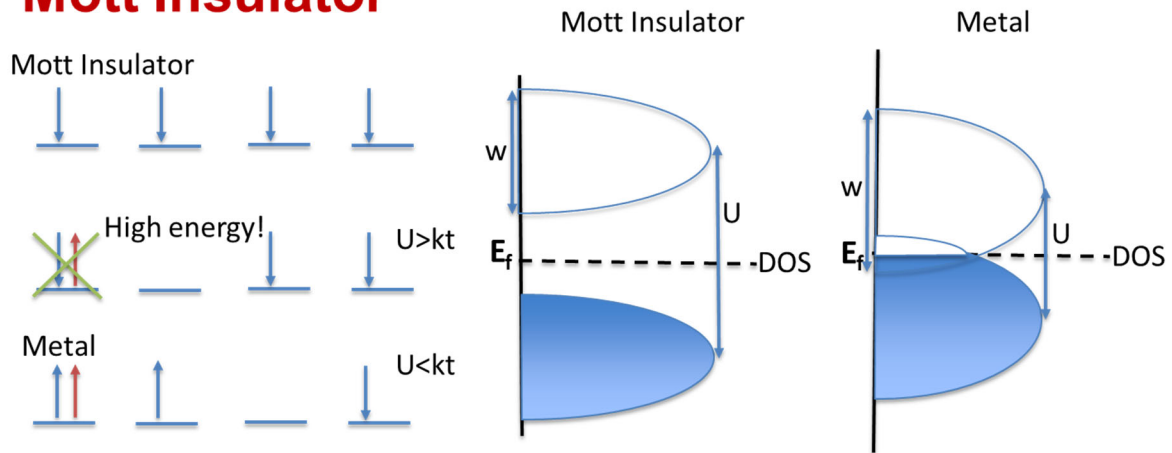


Figure 2.7. The Mott transition (metal-to-insulator) in VO_2 . U is the Hubbard intra-atomic correlation energy. When U is bigger than the kinetic energy t , it can prevent electrons from hopping and delocalization and the insulator state dominates. The bandgap is defined by U which is a correlation gap.

2.1.4. Control of transition through strain engineering (lattice and orbital degrees of freedom)

2.1.4.1. Peierls point of view

In this view, the changes in lattice degrees of freedom, rearrange the orbital degeneracy and their occupancy. It is shown experimentally that the tensile strain along the c-axis increases the insulator to metal transition¹⁷. The changes in V-O bond length perpendicular to c-axis as a result of strain, perturb the bonding π and non-bonding π^* orbitals. The relative energy of π^* orbital and its occupancy affect the transition temperature. If the π^* is shifted up due to compressive stress perpendicular to c-axis and along $\langle 110 \rangle$ direction (increase in the p-d orbitals' overlap) as shown in Figure 2.8, the $d_{||}$ orbital becomes stabilized (the first requirement for metal to insulator transition), which pushes the MIT to a higher temperature.

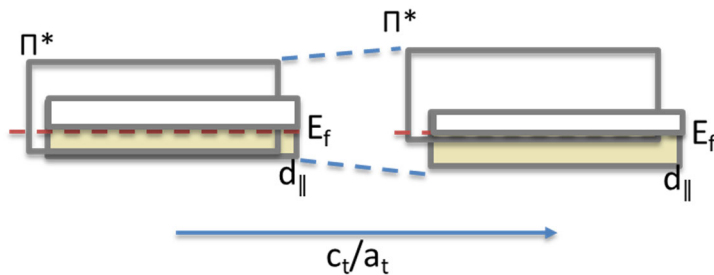


Figure 2.8. The schematic depiction of orbital occupancy changes as c/a ratio in rutile VO_2 varies (strain along the axes) from Peierls point of view.

2.1.4.2. Mott point of view

In this view, there is a competition between U (localization) and t (delocalization) which derives the transition¹⁹. Modifying the bandwidth (w) directly affects the energy t . Compressive strain along the c-axis increases the bandwidth and consequently enhances t which leads to the lowering of the insulator to metal transition temperature as shown in Figure 2.9.

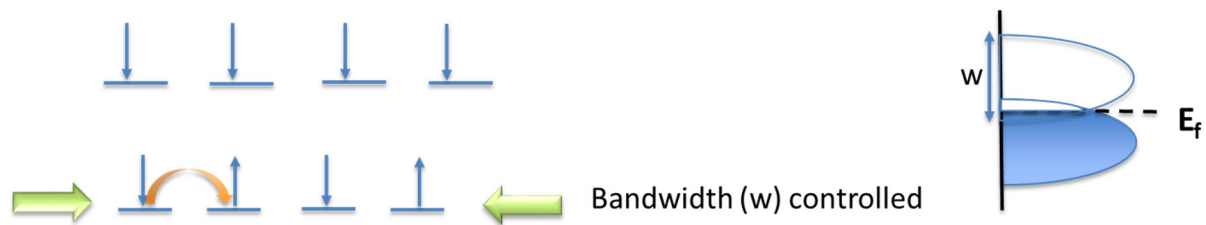


Figure 2.9. Change in the bandwidth through strain engineering and its effect on electron hopping in VO₂ from Mott point of view.

2.1.5. Control of transition through defect engineering (charge degree of freedom)

2.1.5.1. Peierls point of view

Another way to control the transition is through doping. According to Goodenough, adding holes or any p-type dopant distorts the oxygen octahedral and displaces the vanadium from the center of octahedral. This means V-V and V-O bond length will effectively change. The difference in V-V bond length is what Goodenough refer as an anti-ferroelectric component of the metal to insulator transition which leads to stabilization of the bottom half of d_i. Also, the disturbance in V-O bonding affect the π^* and push it up as shown in Figure 2.10a. As a result, it is expected that adding holes increase the temperature for the insulator to metal transition. Adding electrons, on the other hand, introduce electrons into π^* orbital (downshift) and increase the conductivity of the metallic phase as shown in Figure 2.10b. That is the metal to insulator transition temperature is decreased.

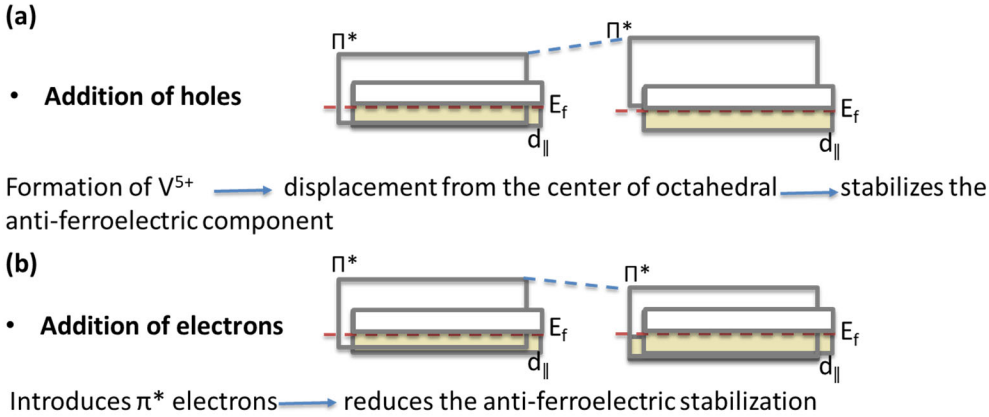


Figure 2.10. Effect of addition of holes and electrons on d-orbital bands' level and electron occupancy in VO_2 from Peierls point of view.

2.1.5.2. Mott point of view

Doping the system with electrons and holes changes the effective U (interaction) between electrons. If added to the system, electrons and holes can reduce the U , Coulombic repulsion. That allows certain electrons to hop at lower cost and lower temperature and lead to the metallic state as shown in Figure 2.11.

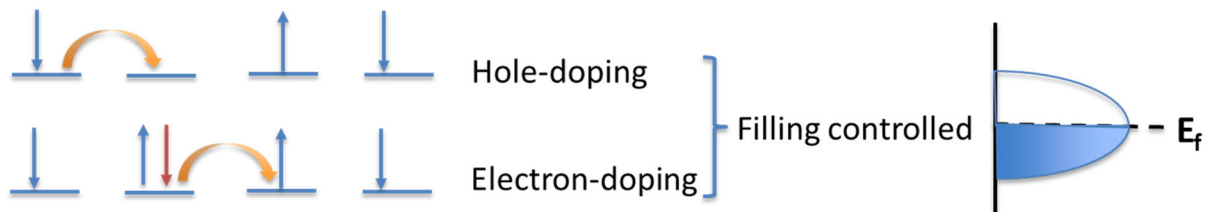


Figure 2.11. Effect of introduction of holes and electrons in changing coulombic interaction and thus VO_2 metal-to-insulator transition.

2.1.6. Control of transition through spin engineering (spin degree of freedom)

Spin ordering and its interplay are rather more complex (Figure 2.12). If electron hopping is hindered due to magnetic ordering, the insulating state is favored. If the spin direction of the adjacent localized site is opposite of the initial site, the electron feels higher energy on one of the two sites due to Hund's rule coupling²⁰. Thus, the more coherent the system, it is more favorable

for an electron to hop. In other words, an electron can hop without magnetic scattering. At higher temperature, given enough energy, the ferromagnetic ordering is favored. The spin fluctuation is also known to cause the transition.

In this study, we used a strong ferromagnet with the robust spin to induce spin ordering in VO₂ through the interface. The spin order is coupled with lattice degree of freedom and has the ability to pin the structural transition.

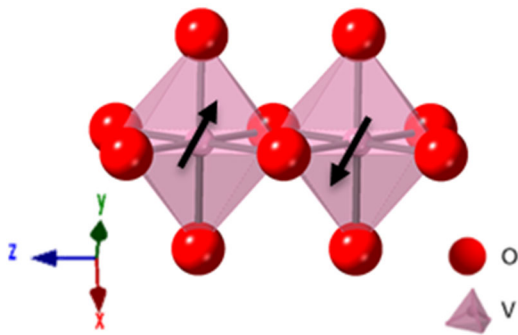


Figure 2.12. The spin ordering affects electron hopping due to Hund's rule coupling in VO₂.

In order to control the VO₂ characteristics, it needs to be grown epitaxially. As it was explained, the stimuli need to take an effect in a certain direction, in order to get specific properties. Besides, from an application point of view, if VO₂ is being employed in the bulk form, after a certain number of cycles, it would crack due to volume changes across the structural transition. However, thin films can withstand going through transition cycles which increases the lifetime of devices. As a result, VO₂-based devices need to rely on epitaxial VO₂ thin films.

2.2. Thin film epitaxy

Epitaxy is defined as extended single crystalline growth of a film following the crystalline substrate ordering. The term comes from Greek roots of "epi" and "taxis", meaning "above" and "an ordered manner", respectively. The film can be the same material as the substrate which is

known as homoepitaxy, or it can be different being referred to as heteroepitaxy. This method allows us to create different single-crystalline layers in the semiconductor industry, quantum wells in electronic and optical devices, superconductor devices, etc.... Misfit strain, then, can be defined as the difference between lattice parameters of the film and substrate. If the lattice parameter of the film and substrate are identical, there is no misfit strain.

2.1.1. Different growth modes

Three different growth modes have been introduced for thin film growth; Frank-van der Merwe, Volmer-Weber, and Stranski-Krastanov²¹. These growth modes depend on the film, substrate, and the interface surface energies as shown in Figure 2.13.

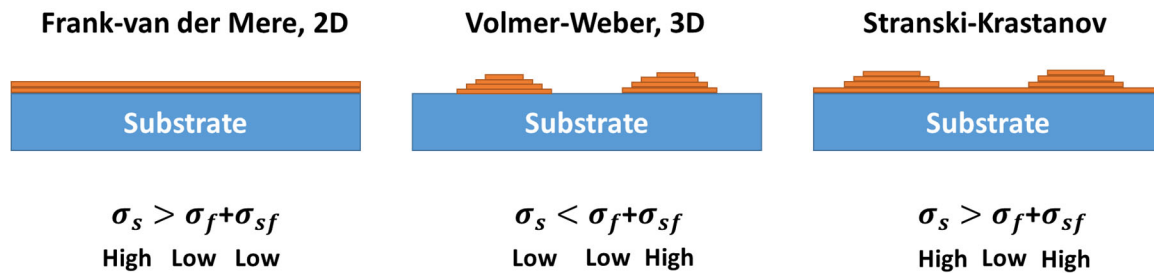


Figure 2.13. Different growth modes of thin films depending on the free surface energy of the film σ_f , substrate σ_s , and the interfacial energy between film and substrate σ_{sf} .

2.1.1.1. Frank-van der Merwe

This mode is also known as 2D growth mode, where the surface energy of the substrate is high and deposited atoms tend to have a strong bond with the substrate and consequently grow monolayer by monolayer.

2.1.1.2. Volmer-Weber

This mode called also 3D mode, where the surface energy of the film is high and deposited atoms tend to bond with themselves and form 3D islands which propagate and reach

each other eventually. This growth mode provides in-plane rotation since each island may have different in-plane alignments and form a grain boundary where they meet each other.

2.1.1.3. Stranski-Krastanov

This mode is a combination of 2D and 3D growth modes. In this mechanism, the interface energy between substrate and film is high leads to an initial 2D growth up to a critical thickness for 1-5 monolayers followed by 3D island nucleation and propagation on top of it.

2.2.2. The fundamental difference between lattice-matching epitaxy (LME) and domain matching epitaxy (DME)

In LME, at the interface of the film and the substrate, the matching is considered between lattice parameters. The misfit strain for this kind of matching needs to be smaller than 7-8%²¹. In this case, the film grows pseudomorphically adopting the lattice parameter of the film up to a certain thickness which is called critical thickness. After that, dislocations (missing or extra planes) starts nucleating at the film surface and then glide into the interface to relax the film. For certain application where the interface of the film/substrate is critical, the selection of the material and the growth method is a defining factor to stay below the critical thickness and avoid the dislocation formation.

On the other hand, DME considers the interface matching between lattice planes, not lattice parameters. DME allows us to grow epitaxial films even though the strain is above 7-8%²². In this framework, the film can have a different orientation (fixed) than or similar to the substrate, which depends on the nature of the misfit. Here, the misfit is being accommodated by matching of integral multiples of planes which are called domains, and there is one extra/missing plane (dislocation) corresponding to each domain. If the misfit is small, then LME occurs. If the misfit is large, DME

governs. The size of the domains in DME varies systematically based on the amount of misfit strain. In the following, the misfit strain is being explained in a different regime.

2.2.3. Misfit strain

2.2.3.1. Misfit strain in LME regime

In conventional LME, the misfit strain is defined as:

$$\varepsilon = \frac{a_f}{a_s} - 1 \quad \text{Equation (2.3)}$$

where a_f and a_s are lattice constant of the film and substrate, respectively. The value of ε needs to stay below 7-8% in this regime. As the strain gets larger, the critical thickness gets smaller²³.

The critical thickness can be calculated as:

$$h_c = \frac{b(1-\nu\cos^2\theta)\sin\theta\cos\phi}{4\pi(1+\nu)\varepsilon} \ln\left(\frac{\alpha h_c}{b}\right) \quad \text{Equation (2.4)}$$

where b is the magnitude of Burgers vector of the dislocation, ν is the Poisson's ratio, θ is the angle between Burgers vector and dislocation line, ϕ is the angle between the normal of the dislocation plane and film plane, and α is the dislocation core radius factor which varies with strain ε .

2.2.3.2. Misfit strain in DME regime

In DME regime, the initial misfit strain is being calculated according to equation (2.5). This strain can be relaxed by matching of m planes of the film with n planes of the substrate in a domain (m and n are integers). If this matching occurs, then the residual strain can be calculated according to:

$$\varepsilon_r = \frac{m d_f}{n d_s} - 1 \quad \text{Equation (2.5)}$$

where d_f and d_s are lattice planes of the film and substrate, respectively. The matching of d_f and d_s also depends on crystal symmetry. For example, (111) planes of a cubic crystal film can be

matched with (0001) planes of a hexagonal crystal substrate. If perfect matching occurs, $\varepsilon_r = 0$, and $md_f = nd_s$. If $\varepsilon_r \neq 0$, then domains may alternate with a certain frequency of α to accommodate the residual strain and provide perfect matching ²²:

$$(m + \alpha)d_f = (n + \alpha)d_s \quad \text{Equation (2.6)}$$

That is m/n matching alternates with (m+1)/(n+1) matching with the frequency of α . If the amount of strain is smaller than 50%, then m and n are consecutive. Above 50%, n is some function of m, f(m). Thus, we can write:

$$(m + \alpha)\varepsilon = \begin{cases} 1, & \varepsilon \leq 0.5 \\ f(m), & \varepsilon > 0.5 \end{cases} \quad \text{Equation (2.7)}$$

Figure 2.14 shows the systematic drop of integral multiple with increasing strain.

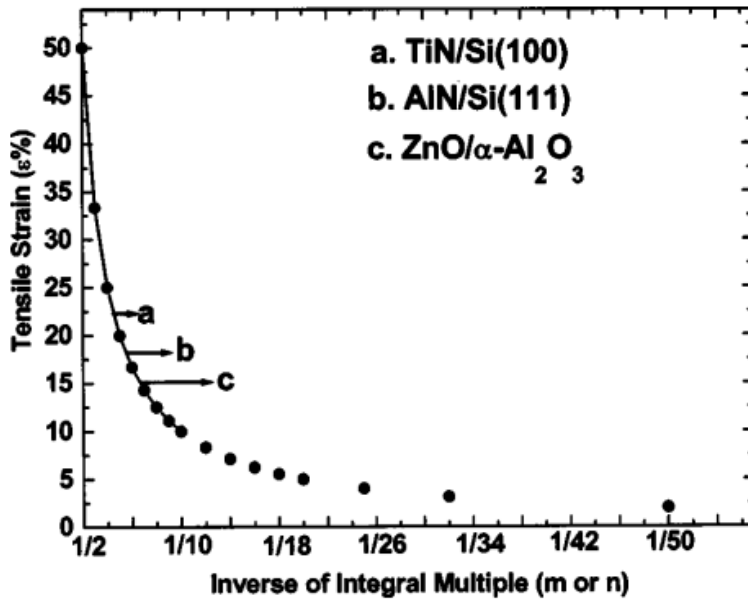


Figure 2.14. The systematic decrease of integral multiple with strain ²².

The matching of integral planes across the hexagonal film/hexagonal substrate and cubic film/hexagonal film/substrate interfaces can be calculated according to Equation (2.8) and (2.9), respectively:

$$(n+\alpha)\sqrt{\frac{4}{3}\left[\frac{h_2^2+h_2k_2+k_2^2}{a_2^2}\right]}+\frac{l_2^2}{c_2^2}=(m+\alpha)\sqrt{\frac{4}{3}\left[\frac{h_1^2+h_1k_1+k_1^2}{a_1^2}\right]}+\frac{l_1^2}{c_1^2}\text{Equation (2.8)}$$

$$(n+\alpha)\sqrt{\frac{4}{3}\left[\frac{h_2^2+h_2k_2+k_2^2}{a_2^2}\right]}+\frac{l_2^2}{c_2^2}=(m+\alpha)\sqrt{\frac{(h_1^2+k_1^2+l_1^2)}{a_1^2}}\text{Equation (2.9)}$$

where a_1, c_1 and a_2, c_2 are lattice constants for film and substrate or buffer layer; and m ($h_1k_1l_1$) planes of the film are matching with n ($h_2k_2l_2$) planes of the substrate or buffer layer.

In DME regime, as the strain increases, the critical thickness above which dislocation can form become smaller. As a result, it is possible to decrease the critical thickness to one or two monolayers where dislocations can nucleate at steps and glide only one or two monolayers leaving the rest of the film relaxed. This gives an advantage for multiple reasons. First, the large dislocation glide barrier, especially in III-nitride systems, is being removed. Second, there was a large number of surface steps within the monolayer which provides lower dislocation nucleation barrier. Third, it is possible to confine the threading dislocation near the interface. That requires the initial 2D growth which will be explained later in the growth section.

Apart from the misfit strain, there are other sources of strain in thin films including thermal strain and defect strain which needs consideration.

2.2.4. Thermal mismatch strain

Thermal mismatch strain emanates from the difference between thermal expansions coefficients of the film and the substrate. The thermal mismatch strain can be calculated as:

$$\varepsilon_T = (\alpha_f - \alpha_s)\Delta T\text{Equation (2.10)}$$

where α_s and α_f are the thermal expansion coefficient of substrate and film, respectively. ΔT is the temperature difference between the growth temperature and room temperature ($\Delta T = T_{@growth} - T_{RT}$). Thermal strains are typically small and as a result hard to relax. There are two reasons behind this; first, the critical thickness corresponding to small strain is large, and second,

this strain being introduced to the film during cool-down when the film is already formed. As a result, the dislocation needs to glide a larger distance to the interface. Thermal strain can be the source of crack and lamination if the films are grown thick without thermal strain consideration.

2.2.5. Defect strain

This strain is associated with the presence of 0D (point defects), 1D (dislocations), 2D (grain boundaries), and 3D defects (stacking faults). These defects can cause local strains associated with a stress field around them. Defect strain can add up to or subtract from the misfit strain. Thus, they can affect the critical thickness value and help to stabilize a pseudomorphic phase. These defects are especially potent if they are charged which gives them the ability to change the property of the material.

2.2.6. Stress-strain relationship

Stress and strain play a critical role in thin film heterostructures' properties. The source of strain can be any of the above-mentioned factors. The relationship between strain-stress is explained in cubic and hexagonal films.

2.2.6.1. The stress-strain relationship in cubic thin films

The general relationship between stress and strain in a cubic crystal can be written as:

$$\begin{pmatrix} \sigma_{11} \\ \sigma_{22} \\ \sigma_{33} \\ \sigma_{23} \\ \sigma_{13} \\ \sigma_{12} \end{pmatrix} = \begin{pmatrix} C_{11} & C_{12} & C_{12} & 0 & 0 & 0 \\ C_{12} & C_{11} & C_{12} & 0 & 0 & 0 \\ C_{12} & C_{12} & C_{11} & 0 & 0 & 0 \\ 0 & 0 & 0 & C_{44} & 0 & 0 \\ 0 & 0 & 0 & 0 & C_{44} & 0 \\ 0 & 0 & 0 & 0 & 0 & C_{44} \end{pmatrix} * \begin{pmatrix} \epsilon_{11} \\ \epsilon_{22} \\ \epsilon_{33} \\ 2\epsilon_{23} \\ 2\epsilon_{13} \\ 2\epsilon_{12} \end{pmatrix} \quad \text{Equation (2.11)}$$

where C_{ij} is the stiffness coefficient, σ_{xy} and ϵ_{xy} are the stress and strain, respectively, along the xy direction; as x, y, and z the principle axes in a crystal correspond to 1, 2, and 3, respectively.

For thin films, $\sigma_{33} = 0$, since there is no stress along the out-of-plane direction. Thus, we will have:

$$\sigma_{33} = C_{12}\varepsilon_{11} + C_{12}\varepsilon_{22} + C_{11}\varepsilon_{33} = 0 \quad \text{Equation (2.12)}$$

We can also write the relationship between stiffness coefficients and shear modulus μ , lamé constant λ , and Poisson's ratio ν as:

$$C_{11} = \lambda + 2\nu \quad \text{Equation (2.13)}$$

$$\lambda = \frac{\nu\mu}{1-2\nu} = C_{12} \quad \text{Equation (2.14)}$$

$$\mu = 0.5(C_{11} - C_{12}) = C_{44} \quad \text{Equation (2.15)}$$

Accordingly, we can write:

$$\frac{\varepsilon_{33}}{\varepsilon_{11} + \varepsilon_{22}} = -\frac{\nu}{1-\nu} \quad \text{Equation (2.16)}$$

If the crystal is cubic, we can assume $\sigma_{11} = \sigma_{22}$ and $\varepsilon_{11} = \varepsilon_{22}$. From the matrix:

$$\sigma_{11} = C_{11}\varepsilon_{11} + C_{12}\varepsilon_{11} + C_{12}\varepsilon_{33} \quad \text{Equation (2.17)}$$

Using Equation (2.16) and (2.17), we will have:

$$\sigma_{11} = \frac{\varepsilon_{11}2\mu(1+\nu)}{1-\nu} \quad \text{Equation (2.18)}$$

In thin films, dislocations' glide is determined by the critical resolved shear stress within the primary slip system which needs to exceed the yield stress of the material, where ε_{11} is the initial misfit strain. The critical resolved shear stress in the system follows ²³:

$$\tau_r = \sigma_{11}\cos\phi\cos\lambda \quad \text{Equation (2.19)}$$

where ϕ is the angle between the normal to the slip plane and stress direction and λ is the angle between the Burgers vector and stress direction.

2.2.6.2. The stress-strain relationship in hexagonal thin films

The general relationship between stress and strain in the hexagonal crystal can be written as ²⁴:

$$\begin{pmatrix} \sigma_{11} \\ \sigma_{22} \\ \sigma_{33} \\ \sigma_{23} \\ \sigma_{13} \\ \sigma_{12} \end{pmatrix} = \begin{pmatrix} C_{11}C_{12}C_{13} & 0 & 0 & 0 & 0 & 0 \\ C_{12}C_{11}C_{12} & 0 & 0 & 0 & 0 & 0 \\ C_{13}C_{13}C_{33} & 0 & 0 & 0 & 0 & 0 \\ 0 & 0 & 0 & C_{44} & 0 & 0 \\ 0 & 0 & 0 & 0 & C_{44} & 0 \\ 0 & 0 & 0 & 0 & 0 & 0.5(C_{11} - C_{12}) \end{pmatrix} * \begin{pmatrix} \epsilon_{11} \\ \epsilon_{22} \\ \epsilon_{33} \\ 2\epsilon_{23} \\ 2\epsilon_{13} \\ 2\epsilon_{12} \end{pmatrix} \quad \text{Equation (2.20)}$$

where C_{ij} is the stiffness coefficient, σ_{xy} and ϵ_{xy} are the stress and strain, respectively, along the xy direction; as x , y , and z the principle axes in a crystal correspond to 1, 2, and 3, respectively. In the hexagonal system, the relationship between stiffness coefficients and shear modulus μ , lamé constant λ , and Poisson's ratio ν can be written as:

$$\lambda + 2\mu = \frac{1}{15}(8C_{11} + 4C_{13} + 3C_{33} + 8C_{44}) \quad \text{Equation (2.21)}$$

$$\mu = \frac{1}{30}(7C_{11} - 5C_{12} + 2C_{33} + 2C_{44} - 4C_{13}) \quad \text{Equation (2.22)}$$

$$\lambda = \frac{1}{15}(C_{11} + C_{33} + 5C_{12} + 8C_{13} - 4C_{44}) \quad \text{Equation (2.23)}$$

In polar thin films, where c -axes is the out-of-plane direction, we can write:

$$\sigma_{33} = C_{13}\epsilon_{11} + C_{13}\epsilon_{22} + C_{33}\epsilon_{33} = 0 \quad \text{Equation (2.24)}$$

And we will have:

$$\epsilon_{33} = -\frac{C_{13}}{C_{33}}(\epsilon_{11} + \epsilon_{22}) \quad \text{Equation (2.25)}$$

In the basal plane, we can assume $\epsilon_{11} = \epsilon_{22}$.

In the non-polar film, we can write:

$$\sigma_{11} = C_{11}\epsilon_{11} + C_{12}\epsilon_{22} + C_{13}\epsilon_{33} = 0 \quad \text{Equation (2.26)}$$

Therefore, we will have:

$$\epsilon_{22} = -\frac{C_{11}}{C_{12}}\epsilon_{11} - \frac{C_{13}}{C_{12}}\epsilon_{33} \quad \text{Equation (2.27)}$$

REFERENCES

1. Goodenough, J. B. The two components of the crystallographic transition in VO₂. *J. Solid State Chem.* **3**, 490–500 (1971).
2. Cavalleri, A. *et al.* Picosecond soft x-ray absorption measurement of the photoinduced insulator-to-metal transition in VO₂. *Phys. Rev. B* **69**, 153106 (2004).
3. Jin, P., Yoshimura, K. & Tanemura, S. Dependence of microstructure and thermochromism on substrate temperature for sputter-deposited VO₂ epitaxial films. *J. Vac. Sci. Technol. A Vacuum, Surfaces, Film.* **15**, 1113–1117 (1997).
4. Suh, J. Y., Lopez, R., Feldman, L. C. & Jr, R. F. H. Semiconductor to metal phase transition in the nucleation and growth of VO₂ nanoparticles and thin films. *J. Appl. Phys.* **96**, 1209–1213 (2004).
5. Brassard, D., Fourmaux, S., Jean-Jacques, M., Kieffer, J. C. & Khakani, M. A. El. Grain size effect on the semiconductor-metal phase transition characteristics of magnetron-sputtered VO₂ thin films. *Appl. Phys. Lett.* **87**, 3 (2005).
6. Narayan, J. & Bhosle, V. M. Phase transition and critical issues in structure-property correlations of vanadium oxide. *J. Appl. Phys.* **100**, 3524 (2006).
7. Muraoka, Y. & Hiroi, Z. Metal-insulator transition of VO₂ thin films grown on TiO₂ (001) and (110) substrates. *Appl. Phys. Lett.* **80**, 583–585 (2002).
8. Yang, T.-H. *et al.* Semiconductor-metal transition characteristics of VO₂ thin films grown on c- and r-sapphire substrates. *J. Appl. Phys.* **107**, 6 (2010).
9. Gupta, A., Narayan, J. & Dutta, T. Near bulk semiconductor to metal transition in epitaxial VO₂ thin films. *Appl. Phys. Lett.* **97**, 3 (2010).

10. Gupta, A., Singhal, R., Narayan, J., Avasthi, D. Electronic excitation induced controlled modifications of semiconductor-to-metal transition in epitaxial VO₂ thin films. *J. Mater. Res.* **26** (23), 2901-2906 (2011).
11. Zhong, X., LeClair, P., Sarker, S. K. & Gupta, A. Metal-insulator transition in epitaxial VO₂ thin films on TiO₂ (100). *Phys. Rev. B* **86**, 094114 (2012).
12. Qazilbash, M. M. *et al.* Nanoscale imaging of the electronic and structural transitions in vanadium dioxide. *Phys. Rev. B* **83**, 165108 (2011).
13. Qazilbash, M. M. *et al.* Mott transition in VO₂ revealed by infrared spectroscopy and nano-imaging. *Science* **318**, 1750–1753 (2007).
14. Fujimori, A., Bocquet, A. E., Saitoh, T. & Mizokawa, T. Electronic structure of 3d transition metal compounds: systematic chemical trends and multiplet effects. *J. Electron Spectros. Relat. Phenomena* **62**, 141–152 (1993).
15. Tokura, Y. & Nagaosa, N. Orbital physics in transition-metal oxides. *Science* **288**, 462–468 (2000).
16. Hearn, C. J. Phonon softening and the metal-insulator transition in VO₂. *J. Phys. C Solid State Phys.* **5**, 1317 (1972).
17. Aetukuri, N. B. *et al.* Control of the metal-insulator transition in vanadium dioxide by modifying orbital occupancy. *Nat. Phys.* **9**, 661 (2013).
18. Zylbersztein, A. & Mott, N. F. Metal-Insulator Transition in Vanadium Dioxide. *Phys. Rev. B* **11**, 4383–4395 (1975).
19. Pergament, A., Stefanovich, G. & Markova, N. The Mott criterion: So simple and yet so complex. *arXiv Prepr. arXiv1411.4372* (2014).
20. Imada, M., Fujimori, A. Metal-insulator transitions. *Rev. Mod. Phys.* **70**, 1039-1261 (1998).

21. Matthews, J., Blakeslee, A. E. Defects in epitaxial multilayers: I. Misfit dislocations. *J. Cryst. Growth.* **27**, 118-125 (1974).
22. Narayan, J. & Larson, B. C. Domain epitaxy: A unified paradigm for thin film growth. *J. Appl. Phys.* **93**, 278–285 (2003).
23. Narayan, J. Recent progress in thin film epitaxy across the misfit scale (2011 Acta Gold Medal Paper). *Acta Mater.* **61**, 2703–2724 (2013).
24. Moatti, A. & Narayan, J. High-quality TiN/AlN thin film heterostructures on c-sapphire. *Acta Mater.* **145**, 134-141 (2018).

CHAPTER 3

3. Experimental Techniques

3.1. Buffer layers and substrates

3.1.1. NiO

NiO is an antiferromagnetic transition metal oxide with NaCl structure which belongs to $Fm\bar{3}m$ space group (Figure 3.1). The lattice constants of the NiO cubic unit cell equals 4.178 Å. NiO is a Mott-Hubbard insulator with an optical band gap of 4.3 eV. It is explained that the band splitting in NiO is due to the antiferromagnetic lattice¹. The crystal lattice for such a splitting need to be simple cubic. In NiO, the t_{2g} band in d-orbital is full with six electrons and the e_g band has the potential to be filled with four electrons. The antiferromagnetic sublattice in NiO could split the e_g band into two bands with two electrons in each per atom (Figure 3.1). The gap between these two bands is defined as U . However, it is uncertain if the carriers remain in the e_g band.

NiO makes an excellent buffer layer for VO_2 since VO_2 structure can be fully relaxed on top of it through domain matching epitaxy (this will be explained in the following sections). The thermal expansion coefficient of NiO is reported to be $2.1 \times 10^{-5} \text{ K}^{-1}$.

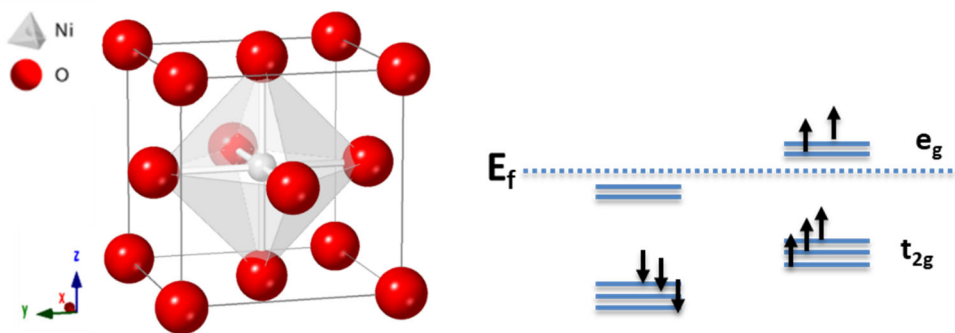


Figure 3.1. The NiO unit cell including Ni cation surrounded by oxygen octahedron and its d-orbital band structure. NiO has an antiferromagnetic nature which is the cause of its insulating properties.

3.1.2. C-YSZ (cubic-yttria stabilized zirconia)

At room temperature, the crystal structure of ZrO_2 depends on the amount of yttria used to stabilize the structure. Pure ZrO_2 has a monoclinic structure, and as the yttria content increases from 3 to 8 mol%, the structure changes from tetragonal to cubic. Cubic YSZ belongs to fluorite structure and space group of $\text{Fm}\bar{3}\text{m}$. The lattice constant of c-YSZ is reported to be 5.514 \AA .

YSZ makes an excellent buffer layer on a silicon substrate due to its chemical stability on Si. The free energy formation of ZrO_2 ($\Delta G(800 \text{ K}) = -941.6 \text{ kJ mol}^{-1}$) is reported to be more negative than that of SiO_2 ($\Delta G(800 \text{ K}) = -734.2 \text{ kJ mol}^{-1}$). YSZ is reported to have a high dielectric constant (~ 25) and large bandgap (7.8 eV)². The thermal expansion coefficient of YSZ equals $\sim 11.4 \times 10^{-6} \text{ K}^{-1}$ ³.

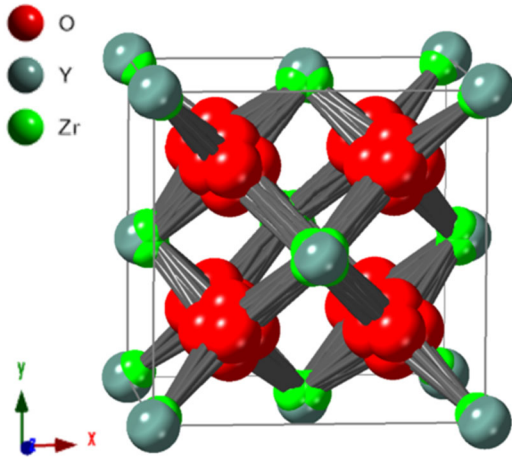


Figure 3.2. The cubic yttria stabilized ZrO_2 unit cell.

3.1.3. Nickel

Nickel crystallizes into a face-centered cubic lattice that belongs to the space group of $\text{Fm}\bar{3}\text{m}$ (Figure 3.3). The lattice constant is reported to be 3.45 \AA for this structure. Ni is a strong ferromagnetic which is reported to have the magnetic moment of $0.6 \mu_B$ ⁴.

The thermal expansion is reported to be $\sim 13 \times 10^{-6} \text{ K}^{-1}$ and the electrical resistivity is $\sim 8 \times 10^{-8} \Omega \cdot \text{m}$.

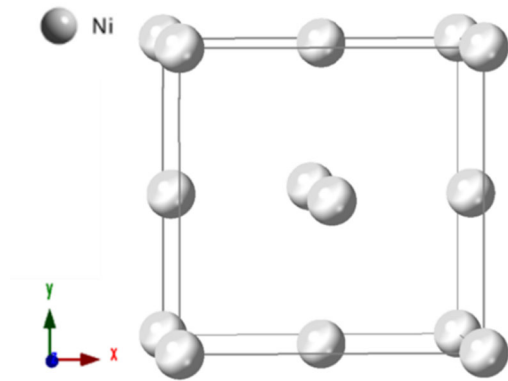


Figure 3.3. The face-centered cubic lattice of nickel.

3.1.4. TiN

Titanium nitride makes an excellent buffer layer due to its extraordinary behavior including being a diffusion barrier. TiN is extremely hard material with a metallic electrical resistivity of $15 \mu\Omega \cdot \text{cm}$. The thermal expansion coefficient is reported to be $9.35 \times 10^{-6} \text{ K}^{-1}$. These properties make TiN a perfect bottom electrode in the electronics industry, as well. TiN has a NaCl structure and belongs to $Fm\bar{3}m$ space group. The lattice constant reported for this material is 4.244 \AA .

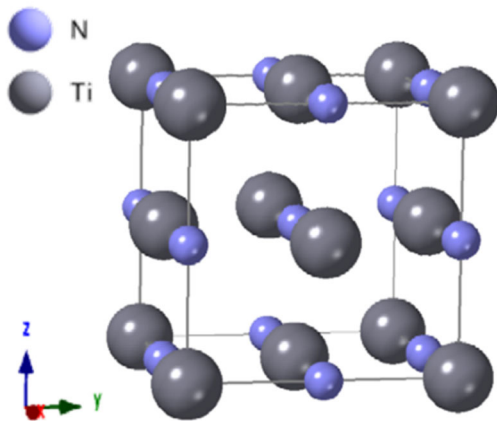


Figure 3.4. The titanium nitride TiN unit cell following NaCl structure.

3.1.5. TiO₂

TiO₂ can crystallize into three different natural polymorphs of anatase, rutile, and brookite (Figure 3.5). Thermodynamically, rutile has the most stable structure. Rutile belongs to the space group of P4₂/mnm with the lattice constants of a=4.593 Å and c=2.958 Å. The bandgap is reported to be 3 eV with the refractive index of 2.9^{8,9}. This structure consists of chains of edge-sharing octahedra which defines its crystal band structure. For comparison, the anatase crystal and band structure are provided in Figure 3.6¹⁰. Anatase belongs to a space group of I4₁/amd with a=3.785 Å and b=9.514 Å. Anatase also consists of edge-sharing distorted octahedral, but there is no rotation. Instead, the anatase structure has a bigger volume to compensate for that. The brookite structure forms in rather an extreme condition and it is not common. The thermal expansion coefficient of rutile along [100] direction is reported to be $6.99 \times 10^{-6} \text{ K}^{-1}$ ¹¹.

TiO₂ is an n-type semiconductor and has been widely used in different applications especially in dye-sensitized solar cells¹². TiO₂ can provide a perfect buffer layer for oxide thin films.

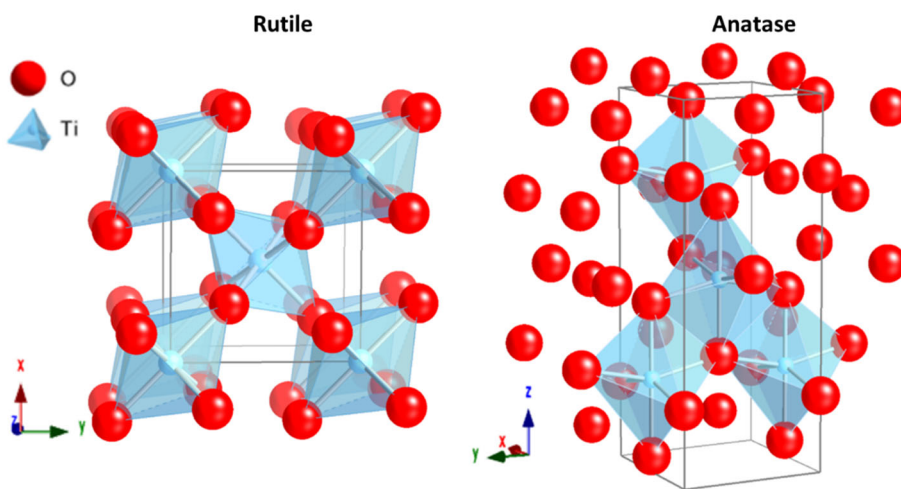


Figure 3.5. The rutile and anatase phase of TiO₂ unit cells. In rutile, Ti cations are surrounded by oxygen octahedra which rotate alternatively. While in anatase, there are distorted octahedra.

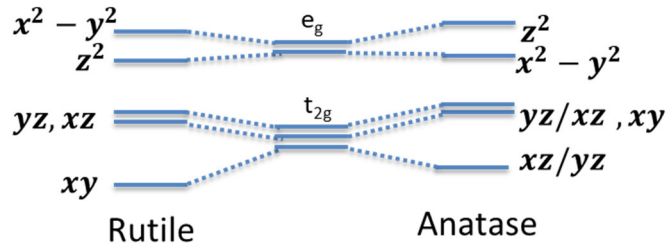


Figure 3.6. The crystal band splitting in rutile vs anatase due to edge-sharing octahedra. In anatase, however, the distortion changes the bands' level and energy.

3.1.6. Silicon

Silicon belongs to the diamond structure with the space group of $Fd\bar{3}m$ (Figure 3.7). The lattice constant equals 5.42 \AA . Si is considered a group IV semiconductor. It can be both n-type and p-type with different doping concentration. Silicon is the major substrate for the electronics industry due to its abundance and low cost. Thus, integrating with silicon is considered one of the technological consideration. The formation of SiO_2 needs to be controlled for precise applications. The thermal expansion coefficient of Silicon equals $\sim 2.6 \times 10^{-6} \text{ K}^{-1}$ ¹³. The band gap of silicon can vary based on the doping concentration, while the common value is $\sim 1.14 \text{ eV}$ at room temperature. The dielectric constant is reported to be 12.

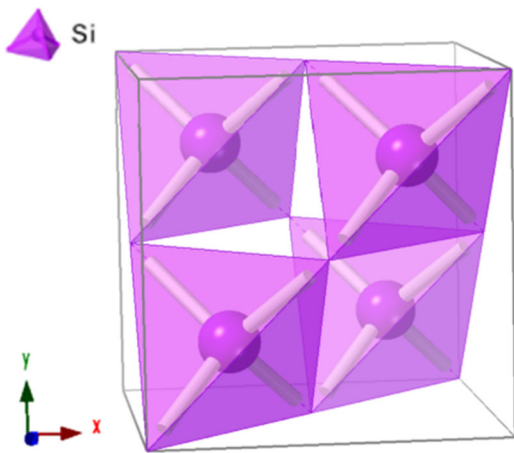


Figure 3.7. The silicon unit cell including Si tetrahedra.

3.1.7. Sapphire

Sapphire has a unique property of being transparent which makes this substrate a perfect candidate for the optical device applications especially integrated with III nitrides. Sapphire or corundum has a hexagonal structure with $a=4.762 \text{ \AA}$ and $c=12.995 \text{ \AA}$ (Figure 3.8). This structure belongs to the space group of $R\bar{3}C$. The thermal expansion coefficients of sapphire are reported to be $\sim 6.2 \times 10^{-6}$ and $7.07 \times 10^{-6} \text{ K}^{-1}$ respectively along a-axis and c-axis¹⁴. There are different cuts available for this substrate for use in growing devices; c-plane (0001), r-plane ($1\bar{1}02$), m-plane ($1\bar{1}00$), and a-plane ($2\bar{1}\bar{1}0$).

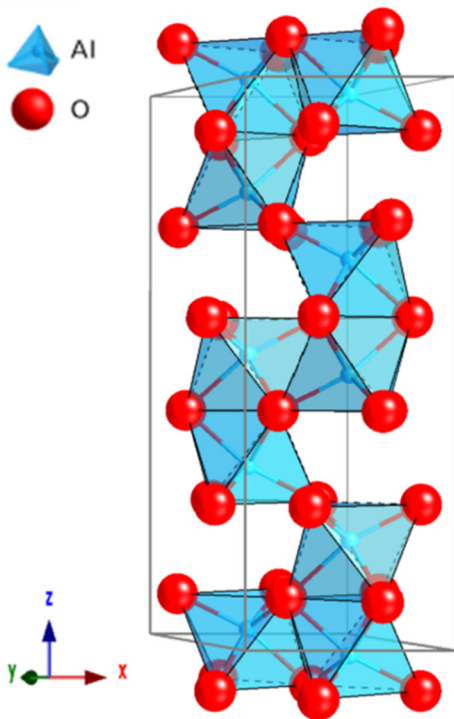


Figure 3.8. The hexagonal lattice structure of sapphire including oxygen octahedral surrounding Al cations.

3.2. Excimer lasers

The word laser stands for light amplification by stimulated emission of radiation. There are a different type of lasers. The medium of the laser can be solid-state, semiconductor, gas, or liquid.

These lasers provide coherent light with different wavelengths. Among those excimer lasers are widely used for pulsed laser applications¹⁵. There is a discharge tube at the heart (Figure 3.9). This tube is filled with a low-pressure inert gas (Kr, Ar, Xe) and a halogen gas (F or HCl). This mixture is pressurized by an inert Ne or He gas. There are two parallel electrodes extending the whole length of the tube. The pulsation is a result of discharging across these electrodes. Thus, the plasma forms which contains an excited complex (ArF, KrF, XeF, F₂) called excimer emitting ultraviolet laser beam upon returning to ground state. Here, there is no need for multiple pass cavity which is very important from a design point of view.

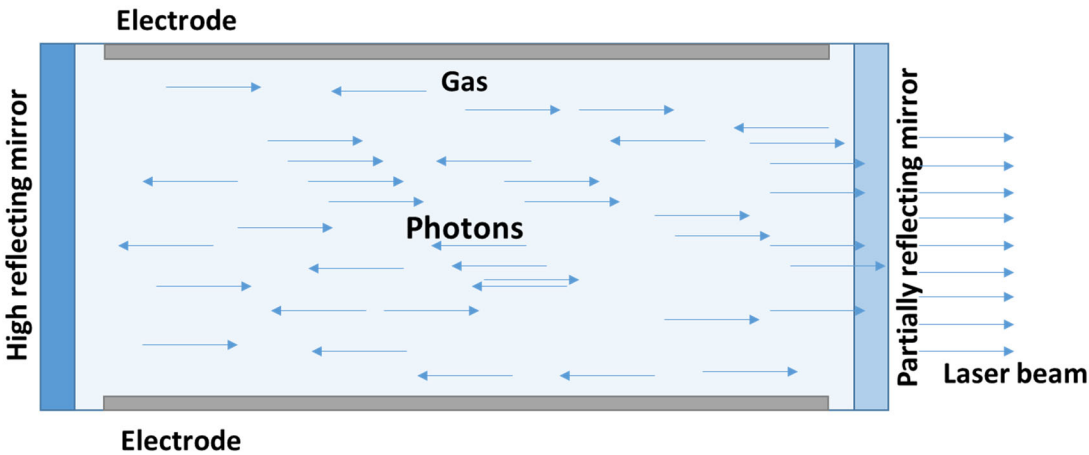


Figure 3.9. The schematic of an excimer laser chamber including a discharge tube.

3.2.1. Pulsed laser technique for thin-film deposition

A pulsed laser with the duration in the range of nanosecond has been used to deposit thin films through vaporizing the target material and producing high-temperature and high-density plasmas. The luminous plasma elongates perpendicular to the surface preferentially^{16,17}. Thus, it makes the deposition to be forward directed. The local temperature can raise up to 10^5 - 10^7 K with this method and the kinetic energy of the species is reported to be in the range of 10-100 eV¹⁸. The velocity of species has mass dependency^{18,19}. The density of the plasma is in the range of

10^{19} - 10^{21} cm^{-3} which is attributed to high evaporation flux rate. The thickness variation across the film shows a $\cos\theta$ dependence, where θ is the angle between the radial vector and normal to the target surface²⁰. Slight spatial composition variation is reported across the multi-elemental films which depend on the laser energy density²¹.

Laser-solid interaction can be divided into two parts:

1. Interaction of the laser beam with the target material
2. Interaction of the laser beam with the formed plasma

3.2.2. Interaction of laser with material

This interaction depends on the coupling of the laser with the solid. The high energy density laser can melt or evaporate the surface material. Then, the one-dimension heat flow equation with proper boundary condition can be solved (The phase change of material needs to be taken into account). The defining factors here are pulsed laser energy, duration, shape, and wavelength. Also, the parameter related to the target material like reflectivity, absorption coefficient, heat capacity, density, and thermal conductivity is critical. Using a simple energy balance, the amount of material that is evaporated (Δx) equals the energy of the laser minus the conduction loss by the substrate and absorption loss by the plasma. The E_{th} is then defined as the minimum laser energy needed to evaporate an appreciable amount of material^{16,21}.

$$\Delta x = \frac{(1-R)(E-E_{th})}{\Delta H + C_v \Delta T} \quad \text{Equation (3.1)}$$

where R , ΔH , C_v , and ΔT are the reflectivity, latent heat, volume heat capacity, and maximum rise in temperature, respectively. The thermal diffusion distant ($\sqrt{2Dt}$) must be larger than the absorption length of the laser ($\frac{1}{\alpha_t}$) in the target material. If not, the evaporation depends on the laser length, not thermal conductivity. For small bandgap semiconductors and metals, where thermal

diffusion is large, this equation holds. However, for insulator and polymers that is not the case. Here, there is a linear relationship between energy density and evaporation rate, if the characteristic of the material does not change with laser.

3.2.3. Interaction of the laser with the formed plasma

When the surface is heated by the laser, it emits electrons and positive ions. At a very low electron density, where the vapor is slightly ionized and the density of neutral atoms is high, in a collision with neutral atoms, electrons tend to absorb photons. This leads to an enhancement of the absorption coefficient (α_p), and electron-ion collisions become the dominant heating mechanism^{16,21}.

$$\alpha_p = 3.69 \times 10^8 \left(\frac{Z^3 n_i^2}{T^{0.5} \nu^3} \right) \left[1 - \exp\left(-\frac{h\nu}{KT}\right) \right] \quad \text{Equation (3.2)}$$

where Z is the average charge, n_i is the ion density, T is the temperature of the plasma, h is Planck's constant, K is the Boltzmann constant, and ν is the frequency of the laser light. Only in the distances close to target where the charged ion density is high ($\propto n_i^2$), does the plasma absorb the laser energy²². The assumption here is that the frequency of the plasma is smaller than the laser beam, to limit the reflection by plasma. The $\left[1 - \exp\left(-\frac{h\nu}{KT}\right) \right]$ term illustrates the losses due to stimulated emission which is affected by plasma temperature and laser wavelength. At low temperature for an excimer laser, the temperature dependency exhibits $T^{-0.5}$, while at a higher temperature and higher wavelength lasers like CO₂ laser, there is a $T^{-1.5}$ dependency.

Due to high expansion velocity of the leading plasma edge, the density of charged particles rapidly decreases with time and distance from the target and makes plasma transparent to the laser. This high expansion velocity is due to the large gradient density. The part of the plasma that absorbs laser can act as an HT-HP confined gas in a small dimension that becomes transparent as

if it is allowed to expand in a vacuum. The pressure gradient near the edge due to vacuum cause high velocity. At the beginning of this stage, the mean free path between particles is short due to the high particle density of 10^{19} - 10^{20} cm^{-3} . Thus, plasma can be considered as a fluid.

3.2.4. Adiabatic plasma expansion

After the termination of the laser pulse, there is an initial isothermal expansion of plasma. The temperature depends on the dimension of the plasma by the adiabatic thermodynamic equation¹⁶:

$$T[(X(t)Y(t)Z(t))]^{\gamma-1} = \text{Constant} \quad \text{Equation (3.3)}$$

where γ is the specific heat capacities ration, considering constant pressure and volume. The thermal energy converts to kinetic energy, thus the expansion velocity is high. This velocity is 3-10 times the velocity of the sound, based on the γ value. This is coming from the fact that the maximum velocity of the gas in a vacuum is $\frac{2\alpha}{\gamma-1}$, and α is the sound velocity. The expansion of plasma, can be calculated as^{16,23}:

$$X(t) \left[\frac{d^2X}{dt^2} \right] = Y(t) \left[\frac{d^2Y}{dt^2} \right] = Z(t) \left[\frac{d^2Z}{dt^2} \right] = \frac{KT_0}{M} \left[\frac{X_0Y_0Z_0}{X(t)Y(t)Z(t)} \right]^{\gamma-1} \text{Equation (3.4)}$$

where X_0 , Y_0 , and Z_0 are the initial orthogonal edges of the plasma. This equation represents the temperature, dimension, and mass dependency. The expansion for different particles varies based on their masses. The transverse dimension of Y and Z \sim 1-4 mm, are larger than X \sim 20-100 μm initially. After then the maximum velocities are in the direction of smaller dimension and expansion direction changes which explains the outward direction of plasma perpendicular to the target surface. When the laser hits the target, the plasma is elongated along Y axes, after termination of the pulse, the plasma is still elongated but along the Z axes according to Figure 3.10.

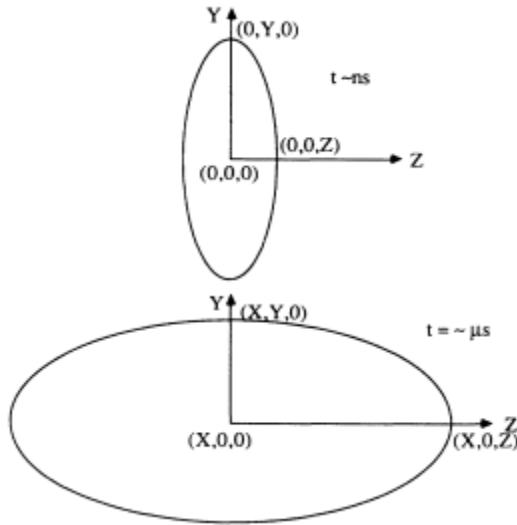


Figure 3.10. The top diagram shows the initial shape of plasma after laser termination, and the lower diagram represents the shape of plasma before it hits the substrate and after adiabatic expansion ²¹.

3.3. Characterization techniques

3.3.1. X-ray diffraction

The crystalline structure of the films is characterized using X-ray diffraction. X-ray diffractometers include an X-ray tube and an X-ray detector. A cathode ray tube is being used to generate electrons by heating a filament. These electrons get accelerated by applying voltage toward the target material (Cu, Fe, Mo, Cr). Given enough energy, these electrons are able to knock inner shell electrons out of the target which in turns produce characteristic X-ray due to the transition of atoms from outer shells to an inner shell ²⁴. This spectrum includes $K_{\alpha 1,2}$, $K_{\beta 1,2}$ which are quantized energy related to the transition between electron shells of the target from L to K and from M to K shell, respectively as shown in Figure 3.11. This spectrum is filtered through crystal monochromators. The most common X-ray beam is CuK_{α} with the wavelength of 1.5418 \AA . This beam now being directed toward the sample, as the sample and detector rotate to collect and record the intensity of the reflected X-ray from the sample.

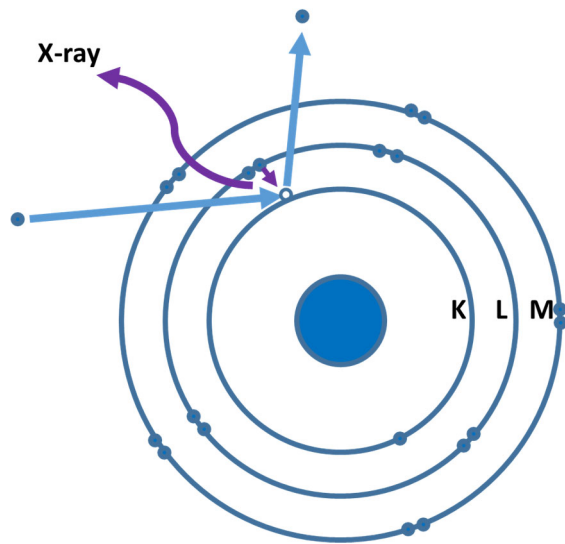


Figure 3.11. The X-ray generation through electron dislodges from the inner shell and transition of the outer shell electrons to the inner shell.

3.3.1.1. θ - 2θ scan

The geometry of the diffractometer for the θ - 2θ scan is such that as the sample rotates at an angle of θ with regards to the X-ray beam, and the detector rotates at the angle of 2θ to catch the reflected beam. The θ - 2θ scans are based on Bragg's law which is a special case of Laue diffraction, where angles for coherent and incoherent scattering from crystal lattice planes upon the incident of x-ray beam will be determined. The general relationship between the incident beam, incident angle, and the spacing between lattice planes is $n\lambda = 2d\sin\theta$, where λ is the wavelength of the X-ray beam, θ is the angle of the incident beam, and d is the d-spacing of the crystal lattice²⁵. Reflections at a given angle (2θ) correspond to the lattice plane distances (d) that coherently reflected from those family of planes (hkl) (out-of-plane in case of thin films). If the film is textured or epitaxy, there is only one family of planes aligned parallel with respect to substrate planes. In order to check the in-plane alignment, Φ -scan can be employed.

3.3.1.2. Φ -scan

The azimuthal scan or Φ -scan is being used to determine the epitaxial nature of films since it gives information regarding the in-plane alignments. In this scan, the sample is rotated 360° around the selected plane normal while tilted at a given angle of ψ , which is the angle between out-of-plane direction and the normal of the selected plane²⁶. Thus, it gives information related to the symmetry of the selected plane. Typically, this plane is selected from low index planes with high structure factor. Also, ψ cannot be 90° due to geometry limitation of the instrument. The angle between out-of-plane $(h_1k_1l_1)$ and this plane $(h_2k_2l_2)$, ψ , can be calculated as:

$$\cos(\psi) = \frac{\vec{n}_1 \cdot \vec{n}_2}{|\vec{n}_1||\vec{n}_2|} \quad \text{Equation (3.5)}$$

where \vec{n}_1 and \vec{n}_2 are the normal to $(h_1k_1l_1)$ and $(h_2k_2l_2)$ planes, respectively. For the cubic crystal lattice, we will have:

$$\cos(\psi) = \frac{h_1h_2+k_1k_2+l_1l_2}{\sqrt{h_1^2+k_1^2+l_1^2} \cdot \sqrt{h_2^2+k_2^2+l_2^2}} \quad \text{Equation (3.6)}$$

For the selected plane, the X-ray beam needs to be adjusted at the angle of θ and the detector at 2θ , which is based on the appearance of $(h_2k_2l_2)$ planes at the 2θ position from the standard θ - 2θ powder scan of the target material. The schematic Figure 3.12 shows the geometry of the sample with respect to the X-ray source and detector.

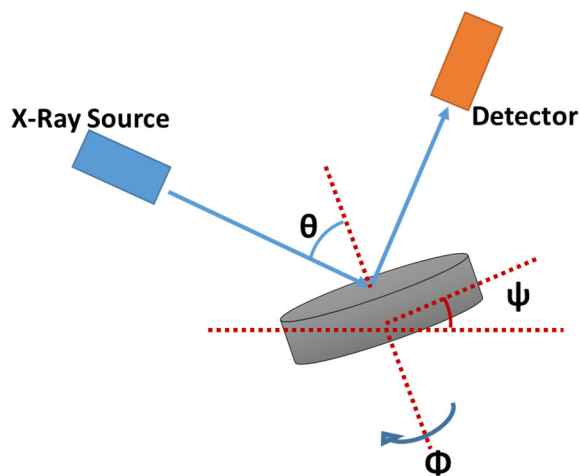


Figure 3.12. Schematic illustration of Φ -scan geometry.

If the film planes are not aligned epitaxially, there is no preferential lateral distribution. However, if there is an in-plane alignment, sharp reflections can be observed in this scan. If the same scan is employed for the substrate/buffer layers, then the in-plane alignment across the interface can be defined, since the relative peak positions can be used to calculate in-plane rotation between film's plane and substrate's/buffer layer's planes.

3.3.2. Scanning electron microscopy (SEM)

The scanning electron microscope (SEM) has a high-energy electron beam which interacts with the sample and provides information regarding chemical composition, structure, and microstructure of the materials. When the electron beam hits the atoms, multiple situations can be envisaged. It can knock out the outer layer electrons which are called secondary electrons. It can dislodge the inner layer electron (also are considered secondary electrons) and as a result electrons from outer layer transition to the inner layer and generate X-ray. It can bounce and deflect by the positive core which is called a backscattered electron ²⁷. The schematic Figure 3.13 represents secondary and backscattered electrons.

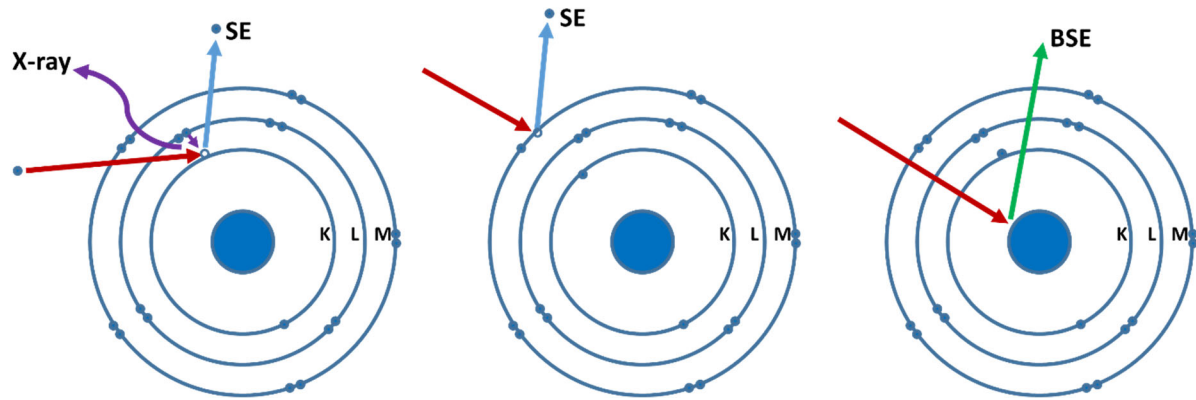


Figure 3.13. Emission of secondary electrons (SE), backscattered electrons (BSE), and X-ray upon the incident of the electron beam.

The secondary electrons (SE) are being detected and used for imaging mode as a result of inelastic interaction. These electrons have low energy and as a result, they give information about the surface (a few nm). These electrons later are accelerated to have enough energy to be analyzed and displayed. The brightness of the signal depends on the number of secondary electrons. The secondary electrons emitted from edges and steep surfaces are more due to the increased incident angle. Thus, these areas tend to be brighter. This property helps us build a topography map of the surface.

The backscattered electrons (BSE) are high energy electrons that are deflected through elastic interaction. The higher the atomic number, the more backscattered electrons are deflected. Thus, the heavier atoms show up brighter in the image. As a result, these electrons give information regarding the atomic map. The detector needs to be mounted above the sample to collect BSE electrons as shown in Figure 3.14. These electrons can also be collected by electron backscattered diffraction (EBSD) detector providing different information.

The generated X-ray can also be collected, which gives information related to elemental map and concentration.

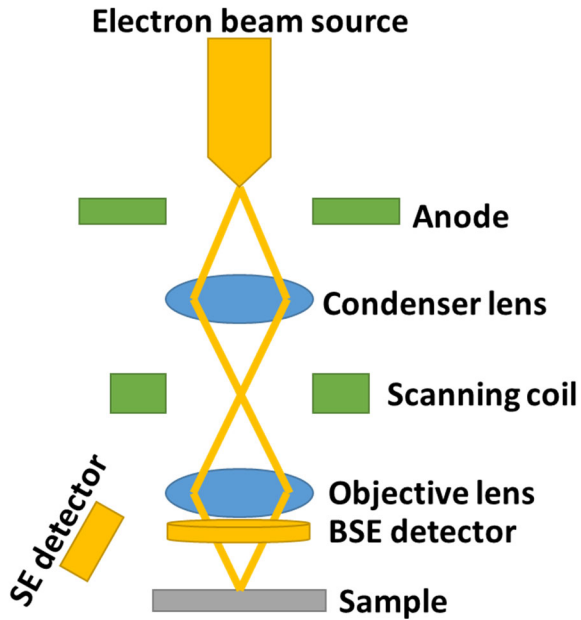


Figure 3.14. The Scanning electron microscope schematic.

3.3.2.1. Electron backscattered diffraction (EBSD)

Electron backscattered diffraction (EBSD) is a technique that provides information regarding structure, crystal orientation, and phase of the materials. It can be used for single-crystal or polycrystal materials ^{28,29}. The BSE electron may exit near the Bragg angle and gives information about the lattice planes and orientations. These diffracted BSE electrons form Kikuchi bands corresponding to each crystal plane. These band can be indexed by Miller indices. In a polycrystalline material, these Kikuchi bands define the orientation of each grain. In single crystalline heterostructures, other than confirmation of the quality, it can provide alignment information across the interface of multiple single-crystalline layers. The resolution of this technique is reported to be 25-100 nm. In order to increase the resolution, the transmission mode needs to be used.

3.3.2.2. Transmission Kikuchi diffraction (TKD)

Transmission Kikuchi diffraction (TKD) is a technique that collects information from underneath an electron transparent sample. The resolution in this method is increased to 5-10 nm compared to EBSD. TKD provides a higher signal to noise ratio and can be used for detailed quantitative analysis³⁰. The sample preparation, however, is more difficult, since they need to be electron transparent. The sample preparation method used for transmission electron microscope can be employed here.

3.3.3. Transmission electron microscopy (TEM)

Transmission electron microscope (TEM) uses a beam of the electron which transmits through the electron transparent sample (<100 nm). In the optical microscope, the maximum resolution (d) is limited to the wavelength of the photons (λ) and the aperture³¹;

$$d = \frac{\lambda}{2n\sin\alpha} \quad \text{Equation (3.7)}$$

where n is the refraction index, and α is the maximum half angle of the cone that is defined by the aperture. Similar to an optical microscope, in an electron microscope, the electron wavelength (λ_e) is a defining factor in resolution;

$$\lambda_e = \frac{h}{\sqrt{2m_0E(1+\frac{E}{2m_0c^2})}} \quad \text{Equation (3.8)}$$

where h is the Plank's constant, m_0 is the mass of the electron, E is the energy of the electron beam, and c is the speed of light. Thus at E=100 KeV, the wavelength of the source is about 2.5 pm. However, due to the objective lens and the aberrations, the resolution is limited to 0.1 nm. It was proved that the coefficient of spherical aberration (C_s) and a chromatic aberration (C_c) for a charged particle traveling through a charge-free region in a round lens system are positive. Thus, it is impossible for a round lens system to compensate for this aberration³².

3.3.3.1. Bright field imaging (BF)

Similar to SEM, the imaging emerges from the interaction of the electron beam with the sample. Here, the electron beam needs to pass through the sample. The contrast is provided by different atomic numbers. Unlike SEM, heavier atoms scatter electron beam more and show up darker in the image. Thickness, also, plays a role. The thicker the sample, the darker it appears.

3.3.3.2. Diffraction contrast-SAED

The contrast here comes from the elastically scattered electrons following Bragg's law. These scattered electrons include information from the crystalline lattice structure. The contrast patterns are called selected-area electron diffraction (SAED). SAED provides us with information regarding crystallinity, where amorphous materials create a thick single ring, polycrystalline materials generate multiple rings that can be indexed by Miller indices for a family of planes, and single crystalline materials form a pattern of spots each of which belongs to a lattice plane. The spot patterns yield information about the atomic alignments and orientation which are especially of importance in heterostructures.

3.3.3.3. Electron energy loss spectroscopy (EELS)

In this mode, the contrast is a result of inelastic scattering of the electron beam by the sample. This inelastic interaction causes a loss of energy. The loss of energy is used to detect elements since it is a characteristic of the bonding state for each element. Thus, electron energy loss spectroscopy (EELS) is used to extract compositional information including stoichiometry and bonding state.

3.3.4. Scanning transmission electron microscopy (STEM)

Scanning transmission electron microscopy (STEM) is a combination of TEM and SEM principles³³. This technique makes it possible to take advantage of the signals that could not be spatially corrected in TEM including secondary electrons, X-ray, scattered electrons, and electron energy loss. Figure 3.15a depicts different phenomena upon electron beam incidence with a material. The electron beam is focused in STEM (unlike parallel beam in TEM) and then rastered across the sample. The signal stream then is combined with the beam position to make a virtual image. This ability provides an advantage over TEM due to enhanced spatial resolution. Figure 3.15b shows the detectors locations in STEM to collect the signals after the incidence of the convergent electron beam. Figure 3.16 illustrated the schematic of TEM and STEM.

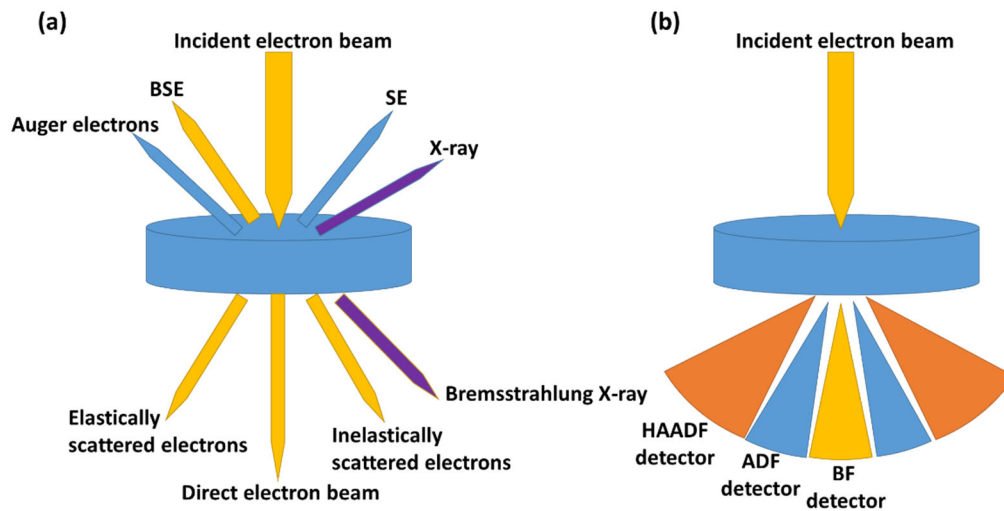


Figure 3.15. Different phenomena upon electron beam incidence with a material (a), and detectors position to collect generated signals, (b) HAADF detector angle > 50 mrad, ADF detector angle > 10 mrad, and BF detector < 10 mrad.

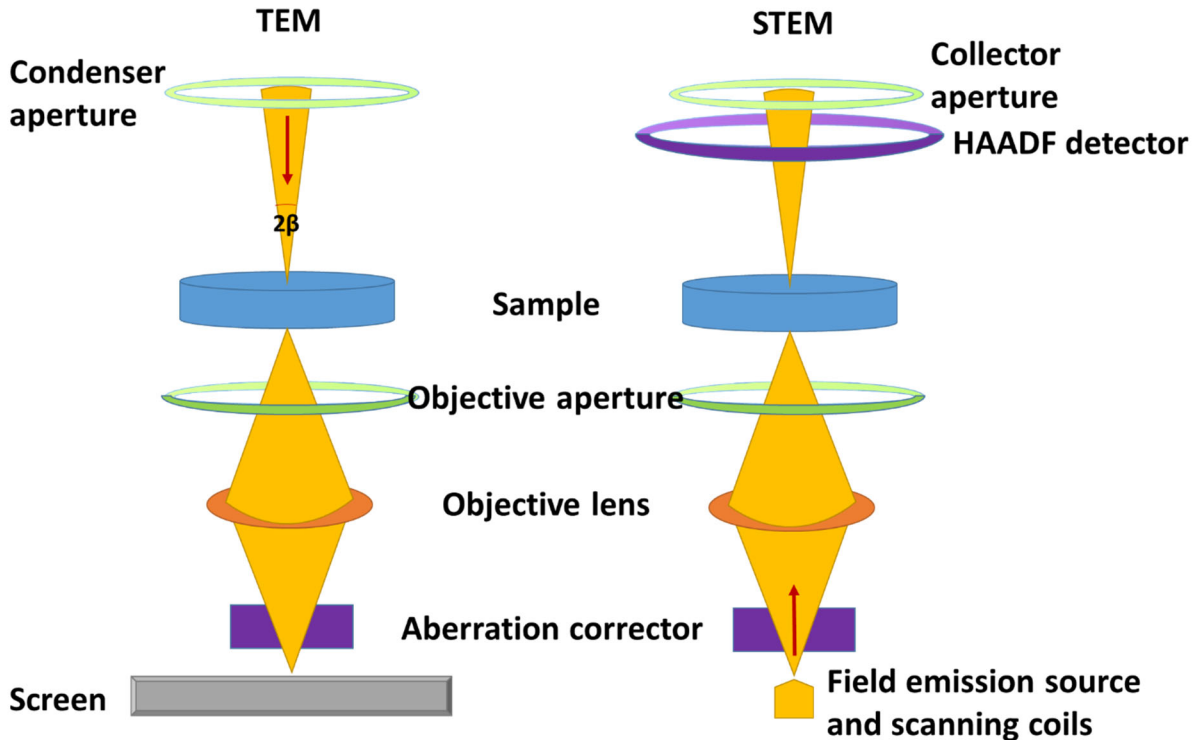


Figure 3.16. Schematic depiction of critical optical elements in conventional TEM vs STEM.

3.3.4.1. High-angle annular dark field image (HAADF)

The deflected electrons by the positive nuclei through a relatively large angle are being collected using a high-angle annular dark field (HAADF) detector. The image that is formed by these scattered electrons is a Z-contrast (z is the atomic number) image since heavier atoms tend to deflect (by coulombic interactions) the beam in higher angles and tend to be brighter. The scattered electrons in this technique are elastically incoherently scattered (Rutherford) and do not follow Bragg's law. Figure 3.17 shows a HAADF image of spatially resolved silicon dumbbells, which represents the high spatial resolution of STEM. The high resolution is due to high angle scattering that serves the purpose of providing for good separation between Bragg scattering and Rutherford scattering. The bright field (BF) and annular dark field (ADF) are other imaging modes that collect lower angle coherently elastic scattered beam, and serve different purposes.

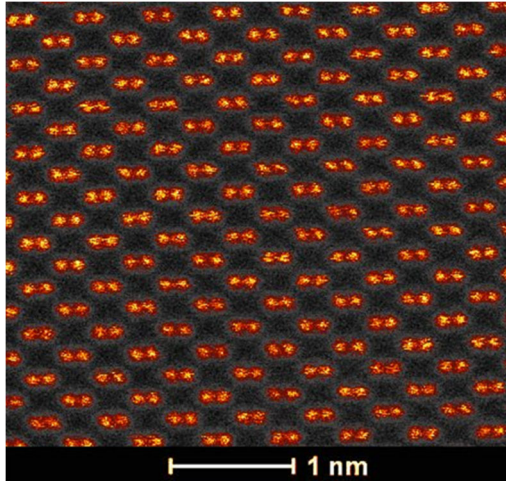


Figure 3.17. HAADF image of silicon dumbbells taken by STEM.

3.3.4.2. Electron energy loss spectroscopy (EELS)

Electron energy loss spectroscopy (EELS) analyzes the transmitted beam and provides information regarding bonding characteristic, stoichiometry, orbital occupancy, and nature of defects.

3.3.5. Electron transparent sample preparation

The sample preparation can be done by conventional mechanically polishing, using a focused ion beam (FIB) to thin down the sample, or the combination of both. FIB benefits from heavy ions that are capable of milling the sample by a sputtering process³⁴. The resolution of this technique can be the order of nanometers by controlling the beam characteristics like current and voltage and the angle of the sample with respect to the incident ion beam. Normally, the FIB milling process is being observed in an SEM using a second electron beam. The angle between these two beams is adjusted at 52 °.

3.3.6. Electrical measurement

3.3.6.1. Van der Pauw measurement

Van der Pauw method is used to measure sheet resistance, and in this study is employed to measure the resistivity of thin films. This is a powerful technique that gives the average resistivity across the film irrespective of its shape³⁵. In this method, four probes are located around the perimeter of the film as shown in Figure 3.18. The average resistivity of the film is ρ ;

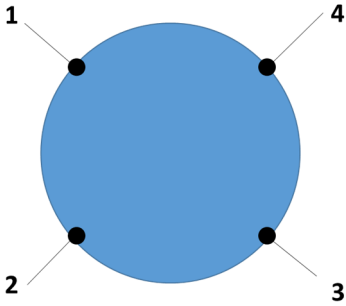


Figure 3.18. The four probes placement for Van der Pauw measurement.

$$\rho = R_s t \quad \text{Equation (3.9)}$$

where R_s is the film resistance and t is the film thickness. To make the measurement, the current is conducted along one edge like I_{12} and voltage is measured along the opposite side like V_{34} . Thus, the resistance can be measured as:

$$R_{12,34} = \frac{V_{34}}{I_{12}} \quad \text{Equation (3.10)}$$

The resistance can be also measured along the vertical edge ($R_{23,41}$) to remove the shape factor. The film resistance R_s then can be measured by Van der Pauw formula;

$$e^{-\pi \frac{R_{12,34}}{R_s}} + e^{-\pi \frac{R_{23,41}}{R_s}} = 1 \quad \text{Equation (3.11)}$$

The measurement can be more accurate if the reverse polarity is also applied and the R values being averaged out before using in Van der Pauw equation.

3.3.6.2. Hall measurement

For Hall Effect measurement, the Van der Pauw geometry can be used³⁵. A magnetic field is applied perpendicular to the surface as shown in Figure 3.19. When a charged particle is placed in a magnetic field of B, it experiences Lorentz force;

$$F_{Lorentz} = q[E + (v \times B)] \quad \text{Equation (3.12)}$$

where q and v are the charge and velocity of the particle, respectively. E is the internal electric field due to the uneven distribution of the charge. This generates a voltage perpendicular to the current of the charged particles, called Hall voltage (V_H);

$$V_H = \frac{IB}{qnt} \quad \text{Equation (3.13)}$$

where I is the current, n is the density of charged particles, and t is the thickness of the film ($nt=n_s$, where n_s is the film density).

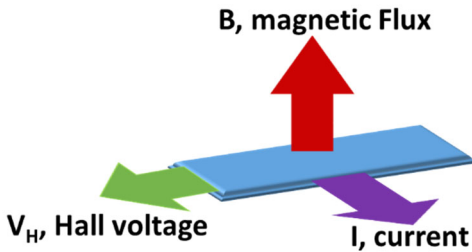


Figure 3.19. Illustration of Hall Effect voltage, I, and B relationship.

Using the resistivity R_s (can be measured by Van der Pauw method), the mobility can be defined as:

$$\mu = \frac{V_H}{R_s IB} \quad \text{Equation (3.14)}$$

If there are two types of carriers in the film, the resistivity of the film can be written as:

$$\rho = \frac{1}{q(n\mu_n + p\mu_p)} \quad \text{Equation (3.15)}$$

where n and p are electron and hole concentrations, respectively. μ_n and μ_p are the mobility of electrons and holes, respectively.

3.3.7. Magnetic measurement

The superconducting quantum interference device (SQUID) is used to measure magnetic properties. This device consists of two parallel Josephson junctions formed by two superconductors separated by a very thin insulating layer in a loop as shown in Figure 3.20³⁶. The sample is being vibrated inside the loop. In the absence of the sample, the applied current is split equally between two branches. The vibrating magnetic sample inside the loop generates a current due to its magnetic flux. The induced current is in the same direction as the initial current in one branch and in the opposite direction in the other branch, which causes a phase difference in the flux between two branches. The phase difference then is converted to a voltage. The generated voltage is proportional to the induced magnetic field by the sample. Squid is sensitive enough to measure 5×10^{-18} T.

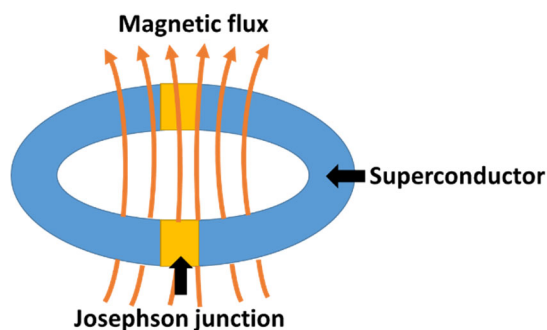


Figure 3.20. Diagram of SQUID.

3.3.8. Raman spectroscopy

Raman spectroscopy is a technique that provides information regarding bonding characteristics (vibrational, rotational, and other low-frequency modes) of a molecule³⁷. Any

external or internal stimuli that affect the bonding characteristics or polarization affect the Raman spectrum of the molecule. Thus, it is used to identify molecules. Raman uses a laser beam that interacts with the material. This technique relies on inelastic scattering as a result of laser interaction with material as shown in Figure 3.21. The incident beam excites the molecule into a virtual state which after returning to another lower state, emits a photon which can have higher or lower energy than the incident beam. The state after emission is different than the initial ground state. This shift in energy/frequency called Stokes shift. The Raman effect occurs due to the interaction of the electric field of the incident beam with the electron cloud in a way that it induces a dipole moment within the molecule depending on its polarizability.

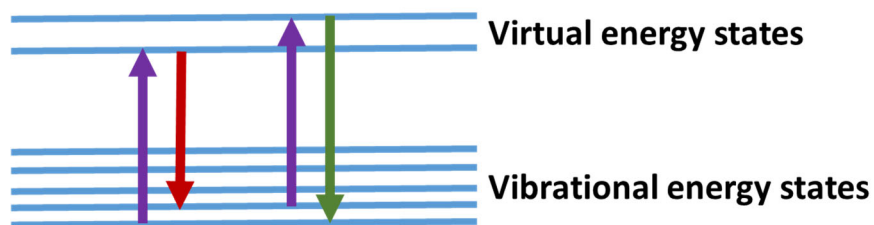


Figure 3.21. Energy level diagram before and after Raman scattering.

Raman shifts are reported in wavenumbers;

$$\Delta\omega = \left(\frac{1}{\lambda_0} - \frac{1}{\lambda_1}\right) \quad \text{Equation (3.16)}$$

where $\Delta\omega$, λ_0 , and λ_1 is the Raman shift, excitation wavelength, and incident beam wavelength, respectively.

REFERENCES

1. Mott, N. F. & Transitions, M.-I. Taylor and Francis. (1990).
2. Wang, S. J., Ong, C. K., You, L. P. & Xu, S. Y. Epitaxial growth of yttria-stabilized zirconia oxide thin film on natively oxidized silicon wafer without an amorphous layer. *Semicond. Sci. Technol.* **15**, 836–839 (2000).
3. Fork, D. K., Fenner, D. B., Connell, G. A. N., Phillips, J. M. & Geballe, T. H. Epitaxial yttria-stabilized zirconia on hydrogen-terminated Si by pulsed laser deposition. *Appl. Phys. Lett.* **57**, 1137–1139 (1990).
4. Baberschke, K. The magnetism of nickel monolayers. *Appl. Phys. A Mater. Sci. Process.* **62**, 417–427 (1996).
5. Nix, F., MacNair, D. The thermal expansion of pure metals: copper, gold, aluminum, nickel, and iron. *Phys. Rev.* **60**, 597-605 (1941).
6. Narayan, J. *et al.* Epitaxial growth of TiN films on (100) silicon substrates by laser physical vapor deposition. *Appl. Phys. Lett.* **61**, 1290–1292 (1992).
7. Houska, C. R. Thermal expansion and atomic vibration amplitudes for TiC, TiN, ZrC, ZrN, and pure tungsten. *Solid State Commun.* **1**, 246 (1963).
8. Fujishima, A., Zhang, X., Tryk, D. TiO₂ photocatalysis and related surface phenomena. *Sur, Sci. Rep.* **63**, 515-582 (2008).
9. Bak, T., Nowotny, J., Sucher, N. J. & Wachsman, E. Effect of Crystal Imperfections on Reactivity and Photoreactivity of TiO₂ (Rutile) with Oxygen, Water, and Bacteria. *J. Phys. Chem. C* **115**, 15711–15738 (2011).
10. Wen, B. *et al.* Electronic structure and photoabsorption of Ti³⁺ ions in reduced anatase and rutile TiO₂. *Phys. Chem. Chem. Phys.* **20**, 17658-17665, (2018).

11. Hummer, D., Heaney, P., Post, J. Thermal expansion of anatase and rutile between 300 and 575 K using synchrotron powder X-ray diffraction. *Powder Diffr.* **22** (4), 352-357 (2012).
12. Guo, W. *et al.* Rectangular Bunched Rutile TiO₂ Nanorod Arrays Grown on Carbon Fiber for Dye-Sensitized Solar Cells. *J. Am. Chem. Soc.* **134**, 4437–4441 (2012).
13. Sinha, A. K., Levinstein, H. J. & Smith, T. E. Thermal stresses and cracking resistance of dielectric films (SiN, Si₃N₄, and SiO₂) on Si substrates. *J. Appl. Phys.* **49**, 2423 (1978).
14. Lucht, M. *et al.* Precise measurement of the lattice parameters of α -Al₂O₃ in the temperature range 4.5–250 K using the Mössbauer wavelength standard. *J. Appl. Crystallogr.* **36**, 1075–1081 (2003).
15. Küper, S., Stuke, M. Femtosecond UV excimer laser ablation. *Appl. Phys. B.* **44** (4), 199-204 (1987).
16. Singh, R. K., Holland, O. W. & Narayan, J. Theoretical model for deposition of superconducting thin films using pulsed laser evaporation technique. *J. Appl. Phys.* **68**, 233–247 (1990).
17. Weimer, W. A. Plasma emission from laser ablation of the high-temperature superconductor YBa₂Cu₃O₇. *Appl. Phys. Lett.* **52**, 2171–2173 (1988).
18. Zheng, J. P., Huang, Z. Q., Shaw, D. T. & Kwok, H. S. Generation of high-energy atomic beams in laser-superconducting target interactions. *Appl. Phys. Lett.* **54**, 280–282 (1989).
19. Venkatesan, T., Wu, X. D., Inam, A. & Wachtman, J. B. Observation of two distinct components during pulsed laser deposition of high T_c superconducting films. *Appl. Phys. Lett.* **52**, 1193–1195 (1988).
20. Neifeld, R. A. *et al.* Systematics of thin films formed by excimer laser ablation: Results on SmBa₂Cu₃O₇. *Appl. Phys. Lett.* **53**, 703–704 (1988).

21. Singh, R. K. & Narayan, J. Pulsed-laser evaporation technique for deposition of thin films: Physics and theoretical model. *Phys. Rev. B* **41**, 8843–8859 (1990).
22. Eason, R. *Pulsed laser deposition of thin films: applications-led growth of functional materials*. (2007).
23. Wood, R. F. & Giles, G. E. Macroscopic theory of pulsed-laser annealing. I. Thermal transport and melting. *Phys. Rev. B* **23**, 2923–2942 (1981).
24. Cullity, B. & Stock, S. *Elements of X-ray Diffraction*. (2014).
25. Bunaciu, A. A., Udriștioiu, E. gabriela & Aboul-Enein, H. Y. X-Ray Diffraction: Instrumentation and Applications. *Crit. Rev. Anal. Chem.* **45**, 289–299 (2015).
26. He, B., Preckwinkel, U., Smith, K. Fundamentals of two-dimensional X-ray diffraction (XRD²). *Adv. X Ray. Anal.* **43**, 273-280 (2000).
27. Goldstein, J. *Practical scanning electron microscopy: electron and ion microprobe analysis*. (2012).
28. Mariani, E., *et al.* Electron backscatter diffraction (EBSD) in the SEM: applications to microstructures in minerals and rocks and recent technological advancements. ISSN: 1698-5478 (2008).
29. Voutou, B., Stefanaki, E. Electron microscopy: the basics. Aristotle University of Thessaloniki, Greece (2008).
30. Sneddon, G., Trimby, P., Cairney, J. Transmission Kikuchi diffraction in a scanning electron microscope: A review. *Mater. Sci. Eng: R*, **110**, 1-12 (2016).
31. Williams, D. B. & Carter, C. B. The Transmission Electron Microscope. in *Transmission Electron Microscopy* 3–17 (Springer US, 1996).

32. Hosokawa, F., *et al.* Development of Cs and Cc correctors for transmission electron microscopy. *Microscopy*. **62**, 23-41 (2013).
33. Tanaka, N. *Scanning Transmission Electron Microscopy of Nanomaterials*. (2014).
34. Giannuzzi, L. *Introduction to focused ion beams: instrumentation, theory, techniques and practice*. (2004).
35. Pauw, L. A method of measuring specific resistivity and Hall effect of discs of arbitrary shape. *Philips Res. Repts.* **13**, 1-9 (1958).
36. Clarke, J. & Braginski, A. *The SQUID handbook: Applications of SQUIDs and SQUID systems*. (2006).
37. Derek, J., Graves, P. *Practical Raman spectroscopy*. (Springer-Verlag, 1989).

CHAPTER 4

4. Strain engineering-VO₂ bi-epitaxy integrated with Si through TiO₂/TiN with a novel method of oxidation

4.1. Preparation of TiO₂/TiN/Si heterostructures as buffer layers for VO₂ through a novel method of oxidation (*Acta Materialia*, 103 (2016) 502-511 & *MRS Advances*, 1 (37) (2016) 2629-2634)

Abstract

We have integrated epitaxial TiO₂ on a TiN/Si(100) platform through oxidation of TiN. The oxidation of TiN(100)/Si(100) results in the formation of an epitaxial rutile-TiO₂ (r-TiO₂) with an [110] out-of-plane orientation. We have studied in detail the r-TiO₂ epitaxy and the epitaxial relationship is determined to be TiO₂(1 $\bar{1}$ 0)||TiN(100) and TiO₂(110)||TiN(110). We rationalized this epitaxy using the domain matching epitaxy paradigm. Below the r-TiO₂ epitaxial layer, we observed cuboids, which are mostly voids. We described the mechanism of oxidation where Ti out-diffusion during oxidation leads to the collapse of the nitrogen octahedron. This collapse makes neighboring Ti bonds weaker, promoting these Ti atoms to diffuse out next. Thus, cuboids filled with atomic nitrogen are formed, which then form N₂ gas. The N₂ pressure in these cuboids was estimated to be as high as 359 MPa, assuming all N₂ is retained in the cuboids. This pressure can exceed the fracture stress of TiO₂ and leads to rupture of thin TiO₂ surface, which has been observed under certain conditions.

4.1.1. Introduction

TiO₂ thin films and surfaces have generated great interest due to a variety of novel functionalities and applications¹⁻⁵; however, our understanding of the mechanisms at the

molecular scale for the various phenomenon associated with these functionalities is limited. Titanium dioxide has been used for a variety of applications, including photocatalysts, solar cells, protective corrosion resistant and optical coatings, capacitor-varistors for protection against high voltage transients, white pigments, gate insulators in MOSFETs, spacers in magnetic spin-valve systems, biocompatible implants, Li-batteries, and electrochromic devices^{1,2,5-7}. Formation of epitaxial TiO₂ is needed for the control and the reliability of the transport properties in solid state devices. In addition, wafer scale integration of TiO₂ with Si(100) can lead to novel multifunctional devices. Potential applications of epitaxial TiO₂ can be grouped into three main categories:

1) New epitaxial platforms. It can be used as a platform to grow other epitaxial films like VO₂⁸ while integrated with Si. Considering TiO₂ anisotropy, it can provide strain tunability in upper layers based on the growth direction resulting in new functional heterostructures.

2) New TiO₂ based devices integrated with Si(100). One of the essential features of the development of reliable multifunctional electronic devices is the control of grain boundaries via epitaxial growth and the integration of TiO₂ films with silicon, which is the mainstay substrate material for microelectronics.

3) Capacitor-varistors (higher breakdown voltage). The local conducting channel in capacitor-varistors could be one or two-dimensional defects including domain and grain boundaries. These channels can affect the resistance and breakdown voltage of capacitors as they act as the short current paths. Because of this effect, grain boundaries parallel to the direction of applied voltage become detrimental. Thus, getting rid of grain boundaries in capacitor-varistors, if grown epitaxially, can increase breakdown voltage considerably. It should be mentioned that the dielectric constant, k , of r-TiO₂ (values along the 'a' and 'c' axes are 90 and 170, respectively⁹)

is considerably higher than anatase TiO₂ (in the range of 30– 40²), which makes r-TiO₂ more favorable to be used as a capacitor.

There are several reports on the epitaxial integration of TiO₂ on sapphire substrates^{4,10}. Also, Al-doped TiO₂ (anatase) on MgO(001) was shown to grow cube-on-cube. Anatase and rutile TiO₂/ TiN/Ru⁹, and TiO₂(110)/TiN(100)/STO (200) are also examples of epitaxial integration of TiO₂ with substrates other than silicon where evidence for epitaxial growth was lacking¹¹. However, in microelectronic industries, there is a growing demand for the integration of epilayers with Si(100) where there are very limited systematic studies. Liu et al.¹² and Kim et al.¹³ deposited TiO₂ layer lacking epitaxy on Si, with films being mostly polycrystalline. There is another study on Co-doped TiO₂ anatase on Si(100)¹⁴ where epitaxial growth has been claimed; but, the theta-2theta scan shows several peaks for out of plane orientations of rutile. Moreover, there are some reports on rutile TiO₂/SiO₂/Si and TiO₂/ZnO/Si¹⁵ where films are again polycrystalline. Thus, there is a need for a systematic study on TiO₂ epitaxy and its integration with Si(100). Our group successfully integrated single crystalline rutile and anatase TiO₂ with Si(100) using yttria-stabilized zirconia as a buffer layer^{3,16,17}. In all of these studies (100), out-of-plane growth direction for rutile was achieved. Because different crystallographic planes exhibit different characteristics, it is necessary to grow other out-of-plane orientations on silicon to achieve varying functions for multiple applications. In this paper, we provide a new approach to the epitaxial integration of TiO₂ with Si(100). First TiN (a = 0.424 nm) is grown epitaxially on Si(100) (a = 0.543 nm) via domain matching epitaxy, where a cube-on-cube epitaxy is achieved despite over 22% lattice misfit. In the TiN/Si(100) epitaxy 4/3 (corresponding 25% misfit) and 5/4 (20% misfit) domains alternate by matching an integral multiple of lattice planes across the TiN/Si interface. In the second step, TiN/ Si(100) samples are oxidized to create r-TiO₂/TiN/Si(100) epitaxial

heterostructures. This paper focuses on the details of TiN oxidation and epitaxial relations of TiO₂ with respect to the underlying TiN. Some of the experimental papers mentioned that the diffusion of oxygen is responsible for oxidation^{18–24}. While others tried to show Ti out-diffusion as a main source of oxidation through simulation^{25,26}, but detailed microstructural studies were not carried out. Here we have tried to capture an image at the atomic scale of an epitaxial TiO₂/TiN matrix to investigate the details of TiN oxidation. Through solid-state oxidation of TiN epilayer, (110) out-of-plane orientation was achieved. The atomic arrangement, the nature of strains, and the mechanism behind the strain relaxation across the interfaces are discussed.

4.1.2. Experimental details

Epitaxial TiN/Si(100) heterostructures were grown on Si(100) substrates by pulsed laser deposition (PLD) technique where a Lambda Physik KrF excimer laser (LPX200, $\lambda = 248$ nm, $\tau = 25$ ns) was used to ablate a high purity TiN target. The laser beam was incident at the surface of the target at an angle of 45°. The target was rotated during the ablation to avoid compositional variations on the target surface. The Si(100) substrates were cleaned through a multi-step procedure including the removal of inorganic impurities by acetone vapor, ultrasonic cleaning in methanol, and removal of silicon dioxide from the surface by HF etchant. The cleaned substrates were then dried by a high purity nitrogen gun and immediately loaded into the deposition chamber. The chamber was evacuated to a base pressure of 1×10^{-6} Torr. The TiN thin films were grown at 650 °C for 4500 pulses under vacuum. The energy density and repetition rate were set at 3.5–4 J cm⁻² and 5 Hz, respectively. The TiN layers were subsequently oxidized inside the deposition chamber under an oxygen partial pressure of 1×10^{-2} Torr and 650 °C for 1 min. Eventually, the samples were cooled down to room temperature inside the deposition chamber under an oxygen partial pressure of 1×10^{-4} Torr. The cooldown process took about 30 min. The out-of-plane

orientation of the films was investigated by XRD θ - 2θ scan using a Rigaku diffractometer equipped with a $\text{CuK}\alpha$ source ($\lambda_{\text{ave}} = 0.154 \text{ nm}$). A Philips X'Pert Pro diffractometer was employed for φ -scan XRD to confirm in-plane alignment, and to determine crystallographic alignments and epitaxial growth characteristics across the interfaces. A JEOL 2010F transmission electron microscope with a point-to-point resolution of 1.8 \AA was used to collect atomic resolution images and selected area electron diffraction (SAED) patterns from the interfaces. The FEI Titan 80–300 probe aberration-corrected scanning transmission electron microscope (STEM) operated at 200 KV, was used to collect electron energy loss spectrum (EELS) across interfaces. The SuperX Energy Dispersive Spectrometry (SuperX EDS) was also used to achieve elemental mapping at the atomic level. The monochromator made it possible to achieve the energy resolution of the electron source $\leq 0.15 \text{ eV}$, which allows EELS to be collected at the atomic level. The SuperX EDS system with four Bruker Silicon Drift Detectors (SDD) was able to collect characteristic X-Ray signal at high counts per second.

4.1.3. Results and discussion

4.1.3.1. Epitaxial relationship of $\text{TiO}_2/\text{TiN}/\text{Si}(100)$ heterostructures

The 2θ - θ XRD pattern shown in Figure 4.1 confirms the formation of highly textured r-TiO_2 and TiN layers with $[110]$ and out-of-plane orientations, respectively. Results of φ -scan XRD are depicted in Figure 4.2, where strong φ -peaks from TiO_2 and TiN crystals confirm three-dimensional alignment and epitaxial nature of the films. The crystallographic parameters of the reflection planes utilized to collect φ -patterns are summarized in Table 4.1.

Table 4.1. Crystallographic parameters used to collect ϕ -patterns from (111) reflection of rutile TiO_2 crystal and (220) reflections of TiN, and Si crystals.

	TiO_2	TiN	Si
2θ ($^\circ$)	41.22	61.00	47.57
ψ ($^\circ$)	24.48	45.00	45.00

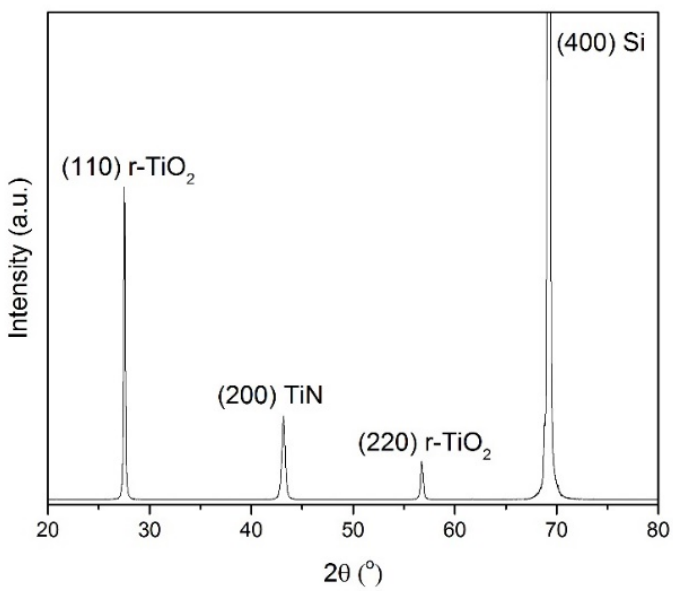


Figure 4.1. XRD θ - 2θ pattern acquired from the $\text{TiO}_2(110)/\text{TiN}(100)/\text{Si}(100)$ heterostructure.

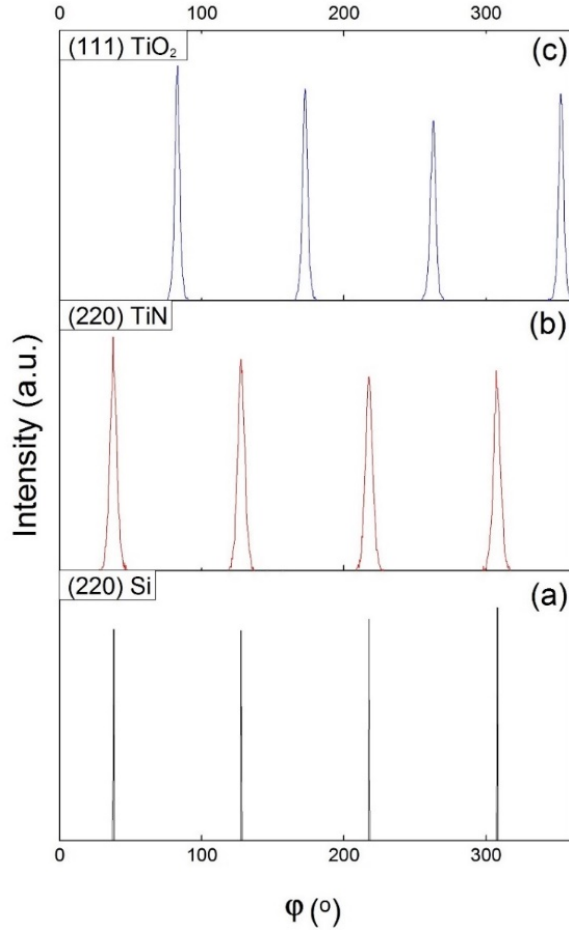


Figure 4.2. Results of XRD ϕ -scan performed on the $\text{TiO}_2(110)/\text{TiN}(100)/\text{Si}(100)$ heterostructure: a) $\text{Si}(220)$ reflection, b) $\text{TiN}(220)$ reflection, and c) $\text{TiO}_2(111)$ reflection.

Considering the TiN/Si interface, the ϕ -signals from $\{220\}$ reflections of these crystals appear at the same angular positions (Figure 4.2a and b). By combining this information with that from Figure 4.1, we derive a cube-on-cube arrangement across the TiN/Si interface. It has been already shown that the 22% misfit strain at this interface relaxes via matching of 4/3 domains (4 planes of TiN and 3 planes of Si) and 5/4 domains with a frequency factor of 0.5^{27,28}. The epitaxial relationship at the TiO_2/TiN interface was determined using the ϕ -patterns in Fig. 4.2b and c. Four sharp ϕ -signals from $\{111\}$ family of planes of TiO_2 originate from (111) and $(\bar{1}\bar{1}\bar{1})$ planes for (110)/ $(\bar{1}\bar{1}\bar{0})$ as well as $(1\bar{1}\bar{1})$ and $(\bar{1}\bar{1}1)$ planes for $(1\bar{1}\bar{0})/(\bar{1}\bar{1}0)$ of titania. The common direction between $\text{TiO}_2\{110\}$ and $\text{TiO}_2\{111\}$ planes is $\langle \bar{1}10 \rangle$ which has an azimuthal

rotation of 45° with respect to TiN axis. With this information, the crystallographic alignment across the TiO_2/TiN interface is established to be $\text{TiO}_2\{110\}||\text{TiN}\{100\}$ and $\text{TiO}_2\{\bar{1}10\}||\text{TiN}\{110\}$.

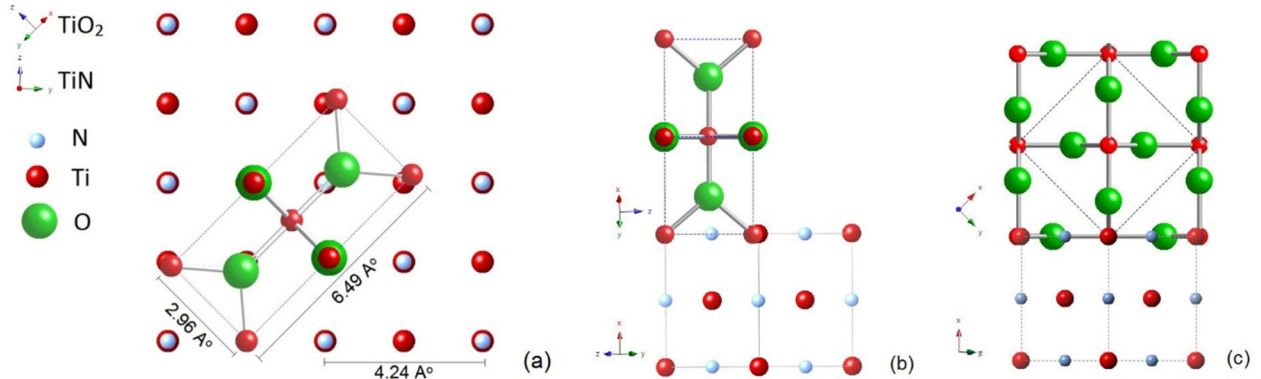


Figure 4.3. Schematic illustration of Real Space crystallographic alignment across TiO_2/TiN interface: a) Top view, b) Cross-section view along $\text{TiO}_2[110]$ common axis, c) Cross-section view along $\text{TiO}_2[001]$ common axis.

Figure 4.3a, b, and c schematically illustrate the atomic arrangement and crystallographic alignment across the TiO_2/TiN interface. This schematic shows that the titanium along the $\text{TiN}\langle 110 \rangle$ direction align with those along the $\text{TiO}_2[110]$ and $\text{TiO}_2[001]$ directions. For the sake of simplicity, let us consider particular planes of TiO_2 and TiN instead of a family of planes. Considering the epitaxial alignment at the TiO_2/TiN interface (Figure 4.3), (110) planes of TiO_2 match with (110) planes of TiN . The inter-planar spacing of $\text{TiO}_2(110)$ and $\text{TiN}(110)$ equal to 3.25 and 2.99 \AA , respectively. This results in an 8.69% compressive misfit strain in TiO_2 lattice which relaxes through $11/12$ and $12/13$ alteration domains with a frequency factor of 0.5 , based on the domain matching epitaxy paradigm²⁸. Along the perpendicular direction in the film plane, $\text{TiO}_2(001)$ planes, with an inter-planar distance of 2.95 \AA , match with $\text{TiN}(\bar{1}10)$ planes, having an inter-planar spacing of 2.99 \AA . This results in a 1.34% tensile misfit strain in the titania lattice. Such a small tensile strain is harder to relax because the critical thickness beyond which the thin

layer can accommodate misfit dislocations becomes larger ^{3,28}. This means that the misfit dislocations nucleating at the free surface of the thin film have to glide a large distance to reach the film/substrate interface to relax the strain. This issue is more critical in the ionic materials such as TiO₂, where a large lattice friction stress is needed for dislocation glide. On the other hand, in large misfit systems, the critical thickness is of the order of a couple of monolayers, where misfit dislocations nucleate at the free surface steps and are able to glide easily and reach the interface. The ease of dislocation glide is dictated by the critical resolved shear stress within the primary slip system. For a dislocation to glide, the resolved shear stress must exceed the yield stress of the material. The yield stress of rutile TiO₂ has been determined to be 3 GPa ²⁹. Critical resolved stress can be calculated by $\tau_r = \sigma \cos\phi \cos\lambda$, in which ϕ is the angle between normal of the slip plane and stress direction, and λ is the angle between the slip direction and direction of the stress σ . In-plane stress $\sigma_{xx}(yy)$, can be obtained as follows ⁴:

$$\sigma_{xx(yy)} = \frac{2\mu(1+\nu)e_{xx(yy)}}{1-\nu} \quad \text{Equation (4.1)}$$

$$e_{xx} = e_{yy} = -e_{zz} \frac{1-\nu}{2\nu} \quad \text{Equation (4.2)}$$

where $\sigma_{xx}(yy)$ and e_{xx} , e_{yy} , which can be calculated by equation (2) assuming isotropic relaxation, are the stress and strains along the X and Y directions and e_{zz} is the out of plane strain that can be calculated through θ - 2θ X-ray diffraction, μ represents the shear modulus (118 GPa for rutile TiO₂ ³⁰), and ν is the Poisson's ratio (0.22 for rutile TiO₂ epilayer ³¹ which is different from bulk value). Therefore, the misfit stresses are obtained as $\sigma[001] = 4.946$ GPa and $\sigma[110] = -33.074$ Gpa. The out of plane stress along $[\bar{1}10]$ is equal to zero, even though the strain is not equal to zero. The primary slip system in rutile TiO₂ is considered as $1/2\langle\bar{1}01\rangle\{101\}$. Considering $1/2[10\bar{1}](101)$ and $1/2[01\bar{1}](011)$ slip systems, resolved shear stress is calculated to be 2.251 GPa along $[001]$ direction and -7.527 GPa along $[110]$ direction. It should be noted that for $1/2[1\bar{1}0](110)$, the resolved shear

stress for both stresses along [001] and [110] would be zero. The critical resolved shear stress along [110] axis is larger than the yield stress. Thus, the misfit dislocations nucleating on the free surface of TiO₂ are able to glide along this slip system. However, along with the [001] direction, the resolved shear stress is smaller than the yield stress of the material. The misfit strain on [001] axis of TiO₂ is small and as of tensile nature. Tensile strains are harder to relax due to the lack of surface steps and higher nucleation barrier. Dislocation nucleation and glide phenomena are the initial steps for the generation of misfit dislocations. The energy of step formation can be negative under compressive strain and is always positive under tensile strain. Therefore, dislocation generation decreases the surface energy if the dislocation relaxes compressive stress, while it is positive if the dislocation relaxes a tensile stress³². Under a compressive strain, the step formation decreases the number of dangling bonds and surface energy. In contrast, the number of surface dangling bonds increases under the tensile strain conditions, since one extra half plane, i.e. misfit dislocation, needs to be inserted in the lattice and an extra row of dangling bonds is added to the surface. However, one atomic plane (one row of dangling bonds) is removed when a compressive strain relaxes³². The unrelaxed in-plane misfit strains result in a small strain along the out-of-plane orientation, i.e. TiO₂ [110]. Our high-resolution θ -2 θ XRD scans (Figure 4.4) through TiO₂ (110) peak confirms the presence of a 0.36% strain in the out-of-plane direction. Here, Si(400) peak was used as a control (standard peak). The out-of-plane strain was calculated based on the displacement of the TiO₂ (110) peak at 2 θ : 27.548 from its standard position at 2 θ : 27.446. Thermal strains e_T which stem from different expansion coefficients between TiO₂ and TiN should be taken into account³³:

$$e_T = (T_{growth} - Room\ Temperature)(a_{film} - a_{substrate}) \text{Equation (4.3)}$$

where a is the thermal expansion coefficient. The thermal expansion coefficient of TiN is $9 \times 10^{-6} \text{ k}^{-1}$ ³⁴ and that for rutile equals to $8.8 \times 10^{-6} \text{ k}^{-1}$ along [100] and is $7.2 \times 10^{-6} \text{ k}^{-1}$ along [001]³⁵. With these values, the thermal strains are calculated to be 0.012% along [100] and 0.112% along [001]. These strains are extremely small and difficult to relax, as explained earlier. Hence, they remain unrelaxed in the system. As a consequence, a portion of the 0.36% residual strain has its origin in the unrelaxed thermal strain and the rest is related to defects. Figure 4.5a displays a low magnification cross-section TEM micrograph acquired from the TiO₂(110)/TiN{100}/Si{100} epitaxial heterostructures. The SAED patterns shown in the inset further confirm three-dimensional alignment and the epitaxial relationships discussed earlier. The thicknesses of TiO₂ and TiN layers were measured to be 140 and 90 nm, respectively. High resolution and STEM image from the TiO₂/TiN is depicted in Figure 4.5b and c, where nonplanar nature of TiO₂/TiN interfaces may indicate the presence of thin TiN_xO_y transition layers.

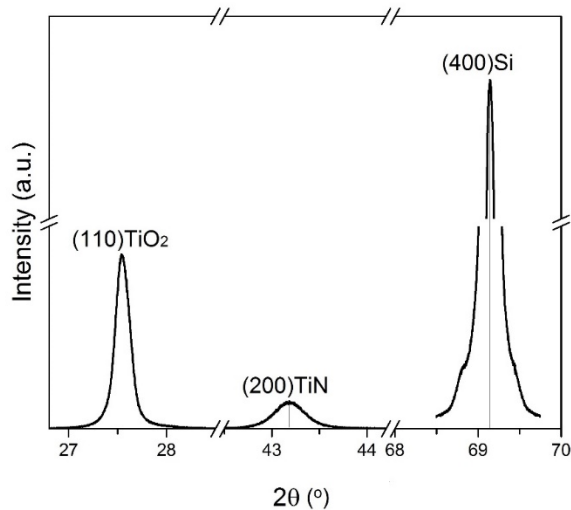


Figure 4.4. High-resolution XRD θ - 2θ pattern performed through TiO₂(110), TiN(200) and Si(400) signals.

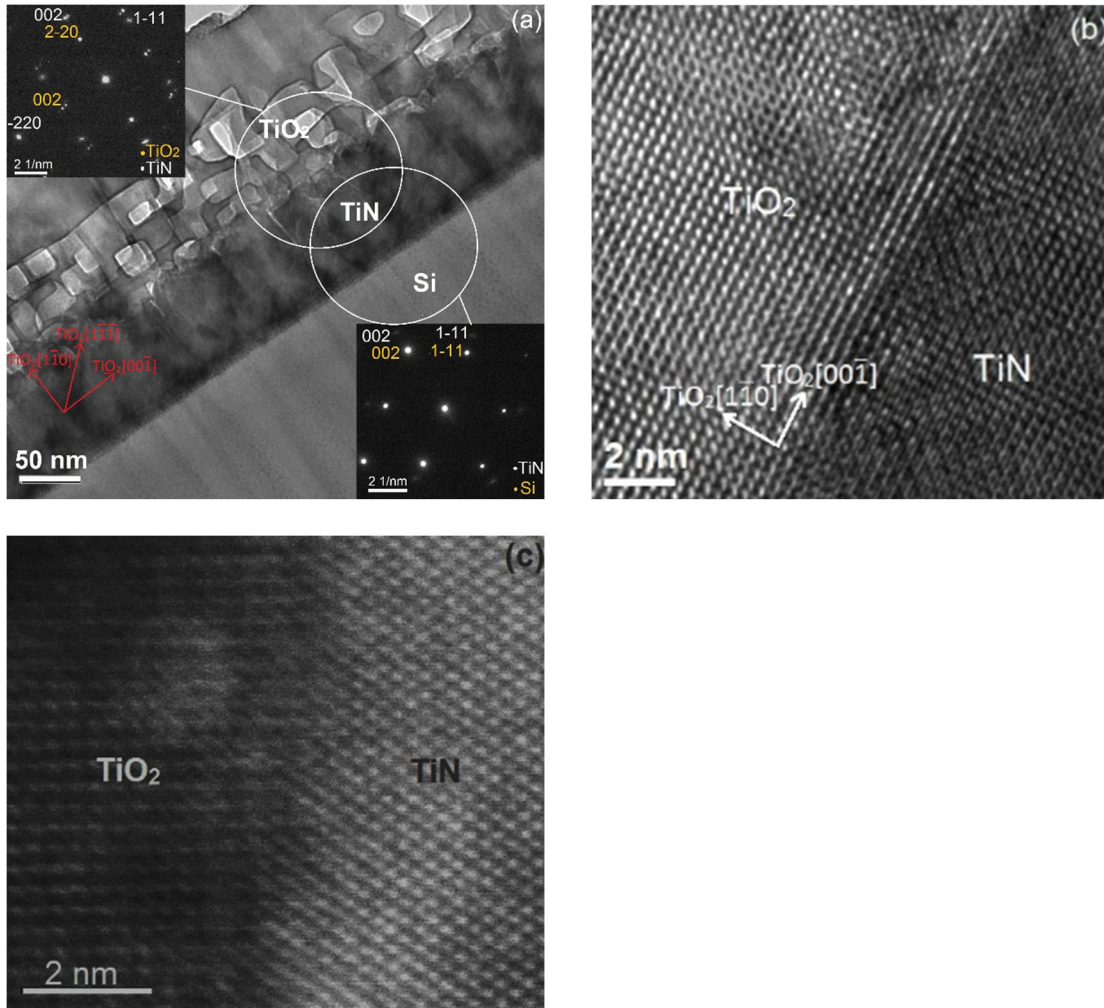
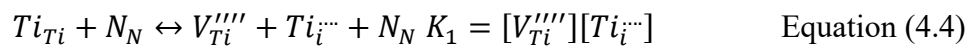


Figure 4.5. Cross-section TEM micrograph and indexed SAED patterns from each interface. The patterns belong to Si [110], TiN [011], and TiO₂ [100] zones, b) High-resolution TEM micrograph of the TiN/TiO₂ interface, c) STEM micrograph of the TiN/TiO₂ interface.

4.1.3.2. Oxidation mechanism

During the first step of the oxidation, titanium rapidly diffuses out to the surface where it reacts with oxygen to form TiO₂. This process results in the formation of titanium vacancies in the inner layers. As shown in Equation (4.4), according to Kroger-Vink notation, titanium cations move to the interstitial sites so that they can diffuse toward the surface:



where X_X , $V_X^{\alpha'}$, and X_i^{α} denote an X atom on its normal lattice site, an ' α ' times ionized X vacancy, and ' α ' positive charged X interstitial, respectively. The overall reaction for the oxidation of TiN to TiO_2 has been expressed as $TiN + O_2 \leftrightarrow TiO_2 + 1/2 N_2(Gas)$ ^{36,37}. Though during this stage, nitrogen remains in its lattice sites, so this reaction should be rewritten as below:

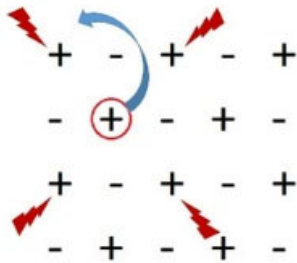
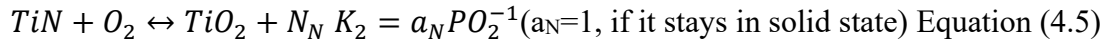


Figure 4.6. Schematic illustration of Ti leaving nitrogen octahedron and weakening neighboring Ti atoms' bond.

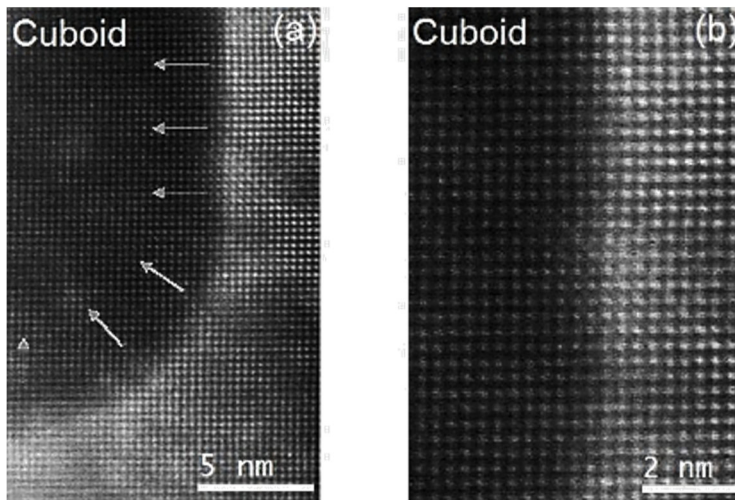


Figure 4.7. Cross-section Z-Contrast STEM micrograph of TiO_2 ; illustrating faceted voids (cuboids) within TiO_2 thin film, a) arrows pointing inside of the cuboid, b) high-resolution image of the interface of the cuboid/ TiO_2 .

Diffusion of Ti collapses the nitrogen octahedron, shown schematically in Figure 4.6. This collapse ends up weakening the neighboring Ti bonds and making them more inclined to diffuse out as well. As a result, the number of Ti vacancies increases, forming the observed cuboids.

Ciacchi also mentioned that Ti vacancies tend to cluster together ²⁶. To form a better illustration of the atomic column and formed cuboids, Z-contrast STEM image has been shown in Figure 4.7.

Thus, cuboids filled with atomic nitrogen formed which then form N₂ gas. The N₂ pressure within cuboids can be calculated by PV = nRT, calculating “n” as n = Number of N₂ molecules can be generate per unit cell of TiN /TiN unit cell volume = $2N_2 \cdot 10^{24} \cdot 10^6 / 4.2^3 = 2.66 \times 10^{28} \text{ m}^{-3}$, and P(Pa)=n(m⁻³)kBT = $2.66 \times 10^{28} \times 1.38 \times 10^{-20} = 3.59 \times 10^8$ (kB = 13.80×10^{-24} J and T = 1000 K). The driving force for N₂ migration to the surface is aided by the high-pressure generated by N₂. The nitrogen out diffusion will reduce the fracture stress needed for rupture. Since the calculated pressure exceeds modulus of rupture of TiO₂ as 140 MPa and Young’s Modulus as 230 GPa ³⁰, it can lead to the formation of cracks, as observed by others ^{18,37}. Since, we did not observe cracking, N₂ out diffusion caused the lowering of rupture stress. Also, the EDS analysis across TiN/TiO₂ interface in Figure 4.8 confirms the presence of these cuboids which has been emptied out. In the meantime, oxygen defuses into the interface of TiN and TiO₂, as stated in Equation (4.6) and (4.7). This process consumes the TiN layer.

$$O_2 \leftrightarrow V_{Ti}'''' + 2O_O + 4h \cdot K_3 = \frac{[V_{Ti}'''']h^4}{P_{O_2}} \quad \text{Equation (4.6)}$$

$$Ti_{Ti} + 2O_O \leftrightarrow 2O_i'' + 2V_{\ddot{O}} K_4 = [O_i'']^2 [V_{\ddot{O}}]^2 \quad \text{Equation (4.7)}$$

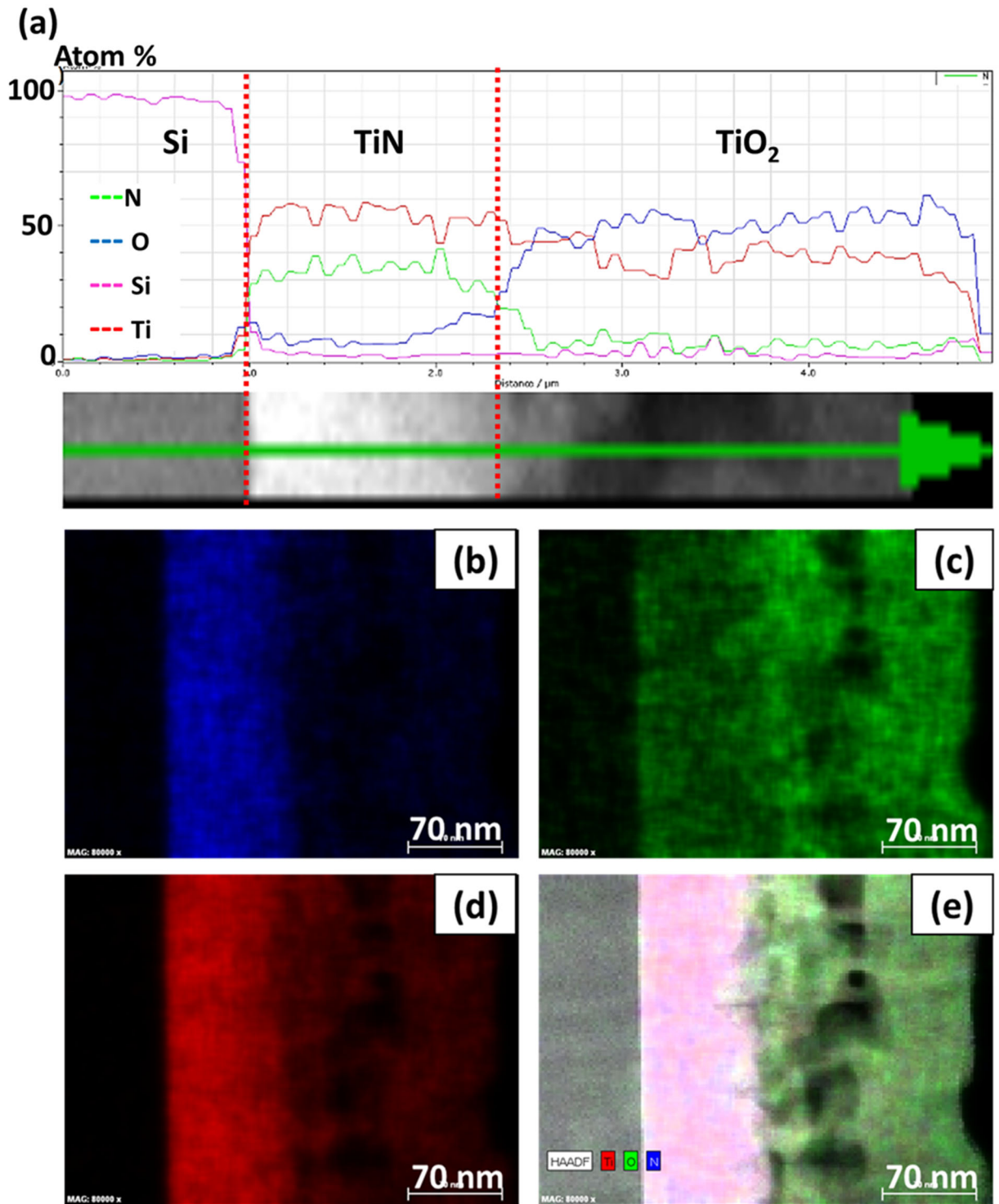


Figure 4.8. EDS analysis a) Across TiO₂(110)/TiN(100)/Si(100) heterostructure, b) N distribution, c) O distribution, d) Ti distribution, and e) Elemental mapping.

Considering the role of surface energies during oxidation, some crystallographic aspects of different surfaces have been mentioned briefly. Among all planes of rutile, (110) is the most stable; however, this factor does not directly determine its activity, and other factors like atomic arrangement on different planes play a role as well³⁻⁵. Based on the Broken Bond model³⁸, the energy of surfaces (J/atom) would be defined as:

$$g_{(hkl)}^{SV} = \frac{N_{s(hkl)}nE_b}{2} \quad \text{Equation (4.8)}$$

where “ $N_{s(hkl)}$ ” is the number density of atoms, atoms/m², on the (hkl) surface and it is assumed there is no surface strain. The “n” is the number of broken bonds for each surface atom. “ E_b ” is the energy of each bond. The n bonds need to be broken to form two (hkl) faces for each surface atom. Hence, every surface atom has an excess internal energy of $nE_b/2$ over the atoms in the bulk. Thus, different faces have diverse surface energies, i.e., 1.65 J m⁻² for the (001), as shown in Figure 4.9 with two Ti and two O broken bonds, 0.89 J m⁻² for the (110) with two Ti broken bonds, 1.12 J m⁻² for the (100) with three Ti broken bonds, and 1.39 J m⁻² for the (101) face with three Ti broken bonds⁴. (111) face with two broken bonds for Ti and one broken bond for O has four times higher surface energy than (110) face³⁹. There are other considerations namely lack of electronic neutrality of the free faces, which increase surface energies based on their arrangements considering TiO₂ ionic nature. The length of the cuboids lies onto low energy surfaces of TiN and TiO₂, namely {100} and {110}. The width of the cuboids lies on the other low energy surfaces of TiN and TiO₂, namely {110} and {100}. The directions for length and width of cuboids were determined by cross-section TEM images and based upon the indexed diffraction pattern presented in Figure 4.5a. The geometry of these cuboids is governed by the Wulff shape representing the shape of an equilibrium cuboids by minimizing the total surface free energy⁴⁰, as shown in Figure 4.10. The g-vectors of the planes form the Wulff shape are in accordance with crystallographic g

vector direction of cuboid surfaces which are shown in the indexed SAED pattern on Figure 4.5a. The cuboids grow as more Ti atoms leave and when two cuboids meet each other, they will join together along $\{111\}$ orientation, as is seen in the cross-section micrograph in Figure 4.5. The larger cuboids merging with smaller cuboids would align themselves with low energy surfaces as shown in Figure 4.5. This behavior has been shown schematically in Figure 4.11. The cuboids are confined near the TiN/ TiO₂ interface, which confirms the oxidation of TiN to TiO₂ via a two-step process and transitioning from step one (diffusion of Ti out) to step two (diffusion of O in) after some time. It should be mentioned that the oxygen diffusion from the surface into the bulk ends up oxidizing TiN and forming TiO₂ all around cuboids. Thus, titanium interstitials need to diffuse out through TiO₂ layer to reach the surface which results in the changes in their valence state from Ti³⁺ to Ti⁴⁺ and introduces an electron into the system based on Equation (4.9) and (4.10), if they need vacancy for their migration.

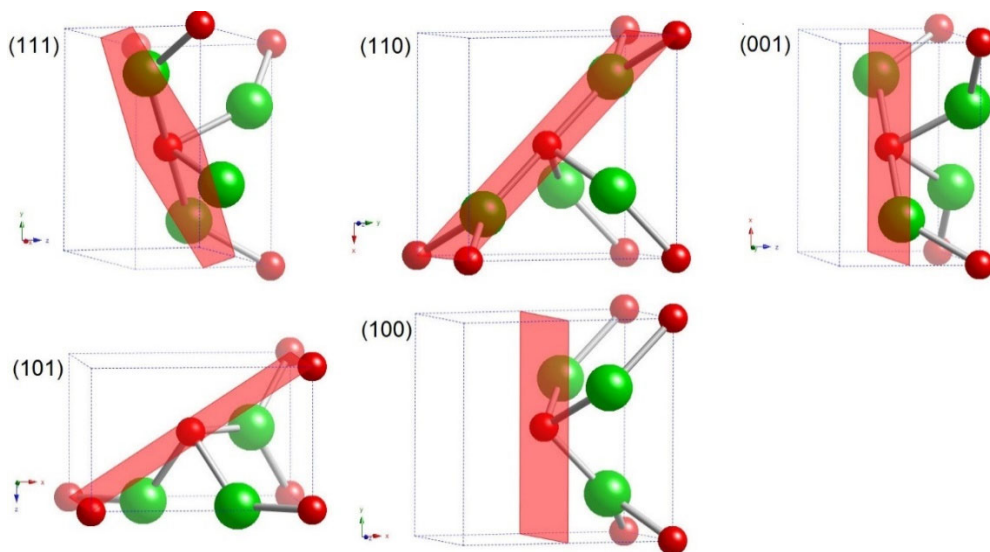


Figure 4.9. Rutile TiO₂ structure sliced at different planes.

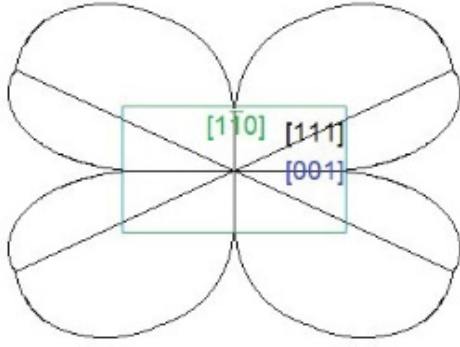


Figure 4.10. Wulff construction belonging to [110] direction of rutile TiO₂ (Surface energies obtained from Refs^{8, 38}).

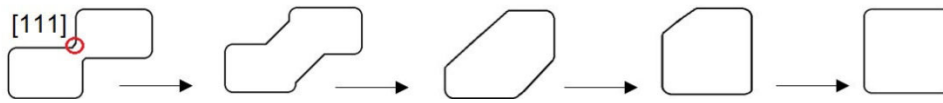


Figure 4.11. Schematic illustration of TiO₂ cuboid Surface transition from (111) to (110) and (001) during merging of the cuboids.

Measuring the oxide thickness formed over a specific period of time, the rate constant and, subsequently, activation energy can be obtained from Equation (4.11) and (4.12)¹⁸, considering assumptions that diffusion species are uncharged, and there is steady state condition for diffusion; that is there is no change in diffusion rate by changing thickness and time⁴¹.

$$D = 2(K(T)) \times t^{0.5} \quad \text{Equation (4.11)}$$

$$K(T) = k_0 \exp\left(-\frac{Q}{RT}\right) \quad \text{Equation (4.12)}$$

where D is the thickness of the oxide layer in nm, k (T) is the rate constant, and t is the oxidation time. K₀ is the pre-exponential factor ($2.2 \times 10^{-6} \text{ cm}^2/\text{s}$ ¹⁸), Q is the activation energy, R is the gas constant (8.314 J/mol.K), and T is the absolute temperature. The Q is calculated to be 1.16 eV for titanium, which is slightly higher than the activation energy for oxygen diffusion, which is very close to the values in the literature for short circuit diffusion routes¹⁸⁻²⁰. Indeed, the diffusion activation energies of Ti and O in the TiO₂ epilayer are smaller than that in the TiO₂ bulk, which may be due to the single-crystalline nature of our films (there are small-angle, subgrain

boundaries $< 1-2^\circ$ in the epitaxial TiO_2) and the presence of cuboids, which ease the migration of titanium cations and oxygen anions.

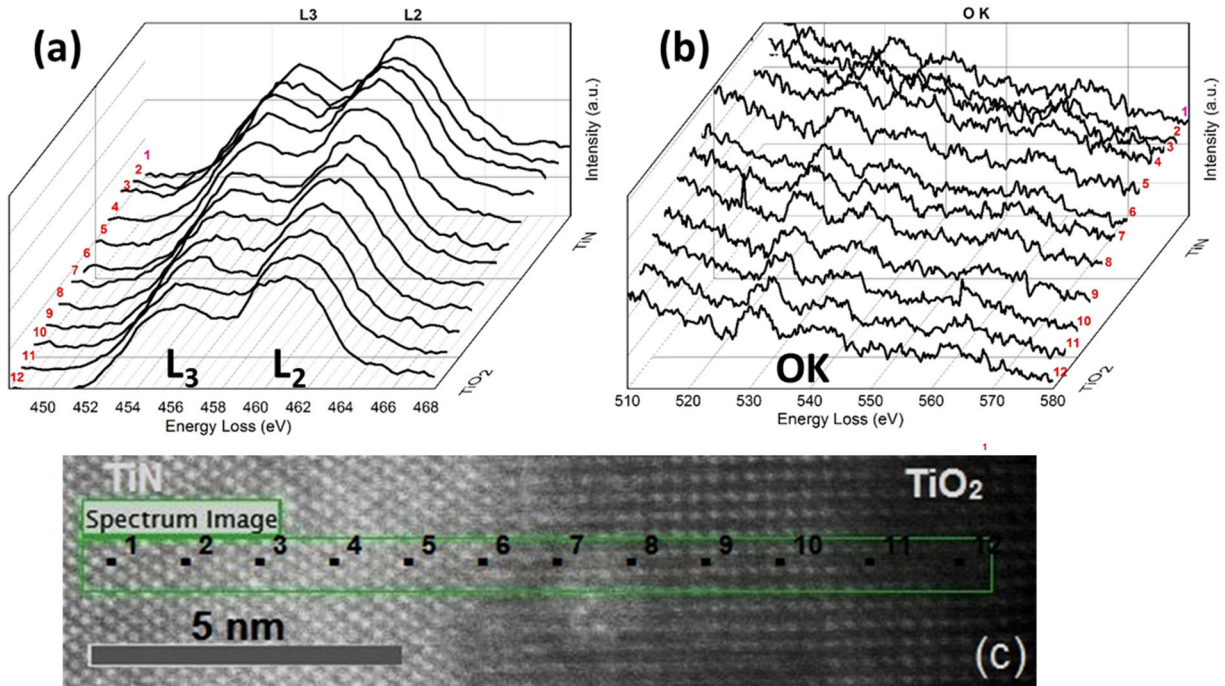


Figure 4.12. EELS mapping analysis across TiN/TiO₂ interface a) In the Ti L_{2,3} edges range, b) In the O K edge range, c) The location of the spots where the EELS data were collected. The numbers correspond to the numbers on figures a and b.

A comparison obtained from the Ti L_{3,2} EELS edges in Figure 4. 12a revealed that moving toward the TiO₂ side, the L_{3,2} onset shifts to higher energy with increasing Ti valence state. Also, the O K spectrum (Figure 4.12b) systematically shifts to lower energy losses with an increasing valence state of Ti. The L₃ edge contains two main peaks; the first one corresponds to transition from 2p_{3/2}Ti level to the 2t_{2g} Ti_x level and the second peak is due to the transition from the 2p_{3/2} Ti level to the 3e_g Ti_x level⁴². It is worth mentioning that the distortion in the tetragonal symmetry would increase the degree of splitting of the 2t_{2g} and 3e_g levels⁴³. This distortion may also affect the higher energy level 4t_{1u}, which is split into 3 sublevels: 4b_{1u}, 4b_{3u}, and 4b_{2u}. Hence, in Figure 4.12a the splitting of the second peak in TiO₂ side is due to the splitting of the 3e_g level. Though,

the trigonal distortion in TiN structure causes t_{2g} level split into two components, while the e_g level remains unchanged⁴⁴. The combination of the spin-orbit coupling and the trigonal distortion end up having the zero-field splitting. Hence, no additional peak can be seen in the TiN side.

Moreover, the O k region in the TiO₂ side includes two major peaks in the range of 520–530 eV (Figure 4.12b) which originate from the transition between oxygen 1s and 2p σ^* states that are hybridized with empty Ti 3d orbitals²⁴. These peaks in the TiN side are not distinguishable. The splitting is caused by the t_{2g} - e_g splitting of the Ti 3d levels. Thus, the first peak is assigned to the O 2p \rightarrow Ti 3d (t_{2g}) and the second one to the O 2p \rightarrow Ti 3d (e_g)⁴². This splitting happens gradually from TiN to TiO₂ side and is not a sharp transition. Also, the second set of bands at the higher energies can be observed in the O k spectra. The presence of these peaks can be explained by interactions between O 2p orbitals and titanium 4s/ 4p orbitals²⁴. In addition, in the orthorhombic distortion, in the TiO₂ structure, the 4t_{1u} level is split into 3 sublevels: 4b_{1u}, 4b_{3u}, and 4b_{2u}⁴². Thus, we may assign the peaks C and D to the lowest unoccupied 4t_{1u} bands and the peak E to transitions to higher 4t_{1u} type bands. In summary, EELS illustration in Figure 4.12 a, b and the diffused interface in Figure 4.12 c, represent the gradual shift of the valance state for Ti, and consequently not a sharp transformation from TiN to TiO₂, where it happens through TiN_xO_y transition layer.

4.1.4. Conclusion

We integrated single crystalline rutile TiO₂ thin film with Si(100) through solid-state oxidation of TiN buffer layer. The epitaxial relationship between the silicon substrate and the TiN buffer layer was established as a cube-on-cube TiN{100}/Si{100}. The epitaxial relationship at the r-TiO₂/TiN interface was proposed as TiO₂(1 $\bar{1}$ 0)||TiN(100) and TiO₂(110)||TiN(110). The mechanism of TiN(100) oxidation was investigated in detail. The first step of oxidation was

established to be the diffusion of Ti atoms leaving Ti vacancies behind. It was indicated that the formation of these vacancies collapses the nitrogen octahedron. As a result, neighboring Ti bonds become weaker and more inclined to diffuse out. The Ti vacancies then coalesce forming small cuboids in which N₂ gas forms. The internal pressure provided by N₂ gas within cuboids was calculated to be high enough, 359 MPa, to make N₂ molecules migrate to the TiO₂ surface and produce some cracks there. However, in our study, the pressure did not exceed the critical value to generate cracks due to N₂ out diffusion which caused the lowering of fracture stress. The presence of the TiN_xO_y transition layer was confirmed by EELS studies associated with the diffusion of oxygen atoms into the TiO₂/ TiN interface during oxidation.

4.2. Thin film bi-epitaxy and transition characteristics of TiO₂/TiN buffered VO₂ on Si(100) substrates (*MRS Advances*, 1 (37) (2016) 2635-2640)

Abstract

Bi-epitaxial VO₂ thin films with [011] out-of-plane orientation were integrated with Si(100) substrates through TiO₂/TiN buffer layers. At the first step, TiN is grown epitaxially on Si(100), where a cube-on-cube epitaxy is achieved. Then, TiN was oxidized in-situ ending up having epitaxial rutile-TiO₂. Finally, VO₂ was deposited on top of TiO₂. The alignment across the interfaces was established as VO₂(011) || TiO₂(110) || TiN(100) || Si(100) and monoclinic-VO₂(01 $\bar{1}$) or monoclinic-VO₂(100) || TiO₂($\bar{1}$ 10) || TiN(110) || Si(110). The inter-planar spacing of rutile-VO₂(001) and TiO₂($\bar{1}$ 10) are equal to 2.904 and 3.248 Å, respectively. This results in a 10.59% tensile misfit strain in rutile-VO₂(001) lattice which relaxes through 9/10 alteration domains, according to the domain matching epitaxy paradigm. Also, the inter-planar spacing of rutile-VO₂(110) and TiO₂($\bar{1}$ 10) are equal to 3.251 and 3.248 Å, respectively. This results in a 0.09% compressive misfit strain in VO₂(110) lattice. We studied semiconductor to metal transition characteristics of VO₂/TiO₂/TiN/Si heterostructures and established a correlation between intrinsic defects and magnetic properties.

4.2.1. Introduction

Combination of semiconducting and magnetic properties has led to the development of spintronic (spin-based electronics). This achievement facilitates production of spin-based devices. Different materials have been investigated for this application and some semiconductors such as VO₂, ZnO, TiO₂, Y₂O₃, and In₂O₃ have shown promising results at room temperature⁴⁵⁻⁴⁹. Among those VO₂ shows, a strongly correlated electron system with a small band gap (~0.7 eV at room temperature) but its magnetic properties have not been studied yet. VO₂ can serve as a smart

material which generally responds to temperature, pressure variations, and electric or magnetic fields. It is worth mentioning that VO₂ has a semiconductor-to-metal transition (SMT) at about 340 K resulting from an ultrafast phase transformation from a high-temperature tetragonal state to a low-temperature monoclinic state⁵⁰⁻⁵². Considering practical applications, there is a problem with the bulk VO₂ that it cannot withstand the repeated thermal cycling, while thin films and nanoparticles are more inclined to tolerate these stresses. Also, the SMT for films and nanoparticles can be tuned to room temperature, which makes their application very unique, such as, thermally activated optical switching^{53,54}, thermal relays and energy management devices^{55,56}, infrared sensors and actuators³⁴, micro-bolometers^{57,58}, electrochromic and photochromic memory and optical devices^{59,60}. Magnetic, electrical, and optical properties of semiconductors are controlled through native defects. Also, they play a role in the diffusion mechanism involved in growth, processing, and device degradation. Point defects affect the electrical and optical properties of semiconductors. These point defects consist of intrinsic native defects i.e. vacancies, interstitials, impurities, and defect complexes. In this study, we provide a new platform of TiO₂/TiN (introduced in section 4.1) to grow bi-epitaxial VO₂ while integrated with Si(100). This paper focuses on epitaxial relations across the interfaces. Metal to semiconductor transition for VO₂ is investigated and discussed. We report the magnetic properties of the VO₂ thin film and the role of defects in defining and tuning these properties.

4.2.2. Experimental details

The VO₂/TiO₂/TiN/Si thin film heterostructures were grown on Si(100) substrates employing pulsed laser deposition (PLD). A Lambda Physik (LPX200) KrF excimer laser, with $\lambda=248$ nm, $t=25$ ns, and the average power of 2.5 W was used to ablate the targets. The laser gas composition was 0.12% F₂, 2.22% He, 4.6% Kr, and 92.94% Ne. The laser beam was incident at

an angle of 45° on the surface of the targets which were rotated during the deposition to provide uniform ablation characteristics of the target surface. The energy density and repetition rate were set at $3\text{-}3.5\text{ J.cm}^{-2}$ and 5 Hz . The TiN buffer was deposited at 920 K for 4000 pulses under 10^{-5} Torr using a high density of 99.9% pure TiN target. Through 2 min oxidation under an oxygen pressure of 10^{-2} Torr, half of TiN epilayer was oxidized to TiO_2 at 920 K ^{61,62}. The VO_2 layer was then deposited at 720 K under an oxygen pressure of 10^{-2} Torr for 3000 pulses. The VO_2 target was made by sintering 99.5% pure VO_2 powder under Ar atmosphere at $1100\text{ }^\circ\text{C}$ for 12 h . A Rigaku diffractometer with Cu-K α radiation ($\lambda=0.154\text{ nm}$) was used to study the out-of-plane orientation of the films. A Philips X'Pert Pro diffractometer was employed for ϕ -scan XRD to confirm in-plane alignment and epitaxial growth characteristics across the interfaces. Transmission Kikuchi Diffraction (TKD) mapping was carried out on FEI Quanta Focused Ion Beam. The sample was prepared by Focused Ion Beam (FIB), an FEI Quanta 3D FEG, to be transparent to an electron beam for TKD technique. The sample with pressed indium dots was mounted on a custom built a rotatable pogo-pin setup in the PPMS. The magnetic measurements were done using Quantum design Super-conducting Quantum Interference Device (SQUID).

4.2.3. Results and discussion

Figure 4.13 shows the θ - 2θ scan of the X-Ray diffraction pattern of VO_2 thin film grown on the Si(100) substrate buffered with TiO_2/TiN layers. The pattern represented either a highly textured or an epitaxial VO_2 layer with the out of plane orientation of (011). Thus, the out-of-plane relationship can be established as $\text{VO}_2(011)\parallel\text{TiO}_2(110)\parallel\text{TiN}(100)\parallel\text{Si}(100)$. In order to investigate the in-plane orientation relationship, ϕ -scan of an X-Ray diffraction pattern (Figure 4.14) was performed using different reflections of the planes. The results reveal a cube-on-cube growth as for the TiN and Si crystals by DME paradigm. Four sharp ϕ -signals from $\{111\}$ family of planes

of TiO_2 originate from (111) and $(\bar{1}\bar{1}1)$ planes for (110)/ $(\bar{1}\bar{1}1)$ as well as $(1\bar{1}1)$ and $(\bar{1}11)$ planes for $(1\bar{1}1)/(\bar{1}11)$ of Titania. The common direction between $\text{TiO}_2\{110\}$ and $\text{TiO}_2\{111\}$ planes is $\langle\bar{1}10\rangle$ which has an azimuthal rotation of 45° with respect to $\text{TiN}\langle 100\rangle$ axis. The (101) reflection of VO_2 layer shows 8 peaks with intervals of 22.5° angular separation from each other. The common direction between $\text{VO}_2\{101\}$ and $\text{VO}_2\{011\}$ planes is $\langle\bar{1}\bar{1}1\rangle$ which has an azimuthal rotation of 22.5° with respect to $\text{Si}\langle 100\rangle$ and $\text{TiO}_2\langle 110\rangle$ axis.

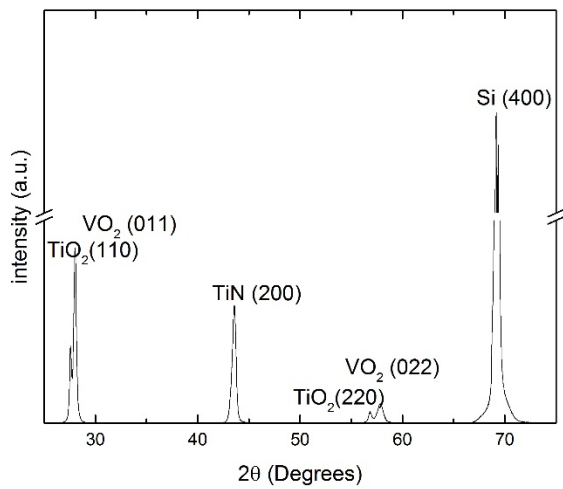


Figure 4. 13. XRD θ - 2θ pattern acquired from the $\text{VO}_2(011)/\text{TiO}_2(110)/\text{TiN}(100)/\text{Si}(100)$ heterostructure.

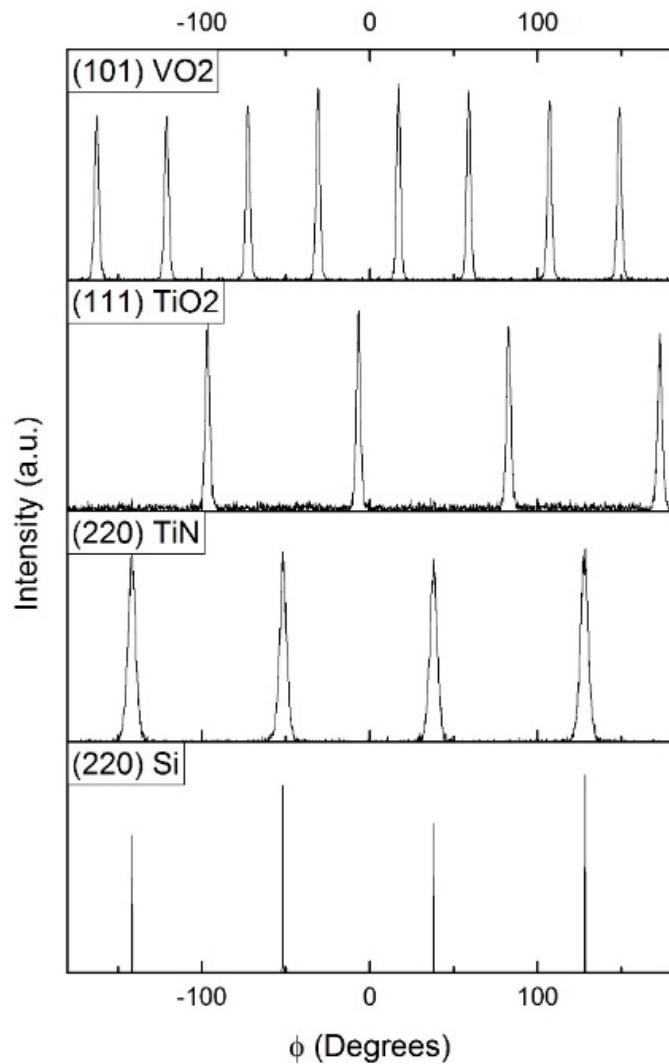


Figure 4.14. Results of XRD ϕ -scan performed on the VO₂(011)/TiO₂(110)/TiN(100)/Si(100) heterostructure: Si(220) reflection, TiN(220) reflection, TiO₂(111) reflection, and VO₂(101) reflection.

For additional details of alignment across interfaces, TKD data were collected from these heterostructures. Figure 4.15a represents the cross-section electron image of the VO₂(011)/TiO₂(110)/TiN(100)/Si(100) heterostructures with the thickness of 110, 100, and 315 nm, for TiN, TiO₂, and VO₂ layers respectively. The band contrast image is displayed in Figure 4.15b which shows where the crystallographic direction undergoes a major change. As it is clear in the VO₂ layer there are vertical grain boundaries illustrating different directions. Figure 4.15c depicts VO₂/TiO₂/TiN/Si heterostructure's phase map, and Figure 4.15d provides a pole figure

map of layers. The Si and TiN have similar Kikuchi, also TiO₂ layer is so thin that makes it hard to detect with this technique. Inverse pole figure map also confirms there are two major colors in VO₂ layer suggesting two major orientations for observed grains. According to the orientation map, two epitaxial relationships are established as VO₂(100) and VO₂(01 $\bar{1}$) || TiO₂($\bar{1}$ 10) || TiN(110) || Si(110). Figure 4.16 a, b, and c & d show the Kikuchi patterns of Si, TiN, TiO₂, and two orientation of VO₂ respectively. These patterns also confirm the cube on cube alignment of Si and TiN. Also, patterns of TiO₂ and VO₂ are in accordance with the established relationship of VO₂(01 $\bar{1}$) || TiO₂($\bar{1}$ 10) and VO₂(100) || TiO₂($\bar{1}$ 10). The orientations in VO₂ grains as represented in Figure 4.15f alternate between normal to (100) and (01 $\bar{1}$) planes. The presence of two types of grains with different orientations explains the appearance of eight peaks in phi-scan XRD with four peaks belonging to each plane. The misfit dislocation nucleation and glide occur at growth temperature where VO₂ is in the rutile structure (monoclinic-VO₂(01 $\bar{1}$) || rutile-VO₂(110) and monoclinic-VO₂(100) || rutile-VO₂(001)). The inter-planar spacing of rutile-VO₂(001) and TiO₂($\bar{1}$ 10) equal to 2.904 and 3.248 Å, respectively. The mentioned matching results in a 10.59% tensile misfit strain in rutile-VO₂(001) lattice which relaxes through 9/10 and 8/9 alteration domains, according to the domain matching epitaxy paradigm²⁸. Also, the inter-planar spacing of rutile-VO₂(110) and TiO₂($\bar{1}$ 10) equal to 3.251 and 3.248 Å, respectively. This results in a 0.09% tensile misfit strain in rutile-VO₂(110) lattice.

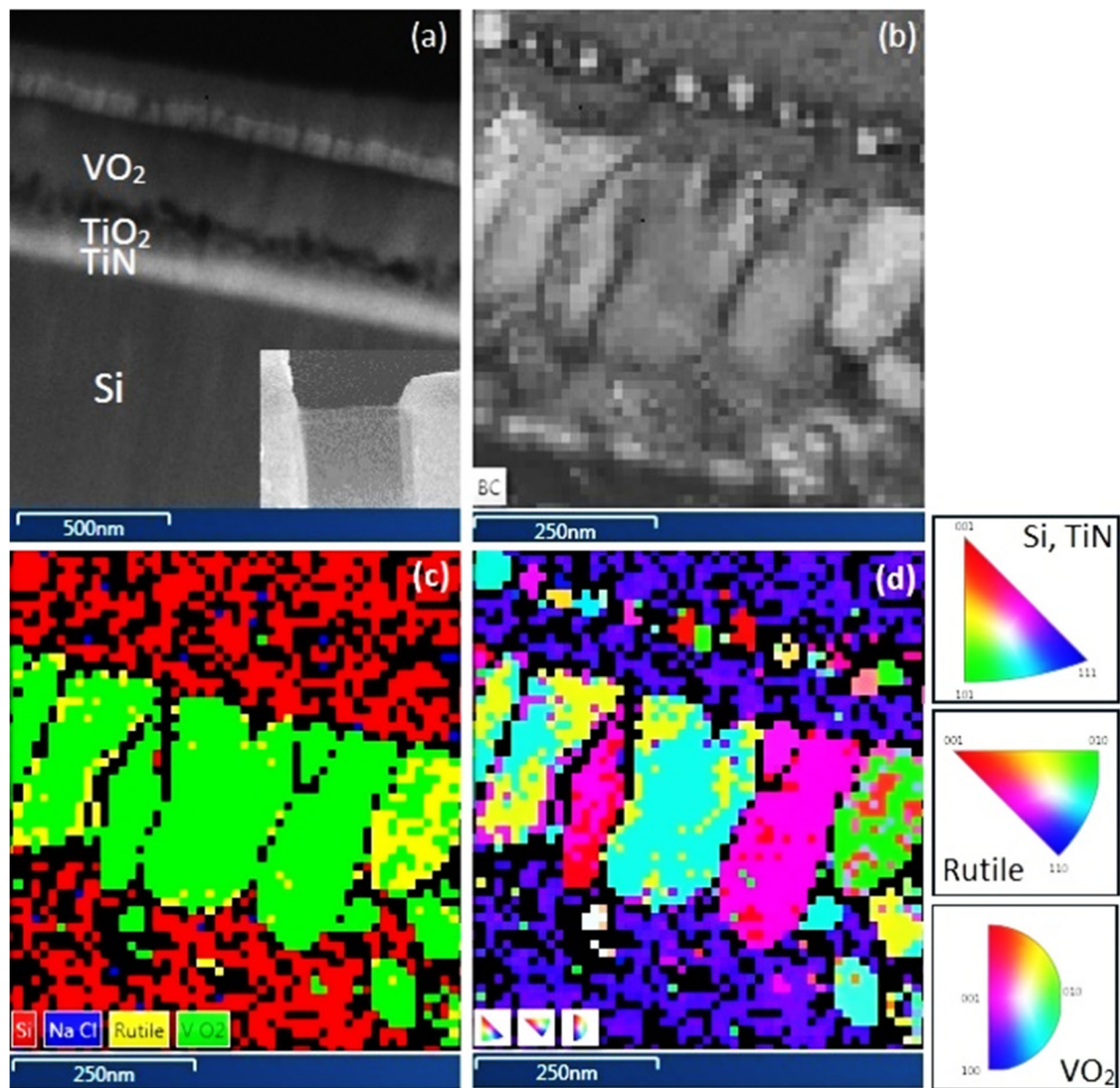


Figure 4.15. TKD result of the FIB slice (a) Cross section electron image and the FIB made sample at the right corner, (b) Band contrast image, (c) Phase map image, and (d) Inverse pole figure map (IPF Y) of interfaces acquired from the $\text{VO}_2(011)/\text{TiO}_2(110)/\text{TiN}(100)/\text{Si}(100)$ heterostructure.

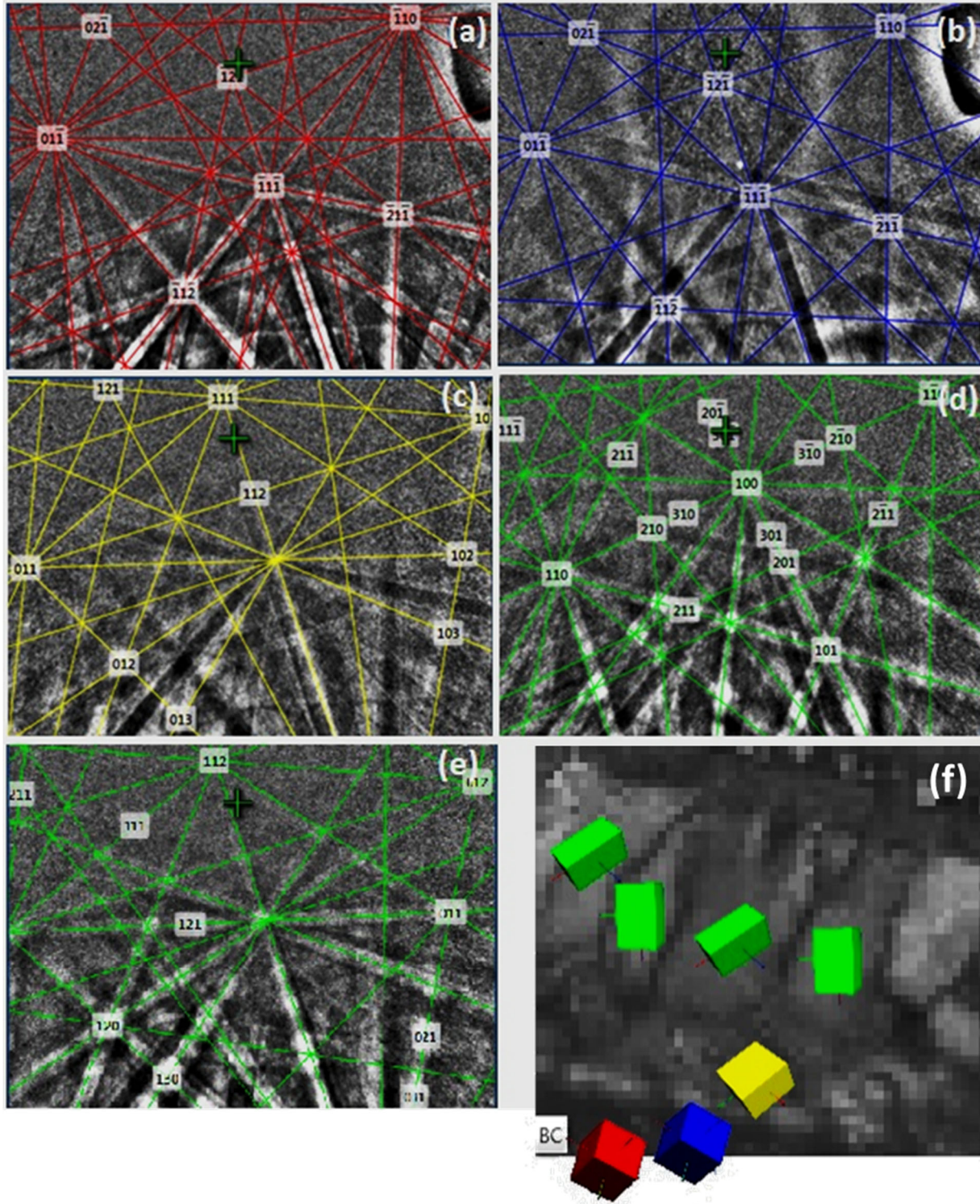


Figure 4.16. Kikuchi patterns of (a) Si, (b) TiN, (c) TiO₂, and (d, e) VO₂ layers. (f) Poles belong to each layer of Si, TiN, TiO₂, and VO₂ in the cross-section band contrast image, respectively from bottom to top.

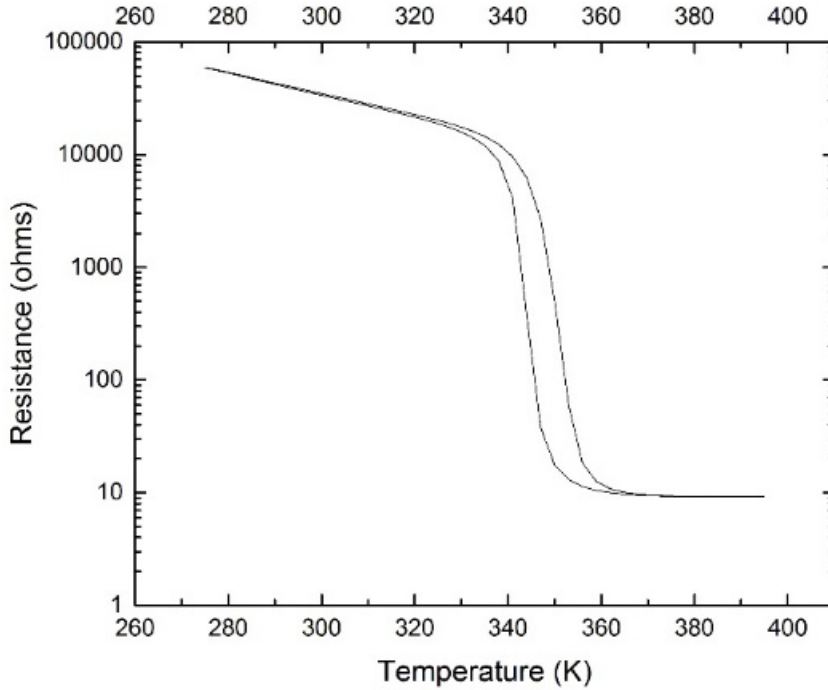


Figure 4.17. Resistance versus temperature in VO₂/TiO₂/TiN/Si heterostructure.

Figure 4.17 displays the semiconductor to metal transition (SMT) temperature of VO₂/TiO₂/TiN/Si heterostructure. A sharp transition in the heterostructure was observed with an amplitude of over five orders of magnitude. The hysteresis is about 8 K and transition temperature is 350 K. Magnetic properties of these films were measured by sweeping the magnetic field from -600 to +600 Oe at three different temperatures of 4, 100, and 300 K. The hysteresis loops are shown in Figure 4.18. It is interesting to note the presence of ferromagnetism in VO₂ thin film. The presence of ferromagnetism is attributed to oxygen vacancy and reduction of Vanadium from V⁴⁺ to V³⁺. In fact, the formation of oxygen vacancies is accompanied by the release of electrons to the lattice which is subsequently trapped by V⁴⁺ cations to preserve charge neutrality. This phenomenon results in the formation of V³⁺ cations. The formation of oxygen vacancies and V³⁺ species can be explained by the following reaction:



where V_O'' represents an oxygen vacancy. This reaction stipulates that the nonstoichiometric VO_2 thin films have a higher charge carrier concentration $[\bar{e}]$ and must exhibit a lower resistivity in the semiconducting state⁵². Ferromagnetic behavior in other heterostructure including VO_2 has been observed previously by our group⁶³.

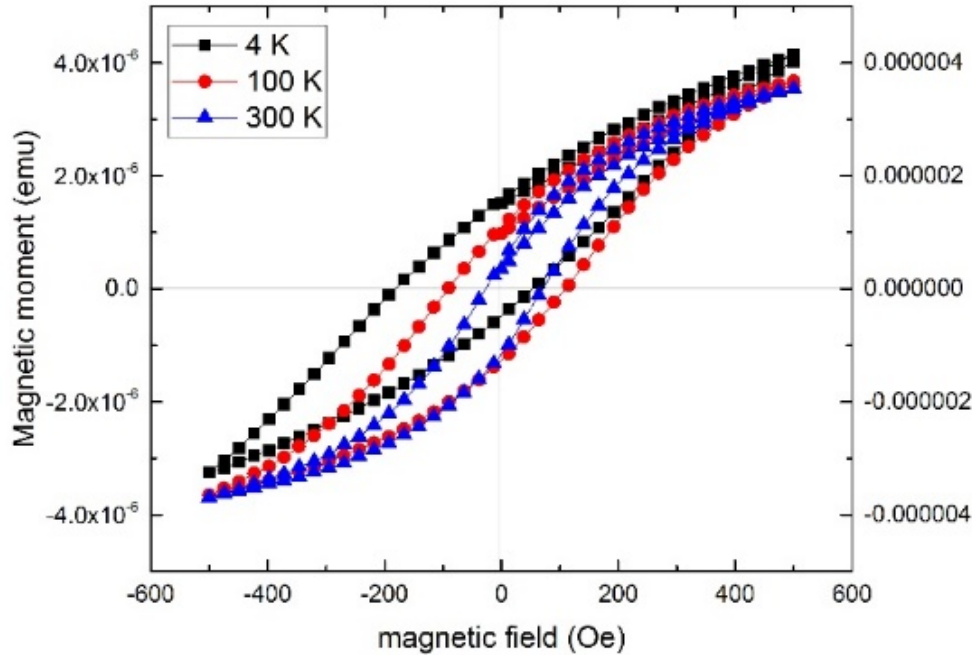


Figure 4.18. Magnetic field dependent magnetization of $\text{VO}_2(011)$ measurement at 4, 100, and 300 K with 200 Oe field cooling.

4.2.4. Conclusion

In this paper, we have successfully integrated VO_2 thin film on Si through a buffer layer of TiO_2/TiN . The TiN was grown cube-on-cube on Si, and TiO_2 was oxidized epitaxially with [110] out-of-plane orientation. VO_2 was then deposited on TiO_2 with an out-of-plane direction parallel to [011]. The in-plane relationship established to be $\text{VO}_2(110)/\text{VO}_2(010) \parallel \text{TiO}_2(011) \parallel \text{TiN}(112) \parallel \text{Si}(112)$ based on transmission Kikuchi Diffraction. Metal to semiconductor transition was defined to be 350 K with 8 K hysteresis, according to resistance versus temperature hysteresis loop. We have observed the ferromagnetic behavior in

VO₂ samples and argued that it is due to the formation of oxygen vacancies or V³⁺ defects with unpaired electrons. Therefore, the formation of oxygen vacancies or non-stoichiometric oxidation state of vanadium in VO₂ is envisaged to be responsible for the observed room-temperature ferromagnetic characteristics.

REFERENCES

1. Esaka, F. *et al.* Comparison of surface oxidation of titanium nitride and chromium nitride films studied by x-ray absorption and photoelectron spectroscopy. *J. Vac. Sci. Technol. A Vacuum, Surfaces, Film.* **15**, 2521–2528 (1997).
2. Diebold, U. The surface science of titanium dioxide. *Surf. Sci. Rep.* **48**, 53–229 (2003).
3. Bayati, M. R., Joshi, S., Molaei, R., Narayan, R. J. & Narayan, J. Ultrafast switching in wetting properties of TiO₂/YSZ/Si (001) epitaxial heterostructures induced by laser irradiation. *J. Appl. Phys.* **113**, 63706 (2013).
4. Bayati, M. R., Molaei, R., Budai, J. D., Narayan, R. J. & Narayan, J. Role of substrate crystallographic characteristics on structure and properties of rutile TiO₂ epilayers. *J. Appl. Phys.* **114**, 44314 (2013).
5. Bayati, M. R., Joshi, S., Narayan, R. J. & Narayan, J. Low-temperature processing and control of structure and properties of TiO₂/c-sapphire epitaxial heterostructures. *J. Mater. Res.* **28**, 1669–1679 (2013).
6. Torres, J., Perry, C. C., Bransfield, S. J. & Fairbrother, D. H. Low-temperature oxidation of nitrated iron surfaces. *J. Phys. Chem. B* **107**, 5558–5567 (2003).
7. Colombo, L. & Seidel, T. PERSPECTIVES-High-k gate deposition: ALD or CVD? Solid State Technology asked executives to comment on the advantages and disadvantages of ALD vs. CVD techniques for gate dielectrics. *Solid State Technol.* **47**, 112 (2004).
8. Bayati, M. R.. Structure and Properties of VO₂ and Titanium Dioxide Based Epitaxial Heterostructures Integrated with Silicon and Sapphire Substrates. North Carolina State University (2013).

9. Choi, G.-J. *et al.* Atomic layer deposition of TiO₂ films on Ru buffered TiN electrode for capacitor applications. *J. Electrochem. Soc.* **156**, G77 (2009).
10. Choi, Y., Yamamoto, S., Abe, H. & Itoh, H. Effects of annealing and quenching treatments on reconstruction of rutile thin films on sapphire substrates. *Surf. Sci.* **499**, 203–209 (2002).
11. Lin, P.-I. *et al.* Characteristics of YBa₂Cu₃O₇ thin films deposited on substrates buffered by various TiO₂ layers. *Jpn. J. Appl. Phys.* **40**, L377 (2001).
12. Liu, X., Liu, Z. G., Yin, J. & Liu, J. M. Microstructure and electrical properties of ferroelectric Pb (Zr_{0.53}Ti_{0.47})O₃ films on Si with TiO₂ buffer layers. *J. Phys. Condens. Matter* **12**, 9189 (2000).
13. Kim, K.-B. *et al.* Coplanar ferroelectric phase shifter on silicon substrate with TiO₂ buffer layer. *2005 European Microwave Conference*, **1**, 1-4. (IEEE, 2005).
14. Nguyen, H. H., Prellier, W., Sakai, J. & Ruyter, A. Substrate effects on the room-temperature ferromagnetism in Co-doped TiO₂ thin films grown by pulsed laser deposition. *J. Appl. Phys.* **95**, 7378–7380 (2004).
15. Cho, M. H. & Lee, G. H. Growth of high quality rutile TiO₂ thin film using ZnO buffer layer on Si (100) substrate. *Thin Solid Films* **516**, 5877–5880 (2008).
16. Bayati, M. R., Gupta, P., Molaei, R., Narayan, R. J. & Narayan, J. Phase tuning, thin film epitaxy, interfacial modeling, and properties of YSZ-buffered TiO₂ on Si (001) substrate. *Cryst. Growth Des.* **12**, 4535–4544 (2012).
17. Bayati, M. R. *et al.* Thin-Film Epitaxy and Enhancement of Photocatalytic Activity of Anatase/Zirconia Heterostructures by Nanosecond Excimer Laser Treatment. *J. Phys. Chem. C* **117**, 7138–7147 (2013).

18. Chen, H.-Y. & Lu, F.-H. Oxidation behavior of titanium nitride films. *J. Vac. Sci. Technol. A* **23**, 1006–1009 (2005).
19. Desmaison, J., Lefort, P. & Billy, M. Oxidation mechanism of titanium nitride in oxygen. *Oxid. Met.* **13**, 505–517 (1979).
20. Groenland, A. W. *et al.* Thermal and plasma-enhanced oxidation of ALD TiN. (2008).
21. Saha, N. C. & Tompkins, H. G. Titanium nitride oxidation chemistry: an x-ray photoelectron spectroscopy study. *J. Appl. Phys.* **72**, 3072–3079 (1992).
22. Tompkins, H. G. Oxidation of titanium nitride in room air and in dry O₂. *J. Appl. Phys.* **70**, 3876–3880 (1991).
23. Yin, Y., Hang, L., Zhang, S. & Bui, X. L. Thermal oxidation properties of titanium nitride and titanium–aluminum nitride materials—A perspective for high temperature air-stable solar selective absorber applications. *Thin Solid Films* **515**, 2829–2832 (2007).
24. Yoshiya, M., Tanaka, I., Kaneko, K. & Adachi, H. First principles calculation of chemical shifts in ELNES/NEXAFS of titanium oxides. *J. Phys. Condens. Matter* **11**, 3217 (1999).
25. Zimmermann, J., Finnis, M. W. & Ciacchi, L. C. Vacancy segregation in the initial oxidation stages of the TiN (100) surface. *J. Chem. Phys.* **130**, 134714 (2009).
26. Ciacchi, L. C. Modelling the onset of oxide formation on metal surfaces from first principles. *Int. J. Mater. Res.* **98**, 708–716 (2007).
27. Chowdhury, R., Vispute, R. D., Jagannadham, K. & Narayan, J. Characteristics of titanium nitride films grown by pulsed laser deposition. *J. Mater. Res.* **11**, 1458–1469 (1996).
28. Narayan, J. & Larson, B. C. Domain epitaxy: A unified paradigm for thin film growth. *J. Appl. Phys.* **93**, 278–285 (2003).

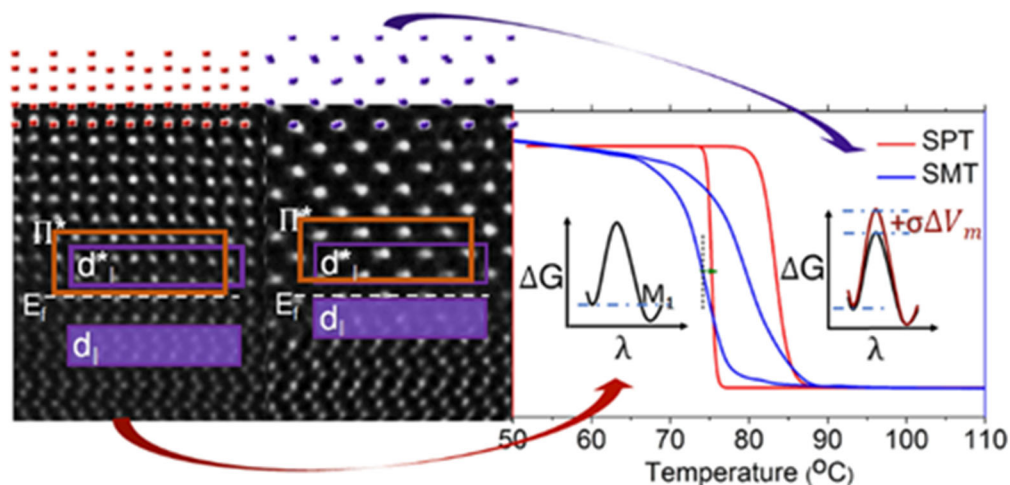
29. Mashimo, T., Nagayama, K. & Sawaoka, A. Anisotropic elastic limits and phase transitions of rutile phase TiO₂ under shock compression. *J. Appl. Phys.* **54**, 5043–5048 (1983).
30. Iuga, M., Steinle-Neumann, G. & Meinhardt, J. Ab-initio simulation of elastic constants for some ceramic materials. *Eur. Phys. J. B-Condensed Matter Complex Syst.* **58**, 127–133 (2007).
31. Riedel, R. & Chen, I.-W. *Ceramics Science and Technology, Materials and Properties.* **2**, (John Wiley & Sons, 2011).
32. Ichimura, M. & Narayan, J. Role of surface step on misfit dislocation nucleation and critical thickness in semiconductor heterostructures. *Mater. Sci. Eng. B* **31**, 299–303 (1995).
33. Narayan, J. Recent progress in thin film epitaxy across the misfit scale (2011 Acta Gold Medal Paper). *Acta Mater.* **61**, 2703–2724 (2013).
34. Kumar, R. T. R. *et al.* Pulsed laser deposited vanadium oxide thin films for uncooled infrared detectors. *Sensors Actuators A Phys.* **107**, 62–67 (2003).
35. Rao, K. V. K., Naidu, S. V. N. & Iyengar, L. Thermal expansion of rutile and anatase. *J. Am. Ceram. Soc.* **53**, 124–126 (1970).
36. Gogotsi, Y. G., Porz, F. & Yaroshenko, V. P. Mechanical properties and oxidation behavior of Al₂O₃–AlN–TiN composites. *J. Am. Ceram. Soc.* **75**, 2251–2259 (1992).
37. Deschaux-Beaume, F., Cutard, T., Fréty, N. & Levillant, C. Oxidation of a Silicon Nitride-Titanium Nitride Composite: Microstructural Investigations and Phenomenological Modeling. *J. Am. Ceram. Soc.* **85**, 1860–1866 (2002).
38. Howe, J. M. Interfaces in materials : atomic structure, thermodynamics and kinetics of solid-vapor, solid-liquid and solid-solid interfaces. (John Wiley & Sons, 1997).
39. Wang, Y. *et al.* Geometric structure of rutile titanium dioxide (111) surfaces. *Phys. Rev. B* **90**, 45304 (2014).

40. Moatti, A. Javadpour, J., Anbia, M., Badiei, A. The correlation between aging time and pore characteristics in the synthesis of mesoporous Al₂O₃. *Ceram. Int.* **40** (7), 10231-10236 (2014).
41. Hones, P., Zakri, C., Schmid, P. E., Lévy, F. & Shojaei, O. R. Oxidation resistance of protective coatings studied by spectroscopic ellipsometry. *Appl. Phys. Lett.* **76**, 3194–3196 (2000).
42. Stoyanov, E., Langenhorst, F. & Steinle-Neumann, G. The effect of valence state and site geometry on Ti L_{3,2} and OK electron energy-loss spectra of Ti_xO_y phases. *Am. Mineral.* **92**, 577–586 (2007).
43. Leapman, R. D., Grunes, L. A. & Fejes, P. L. Study of the L₂₃ edges in the 3d transition metals and their oxides by electron-energy-loss spectroscopy with comparisons to theory. *Phys. Rev. B* **26**, 614 (1982).
44. Dionne, G. F. Magnetoelastic effects of iron-group ions in exchange fields. *J. Appl. Phys.* **91**, 7367–7369 (2002).
45. Park, C.-Y., Yoon, S.-G., Jo, Y.-H. & Shin, S.-C. Room-temperature ferromagnetism observed in Mo-doped indium oxide films. (2009).
46. Wu, C. N. *et al.* Room temperature ferromagnetic behavior in cluster free, Co doped Y₂O₃ dilute magnetic oxide films. *Appl. Phys. Lett.* **101**, 162403 (2012).
47. Zhao, Y. L. *et al.* Reversible ferromagnetism in rutile TiO₂ single crystals induced by nickel impurities. *Appl. Phys. Lett.* **101**, 142105 (2012).
48. Mal, S., Nori, S., Narayan, J. & Prater, J. T. Defect-mediated ferromagnetism and controlled switching characteristics in ZnO. *J. Mater. Res.* **26**, 1298–1308 (2011).
49. Yang, T.-H., Nori, S., Mal, S. & Narayan, J. Control of room-temperature defect-mediated ferromagnetism in VO₂ films. *Acta Mater.* **59**, 6362–6368 (2011).

50. Ramanathan, S. Thin film metal-oxides. *Harvard Univ. Springer New York Dordr. Heidelb. London* (2010).
51. Narayan, J. & Bhosle, V. M. Phase transition and critical issues in structure-property correlations of vanadium oxide. *J. Appl. Phys.* **100**, 103524 (2006).
52. Morin, F. J. Oxides which show a metal-to-insulator transition at the Neel temperature. *Phys. Rev. Lett.* **3**, 34 (1959).
53. Becker, M. F. *et al.* Femtosecond switching of the solid state phase transition in the smart-system material VO₂. in *1994 North American Conference on Smart Structures and Materials* 400–408 (International Society for Optics and Photonics, 1994).
54. Soltani, M., Chaker, M., Haddad, E., Kruzelecky, R. & Margot, J. Micro-optical switch device based on semiconductor-to-metallic phase transition characteristics of W-doped VO₂ smart coatings. *J. Vac. Sci. Technol. A* **25**, 971–975 (2007).
55. Soltani, M., Chaker, M., Haddad, E. & Kruzelesky, R. V. Thermochromic vanadium dioxide smart coatings grown on Kapton substrates by reactive pulsed laser deposition. *J. Vac. Sci. Technol. Int. J. Devoted to Vacuum, Surfaces, Film.* **24**, (2006).
56. Manning, T. D. *et al.* Intelligent window coatings: atmospheric pressure chemical vapour deposition of vanadium oxides. *J. Mater. Chem.* **12**, 2936–2939 (2002).
57. Chen, C., Yi, X., Zhao, X. & Xiong, B. Characterizations of VO₂-based uncooled microbolometer linear array. *Sensors Actuators A Phys.* **90**, 212–214 (2001).
58. Reintsema, C. D., Grossman, E. N. & Koch, J. A. Improved VO₂ microbolometers for infrared imaging: operation on the semiconducting-metallic phase transition with negative electrothermal feedback. in *AeroSense'99* 190–200 (International Society for Optics and Photonics, 1999).

59. Chivian, J. S., Scott, M. W., Case, W. E. & Krasutsky, N. J. An improved scan laser with a VO₂ programmable mirror. *Quantum Electron. IEEE J.* **21**, 383–390 (1985).
60. Ko, C. & Ramanathan, S. Stability of electrical switching properties in vanadium dioxide thin films under multiple thermal cycles across the phase transition boundary. *J. Appl. Phys.* **104**, 6105 (2008).
61. Moatti, A., Bayati, R. & Narayan, J. Epitaxial growth of rutile TiO₂ thin films by oxidation of TiN/Si{100} heterostructure. *Acta Mater.* **103**, (2016).
62. Moatti, A., Bayati, R., Singamaneni, S. & Narayan, J. Epitaxial integration of TiO₂ with Si (100) through a novel approach of oxidation of TiN/Si (100) epitaxial heterostructure. *MRS Adv.* **1**, 2629–2634 (2016).
63. Molaei, R., Bayati, M. R., Alipour, H. M., Nori, S. & Narayan, J. Enhanced photocatalytic efficiency in zirconia buffered n-NiO/p-NiO single crystalline heterostructures by nanosecond laser treatment. *J. Appl. Phys.* **113**, 233708 (2013).

CHAPTER 5



5. Strain engineering-Effect of strain on thermodynamics and Kinetics of structural transitions in VO₂ thin films (*ACS applied materials & interfaces*, 9 (28) (2017) 24298-24307)

Abstract

Unstrained and defect-free VO₂ single crystals undergo structural (from high temperature tetragonal to low-temperature monoclinic phase) and electronic phase transitions simultaneously. In thin films, however, in the presence of unrelaxed strains and defects, structural (Peierls) and electronic (Mott) transitions are affected differently and are separated. In this paper, we have studied the temperature-dependence of structural and electrical transitions in epitaxially grown vanadium dioxide films on (0001) sapphire substrates. These results are discussed using a combined kinetics and thermodynamics approach, where the velocity of phase transformation is controlled largely by kinetics, and the formation of intermediate phases is governed by thermodynamic considerations. We have grown (020) VO₂ on (0001) sapphire with two (001) and (100) in-plane orientations rotated by 122°. The (100) oriented crystallites are fully relaxed by the paradigm of domain matching epitaxy, whereas (001) crystallites are not relaxed and exhibit the

formation of a few atomic layers of thin interfacial V_2O_3 . We have studied the structural (Peierls) transition by temperature-dependent in situ X-Ray diffraction measurements, and electronic (Mott) transition by electrical resistance measurements. A delay of 3°C is found between the onset of structural (76°C) and electrical (73°C) transitions in the heating cycle. This temporal lag in the transition is attributed to the residual strain existing in the VO_2 crystallites. With this study, we suggest that the control of structural and electrical transitions is possible by varying the transition activation barrier for atomic jumps through strain engineering.

5.1. Introduction

The VO_2 (in the form of freestanding bulk single crystals) can exhibit an extremely sharp and ultrafast (subpicosecond regime) first-order phase transformation from monoclinic, $P2_1/c$ (low-temperature, semiconductor phase, M_1 phase) to tetragonal or rutile, $P4_2/mnm$ (high-temperature, metallic phase) structure at 68°C in the absence of any internal and external stresses. This semiconductor to metal transition (SMT) in single crystals normally is associated with 4-5 orders of magnitude change in resistivity and infrared transmission¹. A remarkable feature of this transition is the separation of the V-V pairs. Along the c-axis of the tetragonal phase the V-V separation is 0.287 nm, whereas, for the monoclinic phase, the separation along the a-axis is 0.312 nm and 0.265 nm, where $a_{\text{mono}}=2c_{\text{tet}}$. These changes in V-V separation lead to a doubling of the unit cell. In other words, this transformation occurs through a single atomic jump of vanadium atoms along a_{mono} or c_{tet} . Thus, any external or internal strains along this axis can affect greatly the SMT. This needs to be studied and controlled for reliable device applications. In strain-free crystals, this transition from a high-temperature rutile (R) phase ($a=b=0.455\text{nm}$ and $c=0.285\text{nm}$) transforms directly to a low-temperature monoclinic M_1 phase ($a=0.575\text{nm}$; $b=0.453\text{nm}$; $c=0.538\text{nm}$, $\beta=122.6^\circ$). However, in the presence of internal and external stress centers, the

formation of a transient monoclinic phase M_2 ($a = 0.906\text{nm}$, $b = 0.580\text{nm}$, $c = 0.425\text{nm}$, $\beta = 91.8^\circ$) which is an intermediate of M_1 and R phases, often broadens the apparent phase transition. The formation of the M_2 phase in thin film heterostructures is caused by internal stresses and constraints imposed by the substrates, which can be influenced by the epitaxial growth orientation and relaxation of stresses and strains². The M_2 phase has been shown to be insulating^{3,4}. A monoclinic correlated metal phase (MCM) has been also reported to form ahead of the structural transition when heating in the presence of strains⁵⁻⁸. Formation of the monoclinic metallic phase results in an increased conductivity due to the introduction of charge carriers into the VO_2 system⁷. However, there is no comprehensive explanation for the formation of these monoclinic phases in the presence of strains. The reports of this monoclinic phase challenge the original theory of Zylbersztein and Mott⁹ and suggest that this transition is not a simple Mott-Hubbard transition originating from just electron-electron interactions. Subsequent reports differ as to whether the SMT is Mott, Peierls or a mixture of both transitions.

Using scanning near field infrared microscopy to study $\text{VO}_2/\text{r-sapphire}$ heterostructures, for example, one report shows that the SMT initiates by forming nano-scale metallic puddles that appear at the onset of the transition¹⁰. Another report claims that Raman spectra show the onset of the SMT without the structural phase transition (SPT) when the hole concentration is greater than about 0.018%⁵. Also, the presence of the MCM phase and delay of the SPT in electron diffraction patterns of polycrystalline VO_2 films deposited on amorphous silicon nitride substrate is reported¹¹. Another study shows that the metallic conductivity of $\text{VO}_2/\text{m-sapphire}$ films sets in below the SPT temperature using the current-voltage curve and diffraction measurements¹². Decoupling of the structural and electrical transitions by inducing charge through the metal contacts into VO_2 is also suggested¹³. In the tungsten (VI)-doped vanadium dioxide, it has been

reported that the distortion in the structure breaks the bonds between Peierls-paired vanadium ions, which increases the bandgap¹⁴. Finally, a report shows that the SPT can be prevented from happening in conjunction with the SMT, by maintaining the epitaxial strain within the tetragonal phase of VO₂¹⁵.

However, there are other reports claiming that the Peierls transition is responsible for the VO₂ transition. A computational study by density functional theory (DFT) and the DFT+U (U: Coulomb correlation) band calculations show that the Coulomb correlation effect plays an essential role of driving the Peierls transition and introducing the spin-Peierls ground state into the monoclinic phase¹⁶. Using temperature-dependent x-ray absorption measurement and density-functional theory calculations, one group claims that the structural rearrangement is a key factor in narrowing the insulating bandgap¹⁷.

All of these studies have tried to explain the controlling mechanism during the transition in VO₂, however, they have not taken into account the effect of extrinsic and intrinsic factors on the Mott and Peierls transitions and explain how each of these factors plays an important role in defining the thermodynamics and kinetics of the phase transformation. In other words, the SMT and SPT are affected differently by the presence of dopants, external charges, strains, and stresses. The role of thermal strain has been studied in VO₂/sapphire heterostructure at different thicknesses¹⁸. This study explains how thermal strain causes a shift in both SMT and SPT, however, it does not discuss the critical thickness above which dislocations form and relax the film¹⁸. Yang et al.¹⁵ explained how the epitaxial strains below the critical thickness can prevent the structural transition, and shift the onset temperature of the electrical transition. There are some papers on the effect of strains on the transition temperature, from a thermodynamics point of view^{19–23}. There, the Clapeyron equation has been used to predict the transition temperatures in the presence of

strains. The role of kinetics, however, has not been considered. In this paper, we present a model where the velocity of the phase transformation is largely controlled by the kinetics, and the formation of intermediate phases is governed by the thermodynamics. Our work clearly shows that the SMT is a Mott transition and the SPT is a separate Peierls transition. Any external or internal changes like strains, defects, and dopants affect these mechanisms and their transition temperatures differently. We use a combined kinetics and thermodynamics approach to explain the role of strains on the SPT. In addition, we discuss how strains can shift the SMT by changing the bandgap structure. We grow epitaxial VO₂ on c-sapphire substrate and model the interfaces by the paradigm of domain matching epitaxy (DME) where integral multiples of planes match across the interface. The atomic resolution images, EELS spectroscopy, and temperature dependent XRD have been employed to establish a correlation between the SPT temperature and the microstructure.

5.2. Experimental details

Epitaxial VO₂/c-sapphire heterostructures were grown by pulsed laser deposition (PLD) technique. A Lambda Physik KrF excimer laser was used to ablate the VO₂ target. The depositions were done under 0.125 mTorr oxygen pressure and 550°C. The energy density and frequency were set at 3 Jcm⁻² and 5 Hz, respectively. The XRD θ -2 θ scan and ϕ -scan studies were used to characterize the crystal structure and the epitaxial relationships using a Rigaku SmartLab X-ray diffractometer. The FEI Titan 80-300 probe aberration-corrected scanning transmission electron microscopy (STEM) operated at 200 KV was employed to collect atomic resolution HAADF images with the resolution limit of 0.07 nm, and electron energy loss spectra (EELS) by the energy resolution of the electron source as high as 0.15 eV across interfaces. A JEOL 2010F transmission electron microscope (TEM) was used to collect selected area electron diffraction patterns (SAED) across interfaces to confirm in-plane orientations. Electrical resistance vs. temperature

measurements of VO₂ thin films grown on sapphire (0001) was collected using a physical property measurement system (PPMS) by Quantum Design. The temperature dependence of XRD data from VO₂ thin films grown on c-sapphire measured during the heating and cooling cycles were performed using a PANalytical Empyrean.

5.3. Results and discussion

5.3.1. Structural and microstructural analysis of VO₂ thin films and interfaces

Figure 5.1a shows θ - 2θ XRD patterns taken from VO₂/c-Sapphire heterostructures. The pattern reveals that the monoclinic VO₂ (020) is parallel to the c-axis of sapphire. Since monoclinic VO₂ (002) and (020) reflections overlap, the ϕ -scan XRD and TEM techniques have been employed to distinguish between these two reflections. The ϕ -scan XRD patterns are shown in Figure 5.1b. A threefold symmetry about the c-axis of c-sapphire can be seen in the sapphire (012) reflections ($2\theta=25.58$, $\psi=57.71$). The ϕ -scans for (011) and (012) planes of VO₂ ($2\theta=27.87$, $\psi=44.92$ and $2\theta=44.73$, $\psi=63.37$, respectively) result in six peaks confirming the epitaxial nature of VO₂ grown on c-sapphire substrates. The presence of six peaks in VO₂ ϕ -scan shows that the (011) and (012) oriented planes have twofold symmetry about the growth direction and there are three crystallographically equivalent domains of VO₂ rotated by 120°. Also, there is a splitting of 3° in the ϕ -scan peaks which is related to the angle between (011) and (0 $\bar{1}$ 1) of the tetragonal phase of 63.6°. As the tetragonal phase transforms to the monoclinic phase, the realignment of the lattice will change the angle between domains by 0.6°²⁴. Figure 1c depicts the in-plane rotations of the (010) oriented t-VO₂ unit cell on the c-sapphire basal plane with two possible in-plane orientations each having an azimuthal rotation of 30° with respect to the sapphire [2 $\bar{1}$ $\bar{1}$ 0] axis. For further confirmation of in-plane relationships, electron diffraction patterns (SAED) and STEM-Z images

were taken across the interface. Figure 5.2a represents the low magnification HAADF image taken by STEM, along $[10\bar{1}0]$ sapphire zone axis, showing the columnar growth of VO_2 thin films. The indexed electron diffraction pattern in Figure 2b illustrates two in-plane orientations of (001) and (100). Therefore, it can be concluded that the epitaxial growth of VO_2 (020) with the tetragonal structure at growth temperature occurs such that sapphire $(11\bar{2}0)\parallel\text{t-VO}_2(100)$ and sapphire $(10\bar{1}0)\parallel\text{t-VO}_2(001)$ contain tensile misfit strain of +3.36% and -3.37%, respectively. The 3.36% strain along t- VO_2 (100) at growth temperature leads to the matching of 29 VO_2 planes with 28 substrate planes alternating with the frequency factor of 0.73 at the VO_2 /Sapphire interface according to the domain matching epitaxy paradigm²⁵. The 3.37% strain along t- VO_2 (001) is relaxed through 29/28 planes alternating with the frequency factor of 0.87. Subsequently, when films cool down to room temperature, the tetragonal VO_2 structure transforms to the monoclinic phase, that means there is almost 30° rotation from 90° to 122.6° and $(10\bar{1}0)$ plane (instead of $(11\bar{2}0)$) of sapphire is matched with $\text{VO}_2(100)$ planes. Under this condition, the epitaxial relationships between VO_2 and sapphire are sapphire $(01\bar{1}0)\parallel\text{m-VO}_2(001)$ and sapphire $(01\bar{1}0)\parallel\text{m-VO}_2(100)$, respectively. The interplanar spacing misfit calculations suggest +2.27% and -4.42% misfit strains along (001) and (100) directions respectively. However, since dislocation mobility is low at these temperatures, misfit strain relaxation by dislocation nucleation and glide is very difficult.

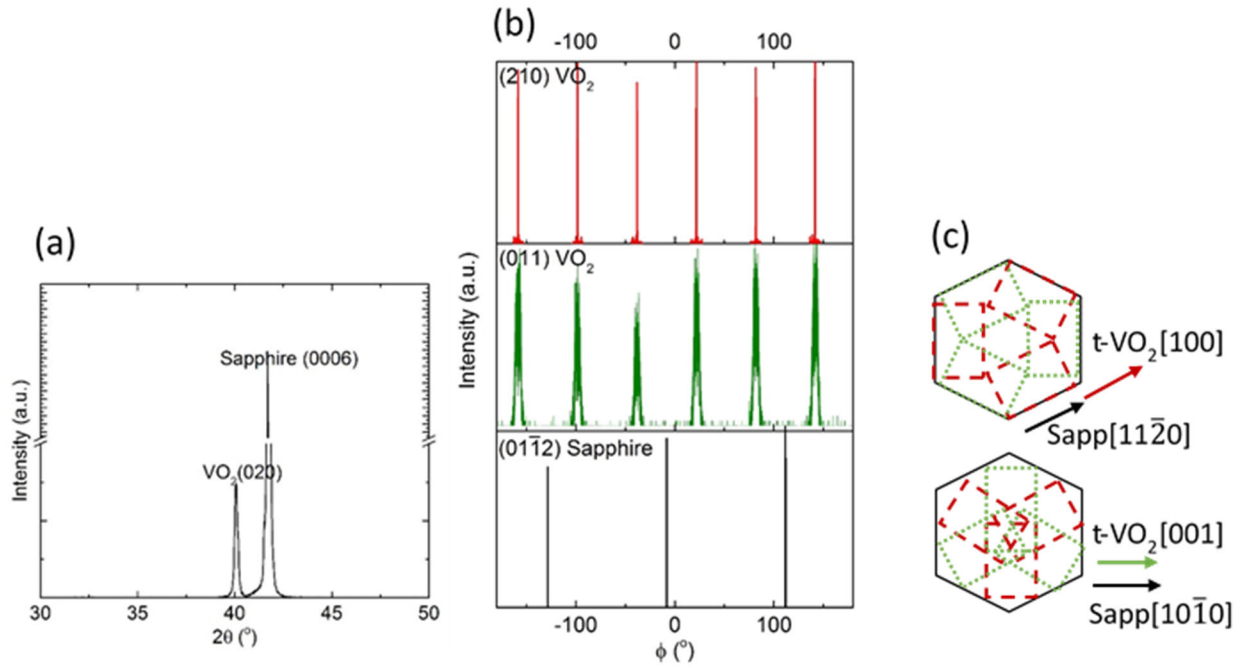


Figure 5.1. a) XRD θ - 2θ pattern acquired from a $\text{VO}_2(020)/\text{Sapphire}(0006)$ heterostructure, b) XRD ϕ -scan on the $\text{VO}_2(020)/\text{sapphire}(0006)$ heterostructure: $\text{Sapphire}(01\bar{1}2)$ reflection, and $\text{VO}_2(011)$ and $\text{VO}_2(210)$ reflections, c) in-plane rotations of the (010) oriented $t\text{-VO}_2$ unit cell on the c -sapphire basal plane with two possible in-plane orientations.

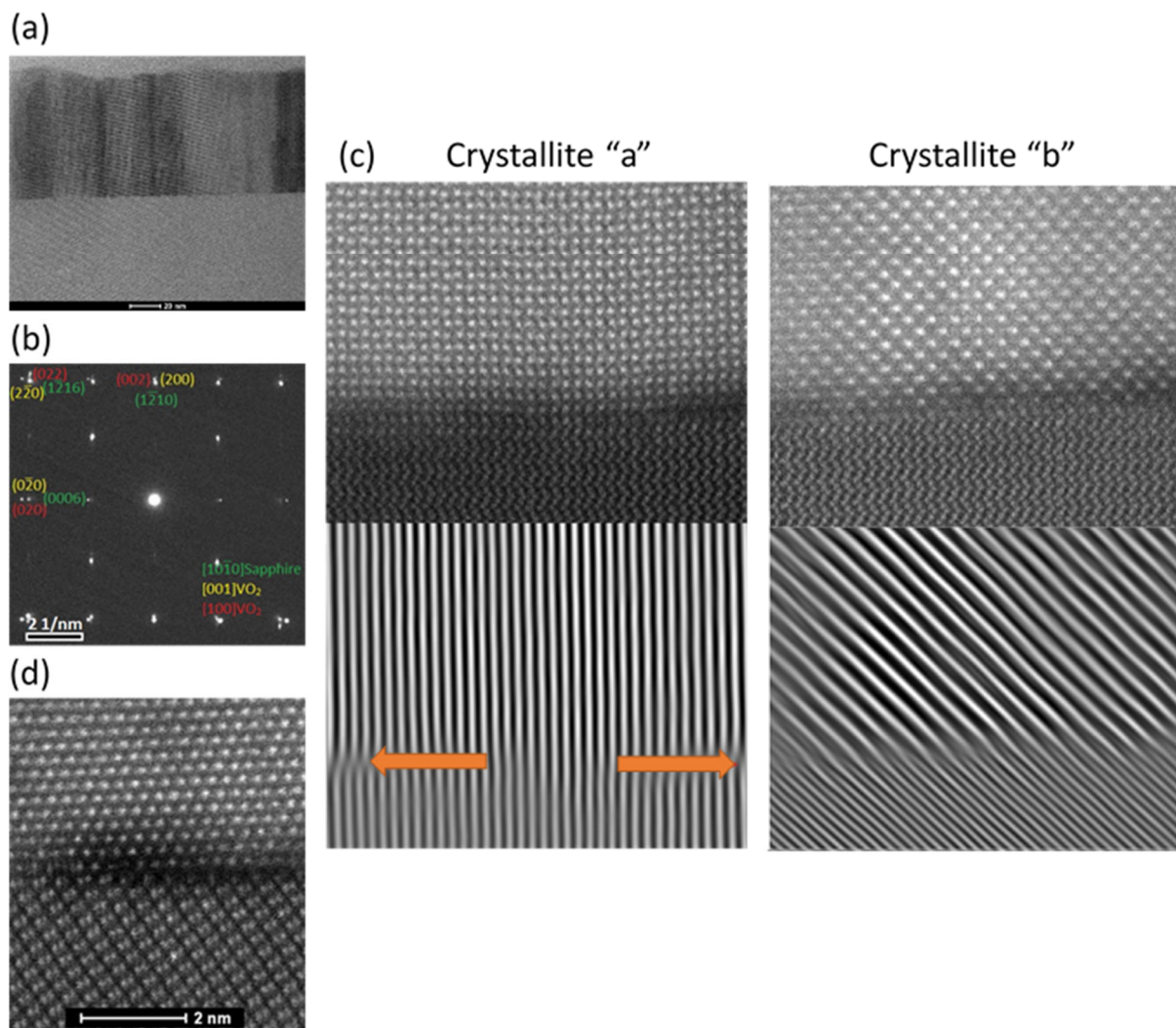


Figure 5.2. a) The low mag HAADF image taken by STEM showing both orientations growing columnar along $[10\bar{1}]_0$ sapphire zone axis, b) diffraction pattern belong to both crystallites of VO_2 along $[001]$ and $[100]$ and $[10\bar{1}]_0$ substrate, c) the associated inverse FFT images with respect to VO_2 (200), sapphire (1210) and VO_2 (022), sapphire (1216) are shown below HAADF images along $[001]$, crystallite “a”, and $[100]$, crystallite “b”, of VO_2 , respectively, d) HAADF image taken along the $[2\bar{1}\bar{1}]_0$ sapphire zone axis.

Figure 5.2c demonstrates the high-resolution HAADF images along sapphire $[01\bar{1}]_0$ and $[001]$ and $[100]$ of VO_2 . The associated inverse FFT images with respect to VO_2 (200), sapphire (1210) and VO_2 (022), sapphire (1216) are shown below HAADF images, respectively. For the sake of discussion, we designate sapphire $(01\bar{1})_0 \parallel \text{m-VO}_2(100)$ and $(01\bar{1})_0 \parallel \text{m-VO}_2(001)$, as “a” and “b” crystallites, respectively. Arrows in the inverse FFT image in Figure 5.2c, along the VO_2

[001] zone axis, point out to the dislocations at the interface. There are 29 planes between these two dislocations, which is consistent with the DME calculations. Along the VO₂ [100] zone axis, however, no dislocations are seen despite the DME prediction. Thus, we need to consider the possibility of dislocation nucleation and glide to the interface within active slip systems of VO₂ thin films. In fact, the dislocation can glide only if the critical resolved shear stress exceeds the yield stress of the material. The yield stress of VO₂ on sapphire has been determined to be 2 GPa²⁶. The critical resolved stress can be calculated to be $\tau_r = \sigma \cos\phi \cos\lambda$, in which ϕ is the angle between the normal of the slip plane and the stress direction, and λ is the angle between the slip direction and direction of the stress, σ . The value for $\sigma_{[100]}$ and $\sigma_{[001]}$ for two different crystallites are calculated to be 5.62 GPa and 5.77 GPa, respectively (assuming that the shear modulus and Poisson ratio of the tetragonal phase are 60 GPa and 0.3, respectively²⁷.) The major slip systems in t-VO₂ are $\{110\}\langle\bar{1}11\rangle$ and $\{211\}\langle\bar{1}11\rangle$. Considering $\{110\}\langle\bar{1}11\rangle$ slip system, the resolved shear stress is calculated to be zero along the [001] direction in crystallite “b” and 3.72 GPa along [100] direction in crystallite “a”. In fact, dislocations cannot glide in this slip system in crystallite “b”, since the critical resolved shear stress is zero. In crystallite “b”, however, the residual shear stress is not zero and equals 2.4 GPa in the $\{211\}\langle\bar{1}11\rangle$ slip system. The tensile strain is harder to relax due to the lack of surface steps and higher nucleation barrier²⁸. Since there is no glide barrier along [001] direction, the higher nucleation barrier may prevent dislocations formation in this orientation. In fact, compressive strains along m-VO₂(100) is relaxed by dislocation glide, while tensile strains remain unrelaxed along m-VO₂(001). In order to further study VO₂/sapphire heterostructure interfaces, a high-resolution EELS analysis is performed across the interface for both orientations of VO₂ as shown in Figure 5.3. A series of EELS spectra were collected across the interface along XX’ and YY’ lines, indicated in the HAADF image

shown in Figure 5.3a. Figure 5.3b and c show the representative EELS spectra from the c-Sapphire substrate, at the interface, and VO₂ thin film from crystallites “a” and “b”, respectively. For crystallite “a”, V-L and O-K edge look very similar to the representative spectra of VO₂ obtained away from the interface^{29,30}. This clearly shows the formation of VO₂ right from the interface. This result is quantitatively analyzed and confirmed in Figure 5.3d which shows the variation in energy positions and amplitude of Gaussian fits corresponding to V-L₃ and V-L₂ peaks, and the O-K pre-peak and the main peak along the XX’ and YY’ scan lines. This shows no change in the energy position of the O-K prepeak at 520 eV from the interface to the bulk in VO₂. The characteristics of O main-peak are found to be very different in c-Al₂O₃ having no O pre-peak as compared to VO₂. Interestingly, the O-K edge at the interface in crystallite “b” is observed to be very similar to the O-K edge in Al₂O₃ for 3-4 monolayers of epitaxial films. In addition, there is a slight asymmetry in the V-L peak which is also observed at the interface for this thickness as shown in Figure 5.3c and e. These results show the formation of V₂O₃ (~0.8 nm thick) layer at the interface in the crystallite “b”. A peak fitting analysis is shown in Figure 5.3e, which shows the existence of intense O pre-peak at the interface towards the grown VO₂ film for a significant thickness. These results are consistent with the HAADF imaging results in Figure 5.2 which shows that epitaxial VO₂ in crystallite “a” follows the DME paradigm for strain relaxation and forms dislocations at every ~29 planes. In crystallite “b”, however, the strain is partially relaxed by the formation of pseudomorphic V₂O₃ layer at the interface but still contains significant residual strain.

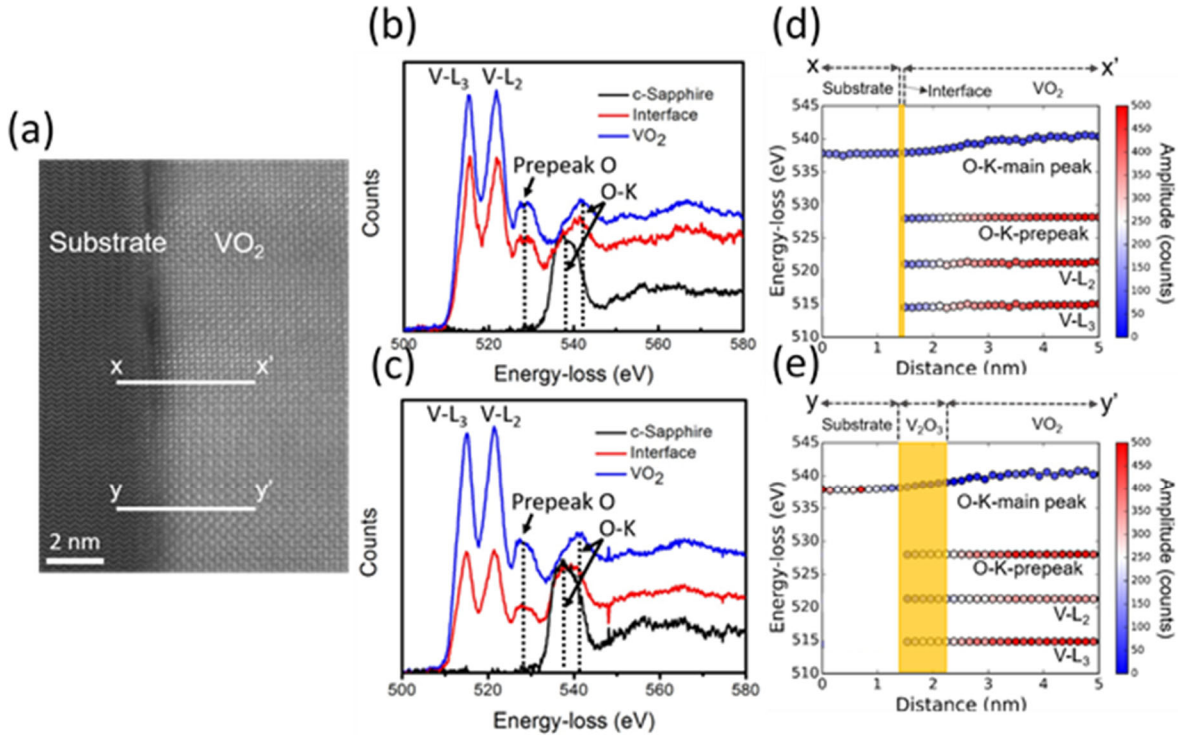


Figure 5.3. a) HAADF image showing two different orientations of VO₂ on sapphire along $[11\bar{2}0]$ substrate, b, and c) selected spectrum collected across the interface in two different orientations as indicated by lines in Figure a, d and e) Peak fit amplitudes for V-L₂, V-L₃, O-K EELS edges along the XX' and YY' lines, respectively.

5.3.2. Electrical analysis and SMT characteristics

Figure 5.4a presents the variation of electrical resistance as a function of temperature for one thermal cycle (heating and cooling). The transition characteristic for VO₂ is clearly seen to proceed from a high-temperature metallic phase to a room temperature semiconductor phase. The transition was characterized by analyzing the derivative of the resistance in terms of temperature ($d[\log(\text{resistance})]/dT$). The results were fitted to a Gaussian profile for both heating and cooling cycles (Figure 5.4b). The SMT was characterized by the following parameters:

- The “transition temperature” (T_{smt}) is defined to be the center of the Gaussian profile;
- The “ ΔH ” is defined as the difference between temperatures at the peak position of heating and cooling cycles;

- The “sharpness” of the SMT which is characterized by the full width at half maximum of the Gaussian profile;
- The “amplitude” (ΔA) of the SMT corresponding to the \log_{10} of the ratio of the resistance in metallic and insulating stages in decades.

Defining the $\Delta G_\alpha = \Delta T \Delta S$ as changes in Gibbs free energy associated with the phase transition, the critical size for the stable nuclei would be $r_c = 2\gamma/\Delta G$; where γ is the interfacial energy, ΔT is the deviation from the equilibrium transition temperature, and ΔS is the discontinuous change in entropy between the two phases. The ΔH is directly related to $\Delta T = 2\gamma/r_c \Delta S$. Thus, ΔH will increase with decreasing r_c . The structural nature of the deposited film is bi-epitaxial. Thus, it is expected ΔH to be larger than the range of 2-6 K observed for single crystalline thin films. The values for SMT characteristics are reported in Table 1. The sharpness is directly related to the overall content of defects per unit volume including point defects, line defects and volume defects. The transition width (1/sharpness) of the transformation decreases as the grain size increases since the number of defective sites per unit volume associated with grain boundaries decreases. For single crystalline films, sharpness is reported to be in the range of 5-10 K. The high value reported for sharpness here, confirms the low density of defects and high quality of the thin film. The amplitude of the transition (ΔA) also depends upon the defect content including grain boundary area and crystalline nature of the films. The presence of defects leads to mid-gap states in the band-gap that lower the resistivity of the semiconductor phase. The large value reported for ΔA , again confirms the high quality of the film. The transition temperature is affected by stresses and strains in thin films, particularly epitaxial strains. The influence of the film thickness on the SMT has been reported before for the same heterostructure and our experimental

results for 85 nm VO₂ films are consistent with their values reported for almost the same thickness

18

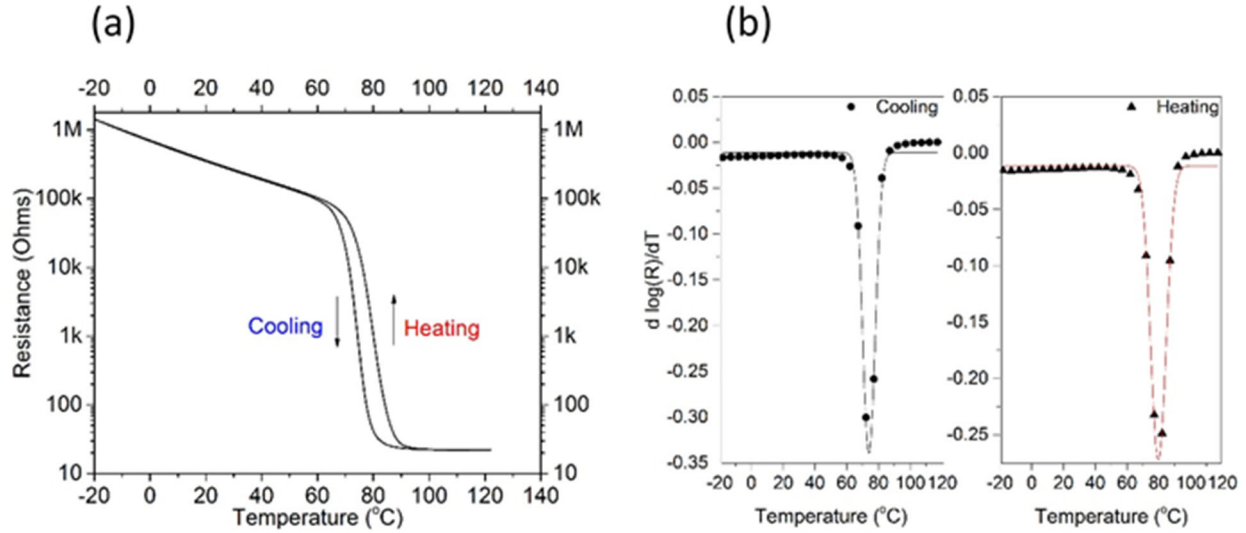


Figure 5.4. a) Electrical resistance vs. temperature of VO₂ thin films grown on sapphire (0001) substrates, b) derivatives of $\log_{10}R(T)$ for the cooling (black, circle) and heating (red, triangle) curves are shown. Symbols represent data points and the lines represent Gaussian fitting.

Table 5.1. Characteristics of the SMT (semiconductor to metal transition) of VO₂ thin films grown on c-sapphire: the transition temperature (T_{smt}), the hysteresis (ΔH), the amplitude (ΔA), and the sharpness of the SMT.

Transition Temperature (°C)	ΔH Hysteresis (°C)	ΔA Transition Amplitude (decades)	Sharpness (K)
77	5.7	4.9	9

5.3.3. Temperature-dependent XRD measurements and SPT characteristics

In order to have a better understanding of the role of strains and stresses, defects, and interfaces on the VO₂ thin films during the transition, the in-situ XRD has been done in a cycle of cooling and heating, illustrated in Figure 5.5. The results show that the (020) planes of monoclinic phase of VO₂ change to (020) planes of tetragonal as the SPT occurs. Figure 5a depicts the XRD

plots for selected temperatures below, during, and above the transition in the heating cycle. As shown in Figure 5.6, the SMT starts well before the SPT (based on electrical measurements); there is a slight shift towards lower 2-theta values without significant changes in the peak height. This peak splitting is associated with the metallic monoclinic (MCM) phase which has been reported by others^{11,12}. The MCM phase differs from the M₂ phase, the transitional phase that occurs in the presence of stress and dopants. The M₂ peak position is located in 2θ positions, smaller 2θ values, before the tetragonal peak position. The slight shift toward higher 2-theta values after the transition, during heating confirms the presence of M₂ phase.

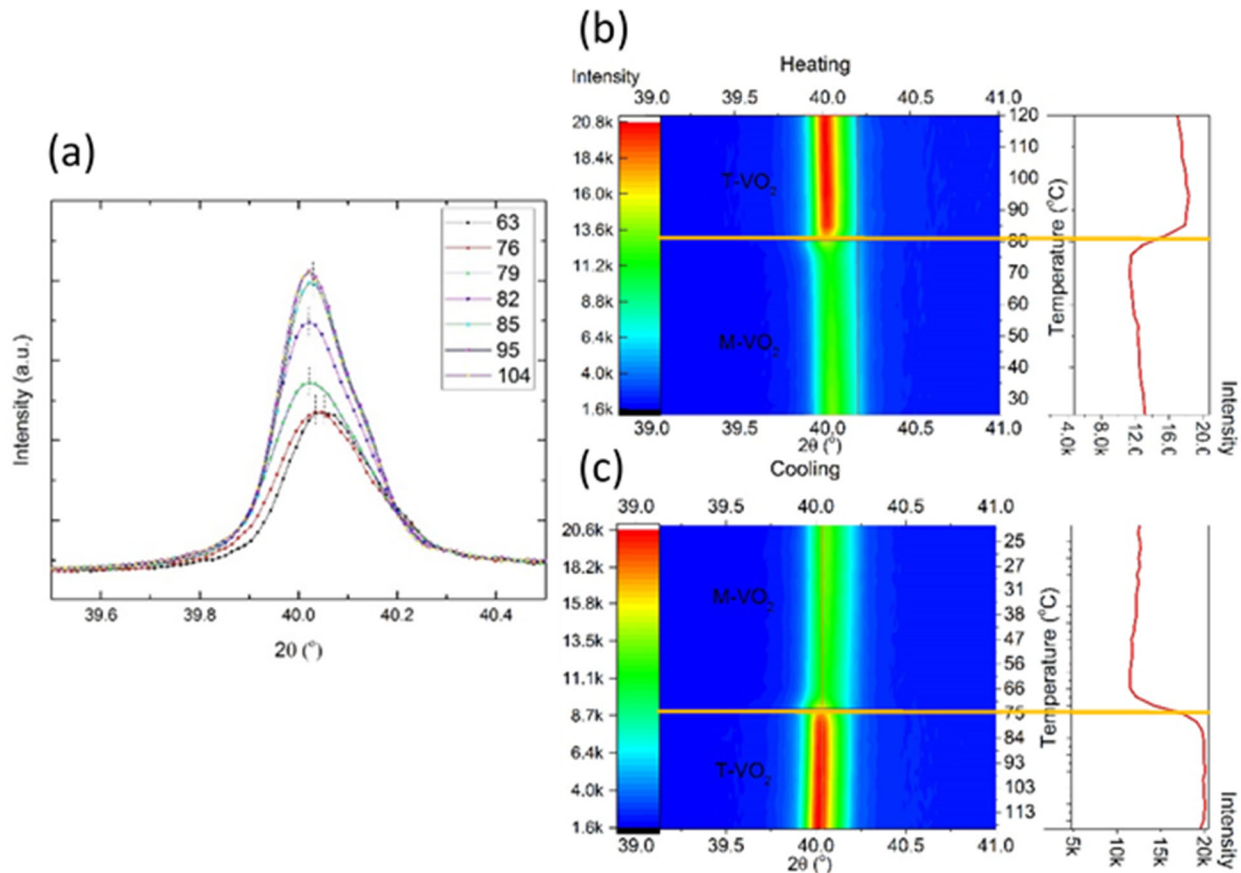


Figure 5.5. a) Selected XRD θ -2 θ patterns before, during, and after transition during heating for VO₂ (020)/ Sapphire (0006) heterostructures, b) temperature dependence of XRD data from VO₂ thin films grown on c-sapphire measured during the heating and, c) cooling. The colors of contour plots represent the peak intensity. Evolution of (020) peaks belong to monoclinic and tetragonal phases has shown different intensity and slight changes in 2 theta position.

The SPT transition temperatures for cooling and heating cycles (Figure 5.5b and c) are 76 and 83°C, respectively, leading to 7°C hysteresis. The SPT is preceding the SMT by almost 3°C as depicted in Figure 5.6. The reason behind this difference will be discussed later. The original position for (020) peaks for monoclinic and tetragonal phases is supposed to be at $2\theta=39.88$ and $2\theta=39.14$, respectively. The experimental values for these peaks are slightly higher than the standard values. This indicates that there is a compressive strain along the out-of-plane direction indicative of the in-plane tension. At the transition temperature, there is a major shift as shown in the strained plot in Figure 5.7a, as the d-spacing changes through SPT. The in-plane tensile strains are also plotted where the Poisson ratio of 0.3 is assumed for the VO₂. The same trend has been shown for the stress values in Figure 5.7b, for increasing temperature. The amount of in-plane strain at room temperature is calculated to be about 0.3%.

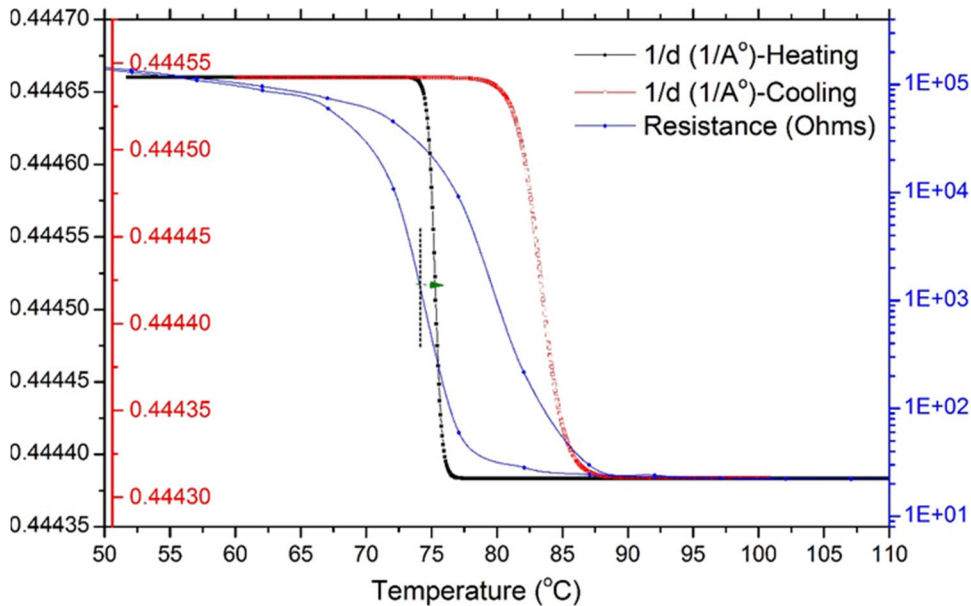


Figure 5.6. Comparison of SMT (semiconductor to metal transition), through resistance measurement, and SPT (structural phase transition), through d-spacing measurement (using Boltzmann fitting), temperatures in a full heating-cooling cycle.

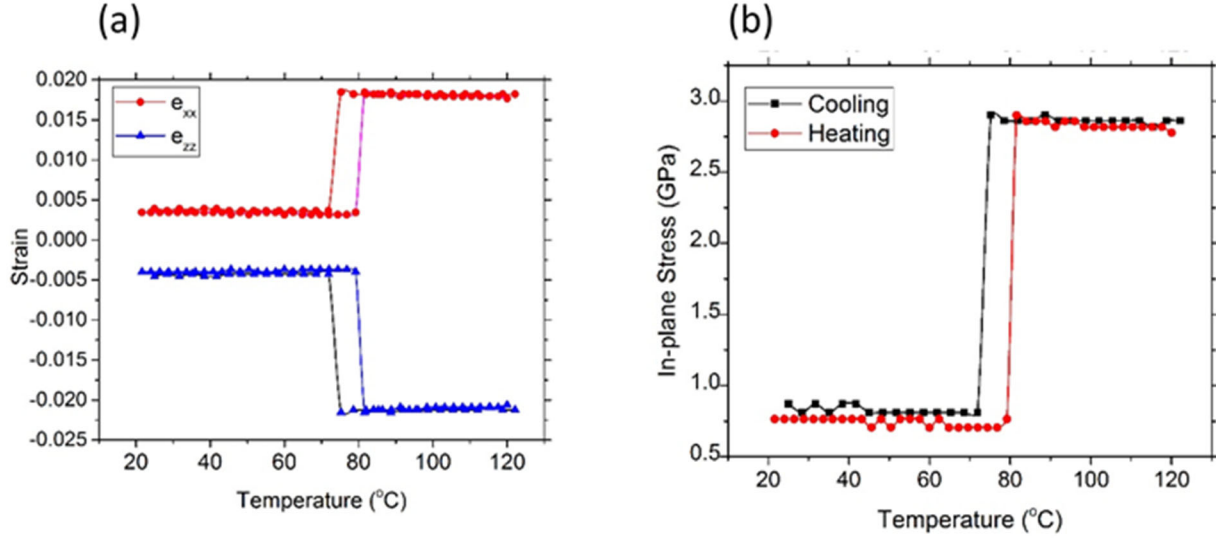


Figure 7. a) Temperature dependence of in-plane and out-of-plane strains in VO₂ thin films grown on c-sapphire, b) stress vs temperature during heating and cooling in VO₂ (020)/ sapphire (0006) heterostructures

5.3.4. Kinetic and thermodynamic models, SPT and SMT-strain correlation

As stated before, SPT and SMT temperatures are different. This behavior is not consistent with most reports, in which electronic and structural transitions overlap each other. However, there are some reports recently claiming that SPT of VO₂ does not always appear during SMT. In this work, it is shown that the SMT initiates at a lower temperature than the SPT. Mott or Peierls transitions or some combination of both are common mechanisms suggested for SMT in VO₂.

Mott-Hubbard transition explains the occurrence of SMT based on electron only interactions³¹. In fact, it introduces two states for movement of electrons and holes forming a band of energies described by Equation 5.1 and 5.2, below.

$$\sum_i e^{ik\alpha_i} \psi_i \quad \text{Equation (5.1)}$$

$$\sum_i e^{ik\alpha_i} \psi'_i \quad \text{Equation (5.2)}$$

Where the ψ_i and ψ'_i are the wavefunctions for an extra electron and hole on atom i , respectively, k is the wavenumber, and α_i is denoting lattice site i . The transition occurs when these two bands overlap. Though, there are simplifying assumptions for this model, e.g. neglecting the

long-range coulombic interactions. Mott predicted the number of electrons or holes per unit volume, n , for transition to occur at $n = \left(\frac{0.2}{a_0}\right)^3$, where a_0 is the Bohr radius.

The Peierls transition, SPT, is based on the interaction of electrons and phonons. In this case, if an atom is moved a distance of $\pm\delta$ in alternating opposite directions, either along the line or at a given angle, then a super-lattice will form that will introduce a gap with the width of $V_0\delta/a$ in which V_0 is energy that depends on the electron-phonon interaction. Peierls distortion can then form if the Fermi surface is flat such that the energy term is split by the distortion. This transition can be driven by increasing temperature.

In previous reports, the effect of strain on the change of SPT temperature has been explained by using thermodynamics approach (Clapeyron equation)¹⁹⁻²³. However, in all of the reports, the role of kinetics has not been considered. In the following, first, we present a model for transformation velocity including both kinetic and thermodynamic aspects. Second, we derive an expression for the effect of strain on the change of the activation barrier affecting the kinetic term of the model. Since the VO₂ transformation is an ultrafast transition, one can consider a thermally activated jump of one vanadium atom along a_{mono} (or c_{tet}), to be responsible for this transformation. Under this condition, as shown in Figure 8a, let the free energy change for an atomic jump be ΔG_α . If there is no strain in the system, the atom jumps from stage I to stage II. However, in the presence of strain, a second strain-induced state is formed. Now, the atom can jump into M_2 , strain-induced metastable state. Eventually, the atom will go to M_1 position which is thermodynamically stable. Now consider the free energy change barrier for this jump, as represented in Figure 5.8b, be ΔG_m . The ΔG_m is defined by kinetics; however, ΔG_α is dictated by thermodynamics. Thus, the velocity of the transformation can be derived:

$$\mathcal{V} = K_p \exp\left(-\frac{\Delta G_m}{kT}\right) \left[1 - \exp\left(\frac{\Delta G_\alpha}{kT}\right)\right] \quad \text{Equation (5.3)}$$

where K_p is the pre-exponential factor equal to $v_o.f.\lambda$ where v_o is the Debye frequency factor, f is the fraction of available sites for jump which equals 1 here, and λ is the atomic jump distance. Thus, $K_p \exp\left(-\frac{\Delta G_m}{kT}\right)$ is the kinetic term and $[1 - \exp\left(\frac{\Delta G_\alpha}{kT}\right)]$ is the thermodynamic term contributing to the velocity of the transformation.

$$\Delta G_{T=T_0} = 0 = \Delta H_0 - T_0 \Delta S_0 \quad \text{Equation (5.4)}$$

$$\Delta G_r = \Delta G_\alpha = \Delta H_r - T_r \Delta S_r \quad \text{Equation (5.5)}$$

$$\Delta G_\alpha = \Delta S. \Delta T_r \quad \text{Equation (5.6)}$$

where $\Delta G_{T=T_0}$ is the Gibbs free energy associated with the phase transition at equilibrium temperature which is zero, $\Delta G_r = \Delta G_\alpha$ is the Gibbs free energy at $T \pm \epsilon$, ΔS is the discontinuous change in entropy between two phases, and ΔT is the deviation from the equilibrium transition temperature. As $\Delta G_\alpha \rightarrow 0$, the transformation velocity $V \rightarrow 0$, which explains the role of thermodynamics. However, ΔG_m , plays a very important role in controlling the velocity; and any change in kinetics barrier can modify the structural transition temperature. In this manner, Yang et.al showed how it is possible to freeze the SPT while the SMT is happening¹⁵. Indeed, the SPT can be suppressed by increasing the kinetics barrier. Figure 5.8b depicts a proposed change in kinetics barrier in the presence of strains, which can then be used to explain the transformation process from kinetics approach in terms of atomic diffusion. The diffusion coefficient considering only the migration energy can be written as:

$$D = f \lambda^2 v_o \exp\left(-\frac{\Delta G_m}{kT}\right) \quad \text{Equation (5.7)}$$

where ΔG_m is the activation energy of migration for the atoms. Thus;

$$V = \frac{Df}{\lambda f_D} \left(1 - \exp\left(\frac{\Delta G_\alpha}{kT}\right)\right) \quad \text{Equation (5.8)}$$

The $f_{D=1}$ is the geometrical factor associated with diffusion. This equation shows how $\mathcal{V} \propto D$, and we can write;

$$D/f\lambda^2v_D = \exp\left(-\frac{\Delta G_m}{kT}\right) \quad \text{Equation (5.9)}$$

$$\ln\left(\frac{D}{f\lambda^2v_D}\right) = -\frac{1}{kT}(\Delta G_m) \quad \text{Equation (5.10)}$$

$$\frac{\partial}{\partial\sigma}\ln\left(\frac{D}{f\lambda^2v_D}\right) = -\frac{1}{kT}\left(\left(\frac{\partial\Delta G_m}{\partial\sigma}\right)_T\right) \quad \text{Equation (5.11)}$$

Now considering $\left(\frac{\partial\Delta G}{\partial\sigma}\right)_T = \Delta V$, where ΔV is the change in the volume, then;

$$\frac{\partial}{\partial\sigma}\ln\left(\frac{D}{f\lambda^2v_D}\right) = -\frac{1}{kT}(\Delta V_m) \quad \text{Equation (5.12)}$$

where ΔV_m is the activation volume for migration.

Integrating the previous equation, we have:

$$\ln\left(\frac{D}{f\lambda^2v_D}\right)_\sigma - \ln\left(\frac{D_0}{f\lambda^2v_D}\right)_0 = -\frac{\sigma}{kT}(\Delta V_m) \quad \text{Equation (5.13)}$$

$$\frac{D}{D_0} = \exp\left(-\frac{\sigma}{kT}(\Delta V_m)\right) \quad \text{Equation (5.14)}$$

D_0 is the diffusion coefficient at $\sigma=0$;

$$D = D_0 \exp\left(-\frac{\sigma}{kT}(\Delta V_m)\right) \quad \text{Equation (5.15)}$$

Thus, new activation energy under the stress σ is:

$$\Delta G_t = \Delta G_0 + \sigma(\Delta V_m) \quad \text{Equation (5.16)}$$

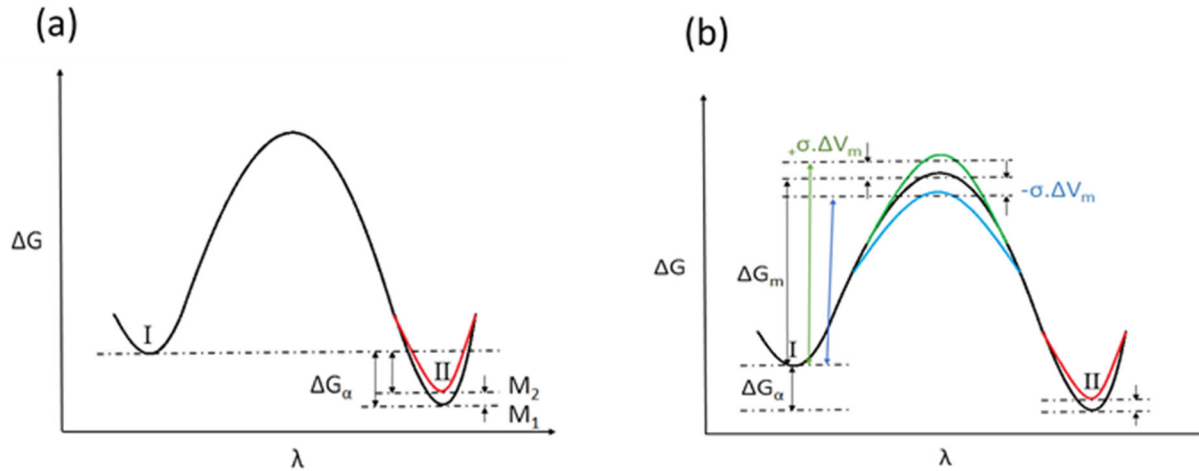


Figure 5.8. a) The energy level of tetragonal (stage I) and monoclinic, M_1 and M_2 (stage II); and the difference between these two stages, ΔG_α , b) changing the activation energy of transformation, ΔG_m , in the presence of compressive and tensile stress.

This equation explains how the compressive stress along c_{tet} or a_{mono} , $-\sigma$, decreases the activation barrier and the tensile stress, $+\sigma$, increases the activation barrier and shift the transition temperature to higher values (Figure 5.8b). Thus, the structural transition will be suppressed by a 0.8 MPa residual tensile stress, assuming the shear modulus and Poisson ratio of the monoclinic phase to be 60 GPa and 0.3, respectively²⁷. That is, the activation barrier has been changed due to the epitaxial tensile strain. It is worth mentioning that the residual strain along the c -axis of the tetragonal phase has a major effect on displacing the transition temperature. Our model is consistent with the electronic orbital occupancy theory³² in the presence of compressive strain (when c/a ratio is decreased) which causes a decrease in the transition temperature. In this model³², however, the focus was on the SMT transition, not SPT, using the electronic orbital theory. Since these two transitions are affected differently in the presence of epitaxial strain, we provide two different models to explain with a focus on SPT.

The presence of stress can also affect the Mott transition. For Mott transition to happen, the band structure and electron concentration at the conduction band need to change. So, we should

consider how strain is affecting the band structure. The early occurrence of a Mott transition in the presence of strain can be explained by the resulting change in the crystal symmetry. In fact, symmetry has a fundamental effect on the band structure of each material; the presence of strain in the structure reduces the crystal symmetry lifting the band degeneracy. Thus, the originally degenerate energy levels can split even in the absence of an SPT. The schematic Figure 5.9 represents the band structure of MCM and shows how a transition to metallic behavior might occur in the absence of a structural transition due to changes within its bandgap. According to our calculations and experimental results, the tensile strain along c-axis of rutile and the compressive strain along the a-axis at crystallite “b” leads to the increase of the c/a ratio. The p-d overlap perpendicular to the c-axis is increased which suggests the orbital occupancy of $d_{||}$ in the metallic phase is increased. This means that the energy of the π^* valence electronic states is increased relative to that of the $d_{||}$ valence states. As a result, an increase in the transition temperature is expected. Measuring the L_2 - L_3 peak position difference from EELS results shown in Figure 5.3, it is found that in crystallite “a” this difference equals 6.4 eV, while in the unrelaxed crystallite “b” it is 6.1 eV. This result shows that the crystal field splitting in monoclinic phase in crystallite “b” is reduced in case of tensile strain along c-axis (higher c/a) which results in the increase of the electrical transition temperature. It was shown earlier that the epitaxial strain in VO_2 and, consequently, its electrical properties can be controlled by buffer oxide layers which influence the orbital occupancy in the VO_2 metallic state and modify the transition temperature and the structural distortion across the transition³². Thus, SMT can be altered by bandgap effects produced by the presence of unrelaxed lattice strains.

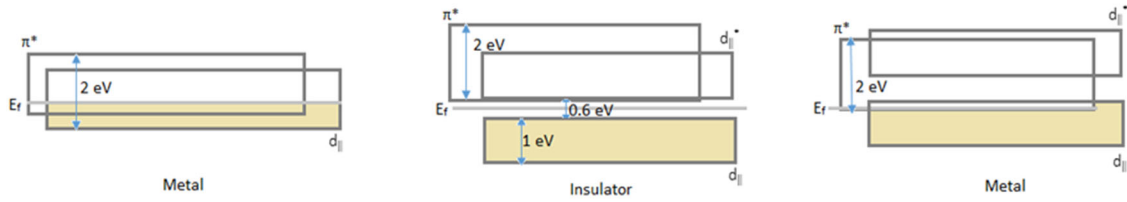


Figure 5.9. Schematic energy band for the metal, insulator, and monoclinic metallic phase of VO₂.

5.4. Conclusion

The (010)VO₂ epitaxial thin films were grown on a c-sapphire substrate via PLD and the microstructural and structural characteristics were investigated by using HAADF images, EELS spectra, and DME calculations. The electronic and structural transitions of VO₂ were investigated using resistance measurements and temperature dependent XRD patterns, respectively. These results confirm that both transition temperatures are shifted toward higher temperatures when compared to bulk values and that the SMT occurs before the SPT, due to the presence of tensile strains in thin films. It is argued that the velocity and temperature of the phase transformation are controlled by the thermodynamics and kinetics, where thermodynamics determines the feasibility and kinetics defines the rate of transformation. Unrelaxed strain in the film changes the activation barrier for the SPT and also modifies the bandgap that affects the Mott transition. Our proposed model provides a better understanding of the SPT mechanism in strained thin films and illustrates how strain might affect Peierls and Mott transitions differently and thereby explains the observed temperature splits in the respective transitions.

REFERENCES

1. Narayan, J. & Bhosle, V. M. Phase transition and critical issues in structure-property correlations of vanadium oxide. *J. Appl. Phys.* 100, 103524 (2006).
2. Okimura, K., Sakai, J. & Ramanathan, S. In situ x-ray diffraction studies on epitaxial VO₂ films grown on c-Al₂O₃ during thermally induced insulator-metal transition. *J. Appl. Phys.* 107, 63503 (2010).
3. Mun, B. S. et al. Nonpercolative metal-insulator transition in VO₂ single crystals. *Phys. Rev. B* 84, 113109 (2011).
4. Mun, B. S. et al. Observation of insulating–insulating monoclinic structural transition in macro-sized VO₂ single crystals. *Phys. status solidi (RRL)-Rapid Res. Lett.* 5, 107–109 (2011).
5. Kim, H.-T. et al. Mechanism and observation of Mott transition in VO₂-based two-and three-terminal devices. *New J. Phys.* 6, 52 (2004).
6. Nag, J., Jr, R. F. H., Payzant, E. A. & More, K. L. Non-congruence of thermally driven structural and electronic transitions in VO₂. *J. Appl. Phys.* 112, 103532 (2012).
7. Kim, H.-T. et al. Hole-driven MIT theory, Mott transition in VO₂, MoBRiK device. *Phys. C Supercond.* 460, 1076–1078 (2007).
8. Arcangeletti, E. et al. Evidence of a pressure-induced metallization process in monoclinic VO₂. *Phys. Rev. Lett.* 98, 196406 (2007).
9. Zylbersztein, A. & Mott, N. F. Metal-Insulator Transition in Vanadium Dioxide. *Phys. Rev. B* 11, 4383–4395 (1975).
10. Qazilbash, M. M. et al. Mott transition in VO₂ revealed by infrared spectroscopy and nano-imaging. *Science* 318, 1750–1753 (2007).

11. Morrison, V. R. et al. A photoinduced metal-like phase of monoclinic VO₂ revealed by ultrafast electron diffraction. *Science* 346, 445–448 (2014).
12. Kim, B.-J. et al. Micrometer x-ray diffraction study of VO₂ films: Separation between metal-insulator transition and structural phase transition. *Phys. Rev. B* 77, 235401 (2008).
13. Tao, Z. et al. Decoupling of Structural and Electronic Phase Transitions in VO₂. *Phys. Rev. Lett.* 109, 166406 (2012).
14. Booth, J. M. & Casey, P. S. Anisotropic structure deformation in the VO₂ metal-insulator transition. *Phys. Rev. Lett.* 103, 86402 (2009).
15. Yang, M. et al. Suppression of Structural Phase Transition in VO₂ by Epitaxial Strain in Vicinity of Metal-insulator Transition. *Sci. Rep.* 6, 23119 (2016).
16. Kim, S., Kim, K., Kang, C.-J. & Min, B. I. Correlation-assisted phonon softening and the orbital-selective Peierls transition in VO₂. *Phys. Rev. B* 87, 195106 (2013).
17. Yao, T. et al. Understanding the nature of the kinetic process in a VO₂ metal-insulator transition. *Phys. Rev. Lett.* 105, 226405 (2010).
18. Théry, V. et al. Role of thermal strain in the metal-insulator and structural phase transition of epitaxial VO₂ films. *Phys. Rev. B* 93, 184106 (2016).
19. Kucharczyk, D. & Niklewski, T. Accurate X-ray determination of the lattice parameters and the thermal expansion coefficients of VO₂ near the transition temperature. *J. Appl. Crystallogr.* 12, 370–373 (1979).
20. Gu, Y., Cao, J., Wu, J. & Chen, L.-Q. Thermodynamics of strained vanadium dioxide single crystals. *J. Appl. Phys.* 108, 83517 (2010).
21. Cao, J. et al. Strain engineering and one-dimensional organization of metal–insulator domains in single-crystal vanadium dioxide beams. *Nat. Nanotechnol.* 4, 732–737 (2009).

22. Fan, W. et al. Superelastic metal-insulator phase transition in single-crystal VO₂ nanobeams. *Phys. Rev. B* 80, 241105 (2009).
23. Cao, J. et al. Constant threshold resistivity in the metal-insulator transition of VO₂. *Phys. Rev. B* 82, 241101 (2010).
24. Yamaguchi, I. et al. Preparation and characterization of epitaxial VO₂ films on sapphire using postepitaxial topotaxy route via epitaxial V₂O₃ films. *Jpn. J. Appl. Phys.* 47, 1022 (2008).
25. Narayan, J. & Larson, B. C. Domain epitaxy: A unified paradigm for thin film growth. *J. Appl. Phys.* 93, 278–285 (2003).
26. Jin, P. et al. Characterization of mechanical properties of VO₂ thin films on sapphire and silicon by ultra-microindentation. *Thin Solid Films* 343, 134–137 (1999).
27. Viswanath, B. & Ramanathan, S. Direct in situ observation of structural transition driven actuation in VO₂ utilizing electron transparent cantilevers. *Nanoscale* 5, 7484–7492 (2013).
28. Moatti, A., Bayati, R. & Narayan, J. Epitaxial growth of rutile TiO₂ thin films by oxidation of TiN/Si{100} heterostructure. *Acta Mater.* 103, (2016).
29. Sachan, R. et al. Forging fast ion conducting nanochannels with swift heavy ions: the correlated role of local electronic and atomic structure. *J. Phys. Chem. C* 121, 975–981 (2017).
30. Zhou, H., Chisholm, M. F., Yang, T.-H., Pennycook, S. J. & Narayan, J. Role of interfacial transition layers in VO₂/Al₂O₃ heterostructures. *J. Appl. Phys.* 110, 73515 (2011).
31. Mott, N. F. & *Transitions*, M.-I. Taylor and Francis. (1990).
32. Aetukuri, N. B. et al. Control of the metal-insulator transition in vanadium dioxide by modifying orbital occupancy. *Nat. Phys.* 9, 661 (2013).

CHAPTER 6

6. Strain engineering-Mechanism of strain relaxation and control of electrical transition in the VO₂ thin-films across the critical thickness

Abstract

Understanding the strain relaxation induced atomic rearrangement at the epitaxial interfaces is critical for developing smart materials using nanoscale thin film technology. VO₂ is one of such *smart* strongly-correlated transition metal oxides which exhibits a structural transition from tetragonal to monoclinic phase at ~ 68°C. Here, we demonstrate an atomically sharp transition from a strained to a relaxed state of VO₂ thin films above and below the critical thickness (15 nm) in VO₂/NiO/c-Al₂O₃ heterostructures and discuss the mechanism of relation and control of electrical transition. Using atomic resolution electron microscopic analysis, we capture the epitaxial nucleation of a relaxed domain of VO₂ over the strained one through the emergence of interface dislocations under domain matching epitaxy. Below this critical thickness, the film isostructurally adopts the low-temperature (monoclinic) phase in the strained state at the growth temperature. The film subsequently turns into a completely relaxed state above the critical thickness as the interfacial dislocations glide to the film/substrate (VO₂/NiO) interface through active slip systems of $\frac{1}{2} [0\bar{1}1](011)$ and $\frac{1}{2} [10\bar{1}](101)$. With this study, we present the mechanism to form epitaxial and atomically sharp strained/unstrained interface in VO₂ *via* dislocation nucleation and opens a new frontier towards manipulation of correlative properties through strain engineering.

6.1. Introduction

As the electronic industry is aiming to achieve a smaller scale of films and electronic devices, it becomes very critical to investigate the behavior of the material in that scale. One of the main characteristics is defined for thin film growth is the critical thickness above which misfit dislocations nucleate and possibly glide to the interface for thin film relaxation^{1,2}. However, in the case of phase-change materials, there is a critical question of whether the structure of the film below the critical thickness belongs to low or high-temperature phase. Besides, how this structure behaves across the critical thickness limit is a question that requires in-situ studies or capturing some evidence at the growth temperature³. Here, we study electron-correlated VO₂ structure's behavior as a phase-change transitional metal oxide as it passes the critical thickness at the growth temperature. Vanadium dioxide is considered a multi-stimuli responsive smart material which undergoes a reversible, fast, and close to room temperature transition⁴⁻⁸. This ability allows VO₂ to be used as memory, FET devices, sensors and etc.⁹⁻¹⁵. The VO₂-based device's performance is depending on the size, defect content, dopant, and crystallinity of this structure^{5,16-20}. This fact explains why it is important to study this material as a function of thickness. While the bulk properties of VO₂ is well studied and established, rather little is known about the thin film (below critical thickness) and the surface characteristics of this phase-change transitional metal oxide.

In this study, we deposited VO₂ at the approximation of the critical thickness where there is some thickness perturbation on the surface to study behavior below and above the critical thickness. Then, we used HAADF images to investigate the nucleation and propagation of the misfit dislocation at the interface of the low and high-temperature phase of VO₂, as they represent the structures that belong to below and above critical thickness scenarios, respectively. The grain

boundary characteristics are described at high and low temperatures. The favorable glide planes are also defined based on slip system and surface energies.

6.2. Experimental details

Epitaxial VO₂/NiO/c-sapphire heterostructures were grown by pulsed laser deposition (PLD) technique. A Lambda Physik KrF excimer laser was employed to ablate a pure VO₂ target. The VO₂ deposition was conducted under 0.125 mTorr oxygen pressure and temperature of 550°C. The laser energy density and frequency were set at 3 Jcm⁻² and 5 Hz, respectively. The FEI Titan 80-300 probe aberration-corrected scanning transmission electron microscopy (STEM) operated at 200 KV was employed to collect atomic resolution HAADF images with the resolution limit of 0.07 nm, and electron energy loss spectra (EELS) were collected with the energy resolution of the electron source to the limit of 0.15 eV.

6.3. Results and discussion

The vanadium dioxide thin films have grown approximately at the critical thickness by PLD methods on the c-sapphire substrate using NiO as a buffer layer. The critical thickness calculations are as follows:

6.3.1. Critical thickness

As the VO₂ reached the critical thickness, the misfit dislocations nucleate at the surface and glide all the way down to the VO₂/NiO interface. The critical thickness (h_c) at which it becomes energetically favorable for a thin film to contain dislocations is h_c :

$$h_c = \frac{b(1-\nu\cos^2\theta)\sin\theta\cos\phi}{4\pi(1+\nu)\epsilon_0} \ln(\alpha h_c/b) \quad \text{Equation (6.1)}$$

Where b is the magnitude of Burgers vector of the dislocation, ν is the Poisson's ratio, θ is the angle between Burgers vector and dislocation line, ϕ is the angle between the normal of the

dislocation plane and film plane, and α is the dislocation core radius factor which varies with strain ϵ_0 . Thus, we will have h_c as:

$$h_c = \frac{0.048b}{\epsilon_0} \ln\left(\alpha \frac{h_c}{b}\right) \quad \text{Equation (6.2)}$$

The slip systems in the VO₂ monoclinic structure are $\frac{1}{2} [0\bar{1}1](011)$ and $\frac{1}{2} [10\bar{1}](101)$. So Burgers vector are calculated to be 1.749 Å and 1.553 Å, respectively. As a result, the critical thickness calculated to be ~15 nm. The role of tensile strain has been explained to increase the kinetic barrier for dislocation nucleation. Even though thermodynamically the critical thickness is calculated at 15 nm, kinetically the dislocation formation is happening at higher values.

To investigate the mechanism of relaxation, we consider three cases: i) above the critical thickness where the VO₂ film is fully relaxed, ii) in the vicinity of the critical thickness where any surface perturbations causes local relaxation using slip system, and iii) below the critical thickness where film is uniformly strained due to the misfit strain. The schematic Figure 6.1 illustrates these three cases. Next, we obtained HAADF images of the mentioned cases.

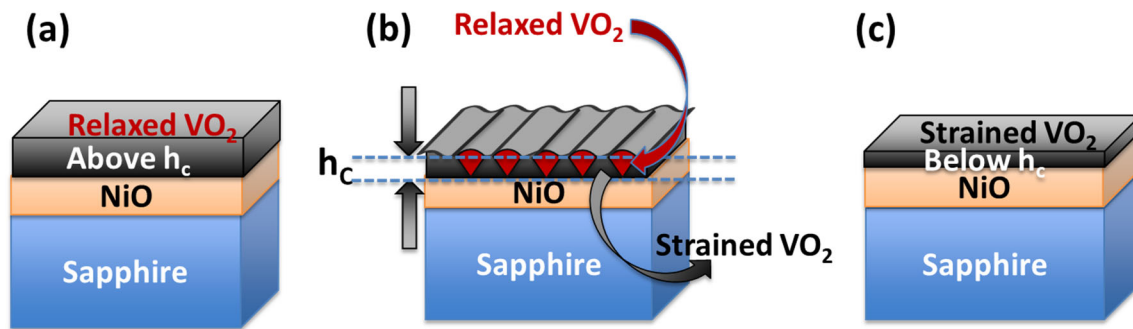


Figure 6.1. a) The schematic illustration of VO₂/NiO/c-sapphire heterostructures where VO₂ is grown above the critical thickness (h_c) of ~15 nm. b) The schematic illustration of VO₂/NiO/c-sapphire heterostructures where VO₂ is grown in the vicinity of the critical thickness. The red area represents a relaxed area where the film is reached h_c value and dislocations glide using the slip plane. c) The schematic illustration of VO₂/NiO/c-sapphire heterostructures where VO₂ is grown below the critical thickness.

Figure 6.2 shows the micrographs belong to the VO₂/NiO/c-sapphire heterostructures. Figure 6.2c and d illustrate the heterostructures where VO₂ is grown above and below the critical thickness, respectively. Above the critical thickness, the VO₂ film is relaxed through DME paradigm²¹. The periodic dislocations are marked in the FFT image at the interface of VO₂/NiO-VO₂ in Figure 6.2a. However, below the h_c , there is no dislocation formation (see the FFT image at the interface of VO₂/NiO-VO₂ in Figure 6.2b). Figure 6.2c and d illustrate the atomic resolution HAADF images associated with the VO₂ above and below the h_c , respectively. It is found that the structure below the h_c belongs to the unrelaxed stabilized monoclinic phase²². This structure was shown to have a smaller difference in the bond length of V-V dimmers²². Figure 6.2e captures an image of a grain which is grown above the h_c within the matrix below the h_c . This image represents the mechanism of relaxation for the VO₂ thin film as it reaches the h_c limit. The h_c is the radius of a sphere as marked in Figure 6.2f, where energetically it is favorable for dislocations to nucleate at the surface and glide immediately toward the interface. These dislocations are frozen at the interface between unrelaxed (below the critical thickness) structure and the relaxed grain since the film does not uniformly reach the h_c limit.

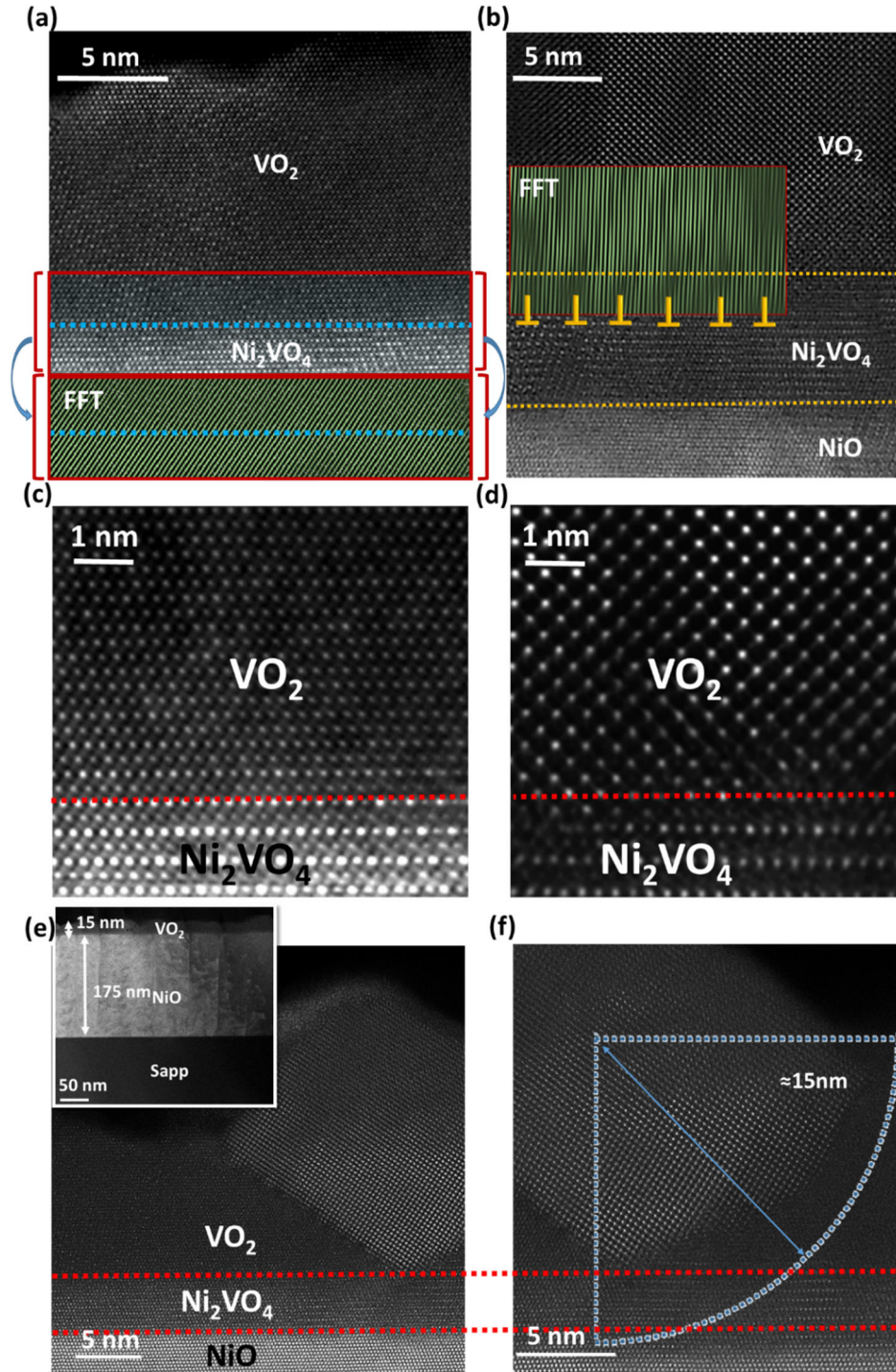


Figure 6.2. a) The HAADF image of VO₂/NiO/c-sapphire heterostructures where VO₂ is grown above the critical thickness of ~15 nm. b) The HAADF image of VO₂/NiO/c-sapphire heterostructures where VO₂ is grown below the critical thickness. c, d) The atomic resolution HAADF image of VO₂ structure belongs to (a) and (b), respectively. e) The HAADF image taken by STEM showing both strained and relaxed state of VO₂ below and above the critical thickness along [1 $\bar{2}$ 1] NiO zone axis. The inset figure represents the low-mag image of the VO₂/NiO/c-sapphire heterostructure and their thicknesses. f) The HAADF image of the relaxed monoclinic VO₂ grain which is reached above the critical thickness.

6.3.2. DME

Figure 6.3a shows the boundary between relaxed-monoclinic and the strained-monoclinic below it. In the inset of Figure 6.3a, the indexed FFT patterns belong to spots marked as 1, 2, and 3 are shown. According to these patterns, the epitaxial relationship is VO₂-monoclinic ($\bar{1}01$) \parallel VO₂-relaxed monoclinic (100) \parallel VO₂-tetragonal (001). Using domain matching epitaxy^{23,24,25}, the misfit strain between the tetragonal (001) and unrelaxed monoclinic ($\bar{1}01$) is calculated to be $\approx 18.58\%$ ($d_{(002)\text{tetragonal}}=5.703\text{\AA}$, $d_{(\bar{1}01)\text{monoclinic}}=4.809\text{\AA}$). This results in 4/5 integral multiple of lattice planes between grains. The 4/5 plane matching and formation of dislocations are shown in HAADF image across the interface in Figure 6.3a. After cooling down and across the transition temperature, no more dislocation is added to the interface since the temperature is low and kinetically it is impossible for new dislocations to form based on misfit strain of room temperature structures, however the tetragonal to monoclinic transition occurs during cooling down in the relaxed grain. As it was explained earlier, the slip systems in the VO₂ monoclinic structure are $\frac{1}{2} [0\bar{1}1](011)$ and $\frac{1}{2} [10\bar{1}](101)$. The slip systems in tetragonal are $\frac{1}{2}\{100\}\langle 001 \rangle$ and $\frac{1}{2}\{101\}\langle 10\bar{1} \rangle$ considered as first and secondary slip system, respectively. The slip direction is along $[10\bar{1}]$ of monoclinic or $[001]$ of the tetragonal phase.

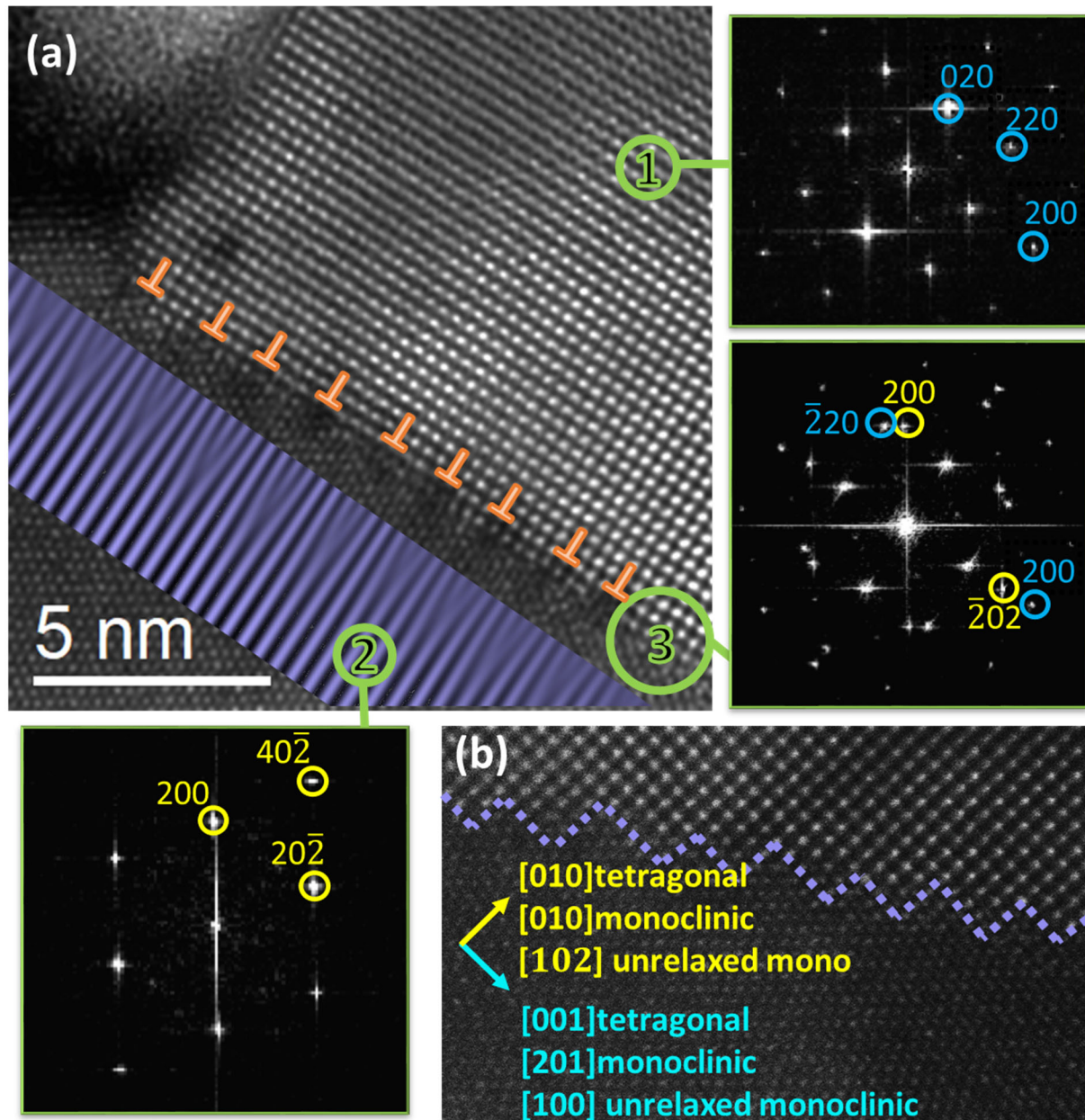


Figure 6.3. a) The HAADF image taken by STEM showing the interface between the strained and relaxed state of VO_2 . The periodic appearance of misfit dislocation at the interface is captured during the transition of strained to a relaxed state. The FFT pattern belongs to the relaxed monoclinic, strained monoclinic, and at the interface of both states is indicated by 1, 2, and 3, respectively. b) The formation of steps along low energy directions at the interface of a strained and relaxed state of VO_2 to minimize the total energy of the system.

6.3.3. Surface energies

In the bottom of the relaxed grain, there is some steps formation along low energy directions which belong to low energy planes to minimize the energy of the systems ²⁶. In the

monoclinic structure, these steps are forming along [010] and [201] directions as it is shown in the HAADF image in Figure 6.3b. That suggests that in the tetragonal structure, the steps were formed along [010] and [001] directions at high temperature. These directions can belong to the low energy surfaces of {100} and {110} in the tetragonal phase of VO₂ being equal to 0.29 J/m² and 0.42 J/m², respectively.

6.3.4. Interface analysis

To further investigate the interface (Figure 6.4a) between relaxed and unrelaxed monoclinic, we used image processing techniques. Figure 4b shows the dislocation cores for two dislocations along the interface. Around the dislocation core, there is a redistribution of atomic arrangement to accommodate the strain. Interestingly along with each dislocation formation in relaxed-monoclinic, there is an atomic column missing in the unrelaxed-monoclinic to locally decrease the energy of the system. These pair of dislocation and missing atomic column are shown in Figure 6.4b. Figure 6.4c represents the strain distribution along the interface. The strain centers are located around the dislocation cores and missing atomic columns as compressive and tensile stresses, respectively. This analysis explains the wave-like behavior of strain centers where the negative and positive source of strain cancel out each other and lower the energy of the system.

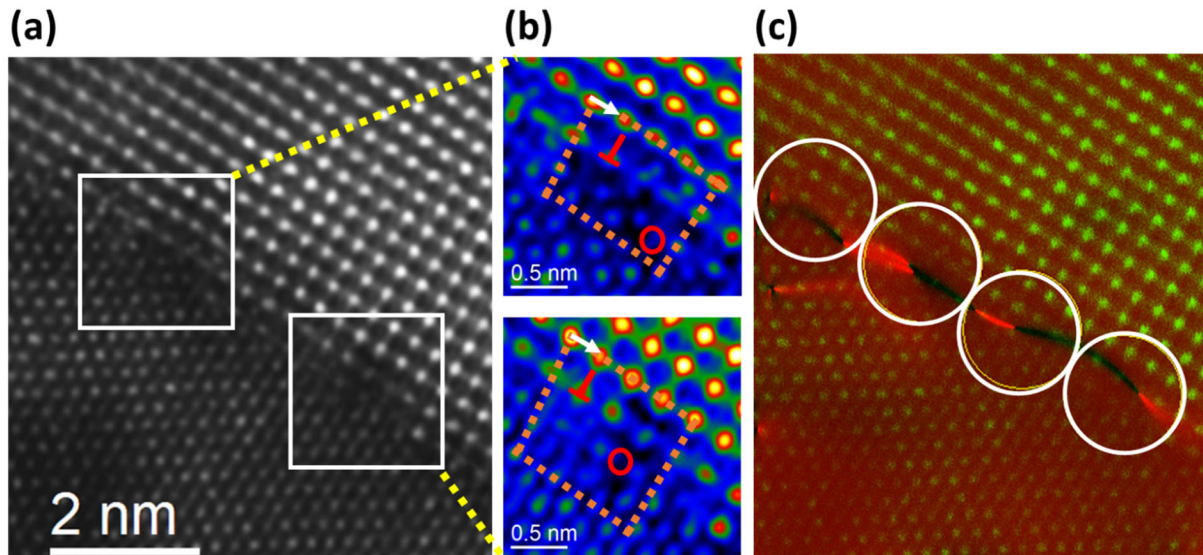


Figure 6.4. a) The indication of two dislocation cores in the HAADF image of the interface. b) the image processing technique used to depict the atomic rearrangements around the dislocations' core. The dislocation loop and Burgers vector is illustrated for each dislocation. There is one atomic column missing, marked by a circle, in the vicinity of each dislocation core, marked by T, to compensate for the generated strain. c) Strain analysis along the relaxed and strained interface represents the strain centers. The red color is a positive strain going to black color for negative strains. The presence of periodic compressive and tensile strains around the dislocation cores also is an indication of atomic rearrangement to minimize the local strain.

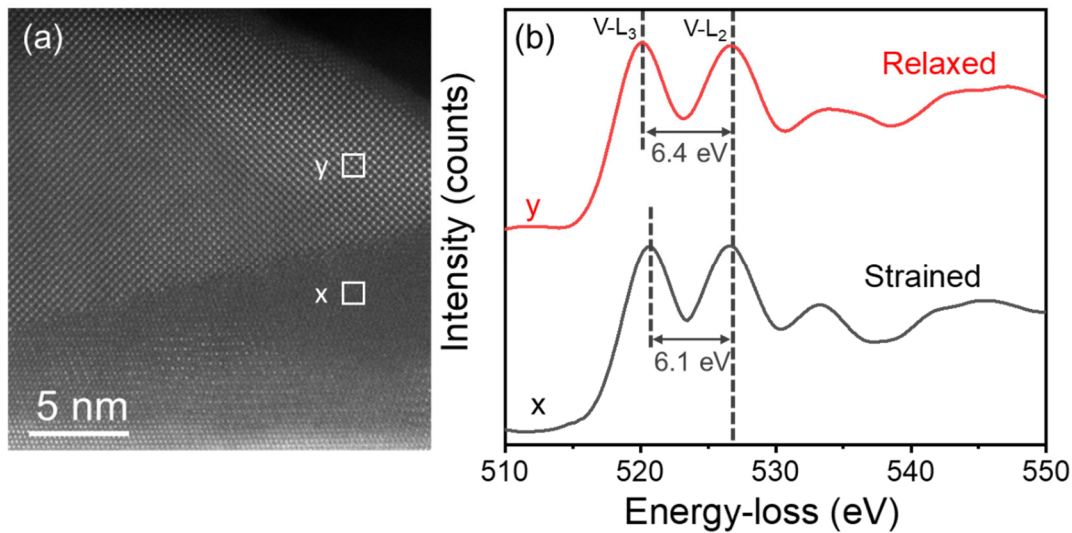


Figure 6.5. a) HAADF image showing two different orientations of VO_2 belong to strained and relaxed states marked by squares x and y, respectively, on NiO buffer layer along $[1\bar{2}1]$, b) selected spectrum collected from two different states marked as x and y belong to strained and relaxed VO_2 , respectively.

Figure 6.5 shows the electron energy-loss spectra (EELS) from the strained (site x) and relaxed (site y) regions of the VO_2 thin film, indicated in the HAADF image in Figure 6.4a. The

presented EEL spectra of the two regions consist of the V-L₃₂ and O-K core-loss edges corresponding to transitions between 2p^{3/2} (V-L₃) and 2p^{1/2} (V-L₂) to 3d and 1s^{1/2} (O-K) to 2p, respectively. While analyzing the EEL spectra, it is observed that the energy-gap between L₃ and L₂ peaks of V core-loss edge reduces to 6.1 eV in the strained region from 6.4 eV in the relaxed region of the film. This suggests the narrowing of the crystal field splitting in the strained phase due to the higher c/a ratio attributed to the presence of tensile strain along the c-axis of the monoclinic VO₂ structure^{21,22}. In addition, the L₃₂ ratios in the two spectra are estimated to be the same which signifies no reduction in vanadium oxidation state in the two regions.

6.3.5. Cryptographic description the interface between strained and relaxed grains

The grain boundary between two grains (Coincidence Site Lattice: CSL method)^{27,28} can be described by $\theta[h_0k_0l_0], (h_{nA}k_{nA}l_{nA})/(h_{nB}k_{nB}l_{nB})$, where, the grain misorientation is defined by θ which is the rotation angle, $[h_0k_0l_0]$ as a common axis between grains, and nA/nB are the normal to the interface planes in unrelaxed and relaxed grains, respectively. At room temperature, as it is shown in Figure 6.5, the grain boundary between unrelaxed and relaxed grains in the monoclinic phase can be described as 30° $[\bar{1}0\bar{1}], (\bar{1}01)/(010)$. The grain boundary is not a pure rotation and has a twist characteristic as well. The twist angle is 90°.

At the deposition temperature, the relaxed grain is at the tetragonal stage which is a typical stage for relaxed high-temperature VO₂. Thus, it is important to investigate the grain boundary characteristic of tetragonal and unrelaxed monoclinic grains (Figure 6.6a) as it undergoes the transition (Figure 6.6b). This grain boundary is characterized as 30° $[\bar{1}0\bar{1}], (\bar{1}01)/(010)$. This boundary is defined between two different structures of tetragonal and monoclinic, where x-axis and y-axis are fixed, and the z-axis is increased by 32.6°, meaning that the β angle is changed from 90° to 122.6°, respectively from tetragonal to monoclinic phase.

During cooling down, the relaxed grain in the tetragonal phase transitions to the relaxed monoclinic structure as shown in Figure 6.6c. However, the unrelaxed grain stays unchanged throughout the whole temperature range. During the transition of the relaxed grain, the x-axis and z-axis switches.

6.4. Conclusion

We capture an atomically sharp transition from a strained monoclinic to a relaxed tetragonal state of VO₂ thin films at a certain critical thickness (~15 nm) during the epitaxial growth on NiO/*c*-Al₂O₃ heterostructures. Below this critical thickness, the film pseudomorphically adopts a strained monoclinic phase even at the growth temperature. As it reaches to the critical thickness limit, the strained monoclinic transitions into a completely relaxed state with the formation of interfacial dislocations which subsequently glide into the film/substrate (VO₂/NiO) interface following DME paradigm through active slip systems of $\frac{1}{2} [0\bar{1}1](011)$ and $\frac{1}{2} [10\bar{1}](101)$. Using atomic resolution electron microscopic analysis, image processing, and strain analysis, we successfully depict the periodic formation of misfit dislocation, the strain centers, and the atomic rearrangement near dislocations' core. Interestingly at the vicinity of dislocation cores, for each dislocation, there is one atomic column missing to locally minimize the energy, which produces periodically positive and negative strain centers. This study provides us with the tool to obtain the desired structure of VO₂ and to manipulate and exploit the strain center at the dislocation core through external and internal stimuli leading to achievement of predictable properties.

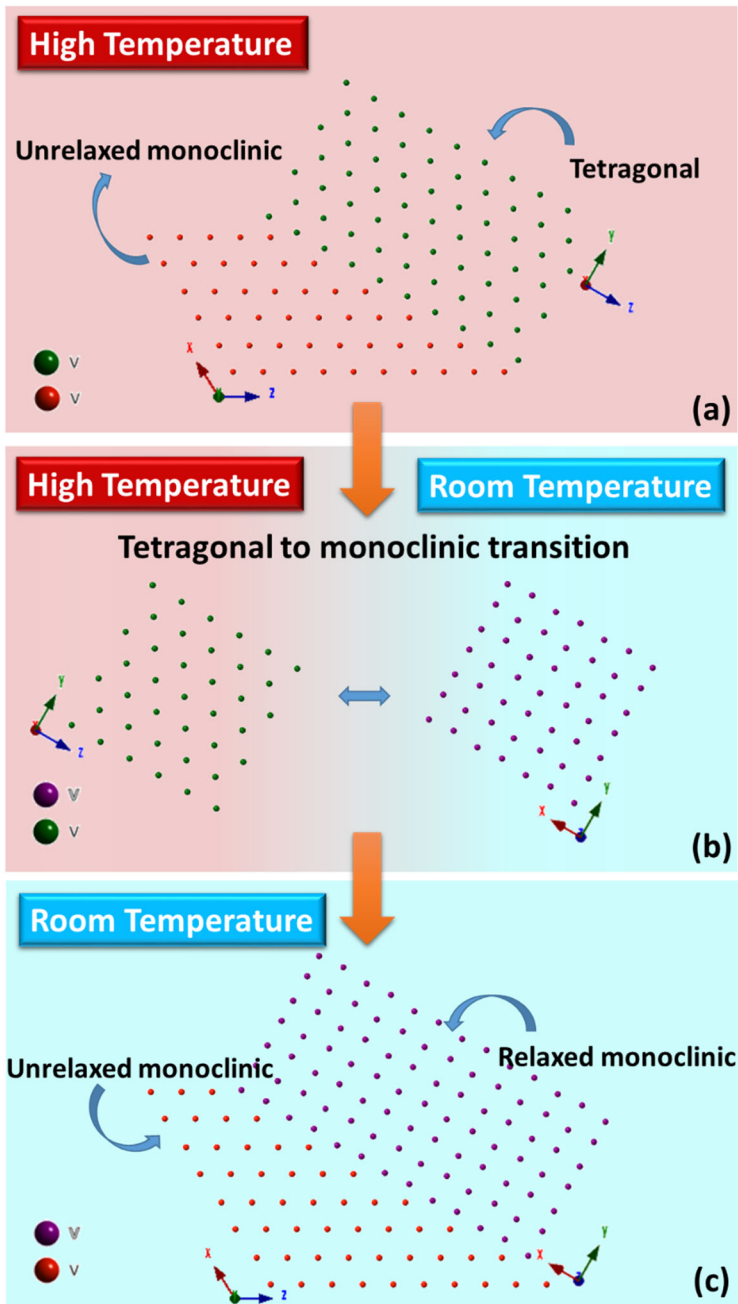


Figure 6.6. a) Schematic illustration of the atomically sharp interface between the strained and relaxed state of VO_2 at high temperature. At high temperature, the relaxed state belongs to the tetragonal rutile VO_2 which is in contact with the strained monoclinic VO_2 . b) The transition of the relaxed state from tetragonal to the monoclinic M_1 phase across the transition temperature of VO_2 . c) Schematic illustration of the interface between the strained and relaxed state of VO_2 at low temperature. At low temperature (RT), the relaxed monoclinic is in contact with the strained monoclinic. The schematic illustration at low temperature agrees with our experimentally captured atomic images.

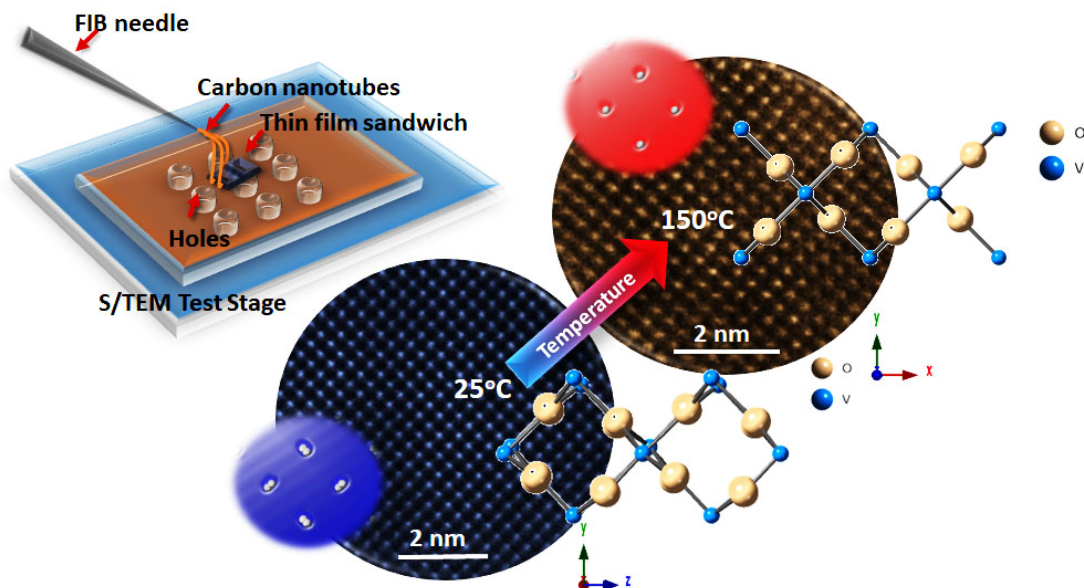
REFERENCES

1. Moatti, A., Bayati, R., Singamaneni, S. & Narayan, J. Epitaxial integration of TiO₂ with Si (100) through a novel approach of oxidation of TiN/Si (100) epitaxial heterostructure. *MRS Adv.* **1** (37), 2629–2634 (2016).
2. Moatti, A. & Narayan, J. High-quality TiN/AlN thin film heterostructures on c-sapphire. *Acta Mater.* **145**, 134-141 (2018).
3. Moatti, A., Sachan, R., Prater, J. & Narayan, J. An optimized sample preparation approach for atomic resolution in situ studies of thin films. *Microsc. Res. Tech.* **81** (11), 1250-1256 (2018).
4. Ramanathan, S. Thin film metal-oxides. Harvard Univ. Springer New York Dordr. Heidelb. London (2010).
5. Narayan, J. & Bhosle, V. M. Phase transition and critical issues in structure-property correlations of vanadium oxide. *J. Appl. Phys.* **100**, 103524 (2006).
6. Viswanath, B. & Ramanathan, S. Direct in situ observation of structural transition driven actuation in VO₂ utilizing electron transparent cantilevers. *Nanoscale.* **5**, 7484–7492 (2013).
7. Becker, M. F. et al. Femtosecond switching of the solid state phase transition in the smart-system material VO₂. in 1994 North American Conference on Smart Structures and Materials 400–408 (International Society for Optics and Photonics, 1994).
8. Moatti, A., Bayati, R., Singamaneni, S. R. & Narayan, J. Thin film bi-epitaxy and transition characteristics of TiO₂/TiN buffered VO₂ on Si(100) substrates. *MRS Adv.* **1** (37), 2635-2640 (2016).
9. Morin, F. J. Oxides which show a metal-to-insulator transition at the Neel temperature. *Phys. Rev. Lett.* **3**, 34 (1959).

10. Soltani, M., Chaker, M., Haddad, E. & Kruzelesky, R. V. Thermo-chromic vanadium dioxide smart coatings grown on Kapton substrates by reactive pulsed laser deposition. *J. Vac. Sci. Technol. Int. J. Devoted to Vacuum, Surfaces, Film.* **24**, (2006).
11. Soltani, M., Chaker, M., Haddad, E., Kruzelecky, R. & Margot, J. Micro-optical switch device based on semiconductor-to-metallic phase transition characteristics of W-doped VO₂ smart coatings. *J. Vac. Sci. Technol. A.* **25**, 971–975 (2007).
12. Manning, T. D. et al. Intelligent window coatings: atmospheric pressure chemical vapour deposition of vanadium oxides. *J. Mater. Chem.* **12**, 2936–2939 (2002).
13. Reintsema, C. D., Grossman, E. N. & Koch, J. A. Improved VO₂ microbolometers for infrared imaging: operation on the semiconducting-metallic phase transition with negative electrothermal feedback. in *AeroSense'99* 190–200 (International Society for Optics and Photonics, 1999).
14. Chivian, J. S., Scott, M. W., Case, W. E. & Krasutsky, N. J. An improved scan laser with a VO₂ programmable mirror. *Quantum Electron. IEEE J.* **21**, 383–390 (1985).
15. Kim, H.-T. et al. Mechanism and observation of Mott transition in VO₂-based two-and three-terminal devices. *New J. Phys.* **6**, 52 (2004).
16. Yang, T.-H., Nori, S., Mal, S. & Narayan, J. Control of room-temperature defect-mediated ferromagnetism in VO₂ films. *Acta Mater.* **59**, 6362–6368 (2011).
17. Kim, H.-T. et al. Hole-driven MIT theory, Mott transition in VO₂, MoBRiK device. *Phys. C Supercond.* **460**, 1076–1078 (2007).
18. Marini, C. et al. Optical properties of V_{1-x}Cr_xO₂ compounds under high pressure. *Phys. Rev. B.* **77**, 235111 (2008).

19. Moatti, A., Sachan, R., Gupta, S. & Narayan, J. Vacancy-Driven Robust Metallicity of Structurally Pinned Monoclinic Epitaxial VO₂ Thin Films. *ACS Appl. Mater. Inter.* **11**, 3547–3554 (2019).
20. Mun, B. S. et al. Observation of insulating–insulating monoclinic structural transition in macro-sized VO₂ single crystals. *Phys. status solidi (RRL)-Rapid Res. Lett.* **5**, 107–109 (2011).
21. Moatti, A., Sachan, R., Prater, J. & Narayan, J. Control of Structural and Electrical Transitions of VO₂ Thin Films. *ACS Appl. Mater. Inter.* **9**, (2017).
22. Moatti, Adele, Sachan, Ritesh, Cooper, Valentino, Narayan, J. Electrical Transition in Isostructural VO₂ Thin-Film Heterostructures. *Sci. Rep.* **9**(1), 3009 (2019).
23. Narayan, J. Recent progress in thin film epitaxy across the misfit scale (2011 Acta Gold Medal Paper). *Acta Mater.* **61**, 2703–2724 (2013).
24. Moatti, A., Sachan, R., Kumar, D., Narayan, J. Catalyst-assisted epitaxial growth of ferromagnetic TiO₂/TiN nanowires. *Acta Mater.* **167**, 112-120 (2019).
25. DK Panupong Jaipan, Chandra Nannuri, Nikhil Reddy Mucha, Mayur P. Singh, et.al. Influence of Gold Catalyst on the Growth of Titanium Nitride Nanowires, *Mater. Focus.* **7** (5), 720–725 (2018).
26. Moatti, A., Bayati, R. & Narayan, J. Epitaxial growth of rutile TiO₂ thin films by oxidation of TiN/Si{100} heterostructure. *Acta Mater.* **103**, 502-511 (2016).
27. Neumann, W. Crystallography of boundaries and interfaces. *Acta Physica. Polonica. A.* **89**, 195-207 (1996).
28. Merkle, K. High-resolution electron microscopy of interfaces in fcc materials. *Ultramicroscopy* **37** (1-4), 130-152 (1991).

CHAPTER 7



7. Strain engineering-Removal of structural transition in VO₂ through strain engineering leading to the lattice pinning

7.1. An Optimized Sample Preparation Approach for Atomic Resolution In-situ

Studies of Thin Films (Microscopy Research and Techniques, 81 (2018) 1250–1256)

Abstract

This work provides the details of a simple and reliable method to prepare electron transparent samples with less damage for in-situ studies in scanning/transmission electron microscopy. In this study, we use epitaxial VO₂ thin films grown on c-Al₂O₃ by pulsed laser deposition, which have a monoclinic-rutile transition at ~68 °C. We employ an approach combining conventional mechanical wedge-polishing and Focused Ion beam to prepare the electron transparent samples of epitaxial VO₂ thin films. The samples are first mechanically wedge-polished and ion-milled to be electron transparent. Subsequently, the thin region of VO₂ films are separated from the rest of the polished sample using a focused ion beam and transferred

to the in-situ electron microscopy test stage. As a critical step, carbon nanotubes are used as connectors to the manipulator needle for a soft transfer process. This is done to avoid shattering of the brittle substrate film on the in-situ sample support stage during the transfer process. We finally present the atomically resolved structural transition in VO₂ films using this technique. This approach significantly increases the success rate of preparing high-quality samples for in-situ studies of thin films and reduces the cost and instrumental/user errors associated with other techniques.

7.1.1. Introduction

The in-situ transmission electron microscopy studies of thin-films are of great interest to investigate phase transformation¹⁻⁴, nucleation and growth⁵⁻⁷, dislocations and point defect behavior⁸⁻¹¹, valance changes of ions, and electrical and mechanical properties^{1,11-14}. In this regard, one of the important aspects is to come up with simple yet reliable methods for preparing electron transparent in-situ samples along with preserving the intrinsic microstructure with less damage. In general, there have been numerous methods proposed for making electron transparent samples such as float-off technique¹⁵⁻¹⁷, mechanical polishing¹⁸⁻²⁰, chemical etching, drop-casting, lithographic techniques and Focused Ion Beam (FIB) lift-out etc²¹⁻²³. Among these, FIB lift-out is the most commonly used approach to prepare TEM samples for in-situ studies of oxides and nitrides thin films and is the main focus of the present work^{24,25}. The simultaneous secondary electron imaging and ion-beam milling in a scanning electron microscope (SEM) makes FIB, an ideal technique for fabricating site-specific samples of thin film heterostructures. However, difficulties in achieving sufficiently thin samples for electron transparency, minimizing structural damage caused by energetic ion-beam, avoiding the introduction of new defects to the system and reducing the complexity of the whole process are all problems encountered in using this technique

²⁶. For instance, energetic Ga⁺ ions are typically implanted into the sample which can alter the local chemical structure as well as amorphize the outer layer. The magnitude and rate of these effects will depend on the atomic number of the specific material. A simulation study suggests that a Ga⁺ beam of 25 KeV, 1000 pA can introduce 20nm of an amorphous layer in Si ²⁷. On the other hand, mechanical wedge polishing followed by a minimal ion-milling is more efficient, cost-effective, and less damaging to the sample as opposed to preparing the entire sample by FIB, but has proven to be challenging in utilizing it for in-situ studies of thin film heterostructures.

The majority of in-situ studies, have involved materials such as nanowires, nanotubes, nanoparticles, and crushed bulk material, but not on thin films, where minimum additional sample preparation is required to directly mount them onto commercially available S/TEM in-situ support stages. The sample preparation technique for thin films for in-situ studies is problematic, particularly with respect to preparing the electron transparent sample and transferring it to the support stage, due to the brittle nature of both the sample and the stage. Figure 7.1 shows one of the failed attempts. The TEM test stage (TTS) repeatedly was breaking during sample transfer when directly attached to the FIB needle due to induced strains from uncontrollable small needle movements. In this work, we devised a low-risk and low-damage method to transfer the sample onto the TTS, by combining mechanical wedge polishing and FIB using a soft transfer approach. FIB is used as a cutting tool to separate the thin area of the wedged sample which is transferred to the TTS using carbon nanotubes as an elastic spacer that connects the sample to the needle. This method promotes the soft transfer of the sample to TTS and minimizes the risk of TTS failure. The sample then can be welded to the chip and the nanotubes removed by a final FIB cut. A detailed procedure is explained in the following sections. As a demonstration, this technique has been employed in the in-situ study of metal-insulator structural transition in VO₂ heterostructures. These

undergo metal-insulator transition accompanied by a change in the structure, and in-situ studies are considered essential²⁸. To fully characterize the VO₂ structural transition. To date, there have been a handful of in-situ TEM studies, primarily investigating VO₂ wires²⁹ which do not require complicated preparation. The present approach provides the opportunity to see atomic resolution structural transition from monoclinic to tetragonal in VO₂ thin films as a function of temperature.

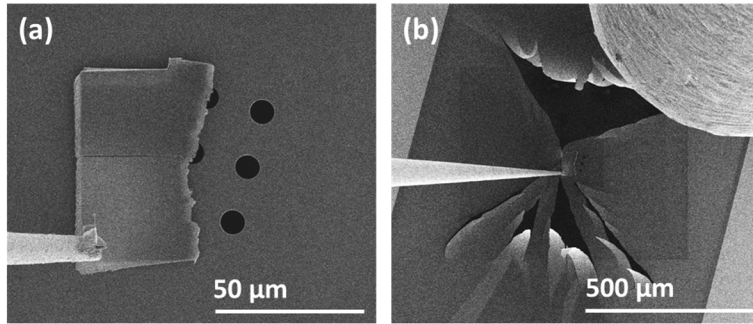


Figure 7.1. The sample is placed on the TTS without nanotubes spacers before (a) and after (b) Pt deposition and shattering, respectively.

7.1.2. Results

7.1.2.1. Sample deposition and wedge polishing procedure

The VO₂/NiO/sapphire single-crystalline thin film (~250 nm) heterostructures were grown using Pulsed Laser Deposition (PLD) technique. A Lambda Physik KrF excimer laser was used to ablate the targets. The energy density and frequency were set at 3.5 J.cm⁻² and 5 Hz, respectively. The temperature during deposition was set at 550°C and oxygen partial pressures were 10⁻⁴ Torr and 1.2×10⁻² Torr for NiO and VO₂, respectively. To make S/TEM samples, first, 2×2 mm² pieces were cut by a diamond saw. The samples were cleaned with acetone and isopropanol ultrasonically for 10 min each. Then, a sandwich was made using M-bond to attach two pieces of the sample with the film side facing each other as shown in Figure 7.2. Following curing for 12 hours at room temperature, the samples were attached to the polishing fixture using crystal bond wax.

We polished one side down to 300 μm (using 0.1 μm diamond paper as the finest paper) using a mechanical polisher (Allied Multiprep) and then repeated the same process by flipping the sample and polishing the other side down to 30 μm . Table 7.1 provides details of the polishing depth for each paper size. Samples were tilted at 2.5° on a diamond paper of 1 μm and polished until interference fringes started to appear. The TEM sample grid was attached to the sample while still glued by the wax to the polishing fixture and cured overnight. The sample was then removed by dissolving the wax in the acetone. The ion milling process was done at a constant angle with the recipe provided in table 7.2. The milling time at low KV was increased to minimize the defects (ion damage) produced by this process. The optical images before and after milling are shown in Figure 7.3a and b, respectively, and the schematic of the wedge polished sample is shown in the inset of Figure 7.3b.

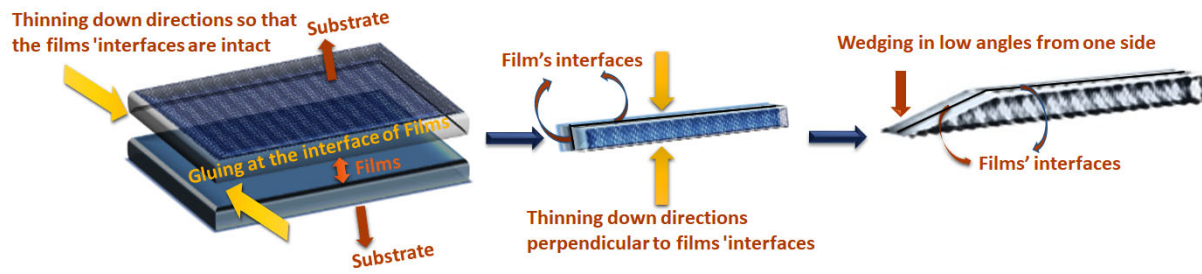


Figure 7.2. Schematic illustration of making a sandwich of two samples with thin films facing each other.

Table 7.1. Wedge polishing recipe with paper grade, depth, and the speed

Step	Paper grade (μm)	Depth(μm)	Speed (rpm)
1	30	-	100
2	15	80	100
3	9	50	100
4	6	30	100
5	3	20	75
6	1	10/wedge polish	30
7	0.1	3/wedge polish	35

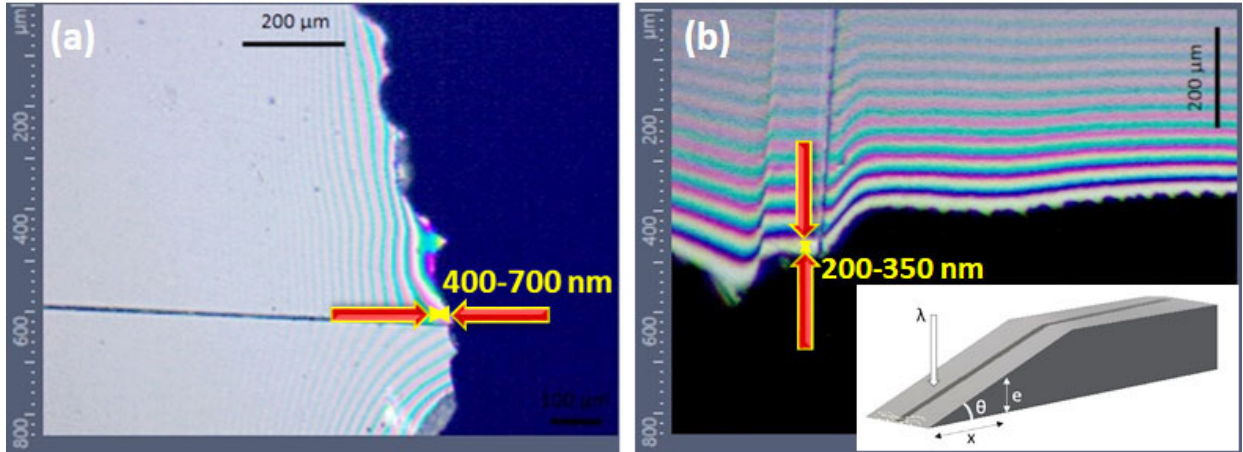


Figure 7.3. The optical images before (a) and after (b) ion milling with the schematic wedge polished sample at the inset.

Table 7.2. Ion milling condition with the angle, energy, and time required

Step	Left Gun		Right Gun		Time (min)
	Angle (°)	Energy (KV)	Angle (°)	Energy (KV)	
1	-7	3	7	3	5
2	-7	2.5	7	2.5	10
3	-7	2	7	2	10
4	-7	1.5	7	1.5	20
5	-7	1	7	1	30
6	-7	0.5	7	0.5	40
7	-7	0.3	7	0.3	40

7.1.2.2. Wedge Fringes

Using the scale bar and a number of fringes, it is possible to estimate the thickness following:

$$2e = 2x \tan\theta = 2x\theta = m\lambda \text{ for dark fringes} \quad \text{Equation (7.1)}$$

$$2e = 2x\theta = (2m + 1)\lambda/2 \text{ for bright fringes} \quad \text{Equation (7.2)}$$

where e is the thickness, x is the distance from the edge, θ is the wedged angle, m is the number of fringes, and λ is the wavelength (Figure 7.3b, inset). Since θ is small, $\tan(\theta) = \theta$ in radians. The

λ varies between 0.4 and 0.7 μm in our case since we did not use the monochromatic optical microscope.

The thickness at x equals the first fringe distance from the edge before and after milling is shown in the inset of Figure 7.3b.

7.1.2.3. FIB lift-out of thin lamella and carbon fiber attachment

After thinning, the sample was transferred to FIB/SEM. At the same time, the TTS also was mounted inside the chamber. The thinned region of the sample was cut as shown in Figure 7.4a which is referred to as “lamella”. We used a 30kV-3nA beam to reduce the amount of damage imparted to the sample; the cutting depth was set to 2 μm . The tilt angle was kept at 52°, normal to the FIB ion beam, throughout the cutting process.

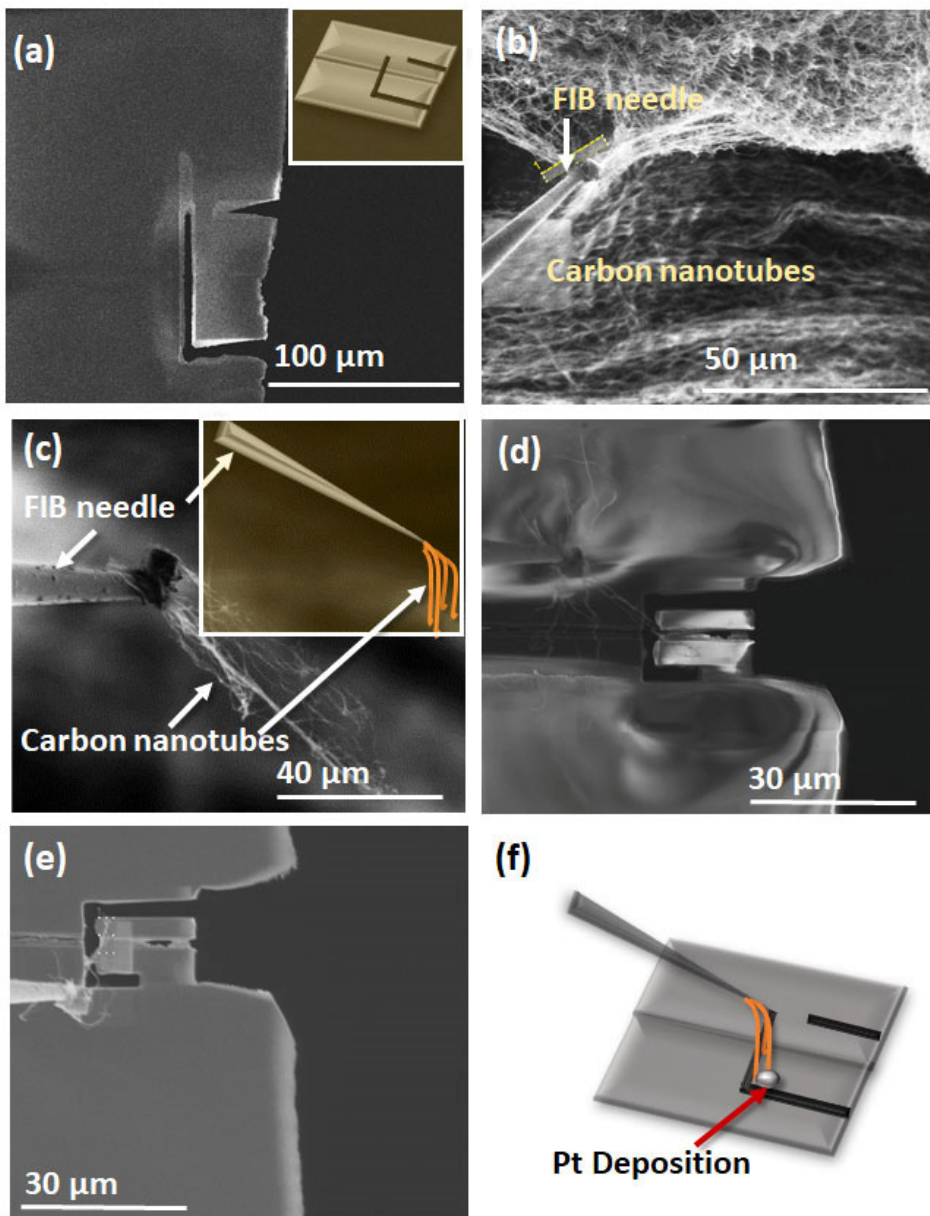


Figure 7.4. (a) Cutting the lamella off the sample with schematic image at the inset, (b) pulling some carbon nanotubes from a bunch of them, (c) attaching carbon nanotube to the needle, (e) attaching carbon nanotube to the lamella, and (f) schematic image of attaching carbon nanotubes to the lamella using Pt deposition.

Once FIB cutting of the sample was nearly completed, carbon nanotubes were attached first to the FIB needle (Figure 7.4 b, and c) and then to the sample (as shown in Figure 7.4 e, and f). Pt deposition was used to attach the nanotubes to the needle at 30kV, 0.3nA and the deposition depth was 1.5 μ m. The needle with attached nanotube was then moved closer to the sample until nanotubes start touching the sample. We then deposited Pt to attach the needle to the sample

through nanotubes with the same beam energy as mentioned before. The final cut was then made to fully free the lamella of the sample.

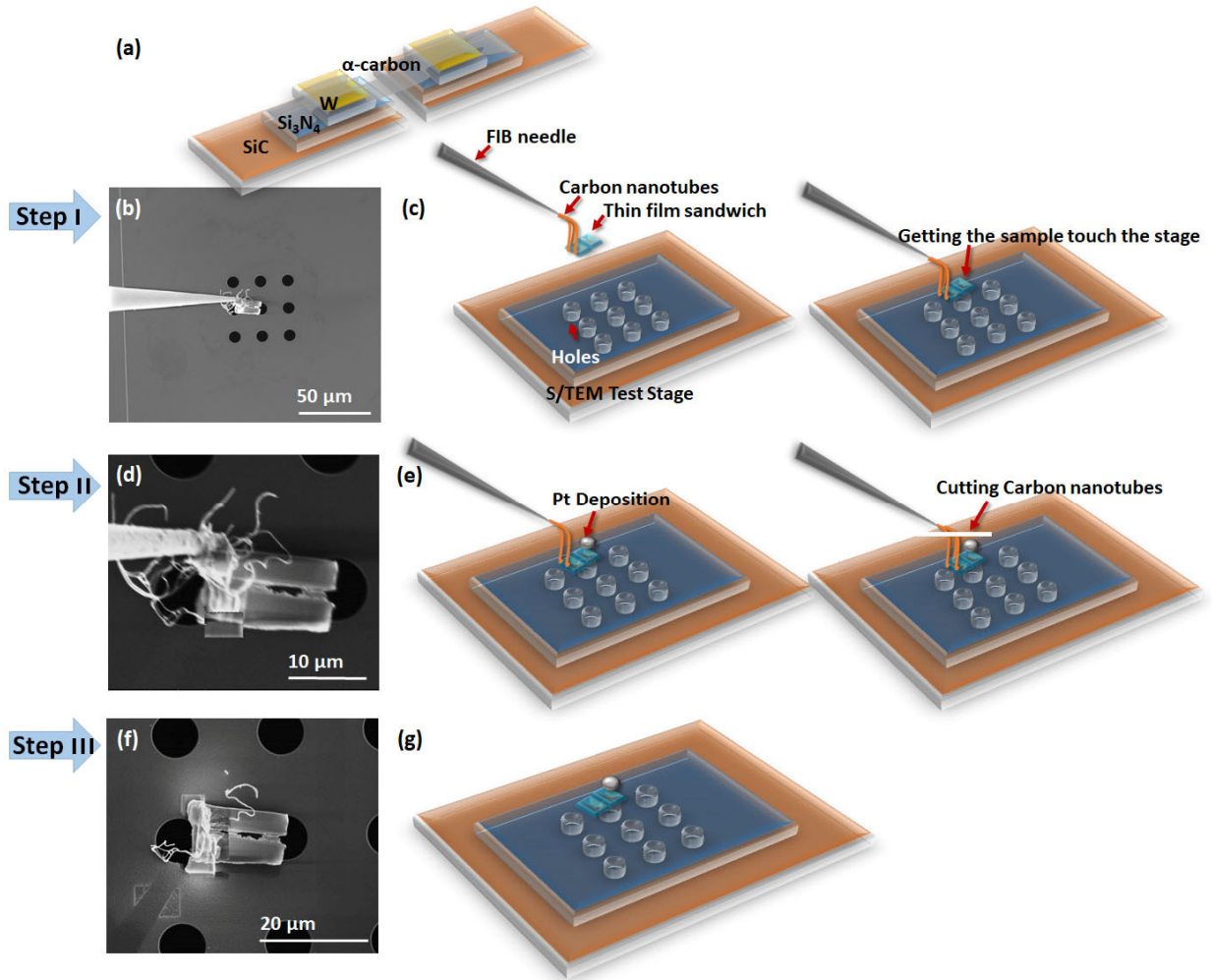


Figure 7.5. (a) The schematic depiction of the Protochips TTSs in which electric field is applied through W and sample is heated by SiC membrane, (b, c) the actual and schematic illustration of the needle carrying the sample by nanotubes to be placed on the TTS, (d, e), depiction of the sample being secured with Pt deposition on the TTS before cutting nanotubes by actual and schematic images, and (f, g) the final sample on the TTS actual and schematic illustrations.

7.1.2.4. Soft transfer of the sample to the S/TEM test stage

In the in-situ TEM study, we used a MEMS-based Protochips electrical chip. As presented in Figure 7.5a, these have a thin brittle Si₃N₄ support membrane-embedded electrical leads, and SiC heaters which enable nanoscale heating and biasing of samples. The lamella was now mounted

onto this stage (Figure 7.5 b, and c; step I). When the carbon nanotubes were not used, we routinely failed in this transfer, as shown in Figure 7.1. As the needle approached the sample, the window invariably shattered because of the uncontrollable needle movement. Using nanotubes as a bridge between the sample and the needle provided the flexibility and ample elasticity to mount the sample on the TTS without fracturing. Using the schematics and images acquired during the transfer process, the whole process of the soft transfer of thin sample on TTS is shown in Figure 7.5. After securing the sample with Pt deposition on the TTS (Figure 7.5d and e; step II), the nanotubes were cut using 5nA beam and the needle was withdrawn (Figure 7.5f and g; step III).

Figure 7.6 illustrates the results obtained in the in-situ STEM investigations on the VO₂ films as a measure of the success of the proposed sample preparation approach. Figure 7.6a provides a high angle annular dark field (HAADF) image of a continuous VO₂ film (~250 nm) epitaxially deposited on the c-Al₂O₃ substrate with a NiO buffer layer. Figure 7.6b shows the atomic resolution HAADF image of the VO₂ thin film, oriented in VO₂ [100] zone axis. The figure shows a high equality epitaxial VO₂ grown on NiO film. An intermixed layer can be seen between VO₂ and NiO films, which is formed due to the higher deposition temperature in PLD. The inset image shows an atomic model of VO₂ and NiO along the respective zone axis. Figure 7.6c and d demonstrates the high-quality atomic resolution HAADF images of VO₂ films at 20 °C (room temperature) and 150 °C, respectively. We used the TTS to heat up the sample and see the changes in the structure and EELS data during the VO₂ metal-insulator transition. The VO₂ structure transforms from monoclinic (room temperature phase) to tetragonal (high-temperature phase) can be observed based on the measured atomic distances. The atomic models of these phases are presented as an inset in the respective images of monoclinic (Figure 7.6c) and tetragonal (Figure 6d) HAADF images. The formation of tetragonal phase has been explained by crystal field theory;

the relative energies and stabilities of the $d_{z^2-y^2}$ and d_{xy} , d_{zx} orbitals depends upon the c/a ratio which defines the VO_2 metal-insulator transition temperature. However, the formation of the insulating phase and the transition mechanism can be explained by either crystal structure changes or antiferromagnetic super-lattice formation. Understanding which mechanism is behind the transition helps to improve the VO_2 -based devices and to control the electrical and optical properties. This experiment reveals important information provided by atomic resolution images and EELS analysis to study phase transformation within the VO_2 structure³⁰. In addition to this study, this technique is suggested to be used for various thermal, electrical and optical in-situ studies of thin films, where a high quality spatial and spectral information can be obtained.

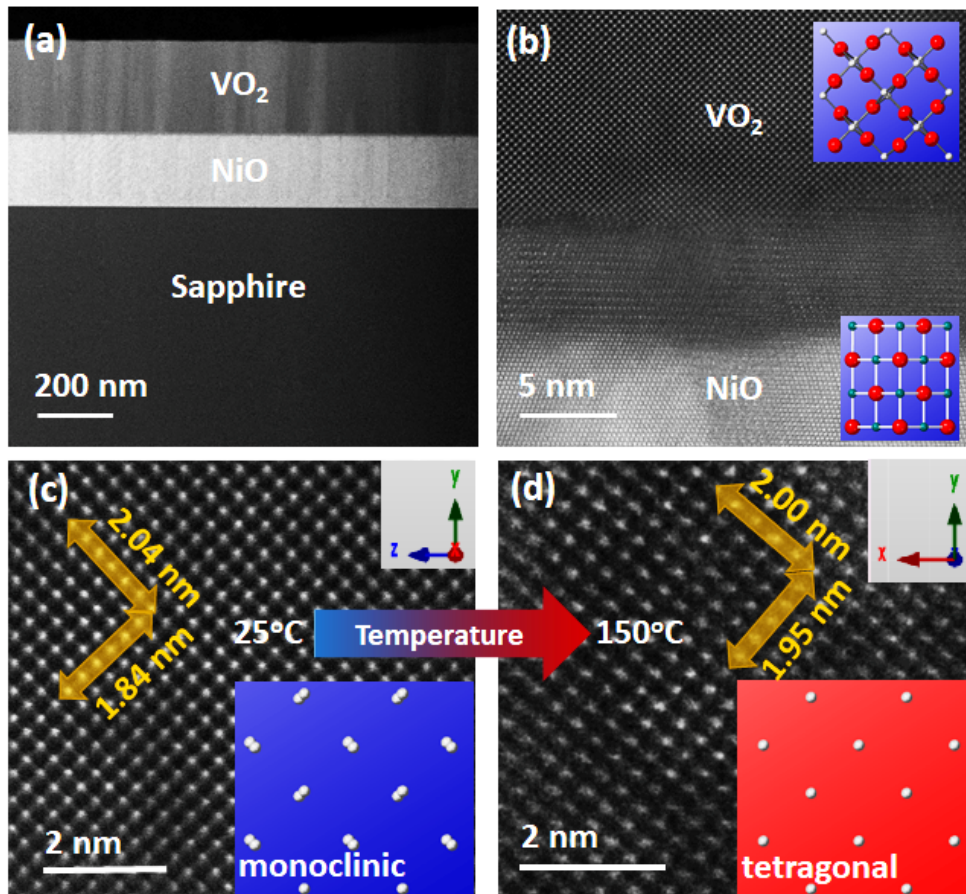


Figure 7.6. The low (a) and high (b) magnification STEM micrographs of the $\text{VO}_2/\text{NiO}/\text{sapphire}$ thin film heterostructures, respectively. The atomic resolution micrographs of VO_2 structure on the heating chip (c) before, and (d) after heating.

7.1.3. Conclusions

We successfully demonstrated a sample preparation method for atomic resolution in-situ studies of thin film heterostructures, by combining mechanical wedge polishing and FIB lift-out approaches. We developed a soft-transfer method for transferring electron transparent thin film samples to the TTS by employing carbon nanotubes as an elastic connect. This eliminated the instrumental and user error introduced during the sample transfer on TTS window and avoids the TTS substrate failure. Using this simple method, we demonstrate the atomic resolution in-situ observations on temperature-dependent structural transition in VO₂ from monoclinic (room temperature) to tetragonal (high temperature). We propose this technique to be highly effective for obtaining a high-quality thin area with low damage for accurate in-situ electron microscopy, which is useful for in-situ thermal, electrical, magnetic, and mechanical studies.

7.2. Electrical Transition in Isostructural VO₂ Thin-Film Heterostructures (*Scientific Reports*, 9(1) (2019) 3009)

Abstract

Control over the concurrent occurrence of structural (monoclinic to tetragonal) and electrical (insulator to the conductor) transitions presents a formidable challenge for VO₂-based thin film devices. Speed, lifetime, and reliability of these devices can be significantly improved by utilizing solely electrical transition while eliminating structural transition. We design a novel strain-stabilized isostructural VO₂ epitaxial thin-film system where the electrical transition occurs without any observable structural transition. The thin-film heterostructures with a completely relaxed NiO buffer layer have been synthesized allowing complete control over strains in VO₂ films. The strain trapping in VO₂ thin films occurs below a critical thickness by arresting the formation of misfit dislocations. We discover the structural pinning of the monoclinic phase in (10±1 nm) epitaxial VO₂ films due to bandgap changes throughout the whole temperature regime as the insulator-to-metal transition occurs. Using density functional theory, we calculate that the strain in the monoclinic structure reduces the difference between long and short V-V bond-lengths (Δ_{V-V}) in monoclinic structures which leads to a systematic decrease in the electronic bandgap of VO₂. This decrease in bandgap is additionally attributed to a ferromagnetic ordering in the monoclinic phase to facilitate a Mott insulator without going through the structural transition.

7.2.1. Introduction

The metal-insulator transition in strongly correlated materials such as vanadium dioxide (VO₂) is usually coupled with the symmetry-lowering structural transition, which is tetragonal rutile P 4₂/mm to monoclinic P 2₁/c. The fundamental understanding and control over electrical and structural transitions in VO₂, which occur often simultaneously, are of immense scientific

importance with profound impact on technological applications ranging from smart switching to sensing devices. Over the years, numerous efforts have been made in this direction, primarily focusing on the manipulation of these transitions via defect and interface engineering³¹⁻³⁵. However, the switching speed and endurance of such devices are often limited by the complexities that emerge from the kinetically slower occurrence of structural transitions (10 picoseconds) as compared to the electrical transition (0.1 picoseconds)³⁶⁻³⁸. This leads to the decoupling between these coexisting transitions in the presence of strain, dopants, and defects in the thermal spectrum and deleteriously affects the performance of such systems^{28,32,34,38}. The coexistence of electrical and structural transitions presents practical challenges in fabricating electronically-correlated VO₂ based solid-state devices³³. In this respect, the development of materials displaying an isolated electrical transition without accompanying structural transition provides an ideal solution. This can be achieved by strain management in VO₂ thin films³⁹⁻⁴². It has been seen that the primary mechanisms of metal-insulator transitions are based on electron-electron interactions (Mott transition) and electron-lattice interaction (Peierls transition). The ratio of which can be effectively steered through strain-induced tuning of *c/a* lattice ratio in VO₂ thin films^{31,43-47}. This is a result of an interplay between these competing mechanisms of electron-electron interaction and electron-phonon interaction, leading to a tunable electrical transition^{31,41,44,48}. Previously, several researchers including our group have shown that it is possible to separate structural and electrical transitions^{28,39,49-52}. However, this raises the question of whether it is possible to totally prevent the occurrence of the structural transition, which had been predicted previously by density functional theory (DFT) calculation suggesting a thermally stable monoclinic metallic phase of VO₂⁵³. The insulating state in monoclinic VO₂ results from electron-electron correlations and electron-phonon interactions. These correlations can be manipulated by charge, spin, orbital, and

lattice degrees of freedom. This means the ratio of the Mott (electron-electron correlations) and Peierls (electron-phonon interactions) transitions can change based on these factors. Thus, if one of these factors can be pinned forcibly in VO₂, the correlation is modified accordingly and an unusual behavior might be realized. Recently, some efforts have been devoted to the suppression of the temperature-dependent phase transition in VO₂^{39,43}.

In our work, we have designed a unique non-equilibrium isostructural monoclinic (no temperature dependency) VO₂ phase on a practical substrate, which demonstrates an uninterrupted insulator-metal transition without undergoing a structural change. This pseudomorphic structure is compared with a fully relaxed VO₂ thin film grown on the same heterostructure above the critical thickness. This unique integration allows us to observe both strain-trapped and fully relaxed VO₂ thin films behavior in the same heterostructure. Basically, we have employed trapped misfit strain to pin the lattice degrees of freedom, while leaving the charge-orbital interactions free to transform at the transition temperature. We expect that the structure pinning in the isostructural VO₂ to affect orbital configuration and bandgap, leading only to the electrical transition with temperature. We have monitored both transitions using in-situ electrical and structural characterization techniques. This phenomenon has a profound impact from an application standpoint since the volume changes of ~0.32% across the structural transition in conventional VO₂ films can cause mechanical instability, microcracking, and deterioration in electrical and optical properties⁵⁴. In addition, the switching speed can also be enhanced since the kinetically slower occurrence of structural transitions (10 picoseconds) as compared to the electrical transition (0.1 picoseconds) has been eliminated. The demonstration of structurally-stabilized VO₂ thin films in the study presents a promising route to enhance the lifetime, endurance, and reliability of VO₂-based smart thin film heterostructures devices.

7.2.2. Experimental details

Thin Film Growth: A KrF excimer laser (Lambda Physik) with 248 nm wavelength and a pulse duration of 25 ns was used to ablate high-quality VO₂ and NiO targets^{20,22}. The whole system is connected to a vacuum chamber with a base pressure of 0.5 μTorr and is connected to gas inlet allowing adjustment of oxygen partial pressure. The c-sapphire substrates were cleaned and mounted inside the vacuum chamber. The cleaning procedure includes acetone-vapor cleaning for 10 min and then substrates were ultrasonicated in methanol for 15 min followed by deionized water ultrasonication for 20 min. The substrates were then dried by a high purity nitrogen gun before loading into the vacuum chamber. The NiO films were grown at 700 °C for 3500 pulses under 0.1 mTorr of oxygen pressure. The VO₂ films were grown at 550 °C for 200 and 3500 pulses for thin and thick samples, respectively under 12 mTorr of oxygen pressure. The energy density and frequency were set at 3-3.5 J/cm³ and 5 Hz, respectively. The samples were cooled down under the same oxygen pressure.

In Situ X-ray Diffraction Measurement: The in-situ XRD measurements were carried out on a PANalytical Empyrean diffractometer using Cu-K_α radiation. This technique was used to determine in-situ structural changes during heating and cooling cycles performing in the 25-120°C range. The diffraction data were acquired using a step size of 0.013° 2θ and the count time of 1 S per step.

Scanning Transmission Electron Microscopy: The samples were prepared using a combination of mechanical polishing and FIB lift-out methods using an FEI Helios DualBeam Focused Ion Beam operating at 2-30 KeV. The samples were mounted on an electrical chip to be able to increase the temperature during the experiment. The details about sample preparation have been published elsewhere. The FEI Titan 80-300 probe aberration-corrected scanning transmission

electron microscope (STEM) operated at 200 KV, was employed to collect HAADF images. The electron energy loss spectra (EELS) were also collected across the interfaces operating at 200 KeV with a 28 mrad collection angle, 19.6 mrad convergence angle, and a 2.5 mm EELS entrance aperture. Spectra were acquired using a 0.25 eV ch^{-1} dispersion with a $\sim 35 \text{ pA}$ probe current and 0.07 nm pixel size to perform elemental analysis of V-L_{2,3} (513, 521 eV), O-K₁ (529, 532 eV), and Ni-L_{2,3} (855, 872 eV). A peak fitting routine was performed on V-L and O-K edges using Gaussian profiles for detailed analysis¹⁹.

Electrical Measurement: The electrical transport measurements were collected by physical property measurements system (PPMS) using Van der Pauw method by Quantum Design over the temperature range of 25- 120 °C during heating and cooling cycles. The resistivity data were collected using a step size of $1 \text{ }^\circ\text{S}^{-1}$ at zero magnetic fields.

Magnetic Measurement: The magnetic properties were measured using a vibrating superconducting quantum interference device (SQUID) magnetometer⁵⁵.

Density functional theory calculations: Density functional theory calculations were performed using the QUANTUM ESPRESSO simulation package (v6.2)⁵⁶. In all cases, a Monkhorst-Pack gamma centered $6 \times 6 \times 6$ k -point grid was employed with energy cutoffs of 80 and 800 Ry for the plane waves and charge density, respectively. Exchange and correlations were approximated using the modified Perdew-Burke-Erzenhoff functional designed specifically for solids (PBEsol)⁵⁷. V ($3s^2 3p^6 4s^2 3d^3$) and O ($2s^2 2p^4$) pseudopotentials from the Garrity-Bennet-Rabe-Vanderbilt (GBRV) high-throughput pseudopotential repository were used⁵⁸.

7.2.3. Results and discussion

To trap the strain uniformly in the VO₂ thin films, we synthesized epitaxial films below the critical thickness where strain energy is insufficient to trigger the nucleation of misfit dislocations. The dislocation formation occurs as the thickness reaches ~15 nm³⁹. The critical thickness calculation has been provided in Appendices. NiO is used as the buffer layer because the VO₂ film on top of it can be almost fully relaxed above the critical thickness through domain matching epitaxy (DME) paradigm to achieve near bulk behavior^{21,59,60}. This sample is used as a control sample. The VO₂/NiO/c-sapphire heterostructures were deposited by pulsed laser deposition (PLD) technique using a 200 nm NiO layer as a buffer. The high angle annular dark field (HAADF) images in Figure 7.7 show the thick and thin VO₂ film heterostructures with VO₂ film thicknesses of 250±1 nm (Figure 7.7a) and 10±1 nm (Figure 7.7d), respectively. The atomic resolution images of the films are also presented in Figure 7.7b and 1e. There is a 10 nm layer of mixed NiO-VO₂ at the interface. The Fourier transform of VO₂ layers and the atomic models of the zone axis belong to HAADF images are also provided in Figure 7.7c and f for thick and thin films, respectively. Although both films were confirmed to be monoclinic from this Figure and more complementary information presented in Appendices Figure S7.1 and Figure S7.2, two different crystallographic alignments in thin and thick VO₂ samples were recognized. In the thick VO₂ film, the planes alignments are NiO(110)∥ monoclinicVO₂(001)∥tetragonalVO₂(001) and NiO($\bar{2}11$)∥ monoclinic VO₂(20 $\bar{1}$)∥ tetragonal VO₂(100) as in-planes and NiO(111)∥ monoclinic VO₂(010) as out-of-planes. While in thin VO₂ films we have NiO($\bar{2}11$)∥monoclinic-VO₂(10 $\bar{2}$) and NiO(110)∥monoclinicVO₂(010) as in-planes and NiO(111)∥ monoclinic VO₂(100) as out-of-plane alignments. The details of plane alignments and DME are presented in Appendices Table S7.1²⁸. The HAADF image in Appendices Figure S7.3a shows the full relaxation of misfit strains within

the thick films by dislocation formation every 10/11 planes. In the case of thin samples, no dislocation formation was observed in the high-magnification HAADF image (Appendices Figure S3b). This shows that the strain is trapped without any relaxation by dislocations.

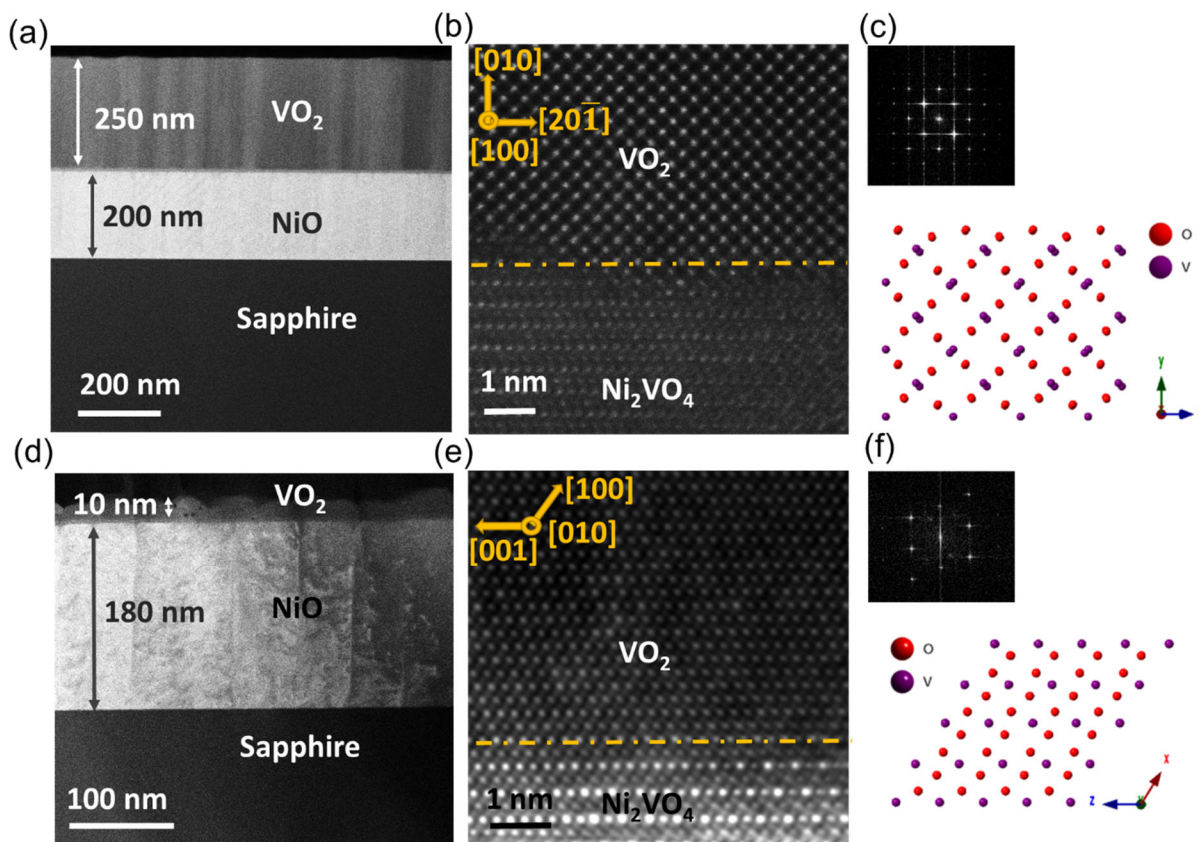


Figure 7.7. (a) The low magnification cross-sectional HAADF image of VO₂/NiO/(0001)sapphire heterostructures of 250 nm (thick) VO₂, (b) the atomic resolution HAADF image of NiO/VO₂ the interface of thick VO₂ films, (c) the Fourier transform of the VO₂ thick films and the corresponding atomic model belong to the zone axis of [100] monoclinic phase (d) The low magnification HAADF micrograph of thin VO₂ films, (e) the atomic resolution HAADF image of NiO/VO₂ the interface of thin VO₂ films, (f) the Fourier transform of the VO₂ thin films and the corresponding atomic model belong to the zone axis of [010] monoclinic phase.

The monoclinic nature of both thin and thick films was verified using XRD patterns and Raman spectroscopy, as shown in Appendices Figure S7.4 and Figure S7.5, respectively. The films were heated up and cooled down to monitor the structural changes across the transition, using the in-situ XRD diffraction and HAADF imaging⁶¹. Temperature-dependent XRD measurements presented in Figure 7.8a show that the VO₂ thick films undergo a sharp structural transition from

(020) tetragonal phase to (020) monoclinic phase during the transition. The 2θ position and the intensity of the (020) out-of-plane are different in tetragonal and monoclinic crystal structures due to the different d-spacing and structure factors. This leads to a clear shift in the in-situ XRD patterns across the monoclinic to tetragonal transition in the thick film of VO₂. On the other hand, there is no sharp structural transformation observed in the only out-of-plane peak (200) belonging to thin VO₂ films in Figure 7.8b, but thermal expansion/contraction was observed during the heating/cooling cycles. From the XRD out-of-plane d-spacing measurements, the thick film, at room temperature, contains only $0.013\pm 0.001\%$ out-of-plane strain which is attributed to thermal strain during the cooling down cycle. However, from the 2θ position of (200) planes of the thin VO₂ sample at room temperature, there is $8.624\pm 0.001\%$ out-of-plane strain compared to bulk VO₂ structure which contains misfit and thermal strains.

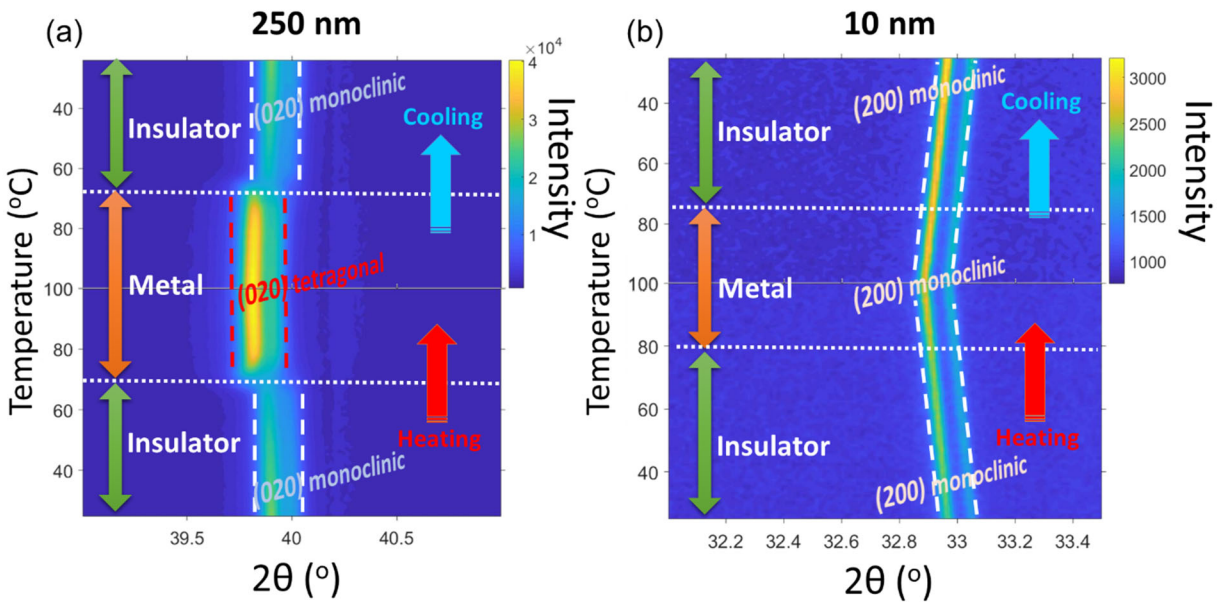


Figure 7.8. In-situ XRD measurements as a function of temperature during heating and cooling cycles of (a) thick sample, and (b) thin sample of VO₂.

Figure 7.9 illustrates electrical and structural changes as a function of temperature for thin and thick samples. The structural change has been defined as an abrupt shift in the d-spacing which is extracted from in-situ XRD patterns. As is seen from temperature-dependent electrical transport measurements in Figure 7.9a and b, both samples undergo a metal-to-insulator transition. The exact value of the metal-to-insulator transition temperatures (T_{MIT}) is derived from Figure 7.9c and d, the derivative of electrical resistivity versus temperature, for thick and thin samples, respectively. The T_{MIT} for the thick sample is almost identical to what has been reported for bulk VO_2 (≈ 68 °C) however, it is increased by 10 degrees (≈ 78 °C), for the thin sample due to residual in-plane tensile strain along the c-axis⁴³. From $1/d$ vs temperature plots in Figure 7.9e and f, in the thick sample, the structural transition is very sharp with an abrupt drop at the transition temperature. However, in the case of the thin sample, there is no abrupt change in $1/d$ and the gradual thermal expansion and contraction during heating and cooling cycles are indicating no structural transition. In the inset of Figure 7.9e, HAADF images at low and high temperatures of thick samples are depicted. The atomic distances after image calibration match with [100] zone axis of the monoclinic (low temperature) and [001] zone axis of the tetragonal (high temperature) structures for the thick sample. The HAADF image of the thin sample (the inset of Figure 7.9f) did not show any change for high and low temperatures and belong to [010] zone axis of the monoclinic structure.

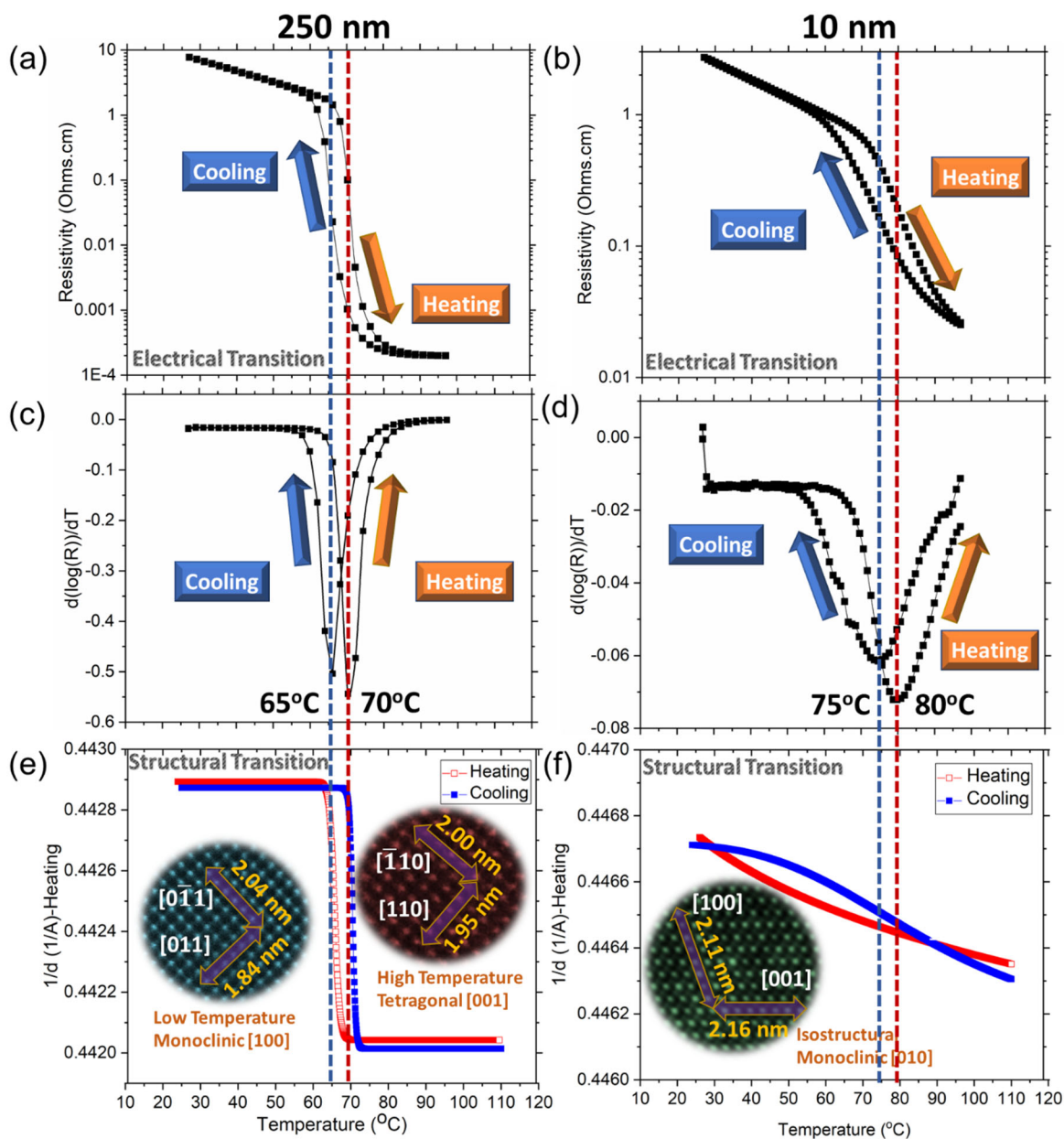


Figure 7.9. The electrical resistivity as a function of temperature for a) thick, and b) thin samples. The derivative of electrical resistivity versus temperature of c) thick, and d) thin sample. The out-of-plane d-spacing (obtained from in-situ XRD measurements) measured as a function of the temperature of e) thin, and f) thick samples. In the inset of the image (e), the low and high-temperature HAADF images are provided in the case of the thick sample and in the inset of the image (f), the isostructural HAADF image of the thin sample is presented. The scale bars in HAADF images are 1 nm.

We carried out in-situ EELS spectroscopy measurements at V-L₃₂ and O-K edges in both thin and thick VO₂ films at ambient (20 °C) and elevated (150 °C) temperatures. We first discuss the shifts/changes in absorption edges (particularly V (L₃, L₂) and O-K pre-peak) in the metallic

and insulator states of both the samples and subsequently compare the results between thin and thick film samples. The intensity axes are all normalized for the comparison. The EEL spectra in Figure 7.10a, c, e, and g show the peaks at ~ 513 eV and ~ 521 eV, corresponding to V-L₃ and V-L₂ edges, respectively, which are induced by the excitation of $2p_{3/2}$ and $2p_{1/2}$ core electrons to unoccupied d-orbitals near the Fermi level (from $2p^63d^1$ to final states of form $2p^53d^2$). While, Figure 7.10b, d, f and h exhibit O-K edge, constituting of a pre-peak and the main peak (~ 532 eV), which arises from the excitation of O 1s (O-K₁) electrons into the 3d band. Various spectra of V-L₃₂ and O-K edges obtained from in-situ EELS under different experimental conditions were fitted with Gaussian peaks and are presented in Appendices Table S7.2. In the case of thick (~ 250 nm) VO₂ film, which represents bulk-like behavior, the intensities of V-L₃ and V-L₂ peaks appear unchanged during the transition from insulating (at low-temperature) to metallic (high-temperature) phase, as shown in Figure 7.10a and c. The changes in these peaks are possibly unresolved due to the insensitivity of core-electron excitations (2p to 3d) in reflecting the narrow bandgap (0.63 eV) closing with temperature. On the contrary, electron excitations from O 1s (O-K) into the p band appears more sensitive to the changes in the electronic structure during the insulating-to-metal transition. The collected spectra consist of O-K pre-peak (~ 529 eV) and σ^* (~ 532 eV) peak, where the pre-peak is indicative of O 1s electron excitation to t_{2g} d-orbitals and includes the information of d_{i^*} orbital and the π^* energy bands. In the experiments, the broadening and the intensity of the pre-peak are carefully monitored, as any variation in pre-peak is reflective of the change in the orbital occupancy, attributing to the insulator to metal transition³¹. See the discussion in Appendices for the orbital occupancy changes across the transition. While comparing O-pre-peak in Figure 7.10b and d, a clear increase in the intensity and FWHM is observed with decreasing the temperature (transiting from metallic to insulator phase at room-temperature). This

broadening in O-pre-peak of insulating phase happens due to the upshifting of the π^* orbital and creating a bandgap (~ 0.63 eV) due to d-orbital splitting at 20 °C (below the T_{MIT})⁶². The upshifting and destabilization of the π^* band level are due to the V displacement perpendicular to the c-axis (antiferroelectric distortion and formation of the V-V pairs) leading to the perturbation in bonding orbitals. The origin of d-orbital splitting is explained to be due to homopolar bonding of V-V and c/a ratio changes (Peierls transition)⁴⁵ or through electron-electron interactions (Mott transition)⁴⁶. At 150 °C, $d_{||}$ and π^* orbitals are highly overlapped and assist in conducting electrons through the overlapped density of states.

The behavior of V-L₃₂ and O-K edges in thin (~ 10 nm) VO₂ films across the transition is observed to be largely similar to the thick (~ 250 nm) films. In the case of the thin film (~ 10 nm) sample, the intensity of V-L₃ and V-L₂ peaks remains unchanged with increasing temperature from 20 °C (Figure 7.10g) to and 150 °C (Figure 7.10e). Furthermore, O-K pre-peak broadens with decreasing temperature, similar to the thick sample. However, the biggest difference is observed in the characteristic absorption edges while comparing the thick and thin samples. First, the differences between V-L₃ and V-L₂ peaks in thick and thin film samples are respectively 6.4 eV and 6.1 eV, which is suggestive of the strained structure of isostructural monoclinic phase in thin VO₂ film²⁸. Second, one finds the O-K pre-peak is estimated to be broader in the thin sample at room temperature. This suggests the overlapping of energy bands in the atomic structure and a shrunk bandgap through a further upshifting of π^* due to structural modification in the thin films. While comparing O-pre-peak of thick and thin VO₂ films at a higher temperature (150 °C), O-K pre-peak in the thin case again appears broader due to upshifting of π^* . This leads to lower conductivity of the thin sample at the metallic stage as compared to the bulk since the conductivity

is coming only from the $d_{||}$ orbital's electron, which is consistent with the resistivity measurements presented in Figure 7.9.

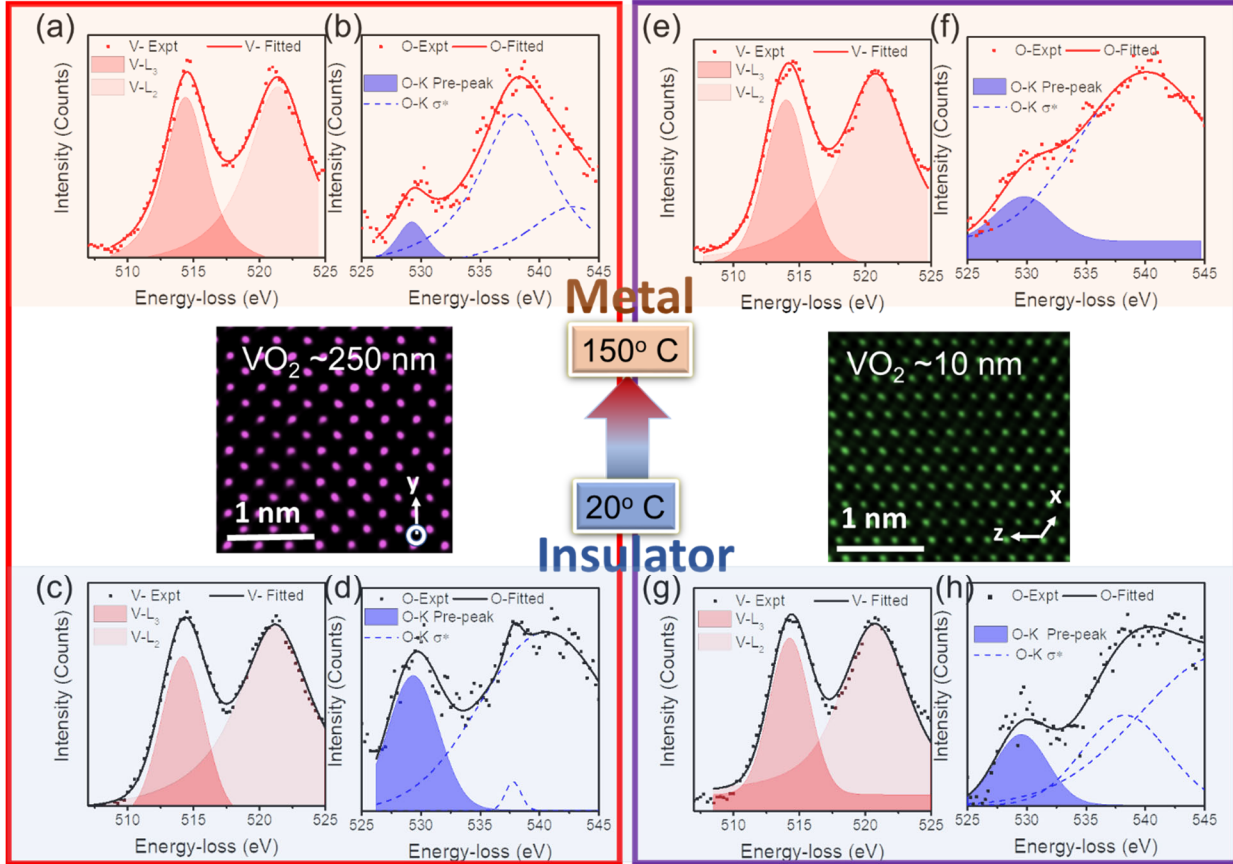


Figure 7.10. In-situ EELS spectra obtained for V-L_{2,3} and O-K₁ edges at high (150 °C) and low (20 °C) temperatures for thick and thin VO₂ films; the peaks at 513 eV and 521 eV correspond to V-L₃ and V-L₂ edges; the peak at 529 eV is indicative of O-K pre-peak constituting π^* and $d_{||}^*$ orbitals. EELS spectra (a, b) at 150 °C and (c, d) at 20 °C are obtained from the thick VO₂ films. Spectra (e, f) at 150 °C and (g, h) at 20 °C represent thin VO₂ films. The atomic resolution HAADF images corresponding to low-temperature structures of thick and thin films with [100] and [010] zone axis, respectively, have shown in the center.

To understand the origin of insulator-to-metal transition difference in thermally stable isostructural monoclinic VO₂. DFT calculations were performed. To account for strong electron correlations we employed the simplified Hubbard $U = 3.10$ eV scheme on the V 3d-states⁶³. This value estimates a bandgap of 0.63 eV for the nonmagnetic monoclinic phase (NM-MI), which is consistent with prior experimental values of 0.6-0.7 eV⁶⁴⁻⁶⁶ and other electronic structure

calculations^{53,66-69}. In all cases, we examined both nonmagnetic (*NM*) and ferromagnetic (*FM*) monoclinic structures with space group *P21/c*. For FM calculations, the magnetization was initiated with (+1) on each V ion with a total magnetization of 5 to allow for self-consistent convergence. Table 7.3 lists the structural parameters for the fully optimized *NM* and *FM* structures obtained with this approach as well as those from previous hybrid calculations⁵³ and corresponding experiments^{70,71}. Similar to Xu et al.⁵³, we find that our fully optimized *NM* monoclinic structure (*NM-MI*) is in good agreement with the experimental monoclinic structure, while our FM monoclinic structure (*FM-M0*) is in good agreement with a recent report of a metallic monoclinic (*mM*) phase. Unlike previous hybrid functional calculations⁵³, we find that the *FM-M0* phase is higher in energy than the *NM-M1* phase by 0.013 eV/f.u. (We note that larger values of *U* function to both increase the *NM-M1* bandgap and increase the energetic differences between the *FM-M0* and *NM-M1* phases while having minimal effects on the structural parameters. e.g. *U* = 4 eV increases the *NM-M1* bandgap to 0.85 eV and favors the *FM-M0* phase by 0.098 meV/f.u.).

Table 7.3. Lattice constants, V-V bond angles and lengths, and dimerization difference Δ_{V-V} for VO₂ groundstate nonmagnetic (*NM-M1*) and ferromagnetic (*FM-M0*) phases. Comparisons to previous experiment and theory are included for validation purposes.

	<i>NM-MI</i> This work	<i>MI</i> Expt. ⁴³	<i>NM-MI</i> Theory ²⁴	<i>FM-M0</i> This work	<i>mM</i> Expt. ⁴⁴	<i>FM-M0</i> Theory ⁴³
<i>a</i> (Å)	5.53	5.75	5.53	5.69	5.69	5.59
<i>b</i> (Å)	4.57	4.54	4.51	4.55	4.59	4.50
<i>c</i> (Å)	5.38	5.38	5.28	5.34	5.29	5.29
β (°)	121.54	122.65	121.93	121.95	122.61	122.05
V-V angle (°)	165	168	166	172		175
V-V bond (Å) short	2.45	2.62	2.44	2.71	2.72	2.69
long	3.13	3.17	3.14	2.99	2.98	2.94
Δ_{V-V} (Å)	0.68	0.55	0.70	0.28	0.26	0.25

To better understand the metal-insulator transition we examined the effects of strain on the NM bandgap. Here, we fixed the in-plane lattice constants for the NM phase to those obtained

from experiment assuming a V-V angle of 122° for both the low temperature (NM-M1_{low}; $a=5.797$ Å, $c=5.427$ Å) and high-temperature phases (NM-M1_{high} $a=5.797$ Å, $c=5.460$ Å). (See Appendices Table S7.3 for further structural details). In both cases, we fully relaxed the out of plane lattice constants; obtaining 4.452 Å and 4.437 Å for NM-M1_{low} and NM-M1_{high}, respectively. However, both structures gave a bandgap of 0.69 eV – not a significant deviation from the optimized NM-M1 value of 0.63 eV.

Table 7.4. Lattice constants, V-V bond angles, and lengths, dimerization difference (Δ_{V-V}), and bandgap (E_{gap}) for VO₂ structures used to explore the effects of dimerization on bandgap.

	<i>NM-MI</i> low	<i>NM-MI</i> high	<i>NM-MI</i> Δ_{V-V} $=0.69\text{Å}$	<i>NM-MI</i> Δ_{V-V} $=0.55\text{Å}$	<i>NM-MI</i> Δ_{V-V} $=0.42\text{Å}$	<i>FM-MI</i> low	
a (Å)	5.797	5.797	5.797	5.797	5.797	5.797	
b (Å)	4.452	4.437	4.429	4.424	4.419	4.483	
c (Å)	5.427	5.460	5.460	5.460	5.460	5.427	
V-V angle ($^\circ$)	166	166	168	170	172	175	
V-V bond (Å)	short	2.58	2.58	2.64	2.70	2.76	2.84
	long	3.39	3.40	3.32	3.25	3.18	3.09
Δ_{V-V} (Å)	0.81	0.82	0.68	0.55	0.42	0.24	
E_{gap} (eV)	0.69	0.69	0.53	0.35	0.19	0.00	

Noting the large difference in V-V short and long bonds (Δ_{V-V}) in the FM and NM structures, we investigated the role that V-V dimerization in tuning E_{gap} . Figure 7.11 depicts the relationship of E_{gap} versus Δ_{V-V} . For this study, we used structures obtained from NM-M1_{high/low} calculations, NM calculations using the atomic coordinates of fully optimized FM structures (with in-plane lattice constants fixed to the low and high temperature phase values) and interpolated intermediate (fixed) structures with $\Delta_{V-V} = 0.42$ Å, 0.55 Å and 0.69 Å (See Table 7.4). Here, we see E_{gap} systematically decreases with decreasing Δ_{V-V} ; and ultimately leading to a metallic transition at $\Delta_{V-V} = 0.24$ Å. Interestingly, this value is close to that of Δ_{V-V} in the fully optimized FM structure. Similar behavior was observed for the MoCl₃ layered compound where a loss in the

Mo-Mo dimerization at high temperature was correlated with an insulator-metal transition⁷². It is also reported that direct bandgap in Ge can be reduced through strain engineering when tetragonal Ge thin films grow below critical thickness on a Si substrate⁷³. The fact that the M1 insulator-metal transition may be correlated with a reduction in Δ_{V-V} similar to the ferromagnetic phase would be consistent with the disappearance of dimerization in the VO₂ rhombohedral phase.

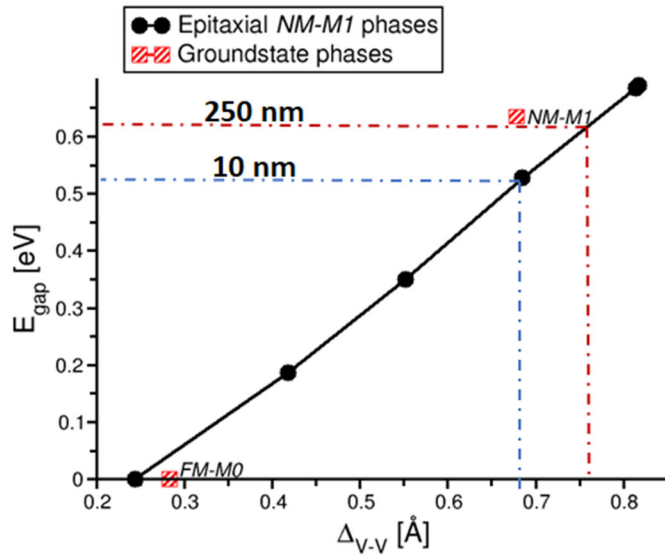


Figure 7.11. Bandgap (E_{gap}) as a function of the difference between short and long bonds (Δ_{V-V}) in VO₂. Black solid circles indicate data obtained from structures fixed to the epitaxially constrained experimental thin film values. Red hashed squares indicate the groundstate phases: NM-M1 (nonmagnetic M1 monoclinic phase) and FM-M0 (ferromagnetic M0 monoclinic phase). For FM phase's bandgaps were obtained from NM calculations of the FM groundstate atomic configurations.

Figure 7.11 shows the approximate bandgap and Δ_{V-V} corresponding to thin and thick VO₂ films, based on resistivity vs temperature measurements. From the resistivity plots, one can deduce the ratio of bandgap values from $\ln \rho$ vs $1/T$ plots (where ρ is conductivity, and T is temperature), to be equal to 1.243 for $E_{g \text{ thick}}/E_{g \text{ thin}}$. This ratio provides the corresponding Δ_{V-V} for thin and thick VO₂ films as shown in Figure 7.11. The decrease in bandgap due to smaller Δ_{V-V} facilitates the insulator to metal transition without going through the structural transition. Since the calculations show that the reduction in bandgap can be promoted through the introduction of ferromagnetic

nature in the monoclinic phase, the temperature-dependent magnetic characterization of the films were performed (see Appendices Figure S7.6), which shows evidence of ferromagnetism and thus long-range ferromagnetic ordering.

It is hypothesized that the insulator-to-metal transition in the isostructural monoclinic VO₂ films is a combination of both electron-electron and phonon-electron interactions, which is tuned by the bandgap modification. In this case, since we have modified the V-V bond length (Δ_{V-V} is smaller) in the thin VO₂ films, the resulting narrowed bandgap facilitates the electron-electron interactions and lead to the insulator-to-metal transition without any structural change with temperature. The presence of Δ_{V-V} perturbs the π^* orbital and makes it narrower due to shorter V-O bonds perpendicular to c-axis, which tends to lift the π^* above the Fermi level. As a result, conductivity is only due to the narrow unoccupied portion of the $d_{||}$ band. Also, the $d_{||}$ orbital is not degenerate due to the monoclinic structure (presence of a small bandgap, between $d_{||}$ and $d^*_{||}$) at a high-temperature. The orbital non-degeneracy can be also inferred from dimerization and the broadening of the O-K π^* for the thin sample compared to thick sample respectively shown in Figure 7.10f and Figure 7.10b. This phenomenon was predicted by Goodenough for the distorted oxygen octahedra system where localized holes have been added to VO₂³⁶.

Based on the temperature-dependent EELS analyses, resistivity measurements, and DFT calculations, a suggestive band structure diagram of both thin and thick VO₂ films at temperatures across the MIT are illustrated in Figure 7.12. At high temperature, the π^* orbital is perturbed and shifted higher energy level in the thin sample (Figure 7.12b) compared to the thick sample (Figure 7.12a). This upshift is due to the non-cooperative displacement of vanadium ions from the center of the octahedral which results in V-V dimerization (with the presence of Δ_{V-V}). At low

temperature (Figure 7.12c and d), the thin sample has less crystal field splitting in both V-L and O-K with smaller bandgap than the thick case.

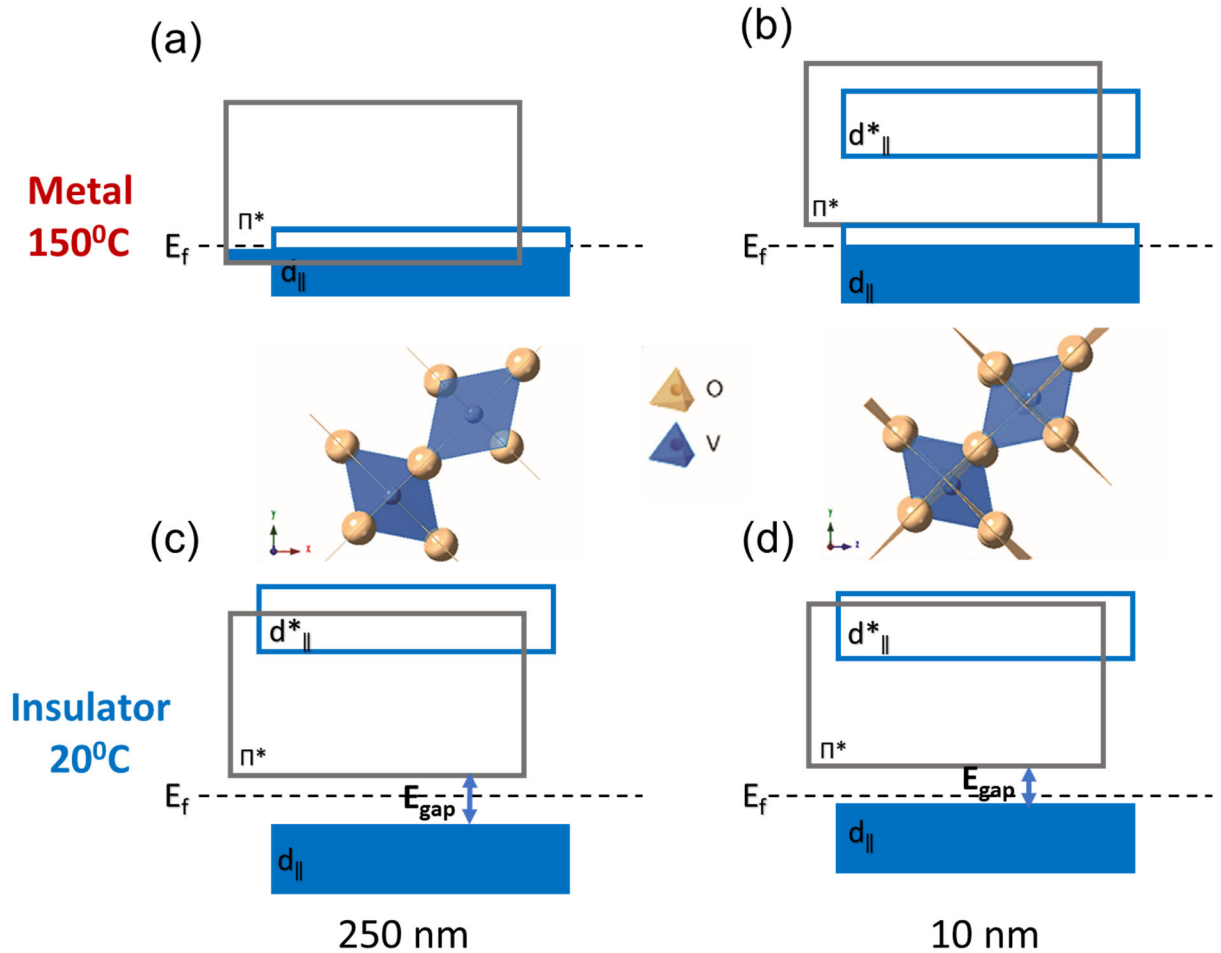


Figure 7.12. Schematic of VO₂ band structure in the metallic state for (a) thick and (b) thin samples, schematic of VO₂ band structure in the insulating state for (c) thick and (d) thin samples. The oxygen octahedron has shown in the center for the high-temperature structures of thick and thin films; the vanadium atom displacement is depicted from the center of the octahedron in the case of thin samples due to strain pinning.

It is shown that electrical and structural transitions in the thick VO₂ film are strongly-correlated through electron-electron interactions between O 2p and V 3d states, which is not the case for the thin strained films. In unstrained VO₂ systems, the lowering of crystal symmetry from tetragonal to monoclinic adds to the lifting of orbital degeneracy, leading to typical bandgap evolution. It is suggested that the electronic structure in the strained monoclinic VO₂ film (10 nm

thick) is strongly modified as compared to the relaxed thick film, resulting in a considerable bandgap narrowing. This is driven by decreasing Δ_{V-V} in the strained ferromagnetic monoclinic VO₂ thin films. This modified structure with lowered bandgap allows the transition to follow Mott physics. At low temperatures below the transition, there are fewer electrons occupying the Fermi level, causing the insulating behavior while simultaneously reducing the overall resistivity of the films. This is also observed experimentally in the present study in the temperature-dependent resistivity measurements. With increasing temperature above the transition temperature, electron concentration rises and closes up the bandgap to form a complete metallic state of monoclinic phase. Overall, we illustrate that the positive impact of all the factors contributing to the formation of the structurally-pinned monoclinic VO₂ film will lead to the technologically improved smart sensing and switching devices. The present process allows wafer-scale integration of VO₂ device layers on sapphire using NiO buffer layer, and it has been extended to silicon wafers utilizing NiO/YSZ/Si(100) heterostructures⁶⁰.

7.2.4. Conclusion

We have shown that by decreasing Δ_{V-V} through misfit strain in epitaxial monoclinic VO₂ thin-film heterostructures, the bandgap decreases such that the structural transition is pinned, while electrical transition occurs. To trap the strain, VO₂ films were grown pseudomorphically below the critical thickness where no strain releasing dislocations are formed for lattice relaxation. It is envisaged that in the strain-trapped thin films at high temperature, the oxygen octahedra are distorted to the point where vanadium ions are not stable in the center of the octahedra and form short and long V-V bonds, which destabilizes the bonding d orbitals. This destabilization affects the bonding and nonbonding orbitals stability and their occupancy which accordingly locks the structural changes over the transition and changes the bandgap and the conductivity of the high-

temperature phase. This study opens up the opportunity to lock other degrees of freedom including spin, orbital, and charges to control critical aspects of transition in VO₂ thin films.

REFERENCES

1. Rozenberg, M. J. et al. Mechanism for bipolar resistive switching in transition-metal oxides. *Phys. Rev. B*. **81**, 115101 (2010).
2. Nian, Y. B., Strozier, J., Wu, N. J., Chen, X. & Ignatiev, A. Evidence for an oxygen diffusion model for the electric pulse induced resistance change effect in transition-metal oxides. *Phys. Rev. Lett.* **98**, 146403 (2007).
3. Kittl, J. A., Prinslow, D. A., Apte, P. P. & Pas, M. F. Kinetics and nucleation model of the C49 to C54 phase transformation in TiSi₂ thin films on deep-sub-micron n type polycrystalline silicon lines. *Appl. Phys. Lett.* **67**, 2308–2310 (1995).
4. Lee, H.-J. & Ramirez, A. G. Crystallization and phase transformations in amorphous NiTi thin films for microelectromechanical systems. *Appl. Phys. Lett.* **85**, 1146–1148 (2004).
5. Boylan, K., Ostrander, D., Erb, U., Palumbo, G. & Aust, K. T. An in-situ tem study of the thermal stability of nanocrystalline NiP. *Scr. Metall. Mater.* **25**, 2711–2716 (1991).
6. Kalb, J., Spaepen, F. & Wuttig, M. Atomic force microscopy measurements of crystal nucleation and growth rates in thin films of amorphous Te alloys. *Appl. Phys. Lett.* **84**, 5240–5242 (2004).
7. Hawley, M., Raistrick, I., Beery, J., Houlton, R. Growth mechanism of sputtered films of YBa₂Cu₃O₇ studied by scanning tunneling microscopy. *Science*. **251** (80), 1587–1589 (1991).
8. Gao, P. et al. In situ TEM studies of oxygen vacancy migration for electrically induced resistance change effect in cerium oxides. *Micron*. **41**, 301–305 (2010).
9. Park, J., Kwon, D.-H., Park, H., Jung, C. U. & Kim, M. Role of oxygen vacancies in resistive switching in Pt/Nb-doped SrTiO₃. *Appl. Phys. Lett.* **105**, 183103 (2014).
10. Liao, Z., Gao, P., Bai, X., Chen, D. & Zhang, J. Evidence for electric-field-driven migration and diffusion of oxygen vacancies in Pr_{0.7}Ca_{0.3}MnO₃. *J. Appl. Phys.* **111**, 114506 (2012).

11. Hugo, R. C. et al. In-situ TEM tensile testing of DC magnetron sputtered and pulsed laser deposited Ni thin films. *Acta Mater.* **51**, 1937–1943 (2003).
12. Sawa, A., Fujii, T., Kawasaki, M. & Tokura, Y. Interface resistance switching at a few nanometer thick perovskite manganite active layers. *Appl. Phys. Lett.* **88**, 232112 (2006).
13. Simões, S., Calinas, R., Vieira, M. T., Vieira, M. F. & Ferreira, P. J. In situ TEM study of grain growth in nanocrystalline copper thin films. *Nanotechnology.* **21**, 145701 (2010).
14. Haque, M. A. & Saif, M. T. A. Application of MEMS force sensors for in situ mechanical characterization of nano-scale thin films in SEM and TEM. *Sensors Actuators A Phys.* **97**, 239–245 (2002).
15. Sachan, R. et al. Ferroplasmons: Intense localized surface plasmons in metal-ferromagnetic nanoparticles. *ACS Nano.* **8**, 9790–9798 (2014).
16. Malasi, A. et al. Two-Dimensionally Ordered Plasmonic and Magnetic Nanostructures on Transferable Electron-Transparent Substrates. *Part. Part. Syst. Charact.* **32**, 970–978 (2015).
17. Sachan, R. et al. Laser-Induced Self-Assembled Nanostructures on Electron-Transparent Substrates. *Part. Part. Syst. Charact.* **32**, 476–482 (2015).
18. Sachan, R. et al. Structure and band gap determination of irradiation-induced amorphous nano-channels in LiNbO₃. *J. Appl. Phys.* **117**, 135902 (2015).
19. Sachan, R. et al. Forging fast ion conducting nanochannels with swift heavy ions: the correlated role of local electronic and atomic structure. *J. Phys. Chem. C.* **121**, 975–981 (2017).
20. Moatti, A. & Narayan, J. High-quality TiN/AlN thin film heterostructures on c-sapphire. *Acta Mater.* **145**, 134-141 (2018).
21. Moatti, A., Bayati, R. & Narayan, J. Epitaxial growth of rutile TiO₂ thin films by oxidation of TiN/Si{100} heterostructure. *Acta Mater.* **103**, 502-511 (2016).

22. Moatti, A., Bayati, R., Singamaneni, S. R. & Narayan, J. Thin film bi-epitaxy and transition characteristics of TiO₂/TiN buffered VO₂ on Si(100) substrates. *MRS Adv.* **1**, 2635-2640 (2016).
23. Moatti, A., Bayati, R., Singamaneni, S. & Narayan, J. Epitaxial integration of TiO₂ with Si(100) through a novel approach of oxidation of TiN/Si(100) epitaxial heterostructure. *MRS Adv.* **1**, 2629-2634 (2016).
24. Giannuzzi, L. A., Drown, J. L., Brown, S. R., Irwin, R. B. & Stevie, F. A. Applications of the FIB lift-out technique for TEM specimen preparation. *Microsc. Res. Tech.* **41**, 285–290 (1998).
25. Giannuzzi, L. A. & Stevie, F. A. A review of focused ion beam milling techniques for TEM specimen preparation. *Micron.* **30**, 197–204 (1999).
26. Mayer, J., Giannuzzi, L. A., Kamino, T. & Michael, J. TEM sample preparation and FIB-induced damage. *MRS Bull.* **32**, 400–407 (2007).
27. Prenitzer, B. I. et al. The correlation between ion beam/material interactions and practical FIB specimen preparation. *Microsc. Microanal.* **9**, 216–236 (2003).
28. Moatti, A., Sachan, R., Prater, J. & Narayan, J. Control of Structural and Electrical Transitions of VO₂ Thin Films. *ACS Appl. Mater. Inter.* **9**, 24298-24307 (2017).
29. Sohn, J. I. et al. Direct observation of the structural component of the metal– insulator phase transition and growth habits of epitaxially grown VO₂ nanowires. *Nano Lett.* **7**, 1570–1574 (2007).
30. Moatti, A., Sachan, R., Prater, J. & Narayan, J. Electrical Transition in Isostructural VO₂ Thin-Film Heterostructures. *Sci. Rep.* **9**, 3009 (2019).
31. Aetukuri, N. B. et al. Control of the metal-insulator transition in vanadium dioxide by modifying orbital occupancy. *Nat. Phys.* **9**, 661 (2013).

32. Théry, V. et al. Role of thermal strain in the metal-insulator and structural phase transition of epitaxial VO₂ films. *Phys. Rev. B.* **93**, 184106 (2016).
33. Mizokawa, T. Metal–insulator transitions: Orbital control. *Nat. Phys.* **9**, 612 (2013).
34. Molaei, R., Bayati, R., Wu, F. & Narayan, J. A microstructural approach toward the effect of thickness on semiconductor-to-metal transition characteristics of VO₂ epilayers. *J. Appl. Phys.* **115**, 164311 (2014).
35. Bayati, R., Molaei, R., Wu, F., Narayan, J. & Yarmolenko, S. Dependence of Semiconductor to Metal Transition of VO₂ (011)/NiO {100}/MgO {100}/TiN {100}/Si {100} Heterostructures on Thin Film Epitaxy and Nature of Strain. *J. Am. Ceram. Soc.* **98**, 1201-1208 (2015).
36. Eames, C. et al. Ionic transport in hybrid lead iodide perovskite solar cells. *Nat. Commun.* **6**, 7497 (2015).
37. Viswanath, B. & Ramanathan, S. Direct in situ observation of structural transition driven actuation in VO₂ utilizing electron transparent cantilevers. *Nanoscale* **5**, 7484–7492 (2013).
38. Tao, Z. et al. Decoupling of Structural and Electronic Phase Transitions in VO₂. *Phys. Rev. Lett.* **109**, 166406 (2012).
39. Yang, M. et al. Suppression of Structural Phase Transition in VO₂ by Epitaxial Strain in Vicinity of Metal-insulator Transition. *Sci. Rep.* **6**, 23119 (2016).
40. Gao, X. et al. Nanoscale self-templating for oxide epitaxy with large symmetry mismatch. *Sci. Rep.* **6**, 38168 (2016).
41. Liao, F. et al. Tuning the metal-insulator transition of vanadium dioxide thin films using a stretchable structure. *J. Alloys Compd.* **705**, 468–474 (2017).

42. Yang, M. et al. Surface-growth-mode-induced strain effects on the metal–insulator transition in epitaxial vanadium dioxide thin films. *RSC Adv.* **5**, 80122–80128 (2015).
43. Quackenbush, N. F. et al. Reducing orbital occupancy in VO₂ suppresses Mott physics while Peierls distortions persist. *Phys. Rev. B.* **96**, 81103 (2017).
44. Quackenbush, N. F. et al. Nature of the metal insulator transition in ultrathin epitaxial vanadium dioxide. *Nano Lett.* **13**, 4857–4861 (2013).
45. Goodenough, J. B. The two components of the crystallographic transition in VO₂. *J. Solid State Chem.* **3**, 490–500 (1971).
46. Zylbersztein, A. & Mott, N. F. Metal-Insulator Transition in Vanadium Dioxide. *Phys. Rev. B* **11**, 4383–4395 (1975).
47. Mott, S. N. F. Metal-insulator transition. **26**, (London ; New York : Taylor & Francis, 1990).
48. Fan, L. L. et al. Strain dynamics of ultrathin VO₂ film grown on TiO₂(001) and the associated phase transition modulation. *Nano Lett.* **14**, 4036–4043 (2014).
49. Breckenfeld, E. et al. Strain effects in epitaxial VO₂ thin films on columnar buffer-layer TiO₂/Al₂O₃ virtual substrates. *ACS Appl. Mater. Inter.* **9**, 1577–1584 (2017).
50. Kim, B.-J. et al. Micrometer x-ray diffraction study of VO₂ films: Separation between metal-insulator transition and structural phase transition. *Phys. Rev. B.* **77**, 235401 (2008).
51. Qazilbash, M. M. et al. Mott transition in VO₂ revealed by infrared spectroscopy and nano-imaging. *Science* **318**, 1750–1753 (2007).
52. Nag, J., Jr, R. F. H., Payzant, E. A. & More, K. L. Non-congruence of thermally driven structural and electronic transitions in VO₂. *J. Appl. Phys.* **112**, 103532 (2012).

53. Xu, S., Shen, X., Hallman, K. A., Jr, R. F. H. & Pantelides, S. T. Unified band-theoretic description of structural, electronic, and magnetic properties of vanadium dioxide phases. *Phys. Rev. B.* **95**, 125105 (2017).
54. Balakrishnan, V., Ko, C. & Ramanathan, S. In situ studies on twinning and cracking proximal to insulator–metal transition in self-supported VO₂/Si₃N₄ membranes. *J. Mater. Res.* **27**, 1476–1481 (2012).
55. Moatti, A., Bayati, R., Singamaneni, S. & Narayan, J. Epitaxial integration of TiO₂ with Si (100) through a novel approach of oxidation of TiN/Si (100) epitaxial heterostructure. *MRS Adv.* **1**, 2629–2634 (2016).
56. Giannozzi, P. et al. Quantum Espresso: a modular and open-source software project for quantum simulations of materials. *J. Phys. Condens. Mater.* **21**, 395502 (2009).
57. Perdew, J. P. et al. Restoring the density-gradient expansion for exchange in solids and surfaces. *Phys. Rev. Lett.* **100**, 136406 (2008).
58. Garrity, K. F., Bennett, J. W., Rabe, K. M. & Vanderbilt, D. Pseudopotentials for high-throughput DFT calculations. *Comput. Mater. Sci.* **81**, 446–452 (2014).
59. Narayan, J. & Larson, B. C. Domain epitaxy: A unified paradigm for thin film growth. *J. Appl. Phys.* **93**, 278–285 (2003).
60. Molaie, R., Bayati, M. R. & Narayan, J. Thin film epitaxy and near bulk semiconductor to metal transition in VO₂/NiO/YSZ/Si (001) heterostructures. *J. Mater. Res.* **27**, 3103–3109 (2012).
61. Moatti, A., Sachan, R., Prater, J. & Narayan, J. An optimized sample preparation approach for atomic resolution in situ studies of thin films. *Microsc. Res. Tech.* **81** (11), 1250–1256 (2018).

62. Nigo, S. et al. Conduction band caused by oxygen vacancies in aluminum oxide for resistance random access memory. *J. Appl. Phys.* **112**, 33711 (2012).
63. Cococcioni, M. & Gironcoli, S. De. Linear response approach to the calculation of the effective interaction parameters in the LDA U method. *Phys. Rev.* **B 71**, 35105 (2005).
64. Cavalleri, A. et al. Band-selective measurements of electron dynamics in VO₂ using femtosecond near-edge X-ray absorption. *Phys. Rev. Lett.* **95**, 67405 (2005).
65. Berglund, C. N. & Guggenheim, H. J. Electronic Properties of VO₂ near the Semiconductor-Metal Transition. *Phys. Rev.* **185**, 1022 (1969).
66. Koethe, T. C. et al. Transfer of Spectral Weight and Symmetry across the Metal-Insulator Transition in VO₂. *Phys. Rev. Lett.* **97**, 116402 (2006).
67. Biermann, S., Poteryaev, A., Lichtenstein, A. I. & Georges, A. Dynamical Singlets and Correlation-Assisted Peierls Transition in VO₂. *Phys. Rev. Lett.* **94**, 26404 (2005).
68. Weber, C. et al. Vanadium dioxide: A Peierls-Mott insulator stable against disorder. *Phys. Rev. Lett.* **108**, 256402 (2012).
69. Gatti, M., Bruneval, F., Olevano, V. & Reining, L. Understanding correlations in vanadium dioxide from first principles. *Phys. Rev. Lett.* **99**, 266402 (2007).
70. Longo, J. M. & P, K. A refinement of structure of VO₂. *Acta Chem. Scand.* **24**, (1970).
71. Yao, T. et al. Understanding the nature of the kinetic process in a VO₂ metal-insulator transition. *Phys. Rev. Lett.* **105**, 226405 (2010).
72. McGuire, M. A. et al. High-temperature magnetostructural transition in van der Waals-layered α -MoCl₃. *Phys. Rev. Mater.* **1**, 64001 (2017).
73. Fang, Y.-Y. et al. Perfectly tetragonal, tensile-strained Ge on Ge_{1-y}Sn_y buffered Si (100). *Appl. Phys. Lett.* **90**, 61915 (2007).

APPENDICES

Appendix A

The critical thickness calculation

The critical thickness (h_c) at which it becomes energetically favorable for a thin film to contain dislocations:

$$h_c = \frac{b(1 - \nu \cos^2 \theta) \sin \theta \cos \phi}{4\pi(1 + \nu)\epsilon_0} \ln(\alpha h_c / b)$$

where b is the magnitude of Burgers vector of the dislocation, ν is the Poisson's ratio, θ is the angle between Burgers vector and dislocation line, ϕ is the angle between the normal of the dislocation plane and film plane, and α is the dislocation core radius factor which varies with strain, ϵ_0 .

The slip systems in the VO₂ monoclinic structure are $1/2[0\bar{1}1](011)$ and $1/2[10\bar{1}](101)$. So Burgers vector calculated to be 1.749 Å and 1.553 Å, respectively.

$$h_c = \frac{0.048b}{\epsilon_0} \ln\left(\alpha \frac{h_c}{b}\right)$$

Thus, for 10nm thick film, the critical thickness calculated to be ~15 nm. The role of tensile strain has been explained to increase the kinetic barrier for dislocation nucleation. Even though thermodynamically the critical thickness is calculated at 15 nm, kinetically the dislocation formation is not happening up to higher values.

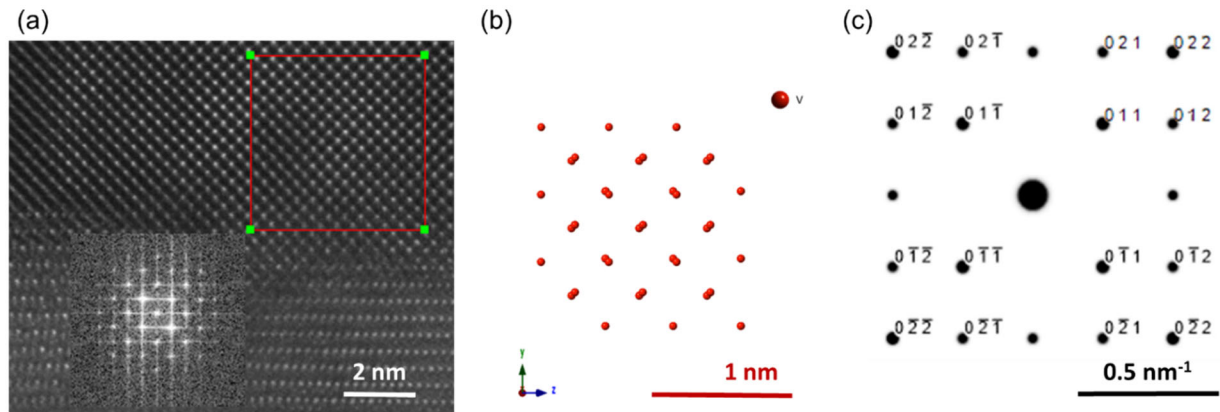


Figure S7.1. a) The HAADF image and its FFT belong to the thick VO₂ film with the zone axis of [100] monoclinic, b) the corresponding atomic alignment, and c) the indexed simulated pattern for the mentioned zone axis in the monoclinic VO₂ structure

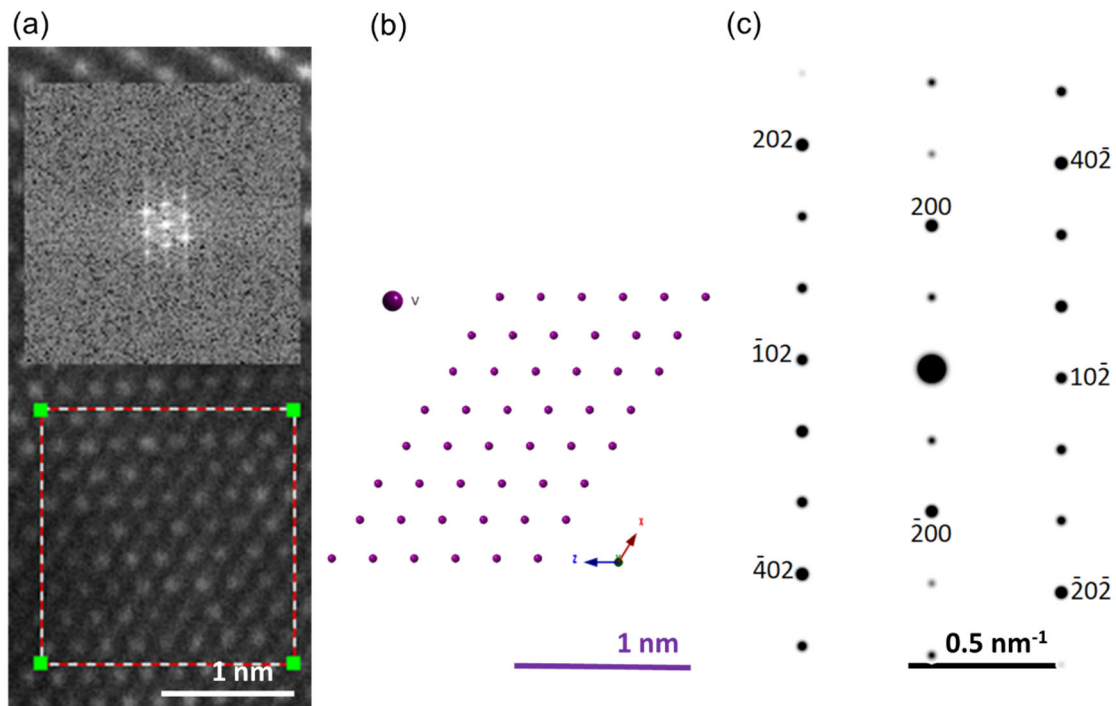


Figure S7.2. a) The HAADF image and its FFT belong to the thin VO₂ film with the zone axis of [010] monoclinic, b) the corresponding atomic alignment, and c) the indexed simulated pattern for the mentioned zone axis in the monoclinic VO₂ structure

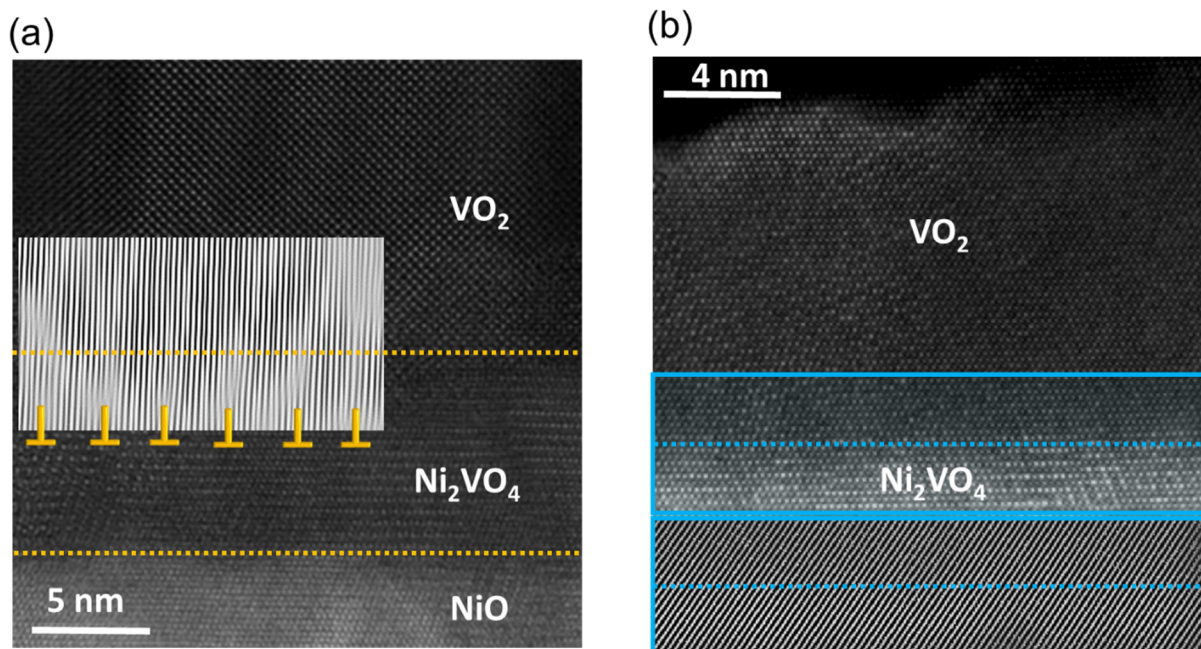


Figure S7.3. a) The HAADF image and inverse FFT at the interface of the thick NiO/VO₂ film, b) the HAADF image and inverse FFT at the interface of the thin NiO/VO₂ film

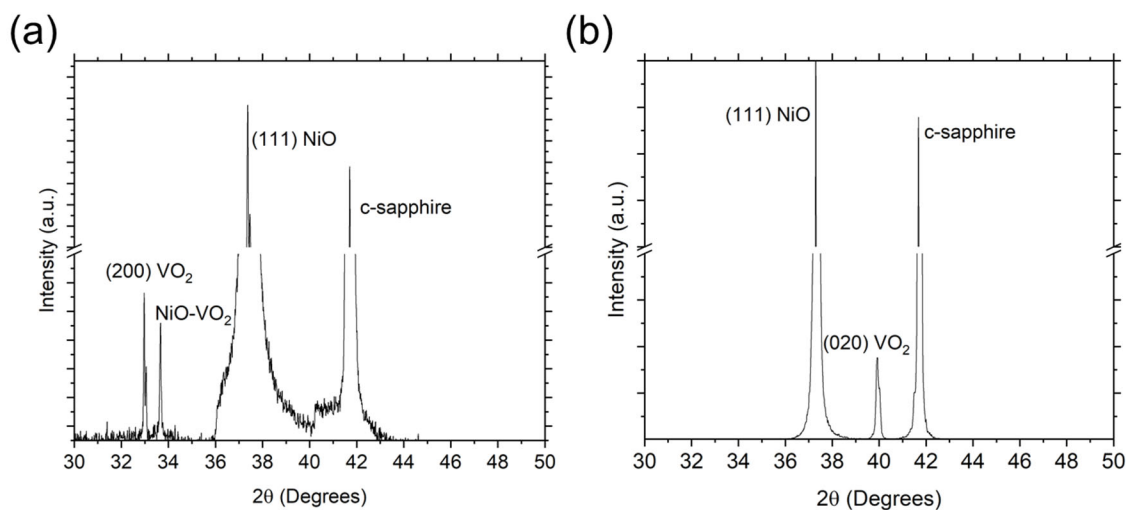


Figure S7.4. X-Ray diffraction of (a) thin VO₂, and (b) thick VO₂ films.

Raman characterization

To further verify the room temperature VO₂ phase formed in thick and thin films, Raman spectroscopic studies were performed, as provided in **Figure S5**. Both the spectra illustrate the main characteristic peaks of the monoclinic structure of VO₂ at 195 cm⁻¹, and 225 cm⁻¹ (assigned

to V-V modes), and 618 cm^{-1} , and 625 cm^{-1} (assigned to V-O modes) ^{1,2}, thus confirm the stable monoclinic phase formation in thick and thin VO₂ films. The peak splitting around 620 cm^{-1} in both samples, indicates the oxygen ions are connected to two vanadium ions with a different bond-length along the c-axis. In an interesting observation, however, the V-O peaks are shifted toward lower frequencies in the case of thin VO₂ samples. These shifts are indicative of V-O shorter bond length due to oxygen octahedral distortion. Also, the intensity of V-V modes has changed in thin VO₂ films compared to thick ones which can be inferred that the pairing and tilting of vanadium ions have changed attributed to the change in V-V bond length while maintaining the monoclinic structure. The presence of metallic monoclinic phase stabilized under high pressure has been shown by Raman spectroscopy previously, the result of which is consistent with the present study ³.

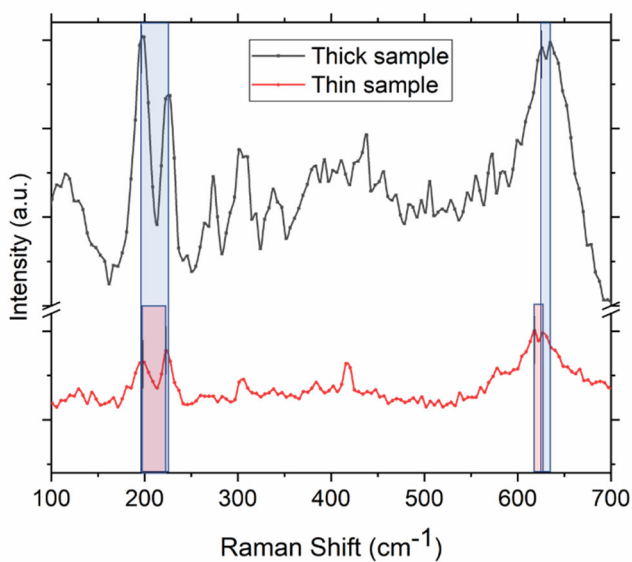


Figure S7.5. Room temperature Raman spectroscopy of thin and thick VO₂ samples with the characteristic peaks belong to the monoclinic phase as indicated.

Orbital occupancy across the metal-to-insulator transition

During the metal-to-insulator transition, the V^{4+} cation moves away from the center of the oxygen octahedron toward the edges and form V-V pairs and the conductivity decreases sharply. At the high-temperature tetragonal state, V^{4+} in the octahedra obstructs the free rotation of the electrons and quenches the orbital angular momentum giving rise to the splitting of the $3d^1$ energies into e_g ($d_{3x^2-r^2}$, d_{yz}) and t_{2g} ($d_{z^2-y^2}$, d_{xy} , d_{zx}) orbitals ⁴. The e_g wave functions are pointing toward O^{2-} thus having higher energies, while t_{2g} pointing between them ⁵. Covalent mixing between the two electrons in d_{xy} and d_{zx} and p_π orbitals of the anion results in the formation of the narrow antibonding π^* and a wider bonding π band. The remaining electron is nonbonding and goes into $d_{z^2-y^2}$ which is directed parallel to the c-axis. This electron is not involved in the V-O bonding and provides V-V bonding along the c-axis, also partially fills the $d_{z^2-y^2}$ which is the reason for rutile phase being metallic and reduces the c/a ratio. The relative energies and stabilities of the $d_{z^2-y^2}$ and d_{xy} , d_{zx} orbitals depend upon the c/a ratio as proposed by Goodenough ⁶, discussed by Hearn ⁷, and experimentally showed by Aetukuri ⁸. We believe that the oxygen octahedra in uniformly strained thin films at high temperature are distorted which means vanadium is not stable in the center of the octahedra and thereby stabilizes the antiferroelectric distortion (the first necessary component of the transition) introduced by Goodenough ⁶. According to this theory, the requirement for the insulating band structure is i) destabilizing the π^* orbital and/or stabilizing the bottom half of the $d_{z^2-y^2}$ orbital by raising the π^* orbital energy above the Fermi level, and ii) splitting of the $d_{z^2-y^2}$ orbital. Goodenough proposed that the distortion of the structure by displacement of V ions perpendicular to c-axis destabilizes the π^* orbital (the antiferroelectric distortion) and a decrease in the c/a ratio stabilizes the bottom half of the $d_{z^2-y^2}$ orbital which fulfills the first requirement, and a homopolar V-V bonding along the c-axis split the $d_{z^2-y^2}$ and defines the energy gap ⁶.

However, Zylbersztein and Mott believed the role of distortion is to destabilize the π^* orbital and to induce the transition and not to determine the electrical gap⁹. They proposed that each V^{4+} has a moment and the energy to form a carrier (defined as band gap) is equal to $U - 1/2(B_1 + B_2) - J_H$, where U is the Hubbard intra-atomic correlation energy, B_1 and B_2 are the bandwidth of upper and lower Hubbard bands here for the motion of electron (V^{3+}) and hole (V^{5+}), and J_H is the coupling energy. Thus, the bandgap is mainly a correlation gap.

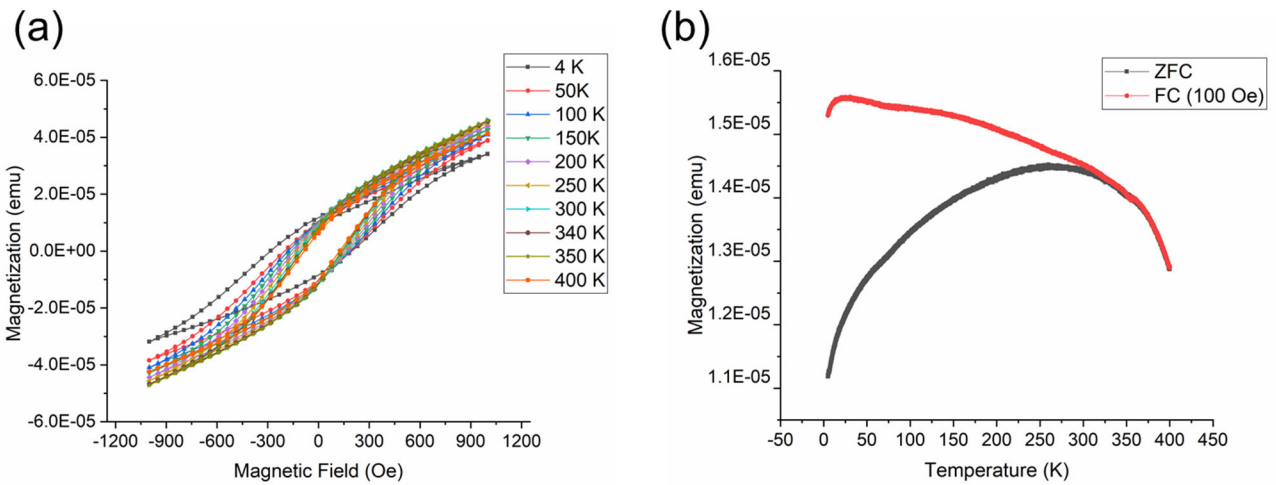


Figure S7.6. (a) The magnetization vs field plots at different temperatures for thin VO_2 samples and (b) temperature dependence of 100 Oe cooled field (CF) and zero cooled fields (ZFC) magnetization plots of the thin sample

Table S7.1. The plane alignments, DME paradigm ¹⁰, and the strains reported for thin and thick VO₂ films.

	In plane alignments	¹ Misfit Strain %	² DME calculations:	Out of plane alignment	Residual out-of-plane Strain %	³ Residual in-plane Strain %
10 nm VO ₂ film	NiO($\bar{2}11$) \parallel M-VO ₂ (10 $\bar{2}$)	-4.2	23/24, $\alpha=0.53$	NiO(111) \parallel VO ₂ (200)	8.624 \pm 0.001	7.392
	NiO(110) \parallel M-VO ₂ (010)	-2.1	47/48, $\alpha=0.82$			
250 nm VO ₂ films	NiO(110) \parallel M-VO ₂ (001) \parallel T-VO ₂ (001)	3.3	29/30, $\alpha=0.67$	NiO(111) \parallel VO ₂ (010)	0.013 \pm 0.001	-0.011
	NiO($\bar{2}11$) \parallel M-VO ₂ (20 $\bar{1}$) \parallel T-VO ₂ (100)	9.9	10/11, $\alpha=0.93$			

¹misfit strains are calculated based on the tetragonal VO₂ phase for 250 nm films. T and M stand for tetragonal and monoclinic, respectively (When the films transform from tetragonal to monoclinic during the cooling, the dislocations are already formed following the tetragonal or high-temperature phase misfit strains.)

²Number of alternating planes matching across the interface and α is the frequency factor.

³Poisson ratio of VO₂ thin films is considered to be 0.3.(ref: Thermodynamics of strained vanadium dioxide single crystals)

Table S7.2. The peak positions and width of the EELS edges for thin and thick VO₂ films at room temperature (RT) and high temperature (HT). The standard deviation in all the measurements was 0.1 eV.

	VO ₂ (250 nm)				VO ₂ (10 nm)			
	RT		HT		RT		HT	
	Peak position (eV)	Width (eV)	Peak position (eV)	Width (eV)	Peak position (eV)	Width (eV)	Peak position (eV)	Width (eV)
V-L3	514.4	3.2	514.5	3.4	514.3	3.3	514.3	3.6
V-L2	520.8	5.1	520.8	5.2	520.4	5.1	520.8	5.3
O-K (π^*)	529.4	4.7	529.3	3.7	529.6	4.6	529.8	4.4

Table S7.3. Atomic Structures (lattice vectors in Å; atomic positions in relative coordinates):

NM-M1:

a	5.526795	0	-0.00013
b	0	4.566773	0
c	-2.81085	0	4.579404
V	0.234492	0.975573	0.030351
V	0.765508	0.024427	0.969649
V	0.765509	0.475573	0.469649
V	0.234491	0.524427	0.530351
O	0.107259	0.2174	0.213241
O	0.892741	0.7826	0.786759
O	0.892741	0.7174	0.286759
O	0.107259	0.2826	0.713241
O	0.401269	0.699094	0.305006
O	0.598731	0.300906	0.694994
O	0.598731	0.199094	0.194994
O	0.401269	0.800906	0.805006

FM-M0:

A	5.691033	0	0.041931
B	0	4.551353	0
c	-2.86001	0	4.512081
V	0.246348	0.996014	0.009994
V	0.753652	0.003986	0.990006
V	0.753652	0.496014	0.490006
V	0.246348	0.503986	0.509994
O	0.102386	0.205785	0.207984
O	0.897614	0.794215	0.792016
O	0.897614	0.705785	0.292016
O	0.102386	0.294215	0.707984
O	0.399526	0.69787	0.302744
O	0.600474	0.30213	0.697256
O	0.600474	0.197871	0.197256
O	0.399526	0.802129	0.802744

NM-M1 (low):

a	5.79684	0	0
b	0	4.451768	0
c	-2.87591	0	4.602425
V	0.23048	0.974878	0.030438
V	0.76952	0.025122	0.969562
V	0.76952	0.474878	0.469562
V	0.23048	0.525122	0.530438
O	0.103839	0.223491	0.206731
O	0.896161	0.776509	0.793269
O	0.896161	0.723491	0.293268
O	0.103839	0.276509	0.706731
O	0.404299	0.703999	0.306964
O	0.595701	0.296001	0.693036
O	0.595702	0.203999	0.193036
O	0.404298	0.796001	0.806964

NM-M1 (high):

a	5.79684	0	0
b	0	4.43667	0
c	-2.89331	0	4.630266
V	0.230687	0.975217	0.030932
V	0.769313	0.024783	0.969068
V	0.769313	0.475218	0.469068
V	0.230687	0.524782	0.530932
O	0.103072	0.224784	0.205209
O	0.896928	0.775216	0.794791
O	0.896928	0.724783	0.294791
O	0.103072	0.275217	0.705209
O	0.404666	0.705402	0.307924
O	0.595334	0.294598	0.692076
O	0.595334	0.205401	0.192076
O	0.404666	0.794599	0.807923

NM-M1 ($\Delta_{V-V}=0.69 \text{ \AA}$):

a	5.79684	0	0
b	0	4.429453	0
c	-2.89331	0	4.630266
V	0.233891	0.977386	0.025945
V	0.766109	0.022614	0.974055
V	0.766109	0.477387	0.474055
V	0.233891	0.522613	0.525945
O	0.104176	0.22338	0.204104
O	0.895824	0.77662	0.795896
O	0.895824	0.72338	0.295896
O	0.104176	0.27662	0.704104
O	0.404929	0.704234	0.306407
O	0.595071	0.295766	0.693593
O	0.595071	0.204233	0.193593
O	0.404929	0.795767	0.806407

NM-M1 ($\Delta_{V-V}=0.55 \text{ \AA}$):

a	5.79684	0	0
b	0	4.423595	0
c	-		
c	2.89331	0	4.630266
V	0.23710	0.97992	0.02096
V	0.76291	0.02008	0.97904
V	0.76291	0.47992	0.47904
V	0.23710	0.52008	0.52096
O	0.10451	0.22300	0.20210
O	0.89549	0.77700	0.79790
O	0.89549	0.72300	0.29790
O	0.10451	0.27700	0.70210
O	0.40575	0.70460	0.30677
O	0.59425	0.29540	0.69323
O	0.59425	0.20460	0.19323
O	0.40575	0.79540	0.80677

NM-M1 ($\Delta_{V-V}=0.42 \text{ \AA}$):

a	5.79684	0	0
b	0	4.419385	0
c	-2.89331	0	4.630266
V	0.240299	0.983175	0.015969
V	0.759701	0.016825	0.984031
V	0.759701	0.483175	0.484031
V	0.240299	0.516825	0.515969
O	0.104804	0.222344	0.200784
O	0.895196	0.777656	0.799216
O	0.895195	0.722344	0.299216
O	0.104805	0.277656	0.700784
O	0.406371	0.704325	0.306812
O	0.593629	0.295675	0.693188
O	0.593629	0.204325	0.193188
O	0.406371	0.795675	0.806812

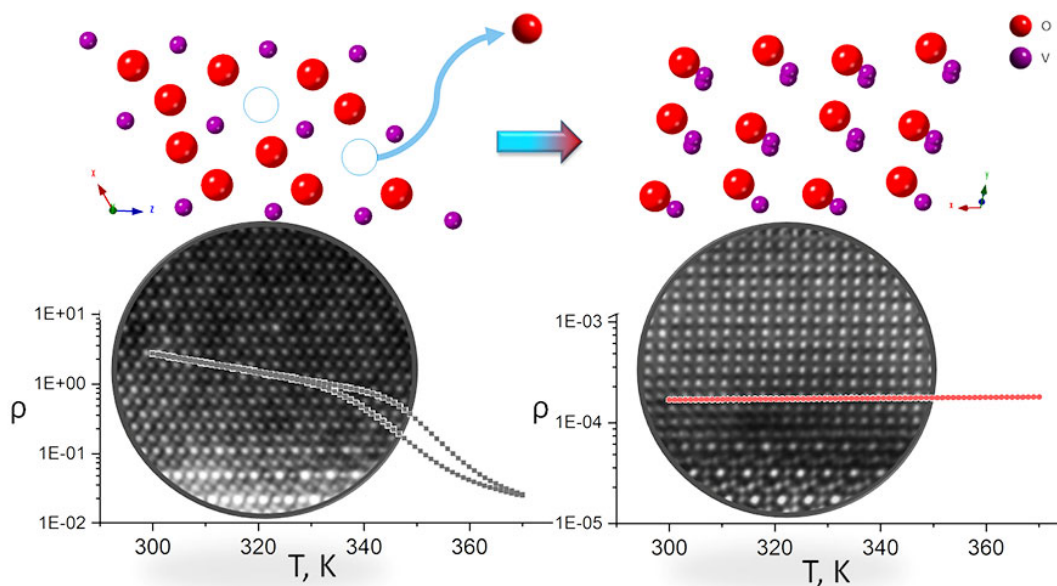
FM-M1 (low):

a	5.79684	0	0
b	0	4.482909	0
c	-2.875914	0	4.602425
V	0.24567	0.99424	0.01203
V	0.75433	0.00576	0.98797
V	0.75433	0.49424	0.48797
V	0.24567	0.50576	0.51203
O	0.10030	0.20900	0.20360
O	0.89970	0.79100	0.79640
O	0.89970	0.70900	0.29640
O	0.10030	0.29100	0.70360
O	0.40157	0.69828	0.30660
O	0.59843	0.30172	0.69340
O	0.59843	0.19828	0.19340
O	0.40157	0.80172	0.80660

REFERENCES

1. Marini, C. et al. Optical properties of $V_{1-x}Cr_xO_2$ compounds under high pressure. *Phys. Rev. B* 77, 235111 (2008).
2. Kim, H. et al. Raman study of electric-field-induced first-order metal-insulator transition in VO_2 -based devices. *Appl. Phys. Lett.* 86, 242101 (2005).
3. Arcangeletti, E. et al. Evidence of a pressure-induced metallization process in monoclinic VO_2 . *Phys. Rev. Lett.* 98, 196406 (2007).
4. Fujimori, A., Bocquet, A., Saitoh, T. & Mizokawa, T. Electronic structure of 3d transition metal compounds: systematic chemical trends and multiplet effects. *J. Electron Spectrosc.* 62, 141-152 (1993).
5. Tokura, Y. & Nagaosa, N. Orbital physics in transition-metal oxides. *Science* 288, 462-468 (2000).
6. Goodenough, J. B. The two components of the crystallographic transition in VO_2 . *J. Solid State Chem.* 3, 490-500 (1971).
7. Hearn, C. Phonon softening and the metal-insulator transition in VO_2 . *J. Phys. C: Solid State Phys.* 5, 1317 (1972).
8. Aetukuri, N. B. et al. Control of the metal-insulator transition in vanadium dioxide by modifying orbital occupancy. *Nat. Phys.* 9, 661 (2013).
9. Zylbersztein, A. & Mott, N. F. Metal-insulator transition in vanadium dioxide. *Phys. Rev. B.* 11, 4383 (1975).
10. Dankwort T, Strobel J, Chluba C, et al. Martensite adaption through epitaxial nano transition layers in TiNiCu shape memory alloys. *J. Appl. Crystallogr.* 49(3), 1009-1015 (2016).

CHAPTER 8



8. Defect engineering-Control of electronic and structural transitions through point defects

8.1. Vacancy-driven robust metallicity of structurally pinned monoclinic epitaxial

VO₂ thin films (*ACS applied materials & interfaces*, 11 (3) (2019) 3547-3554)

Abstract

Vanadium dioxide (VO₂) is a strongly-correlated material with 3d-electrons, which exhibits temperature-driven insulator-to-metal transition with a concurrent change in the crystal symmetry. Interestingly, even modest changes in stoichiometry-induced orbital occupancy dramatically affect the electrical conductivity of the system. Here, we report a successful transformation of epitaxial monoclinic VO₂ thin films from a conventionally insulating to permanently metallic behavior by manipulating the electron-correlations. These ultrathin (~10 nm) epitaxial VO₂ films were grown pseudomorphically on NiO (111)/Al₂O₃ (0001), where the large misfit between NiO and Al₂O₃ were fully relaxed by domain matching epitaxy. Complete

conversion from an insulator to permanent metallic phase is achieved through injecting oxygen vacancies ($x \sim 0.20 \pm 0.02$) into the VO_{2-x} system via annealing under high vacuum ($\sim 5 \times 10^{-7}$ Torr) and elevated temperature (450 °C). The creation of oxygen vacancies partially converts V^{4+} to V^{3+} and generates unpaired electron charges which result in the emergence of donor states near the Fermi level. This ultimately leads to convenient free-electron transport through the oxygen-deficient VO_{2-x} thin films resulting in the metallic character at room temperature. With these results, we propose a defect engineering driven pathway to tune electrical and optical properties in epitaxial VO_2 through the control of oxygen vacancies.

8.1.1. Introduction

Vanadium dioxide is known to be an electron-correlated material near half-filling of orbitals where complex competing interactions of charge, spin, orbital, and lattice degrees of freedom control its properties. Thus, these interactions can result in the emergence of exotic phases with unique electrical, optical, and magnetic properties. The VO_2 undergoes a metal-insulator transition concurrently occurring with the V-V dimerization and changes in the crystallographic structure^{1,2}. This phenomenon has been explained through Mott and Peierls mechanisms or a combination of both; where the former relates to the electron-electron interaction and the latter to the electron-phonon interaction as a physical reason behind the transition^{1,2}. The cooperation between Peierls and Mott mechanisms seems to be accepted and shown experimentally and theoretically^{3,4}, the extent of their contributions, however, is the matter of debate. The reason behind this fact is that in different cases, the contribution of Mott and Peierls to the metal-insulator transition can be tuned through adjusting charge, spin, orbital, and lattice degrees of freedom⁵⁻⁹. In practical applications, these factors are adjustable through strain and defect engineering. These defects include 0D point defects such as vacancies and dopants, and 1D defects like dislocations,

and 3D grain boundaries. The Mott transition can dominate if the electron correlation is enhanced (through decreasing bandwidth)¹⁰. This hypothesis is supported by the orbital-selective Mott transition (OSMT) where the strain or point defects make the orbital occupancy unequal and give one of the orbitals, in multi-orbital systems, the opportunity to get closer to the half-filled condition¹¹. We have shown experimentally that the metal-insulator transition occurs without the crystal structure transition by the strain engineering where the transition is dominated by Mott physics¹². That is, the interplay between lattice degrees of freedom and orbitals modifies the electron correlation. It is shown that charged defects can affect properties such as optical and magnetic properties of oxide and nitride systems¹³⁻¹⁷. In the VO₂ system, it is also shown that the electrical, optical, and magnetic properties can be tuned by using oxygen vacancies¹⁴. These findings show that these potent point defects can be used to manipulate the system significantly. The metal-insulator transition temperature, the thermal hysteresis, and the resistivity of the high and low-temperature phases are shown to be affected by oxygen vacancies in VO₂ thin films. In these cases, it seems that the resistivity of the insulating phase along with the hysteresis amplitude and sharpness have been degraded in the presence of oxygen vacancies. These results raise the question of whether it is possible to stabilize the metallic VO₂. In recent studies, it is shown that the formation of V³⁺, weakens the strong coulombic correlation through oxygen vacancies and stabilizes the tetragonal metallic phase at room temperature^{18,19}. The ionic liquid gating method, as well as high-temperature vacuum annealing, are utilized to produce oxygen vacancies. Even though there are limited studies in this area, none of the previous studies have been done in the stabilized monoclinic structure, where detailed atomic resolution studies are needed to understand the correlation between atomic structure and the concentration of oxygen vacancies and explain how oxygen vacancies can enhance Mott contribution in the transition and metallicity. This

phenomenon provides the potential for VO₂ to be used in non-volatile metallic state devices like memories, switches, etc.

In this study, we investigate the metallicity of VO₂ thin films below the critical thickness where the structural transition can be pinned, and the Mott mechanism contribution can be manipulated. We introduce oxygen vacancies to the system to push the system more toward the stabilization of metallic state. In fact, we inject charge carriers through creating oxygen vacancies to push toward Mott criterion for two Hubbard bands to meet at least for one orbital to obtain metallic behavior, while the monoclinic structure is intact. We believe this effect persists as long as charge carriers exist in the heterostructures, and the charge carrier concentration meets Mott criterion of $n_c = \left(\frac{1}{4a_H}\right)^3 \approx 3 \times 10^{18} \text{ cm}^{-3}$ at room temperature to stabilize the metallic phase^{20,21}.

Here, we utilize defect engineering by introducing oxygen vacancies to affect electron-electron and electron-phonon interactions in the stable monoclinic phase. We synthesize single crystal epitaxial thin VO₂ films (~10 nm) on *c*-Al₂O₃ using NiO buffer layer, where oxygen vacancies are introduced through annealing in a high-vacuum environment. The VO₂ films grow pseudomorphically below the critical thickness and follow the concept of domain matching epitaxy for the large misfit (NiO/Al₂O₃) system to obtain epitaxial VO₂/NiO/Al₂O₃ heterostructures. The in-depth analysis of monoclinic metallic phase and its properties and the orbital occupancy have been conducted by using a detailed high-angle annular dark field (HAADF) imaging, electron energy loss spectroscopy (EELS), Raman spectroscopy, temperature-dependent *in-situ* XRD, and electrical measurements.

8.1.2. Experimental details

Thin film heterostructures were deposited using a KrF excimer laser with the frequency of 5 Hz and energy of 3.5 mJ/cm²^{22–24}. The NiO layer was grown at 700 °C and 1×10⁻⁴ Torr oxygen

pressure, and the VO₂ film was deposited at 550 °C and 1.2×10⁻² Torr oxygen pressure¹⁴. The vacuum annealing procedure was performed at 1×10⁻⁷ Torr and 450 °C for 2 hr.

In-Situ X-ray Diffraction Measurement: A PANalytical Empyrean diffractometer using Cu-K α radiation was used to collect *in-situ* XRD measurements. The *in-situ* structural changes during heating and cooling cycles were monitored using this technique in the 25-120 °C range. The step size of 2 θ was set 0.013° and the count time per step was set 1 S.

Scanning Transmission Electron Microscopy: The HAADF images were collected using an FEI Titan 80-300 probe aberration-corrected scanning transmission electron microscope (STEM) operated at 200 kV. Across thin films interfaces, electron energy loss spectra (EELS) were also acquired at 200 keV with a 28 mrad collection angle, and 19.6 mrad convergence angle. Spectra were collected using a 0.25 eV.ch⁻¹ dispersion with a ~35 pA probe current and 0.07 nm pixel size to perform an elemental analysis. A routine peak fitting was applied on V-L and O-K edges using Gaussian profiles for detailed analysis²⁵. The noise reduction in the data is performed by fast Fourier filtering of the data, following the dark reference.

Electrical Measurement: The physical property measurements system (PPMS) by Quantum Design was used to acquire electrical transport measurements over the temperature range of 25-110 °C during heating and cooling cycles. The resistivity data were collected using a step size of 1 o.S-1 at zero magnetic fields.

Raman. The vibrational phonon modes were determined by WITec confocal Raman microscope (Alpha 3000 M) with a lateral resolution of 200 nm and 532 nm green laser source and were used to characterize the V–V and V-O bonding characteristics. Single crystalline Si (100) (characteristic Raman peak at 520.6 cm⁻¹) was used to calibrate the acquired Raman spectra.

8.1.3. Results and discussion

We compare the results from as-deposited (100)VO₂/(111)NiO/(0001)Al₂O₃ and vacuum annealed (021)VO₂/(111)NiO/(0001)Al₂O₃ heterostructures. The as-deposited samples have been grown below the critical thickness to prevent the lattice relaxation and stabilization of the monoclinic phase in the wide temperature range. In fact, the presence of strain can eliminate or pin the structural transition, where the electrical transition can occur. The vacuum annealing was done to introduce oxygen vacancies into the system while maintaining the VO₂ base structure as monoclinic. To study the crystallographic properties of these VO₂ thin films, XRD patterns of the as-deposited and annealed samples are collected and the results are presented in Figure 8.1a and b. For the as-deposited sample, (100) monoclinic diffraction peak is observed, while for the annealed sample different diffraction peak presents at $2\theta=44.6$ which is indicative of (021) monoclinic planes of VO₂¹⁰. The monoclinic structure in the annealed sample has a different symmetry and is close to what is reported for the high-pressure monoclinic phase of VO₂ belonging to C2/m space group. Interestingly the high-pressure phase of VO₂ shows behavior similar to the vacuum annealed sample^{26,27}. Figure 8.1c represents the schematic depiction of the VO₂/NiO/c-sapphire epitaxial heterostructures. The Scanning Transmission Electron Microscopy (STEM) was used to characterize the phase and provide more information regarding the atomic structure of VO₂ thin films. The high-angle annular dark-field (HAADF) images in Figure 8.1d and e show the cross-section of the VO₂/NiO interface in both as-deposited and vacuum-annealed samples. In both cases, there is an intermixed layer between VO₂ and NiO layers. The HAADF micrograph presented in Figure 8.2a belongs to the as-deposited thin film with [010] zone axis of monoclinic VO₂ and [100] as the out-of-plane direction. Figure 8.2b shows the HAADF image of the vacuum annealed sample with [01 $\bar{2}$] zone axis of monoclinic VO₂ and the normal to (021) planes as the

out-of-plane direction. These data shed light on the crystallographic structure of the annealed sample and confirmed it to be monoclinic. There is a lattice relaxation after annealing due to the presence of oxygen vacancies, which is calculated to be around -1.2% from the XRD data. The HAADF image also confirms the dislocation formation in some area of the interface shown in the inset of Figure 8.2b in the VO_2 sample after annealing, even though the thickness is below the critical thickness. The interface of VO_2/NiO without dislocations is also shown for comparison. This shows that high-temperature annealing gives enough energy to overcome the dislocation nucleation and propagation barrier for partial lattice relaxation.

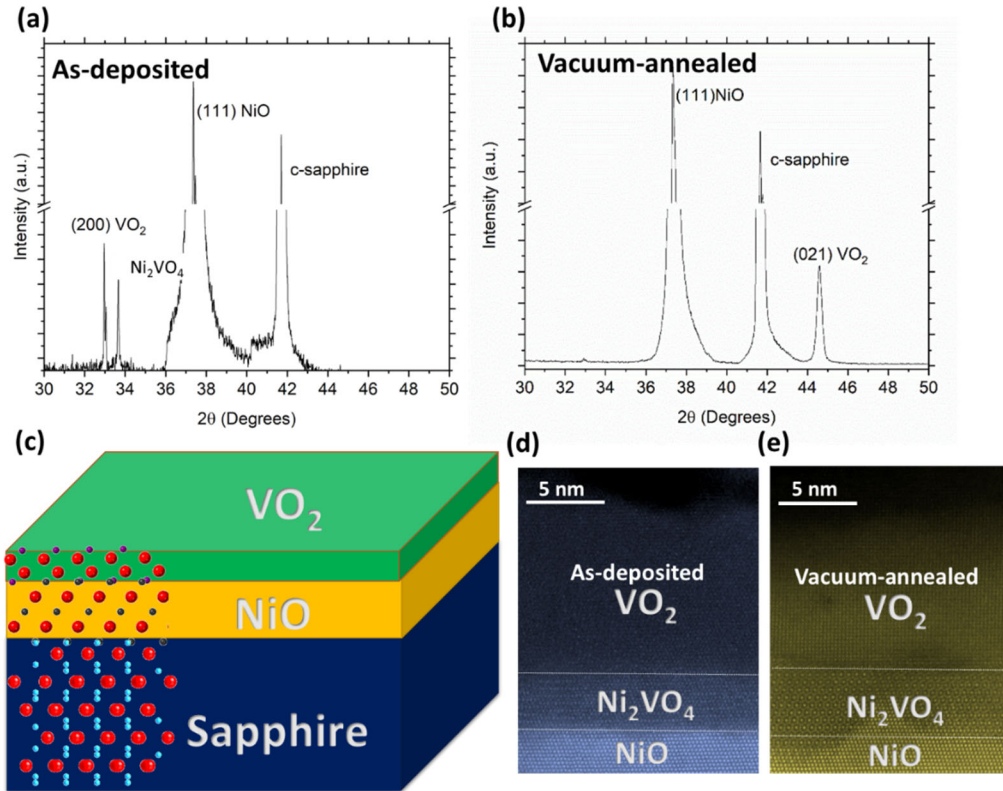


Figure 8.1. The X-ray diffraction pattern of $\text{VO}_2/\text{NiO}/\text{sapphire}$ thin film heterostructures below a critical thickness of ≈ 15 nm (a) as-deposited sample, and (b) after annealing in vacuum. (c) The schematic figure representing $\text{VO}_2/\text{NiO}/\text{sapphire}$ heterostructures, (d, e) the HAADF images of the VO_2/NiO interface showing the formation of a thin NiO-VO_2 layer in the as-deposited and vacuum-annealed samples, respectively.

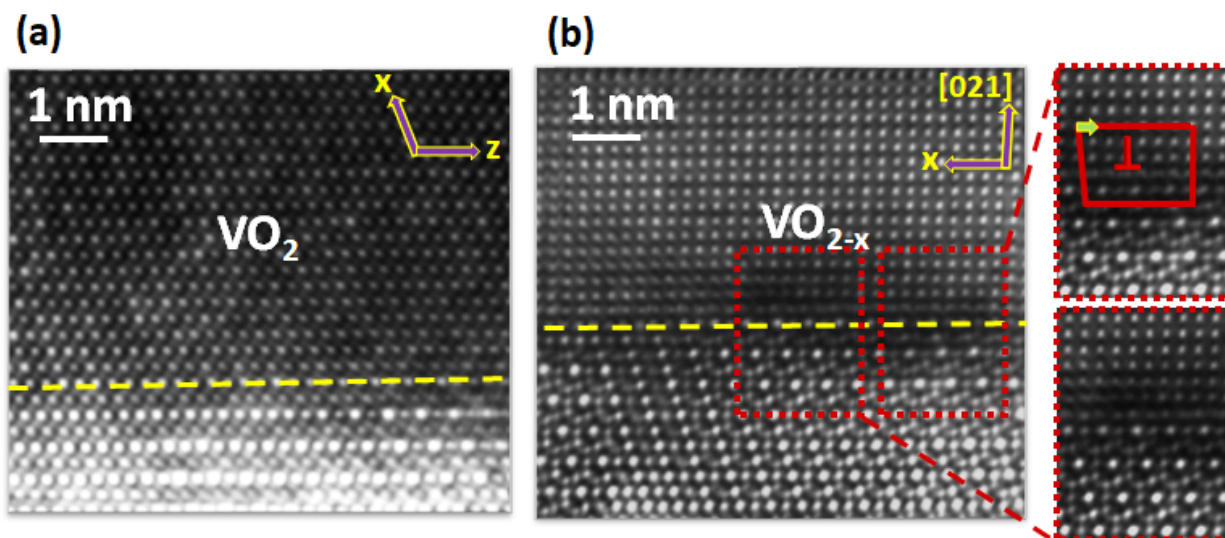


Figure 8.2. HAADF-STEM signal showing atomic resolution imaging produced from VO₂/NiO cross-sectional interface of (a) as-deposited sample with the zone axis of [010], and (b) the HAADF image of the annealed sample in a vacuum with the zone axis of [01 $\bar{2}$]. The inset figures in the (b) show the interface of VO₂/NiO with and without dislocation.

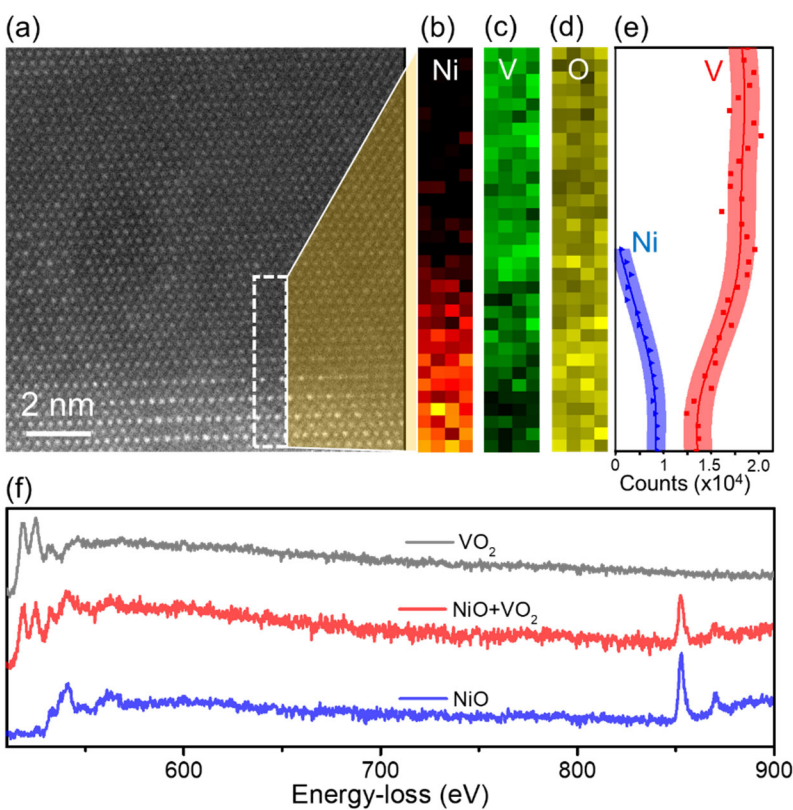


Figure 8.3. (a) HAADF image of the VO₂ thin film, (b) Ni, (c) V, and (d) O elemental maps corresponding to the marked region-of-interest (ROI) in (a) obtained from EELS. (e) The averaged intensity profile of V-L₃₂ and Ni-L₃₂ peaks along the ROI. (f) The representative EEL spectra from pure VO₂, VO₂+NiO and NiO regions from the as-deposited thin film sample.

A detailed EELS is performed on these VO₂ thin films grown on *c*-Al₂O₃ with NiO buffer layer. Figure 8.3 illustrates the elemental distribution of V and Ni obtained by EELS quantification across the interface from the region-of-interest (ROI) marked in the HAADF image shown in Figure 8.3a. The figure shows the presence of V in the VO₂ thin film as well as the intermixed NiO+VO₂ layer (Figure 8.3c). On the other hand, the presence of Ni is just evident in the intermixed/reacted buffer layer (Figure 8.3b), leaving the VO₂ thin film free from impurity atoms. While the change in the characteristics of O-K pre-peak is observed, O is found to be present uniformly over entire ROI as expected and shown in Figure 8.3d. The averaged EELS peak intensity plot along the ROI is also shown in the Figure 8.3e, indicating the presence of V, while having a moderate change in the intensity, in the VO₂ as compared to the intermixed layer. The representative EEL spectra from pure VO₂, NiO+VO₂, and NiO regions are demonstrated in Figure 8.3f. The figure shows the V-L₃₂ (513 eV), O-K (532 eV) and Ni-L₃₂ (855 eV) characteristic edges in the EELS spectra and are consistent with the ones reported in the literature, confirming the formation of VO₂ and NiO.

Figure 8.4 represents the temperature dependent *in-situ* XRD measurements for both as-deposited and vacuum-annealed samples. To further confirm the stability of the metallic monoclinic VO₂ structure over the range of -120 °C to +120 °C the spectrum has been collected for the annealed sample and provided in the Appendix A. No structural transition is observed for the as-deposited sample since the film was grown below the critical thickness (15 nm)²⁸. The annealed sample, also, does not show any structural transition in the above-mentioned range indicating there are neither Magneli phases nor V₂O₃ present²⁰. The V₂O₃ transition occurs at ~-106 °C. Thus, the oxygen deficiency does not result in V₂O₃ formation, but rather VO_{2-x}.

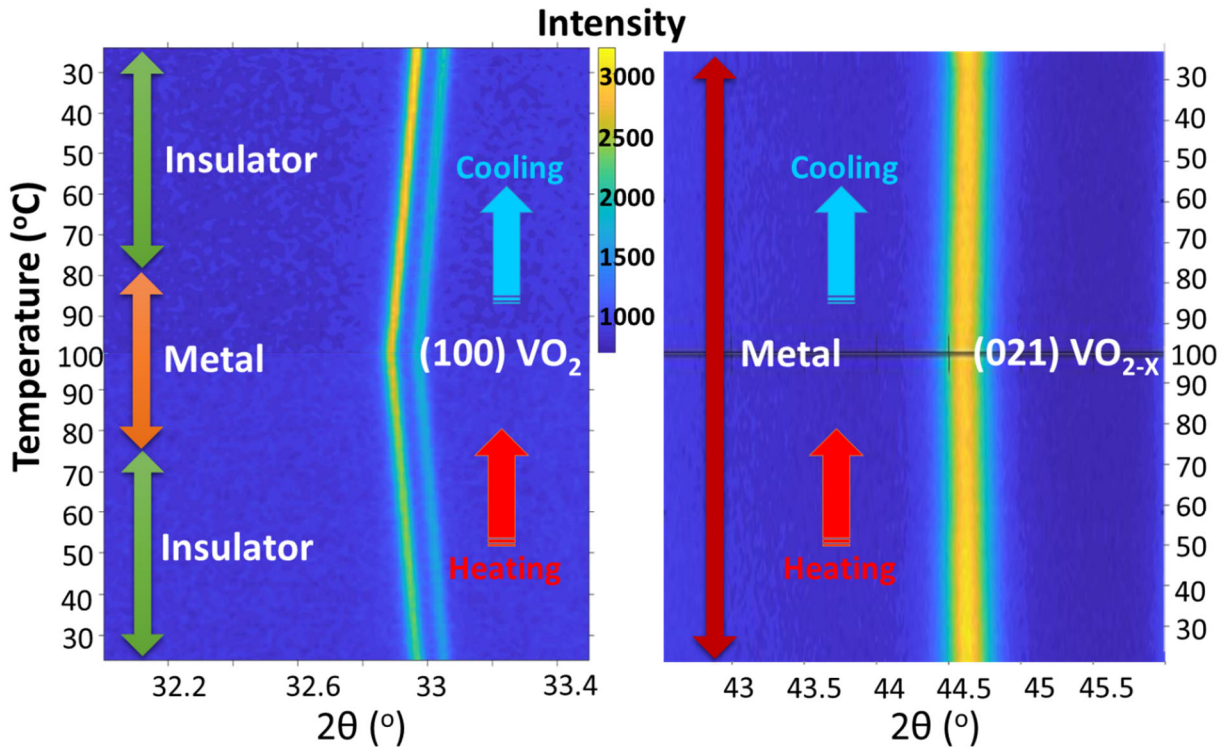


Figure 8.4. Contour plots of in-situ XRD measurements for (a) as-deposited epitaxial VO₂, and (b) annealed epitaxial VO₂ in a vacuum atmosphere.

The temperature dependent electrical resistivity measurements for samples before and after annealing in the vacuum are shown in Figure 8.5. The as-deposited sample shows extended hysteresis belonging to typical strain trapped VO₂ thin films²⁹. The derivative of resistivity vs temperature determines the exact cooling and heating transition temperature to be 75 °C and 80 °C, respectively. After annealing at high temperature under the vacuum, the resistivity of the metallic phase is decreased and during the cooling cycle, the metal-insulator transition vanishes along with the structural transition. Thus, vacancies introduced during vacuum annealing lead to the formation of a stable metallic monoclinic phase at room temperature.

The carrier concentrations, derived from the resistivity vs temperature measurements for high and low temperatures, are reported in table 8.1 for both samples. The electron mobility was determined to be 0.6 cm²/Vs for vacuum-annealed VO₂ thin films using room temperature Hall

Effect measurement which is consistent with the values reported in literature ^{29,30}. The electron mobility is assumed to be the same for the insulating state. This is consistent with previous studies which have shown that the mobility does not change during the transition, while the carrier concentration does ³¹. The electrical measurements represent two orders of magnitude difference in the carrier concentration at high temperature for the annealed sample compared to the as-deposited sample, which is indicative of higher free carrier concentration in the annealed sample. Each oxygen vacancy donates two electrons, which can contribute to the conductivity, if not trapped by any defects or cation interstitial sites. In the optimum condition, if all electrons are free carriers, the oxygen vacancy concentration should be half of the electron concentration calculated from these measurements. At room temperature, there are four orders of magnitude difference between the free carrier concentrations of these two samples. The room temperature Hall Effect measurement value for the annealed sample is 1.12×10^{22} n-type carriers, confirming the presence of free electrons in the annealed sample at room temperature. At room temperature, in the as-deposited sample, the carrier concentration is very close to the Mott criterion of $3 \times 10^{18} \text{ cm}^{-3}$. Injection of oxygen vacancies in the vacuum-annealed sample through electron doping pushes this value above the Mott criterion and makes this sample metallic at room temperature.

The Hubbard model defines a Mott insulator by two characteristics: (I) the relative electron interaction strength, “ U/t ”, where U is the coulombic repulsion, and t is the orbital bandwidth, and (II) the electron density, “ n ” ²¹. For a single electron model, n equals 1 is defined as a half-filled band condition. In multi-orbital systems, this criterion can be defined for each orbital ¹¹. To decrease the bandgap in the insulating phase, U must decrease and/or t increase. When U is sufficiently small, the two Hubbard bands meet, and the system becomes metallic, however, it is not easy to manipulate U in a single-orbital system. Tuning U and t is much easier in a multi-

orbital system in which some orbitals can be tuned while others stay almost intact. Increasing the bandwidth “t” is achievable through elongating the lattice parameters, and the change in U occurs with the charge state and effective spin state. The VO₂ is considered a generalized 2-band multi-orbital system where U and t can be adjusted. Here, it is surmised that U has been diminished by the introduction of free carriers and the presence of V³⁺.

The mechanism through which electrons are generated is as follows using Equation (8.1), (8.2), and (8.3):



E_f is the formation of energy for such mechanisms to happen. One of the electrons may be trapped locally by V⁴⁺ and creat V³⁺. The presence of V³⁺ weakens the electron correlation and the coulombic interaction³³, furthermore, an enhanced number of free carriers by the other non-trapped electron leads the system more toward the metallic stage by decreasing U³⁴.

The vacancy concentration n_v thermodynamically can be calculated using Equation (8.4) and (8.5):

$$\frac{n_v}{n_0} = \exp\left(\frac{-\Delta G_f}{kT}\right) \quad \text{Equation (8.4)}$$

$$n_0 = \frac{\rho N_A}{A} \quad \text{Equation (8.5)}$$

Where n₀ is the total number of available sites, ΔG_f is the vacancy formation energy, k is the Boltzmann constant, T is the temperature, ρ is the density, N_A is Avogadro number, and A is the atomic mass. The equilibrium vacancy concentration at 450 °C, is calculated to be 0.69×10²² using the formation energy of vacancy as 0.097 eV at low oxygen pressure condition³². Thus, the maximum concentration of electron can be added to the system by oxygen vacancies is 1.38×10²²

which is higher than the free carrier concentration measured in the system. This shows that some of the electrons are trapped either by V^{3+} or v_o^* , which has a higher formation energy. The equilibrium vacancy concentration ratio to the total available atomic site $\frac{n_v}{n_o}$, is also calculated to be 0.2 which leads to the stoichiometry changes in VO_2 .

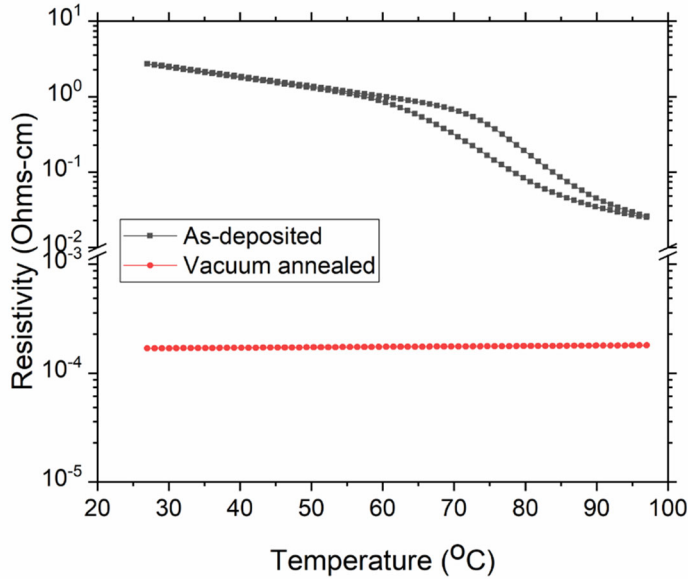


Figure 8.5. The electrical resistivity of $VO_2/NiO/sapphire$ thin film heterostructures, below the critical thickness of 15 nm for as-deposited and vacuum-annealed samples.

Table 8.1. Carrier concentration values calculated for as-deposited and vacuum-annealed samples at room temperature and 100 °C.

n, carrier concentration (cm^{-3})	100 °C	Room temperature
As-deposited sample	8.57×10^{19}	8.51×10^{17}
Vacuum annealed sample	1.21×10^{22}	1.27×10^{22}

To further probe the V-V and V-O bonding characteristics in the vacuum-annealed VO_2 thin films, Raman spectra are acquired and compared with the as-deposited strained VO_2 thin film and near bulk VO_2 thin films as control samples in Figure 8.6a. Sharp Raman peaks are observed

at 129, 196, 224, 308, 386, 498, and 614 cm^{-1} belonging to A_g symmetry and 268, 340, and 445 cm^{-1} for B_g symmetry³⁵⁻³⁷. The remaining spectral peaks at 421, 575 and 751 cm^{-1} are found to originate from the *c*- Al_2O_3 substrate. The Raman spectra present in Figure 8.6a clearly identifies the M_1 phase with the monoclinic structure at room temperature for the control samples. In the M_1 phase, low-frequency V-V lattice vibrational peaks correspond to 193.9 and 228.5 cm^{-1} , while the rest are related to V-O vibrations. It is shown that V-V lattice vibrational peaks are present in the vacuum-annealed sample. Another key observation from Figure 8.6a is the complete annihilation of V-O vibrational peak ($\sim 614 \text{ cm}^{-1}$) upon vacuum-annealing in the VO_2 thin film. The vacuum-annealing process generates oxygen vacancies which lead to distortions in the VO_6 octahedra. But the complete absence of V-O peak is suggestive of metallicity creeping in due to the charge transfer and its delocalization about the V^{+3} -oxygen vacancy in the VO octahedra. The structural changes in strained VO_2 thin films upon vacuum-annealing are analyzed by performing representative fitting routine fits on V-V bonding states in Figure 8.6b³⁸. The spectra reveal that while the V-V₁ full-width half-maximum (FWHM) in the as-deposited VO_2 thin film increases from 11 cm^{-1} to 30 cm^{-1} upon vacuum-annealing, the V-V₂ peak remains sharp (FWHM increases from 7 cm^{-1} to 14.5 cm^{-1}). Since the V-V dimers still exist in the metallic VO_2 phase, the Peierls distortion cannot be correlated with the changes in electronic properties. These prominent V-V dimer vibrational peaks explicitly reveal the characteristics of the distorted monoclinic structure. Similar observations have been made in pressure-induced metallicity of phase 'X' in VO_2 ^{27,38}. In the M_1 phase, a short (2.65 Å) and a long (3.12 Å) alternate along the a-axis resulting in the insulating behavior. Interestingly, Goodenough reported a critical V-V separation distance of 2.93 cm^{-1} , where further compression will lead to delocalization of 3d electrons. The generation of oxygen vacancies creates empty spaces leading to V-V atoms coming closer and overall densification of the VO_2 lattice³⁹. The

reduction in V-V bond length closes the bandgap and pins the metallicity²⁸. Also, the right-shift in peak positions from 197.3 cm⁻¹ to 198 cm⁻¹ (V-V₁) and 224.6 to 228 cm⁻¹(V-V₂) is indicative of hardening of the V-V vibrational modes and stabilization of V-V dimers in the monoclinic phase. These results are consistent with the X-ray diffraction and HAADF TEM imaging studies, highlighting the stabilization of phase-pure epitaxial monoclinic film at room temperature after vacuum annealing. These results are different from previous experiments by Zhang et al. on vacuum-annealing of VO₂ films, where metallicity occurs by destabilization of VO₂ films during vacuum-annealing, forming rutile structure²⁰. The formation of rutile structure can be ascertained by weak Raman scattering around 530 cm⁻¹, coincident with the A_{1g} mode in thermally induced rutile metallic state in VO₂ films^{39,40}. In our case, no such features are present in the high-resolution spectral acquisitions for vacuum-annealed VO₂ films, shown in Figure 8.6c. Hence, it can be concluded that the metallicity in vacuum-annealed VO₂ films throughout the temperature range occurs due to delocalization of electrons from a shortening of V-V bond length in the distorted monoclinic structure.

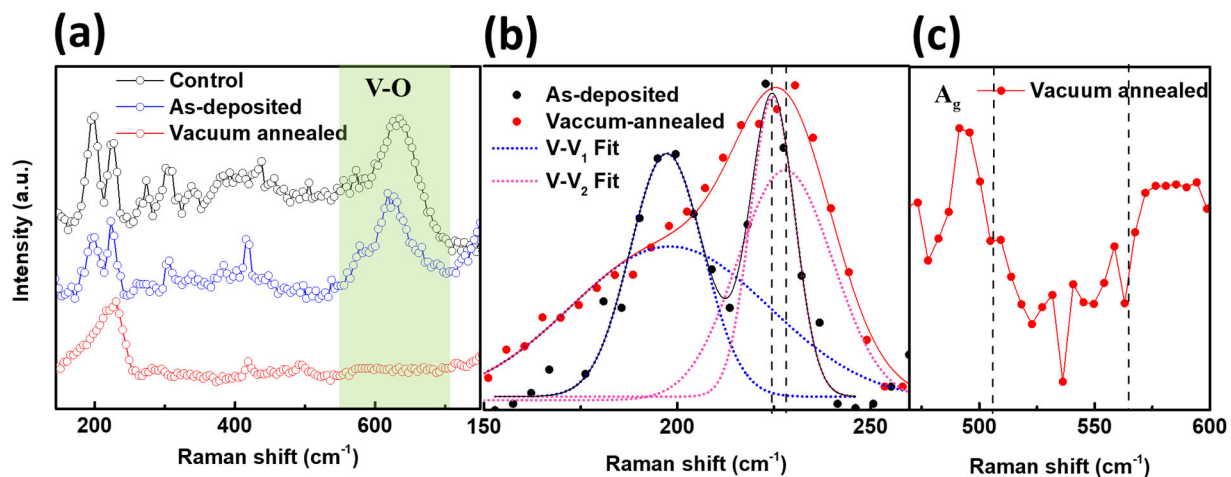


Figure 8.6. (a) Raman spectra for bulk VO₂ (above critical thickness), as-deposited thin film, and vacuum-annealed VO₂ thin film. (b) Raman fitting for V-V₁ and V-V₂ bonds in as-deposited and vacuum-annealed VO₂ thin films. (c) High-resolution Raman spectra for vacuum-annealed VO₂ film, highlighting the absence of rutile-VO₂ vibrational bonding characteristics.

The EELS map scans were acquired from VO₂ structure to detect vanadium and oxygen edge changes before and after annealing and the probable presence of V³⁺ formation. The core loss spectra, Figure 8.7a, belong to control, as-deposited and annealed samples. Comparing the V-L_{2,3} in all three samples, the changes in the annealed sample signifies an increase in the L_{2,3} ratios, which is consistent with the reduction of the vanadium oxidation state. The L₂ and L₃ distance is indicative of the crystal field splitting affected by the misfit strain in the VO₂ thin films. The as-deposited sample contains 6.1 eV distance compared to 6.4 eV for the other two samples, indicating that the control and the annealed samples are relaxed and have less crystal field splitting¹⁰. In the O-K edge, there is a decrease in the pre-peak and an increase in the O-K, showing that oxygen vacancies are present in the annealed sample. All these changes are consistent with the oxygen being removed from the annealed VO₂ structure. The oxygen vacancies can decrease the hybridization between V-3d and O-2p which results in the downshift of π^* orbital. Also, oxygen vacancies introduce electrons into the lowered π^* orbital, which increases the orbital bandwidth and provides conduction, if there is enough electron concentration. The oxygen pre-peak contains d_{||} and π^* orbital occupancy information^{10,28,41}. The oxygen pre-peak in the annealed sample got narrower and there is no clear splitting in the O-K edge, explaining the downshift of π^* orbital and less crystal field splitting compared to the control sample. Figure 8.7b depicts low loss edges of bulk, as deposited, and annealed samples. The low loss edge systematically shifts with oxygen vacancies toward lower eV, which is indicative of the abundant presence of oxygen vacancies. The quantitative analysis of oxygen vacancy concentrations is done using the standard core loss L_{2,3} edges in VO₂ and V₂O₃. Based on this information the amount of x in VO_{2-x} is calculated to be $x \sim 0.20 \pm 0.02$.

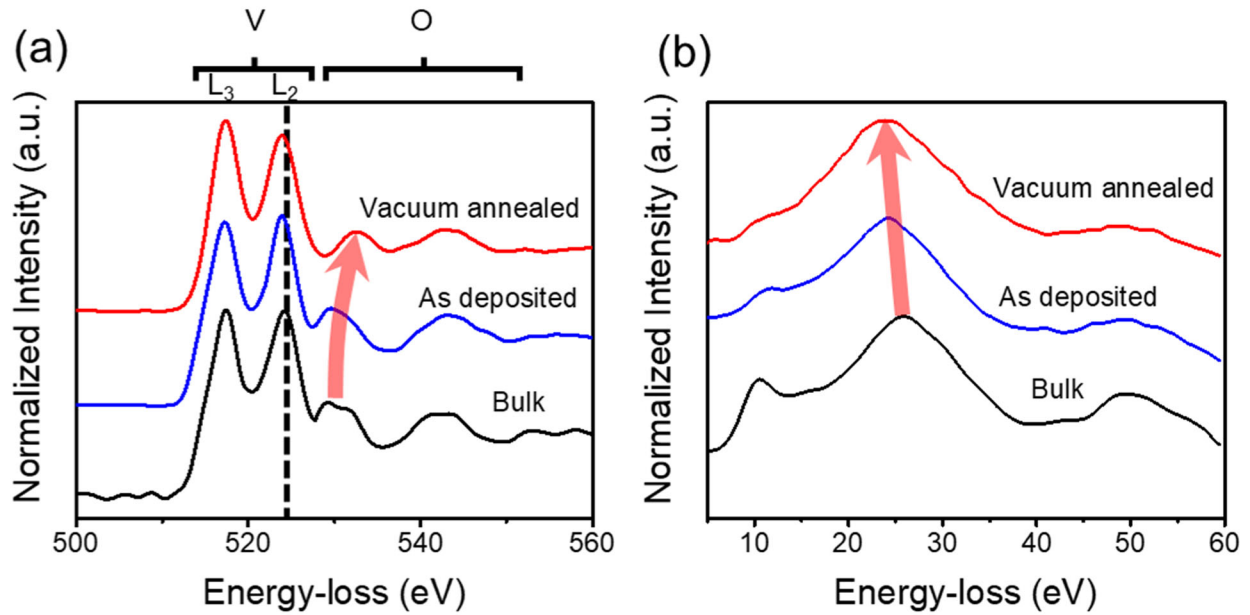
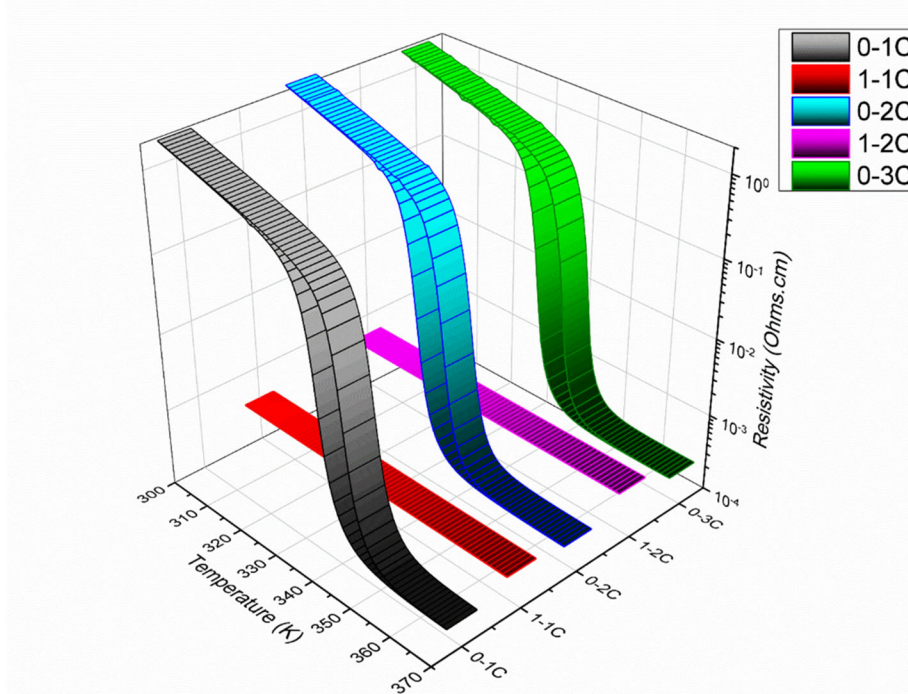


Figure 8.7. STEM-EELS measurements (a) core loss edges, and (b) low loss edges belong to VO₂ thin films in bulk, as deposited, and vacuum annealed samples.

8.1.4. Conclusion

We have achieved a stable metallic monoclinic phase of VO₂ by manipulating the electron-electron correlations through doping the system with oxygen vacancies. These vacancies introduce electrons into the system where they can change the relative electron interaction strength and as a result, modify the electronic properties of the VO₂ without any structural transition. In fact, the enhancement of free carrier concentration pushes the system to meet the Mott criterion and become metallic. Such manipulation can be used to tune electronic and structural transitions for next-generation non-volatile smart memories and devices.



8.2. Switching on/off metal-insulator transition in VO₂ above the critical thickness through oxygen vacancies

In this study, we investigate the metallicity of VO₂ thin films above the critical thickness of ≈ 10 nm in the VO₂/NiO/c-sapphire heterostructures. We introduce oxygen vacancies to the system to investigate the structural changes and behavior of electronic transition in response to that process. The oxygen annealing is then employed to investigate the reversibility of the metallicity. Moreover, the reversible behavior of VO₂ in response to multiple vacua and thereafter oxygen annealing cycles is presented. The annealing is conducted in two different temperatures since this is a diffusion-based process and has an exponential temperature dependency.

8.2.1. Experimental details

Thin film heterostructures were deposited using a KrF excimer laser with the frequency of 5 Hz and energy of 3.5 mJ/cm^2 ²²⁻²⁴. The NiO layer was grown at 700 °C and 1×10^{-4} Torr oxygen pressure, and the VO₂ film was deposited above the critical thickness of ~ 15 nm at 550 °C and

1.2×10^{-2} Torr oxygen pressure¹⁴. The vacuum annealing procedure was performed at 1×10^{-7} Torr in two different temperature of 200 °C and 450 °C for 2 hr. The reverse process of oxygen annealing was done at 1.2×10^{-2} Torr in two different temperature of 200 °C and 450 °C for 2 hr. The experimental techniques that are used are similar to section 8.1.

8.2.2. Results and discussion

We compare the results from as-deposited (pristine), vacuum annealed, and oxygen annealed (020)VO₂/(111)NiO/(0001)Al₂O₃ heterostructures. The pristine samples have been grown above the critical thickness to study the effect of introducing defects without pinning the lattice degree of freedom. The vacuum annealing introduces oxygen vacancies into the system. Thereafter, the oxygen annealing process introduces oxygen to fill out the vacancies. To study the crystallographic properties of vacuum annealed (low and high temperatures) and oxygen annealed VO₂ thin films, XRD patterns of the pristine and annealed samples are collected and the results are presented in Figure 8.8a. For the pristine sample, (020) monoclinic M₁ diffraction peak is observed, while for the vacuum annealed samples, a different diffraction peak shows up which is indicative of (200) M₂ monoclinic planes of VO₂¹⁰. The monoclinic structure in the vacuum annealed samples has a different symmetry belonging to C2/m space group and is similar to what is reported for the high-pressure monoclinic phase of VO₂^{26,27}. The oxygen annealing is employed on vacuum annealed samples and interestingly the peak position switches back to (020) M₁ monoclinic VO₂ as shown in Figure 8.8a. The Scanning Transmission Electron Microscopy (STEM) was used to characterize these phases and sheds light on the atomic structure of these thin films. Figure 8.8b represents the low magnification high-angle annular dark-field (HAADF) image of the VO₂/NiO/*c*-sapphire epitaxial heterostructures where VO₂ is grown above the critical thickness. The HAADF image in Figure 8.9a shows the cross-section of the VO₂/NiO-VO₂

interface in the pristine sample. Figure 8.9b represents the high magnification HAADF image of VO₂ belong to the pristine sample which illustrates M₁ monoclinic phase as it is also shown schematically in the inset figure. Figure 8.9c is a cross-section of the VO₂/NiO-VO₂ interface in the vacuum annealed sample at 450°C. The HAADF image in Figure 8.9d shows a micrograph of this vacuum annealed sample where atoms showing some lobes. This structure is representative of M₂ monoclinic phase of VO₂ as it is illustrated in the inset figure as well. The vacuum annealing is done in a different temperature of 200°C and the HAADF image in Figure 8.9e shows the interface of VO₂/NiO-VO₂ after this process. Figure 9.8f captures the atomic structure of VO₂ in this sample which belongs to M₂ monoclinic phase as shown in the inset figure schematically as well.

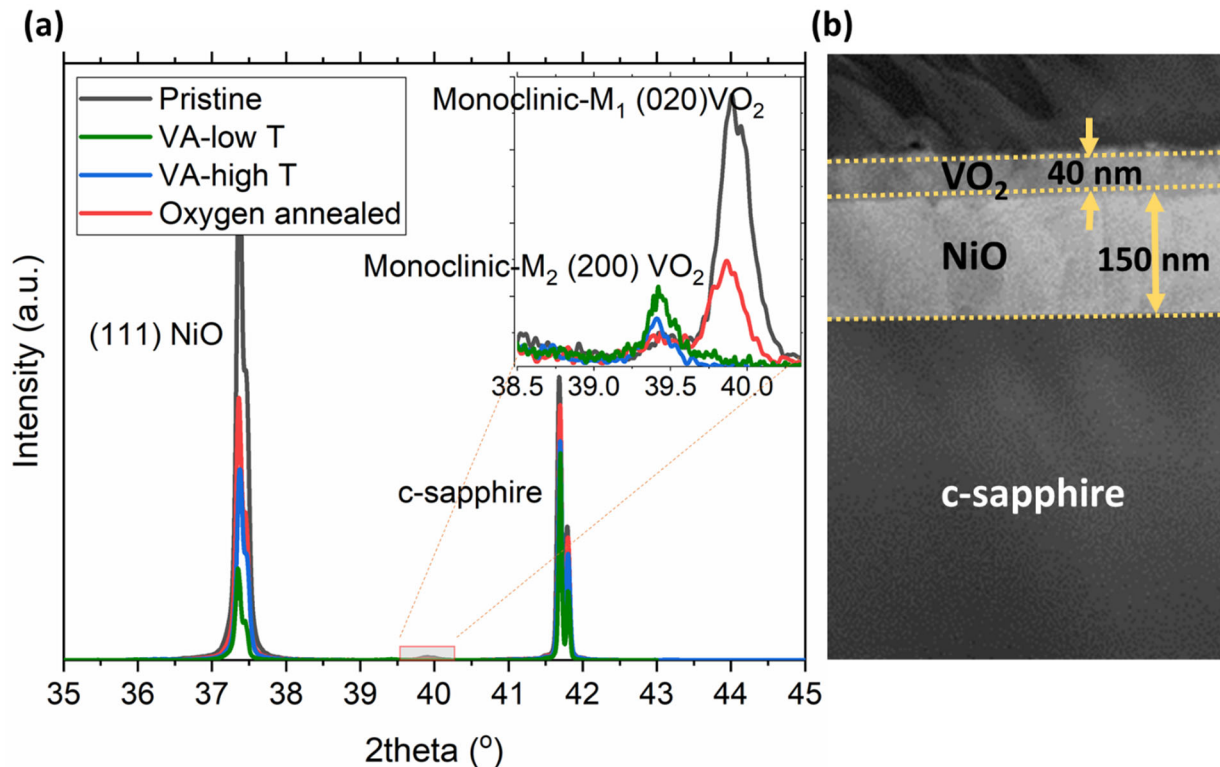


Figure 8. 8. The X-ray diffraction pattern of VO₂/NiO/sapphire thin film heterostructures above the critical thickness of ≈ 15 nm in the pristine, vacuum annealed at low and high temperatures (marked as VA-low T and VA-high T, respectively), and oxygen annealed samples. (b) The low-mag cross-sectional HAADF image of VO₂/NiO/sapphire heterostructures showing VO₂ thickness above the critical thickness.

The temperature dependent electrical resistivity measurements for pristine and annealed samples are shown in Figure 8.10. The pristine sample shows a typical hysteresis belonging to relaxed VO₂ thin films²⁹. After annealing at a low temperature in the vacuum (200°C), the metal-insulator transition gets smeared and the resistivity of the insulating phase drops vastly. Considering the fact that in M₂ phase of VO₂ there are two types of V-V chains and only in one of them the dimerization occurs, the undimerized chain can be more conductive. This can explain the lower resistivity in the insulating phase of this sample. After the transition to the metallic phase, the resistivity is lower compared to the pristine sample. This can be justified with the presence of more charge carrier (oxygen vacancies) in the system.

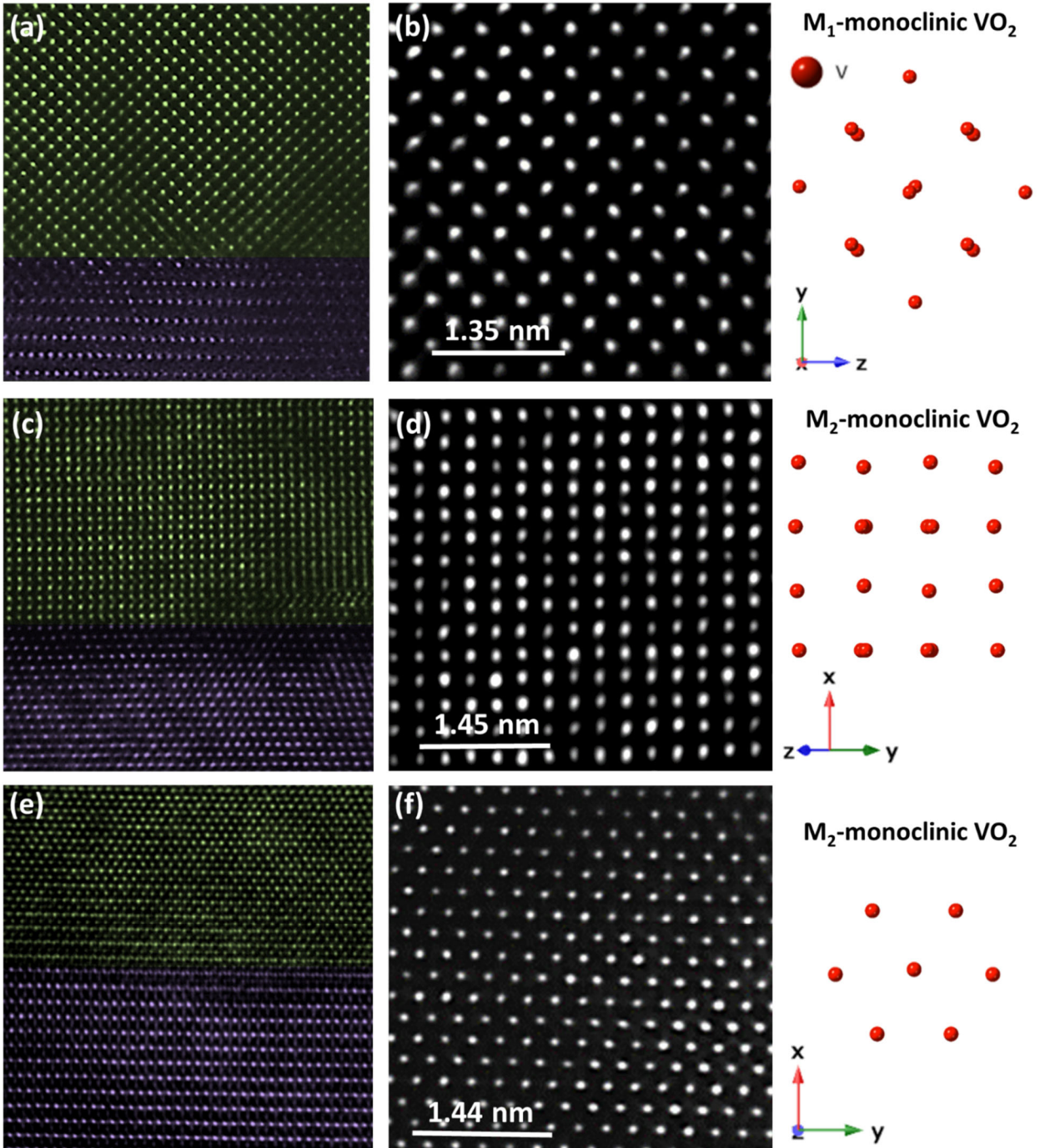


Figure 8.9. a) The HAADF micrograph belongs to the pristine VO₂/NiO-VO₂ thin film with [100] and [110] zone axis of M₁ monoclinic VO₂ and NiO, respectively. b) The atomic scale HAADF image of VO₂ in (a). c) The HAADF micrograph belongs to the high-temperature vacuum annealed VO₂/NiO-VO₂ thin film with [012] and [110] zone axis of M₂ monoclinic VO₂ and NiO, respectively. d) The atomic scale HAADF image of VO₂ in (c). e) The HAADF micrograph belongs to the low-temperature vacuum annealed VO₂/NiO-VO₂ thin film with [001] and $\bar{2}11$ zone axis of M₂ monoclinic VO₂ and NiO, respectively. f) The atomic scale HAADF image of VO₂ in (e). The inset figures provide the schematic of atomic structures for the corresponding micrograph.

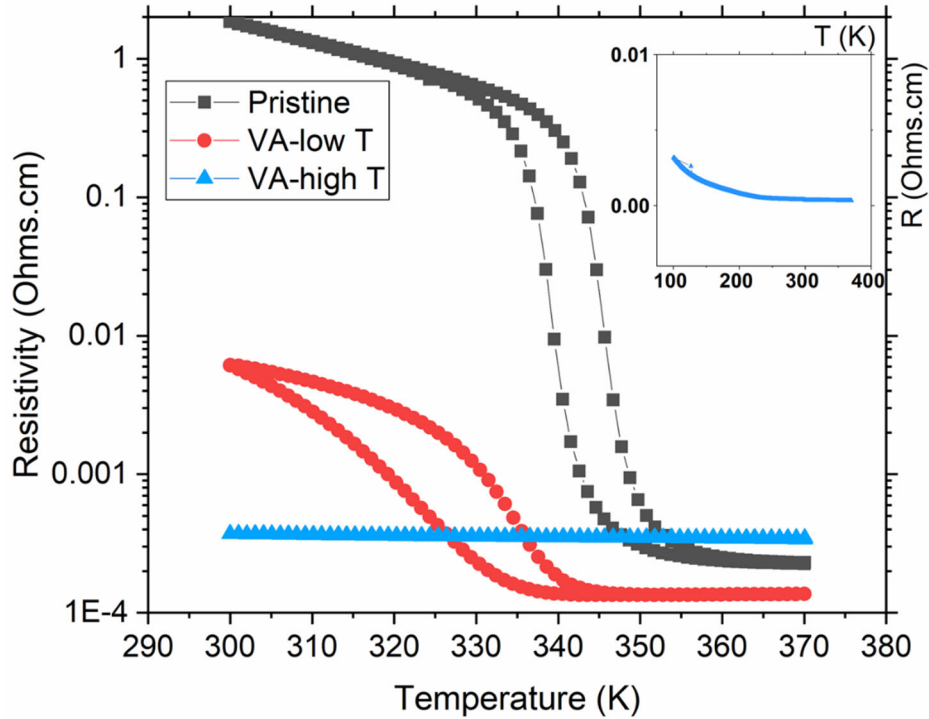


Figure 8.10. The electrical resistivity of $\text{VO}_2/\text{NiO}/\text{sapphire}$ thin film heterostructures, above the critical thickness of 15 nm for pristine, low-temperature vacuum-annealed (VA-low T), and high-temperature vacuum-annealed (VA-high T) samples. The inset figure represents the resistivity vs temperature plot for VA-high T in the full temperature range of 100-370 K.

After annealing at high temperature (450°C) in the vacuum, the metal-insulator transition vanishes. Thus, vacancies introduced during the vacuum annealing derive the formation of a stable M_2 monoclinic phase. When the carrier concentration introduced to the system is above the Mott criterion at room temperature, energetically it is favorable for the system to stay in the metallic state. The inset figure represents the full temperature range behavior for this stabilized phase which shows no sign of V_2O_3 or V_2O_5 formation upon introduction of the vacancies. The base resistivity of this phase is higher than both of the other pristine and low-temperature vacuum annealed sample. The presence of too many charge carriers in this sample increases their collision which justifies the enhanced resistivity. In the low-temperature vacuum annealed sample, the thermodynamic equilibrium vacancy concentration is lower than the high-temperature vacuum annealed sample. That prevents the low-temperature vacuum annealed sample from reaching to

the Mott criterion at room temperature. The high-temperature vacuum annealed sample is exposed to the oxygen annealing for the oxygen to get into its lattice site. Interestingly, after oxygen annealing at the same temperature, the sample goes back to the M_1 state and shows typical metal-insulator transition of the pristine sample. This behavior is illustrated in Figure 8.11. The vacuum and oxygen annealing are repeated consecutively for four samples. No degradation is observed in the hysteresis or metallic behavior as the heterostructures go through multiple cycles of annealing. The transition temperature for the hysteresis behavior, however, shifts to lower temperature and eventually comes back to known relaxed transition temperature for bulk VO_2 .

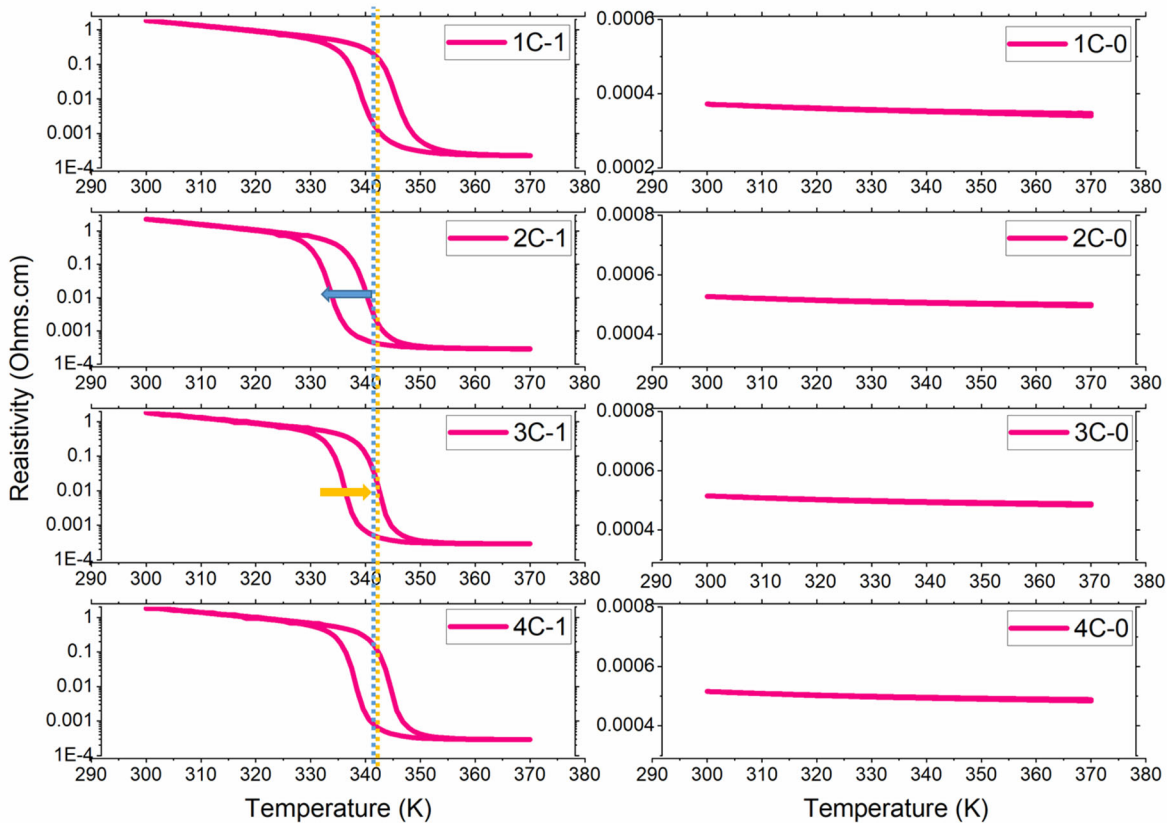


Figure 8.11. The electrical resistivity of $\text{VO}_2/\text{NiO}/\text{sapphire}$ thin film heterostructures before (marked as 1) and after high-temperature vacuum annealing (marked as 0) during four cycles (marked by 1C, 2C, 3C, and 4C).

In the pristine sample, even though the transition temperature is close to bulk behavior, there exist defects and misfit dislocations. Upon annealing at high temperatures, the system tries

to get rid of the defects through the diffusion process. We identified that another relaxation process is taking place at the interface of VO₂/NiO. The system is setting to minimize the stress field around misfit dislocations by the formation of twins at the interface as captured and illustrated in the HAADF image in Figure 8.12. The twinning involves three atomic layers. The presence of steps provides a nucleation site for twin formation. This shows that high-temperature annealing gives enough energy to enable the twin formation and relax the system further to achieve the bulk transition temperature in the 4th cycle. The presence of twins along with dislocations' stress field in the first cycle may cause local compressive strain that leads to lowering of the transition temperature, but eventually, systems come back to relax state to minimize the total energy.

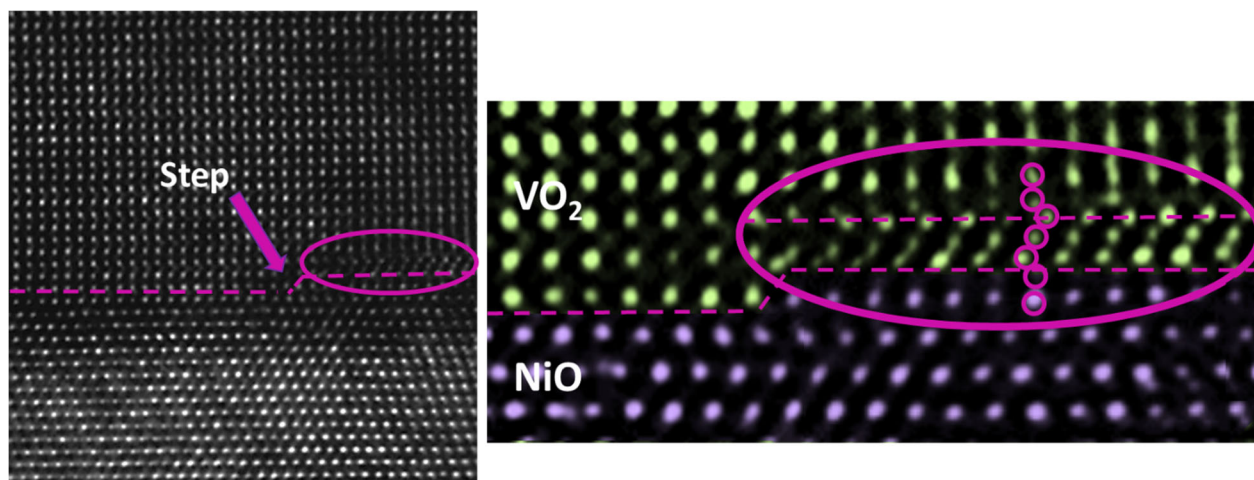


Figure 8.12. The HAADF image of high-temperature vacuum annealed VO₂/NiO/c-sapphire thin film heterostructure. The formation of twins in the vicinity of the step is illustrated at the interface of VO₂/NiO.

8.2.3. Conclusion

We successfully controlled the transition in VO₂ thin films through point defects. The introduction of oxygen vacancies at high concentration is shown to create metallic behavior in VO₂. This behavior is reversible through oxygen annealing. The film relaxation mechanisms are also activated throughout the annealing process, inducing the formation of twins at the interface which affects the transition temperature. After three cycles, the structure reaches a relaxed state.

The metallic behavior is shown to persist in M_2 monoclinic phase of VO_2 . After oxygen annealing, the structure goes back to the M_1 monoclinic phase of VO_2 . This behavior can be exploited in non-volatile memory devices for neuromorphic applications, where there is no need for an external energy source to retrieve information (stored as metallic and insulating behaviors). Considering the incredibly low power (10–15W) of the human brain, energy efficiency is critical for neuromorphic computing.

REFERENCES

1. Goodenough, J. B. The two components of the crystallographic transition in VO₂. *J. Solid State Chem.* **3**, 490–500 (1971).
2. Zylbersztein, A. & Mott, N. F. Metal-Insulator Transition in Vanadium Dioxide. *Phys. Rev. B* **11**, 4383–4395 (1975).
3. Quackenbush, N. F. *et al.* Reducing orbital occupancy in VO₂ suppresses Mott physics while Peierls distortions persist. *Phys. Rev. B* **96**, 81103 (2017).
4. Weber, C. *et al.* Vanadium dioxide: A Peierls-Mott insulator stable against disorder. *Phys. Rev. Lett.* **108**, 256402 (2012).
5. Aetukuri, N. B. *et al.* Control of the metal-insulator transition in vanadium dioxide by modifying orbital occupancy. *Nat. Phys.* **9**, 661–666 (2013).
6. Théry, V. *et al.* Role of thermal strain in the metal-insulator and structural phase transition of epitaxial VO₂ films. *Phys. Rev. B* **93**, 184106 (2016).
7. Mizokawa, T. Metal–insulator transitions: Orbital control. *Nat. Phys.* **9**, 612 (2013).
8. Viswanath, B. & Ramanathan, S. Direct in situ observation of structural transition driven actuation in VO₂ utilizing electron transparent cantilevers. *Nanoscale* **5**, 7484–7492 (2013).
9. Gatti, M., Bruneval, F., Olevano, V. & Reining, L. Understanding correlations in vanadium dioxide from first principles. *Phys. Rev. Lett.* **99**, 266402 (2007).
10. Moatti, A., Sachan, R., Prater, J. & Narayan, J. Control of Structural and Electrical Transitions of VO₂ Thin Films. *ACS Appl. Mater. Interfaces* **9**, (2017).
11. Mukherjee, S. *et al.* Tuning a strain-induced orbital selective Mott transition in epitaxial VO₂. *Phys. Rev. B* **93**, 241110 (2016).

12. Moatti, Adele, Sachan, Ritesh, Cooper, Valentino, Narayan, J. Electrical Transition in Isostructural VO₂ Thin-Film Heterostructures. *Sci. Rep.* **9**(1), 3009 (2019).
13. Moatti, A., Bayati, R. & Narayan, J. Epitaxial growth of rutile TiO₂ thin films by oxidation of TiN/Si{100} heterostructure. *Acta Mater.* **103**, 502-511 (2016).
14. Moatti, A., Bayati, R., Singamaneni, S. R. & Narayan, J. Thin film bi-epitaxy and transition characteristics of TiO₂/TiN buffered VO₂ on Si(100) substrates. *MRS Adv.* **1**, 2635-2640 (2016).
15. Hsu, H. S. *et al.* Evidence of oxygen vacancy enhanced room-temperature ferromagnetism in Co-doped ZnO. *Appl. Phys. Lett.* **88**, 242507 (2006).
16. Vanheusden, K., Seager, C. H., Warren, W. L., Tallant, D. R. & Voigt, J. A. Correlation between photoluminescence and oxygen vacancies in ZnO phosphors. *Appl. Phys. Lett.* **68**, 403–405 (1996).
17. Si, M. S. & Xue, D. S. Magnetic properties of vacancies in a graphitic boron nitride sheet by first-principles pseudopotential calculations. *Phys. Rev. B* **75**, 193409 (2007).
18. Gupta, A., Singhal, R., Narayan, J., Avasthi, D. Electronic excitation induced controlled modifications of semiconductor-to-metal transition in epitaxial VO₂ thin films. *J. Mater. Res.* **26** (23), 2901-2906 (2011).
19. Passarello, D., Altendorf, S. G., Jeong, J., Samant, M. G. & Parkin, S. S. P. Metallization of epitaxial VO₂ films by ionic liquid gating through initially insulating TiO₂ layers. *Nano Lett.* **16**, 5475–5481 (2016).
20. Zhang, Z. *et al.* Evolution of metallicity in vanadium dioxide by creation of oxygen vacancies. *Phys. Rev. Appl.* **7**, 34008 (2017).

21. Pergament, A., Stefanovich, G. & Markova, N. The Mott criterion: So simple and yet so complex. *arXiv Prepr. arXiv1411.4372* (2014).
22. Moatti, A. & Narayan, J. High-quality TiN/AlN thin film heterostructures on c-sapphire. *Acta Mater.* **145**, (2018).
23. Kelly, R., Miotello, A., Chrisey, D. B. & Hubler, G. K. Pulsed laser deposition of thin films. *by DB Chrisey GK Hubler (Wiley, New York, 1994) p 55*, (1994).
24. Moatti, A., Bayati, R., Singamaneni, S. & Narayan, J. Epitaxial integration of TiO₂ with Si (100) through a novel approach of oxidation of TiN/Si (100) epitaxial heterostructure. *MRS Adv.* **1**, 2629–2634 (2016).
25. Sachan, R. *et al.* Forging Fast Ion Conducting Nanochannels with Swift Heavy Ions: The Correlated Role of Local Electronic and Atomic Structure. *J. Phys. Chem. C* **121**, 975–981 (2017).
26. Galy, J. & Miehe, G. Ab initio structures of (M₂) and (M₃) VO₂ high pressure phases. *Solid state Sci.* **1**, 433–448 (1999).
27. Zhang, H. *et al.* The pressure-induced metallization of monoclinic vanadium dioxide. *RSC Adv.* **6**, 104949–104954 (2016).
28. Moatti, Adele, Sachan, Ritesh, Cooper, Valentino, Narayan, J. Electrical Transition in Isostructural VO₂ Thin-Film Heterostructures. *Sci. Rep.* **9** (1), 3009 (2019).
29. Kinaci, A. *et al.* Electronic transport in VO₂—Experimentally calibrated Boltzmann transport modeling. *Appl. Phys. Lett.* **107**, 262108 (2015).
30. Cui, Y., Liu, B., Chen, L., Luo, H. & Gao, Y. Formation energies of intrinsic point defects in monoclinic VO₂ studied by first-principles calculations. *AIP Adv.* **6**, 105301 (2016).

31. Yang, M. *et al.* Suppression of Structural Phase Transition in VO₂ by Epitaxial Strain in Vicinity of Metal-insulator Transition. *Sci. Rep.* **6**, 23119 (2016).
32. Martens, K. *et al.* Field Effect and Strongly Localized Carriers in the Metal-Insulator Transition Material VO₂. *Phys. Rev. Lett.* **115**, 196401 (2015).
33. Schilbe, P. Raman scattering in VO₂. *Phys. B Condens. Matter* **316**, 600–602 (2002).
34. Chen, L. *et al.* Tuning the phase transition temperature, electrical and optical properties of VO₂ by oxygen nonstoichiometry: insights from first-principles calculations. *RSC Adv.* **6**, 73070–73082 (2016).
35. Marini, C. *et al.* Optical properties of V_{1-x}Cr_xO₂ compounds under high pressure. *Phys. Rev. B* **77**, 235111 (2008).
36. Kim, H.-T. *et al.* Hole-driven MIT theory, Mott transition in VO₂, MoBRiK device. *Phys. C Supercond.* **460**, 1076–1078 (2007).
37. Gupta, S. *et al.* Room-temperature ferromagnetism in epitaxial titanium nitride thin films. *Acta Mater.* **166**, 221-230 (2019).
38. Srivastava, R. & Chase, L. L. Raman Spectrum of Semiconducting and Metallic VO₂. *Phys. Rev. Lett.* **27**, 727 (1971).
39. Kim, H.-T. *et al.* Raman study of electric-field-induced first-order metal-insulator transition in VO₂-based devices. *Appl. Phys. Lett.* **86**, 242101 (2005).
40. Baldini, M. *et al.* Pair distribution function analysis: The role of structural degrees of freedom in the high-pressure insulator to metal transition of VO₂. *Phys. Rev. B.* **93**, 245137 (2016).
41. Moatti, A., Sachan, R., Prater, J. & Narayan, J. An optimized sample preparation approach for atomic resolution in situ studies of thin films. *Microsc. Res. Tech.* **81** (11), 1250-1256 (2018).

APPENDICES

Appendix A

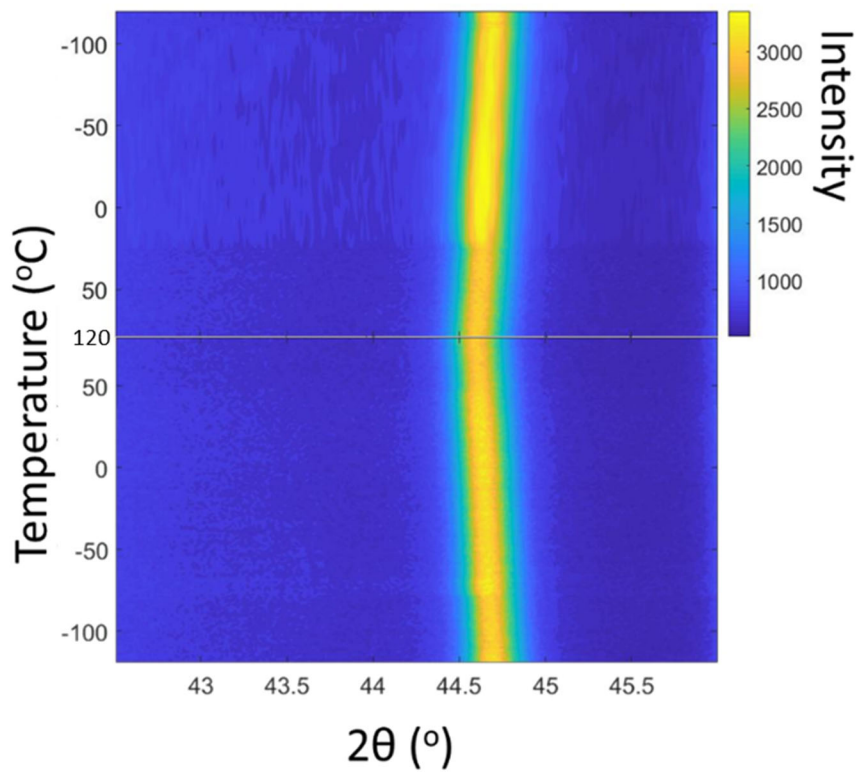


Figure S1. *In-situ* XRD measurements of the vacuum-annealed sample over the range of -120+120 °C, showing no sign of V₂O₃ or Magneli phases formation.

CHAPTER 9

9. Spin engineering-Magnetic tuning of structural phase transition in Ni/VO₂/c-YSZ/Si heterostructures (Structural pinning of M₂ monoclinic induced by spin engineering in VO₂ thin-films)

Abstract

The electron-correlated vanadium dioxide undergoes a metal-to-insulator transition which is considered a combination of Mott and Peierls, where the energy of electron-electron, electron-lattice, spin-spin, and spin-lattice interactions are of the same order of magnitude. Thus, the charge, lattice, and spin degrees of freedom and their interactions lead to the observation that the electronic phase transitions in VO₂ coexist with the structural and other types of transitions. This unique property provides us with the opportunity to manipulate the extent of the contribution of these interactions to control one transition while pinning the others. Here, spin engineering has been used to affect the spin-spin and spin-lattice interactions in VO₂ by introducing a strong ferromagnetic Ni layer with an enhanced coercive field. The coercivity in the Ni layer is engineered by controlling the shape anisotropy via kinetics of growth resulting in continuous islands. The structural pinning of monoclinic M₂ phase of VO₂ is successfully achieved, while the electronic and magnetic transitions are allowed to occur.

9.1. Introduction

Vanadium dioxide is one of the materials known to have strong electron-electron correlations. This material exhibits a metal-to-insulator transition which typically is accompanied by V-V dimerization^{1,2}. The important nature of VO₂ transition is that the energy of many interactions such as electron-lattice interaction, spin-spin interaction and so on is of the same order

of magnitude as the electron-electron correlation and kinetic energy (role of temperature)³⁻⁵. Thus, in combination, they can all play a role in defining the electronic properties of VO₂. That is why the electrical transition occurs simultaneously with the structural transition. VO₂ does not contain a pure Mott transition and it needs assistance from lattice, charge, orbital, and spin degrees of freedom^{6,7}. As a result, to trigger the transition, the interplay between these degrees of freedom is important and offers different opportunities for manipulating the electronic properties of the VO₂^{8,9}, i.e. the structural symmetry changes can drive the electrical transition and vice versa. So, the V-V dimerization is suggested to be the result of the coordination of both Mott and Peierls physics. The simultaneous occurrence of electrical (insulator to metal) and structural (monoclinic to tetragonal) transitions directly affect the endurance and lifetime of thermal switches and sensors. In a recent work, a new and unique strain-stabilized isostructural monoclinic VO₂ epitaxial thin film was unveiled where the insulator-to-metal transition (IMT) occurs without any structural phase transition (SPT)¹⁰. It is shown that if the difference between V-V bond lengths in the monoclinic phase decreases, the bandgap gets smaller which facilitates the Mott transition while pinning the structural transition. In other words, the electron correlation effect gets enhanced by the manipulation of V-V bond length or lattice-electron interaction. The formation of such isostructural VO₂ increases the opportunity for generating ultrafast devices since there is an order of magnitude difference between the rate of occurrence of the structural and electrical transitions^{5,11,12}. The technical challenge for such a work, however, is to keep the thin-film below the critical thickness of about 15 nm. For control above the critical thickness, the engineering of other degrees of freedom will be required. We propose using a strong ferromagnetic material such as Ni as a top layer to introduce additional spin-spin and spin-lattice interactions especially at the interface of Ni/VO₂. Ni has been used previously in combination with VO₂ thin films¹³⁻¹⁶.

However, the focus of those studies was on the magnetic properties of Ni in the vicinity of VO₂ transition. There is no report on the structural pinning of VO₂ in contact with Ni. There are two major concerns with those studies: (i) the VO₂ was used in the polycrystalline form, and (ii) the coercivity of the Ni layer was low and could be improved by enhancing the shape anisotropy. The kinetics of growth defines the island size and their shape, and the formation and glide of misfit dislocations in epitaxially strained thin films. These, in turn, are determined by the growth temperature and the film growth rate. Accordingly, the film morphology is expected to tune the magnetic anisotropy, which has been observed in many experiments. The shape anisotropy and misfit strain (magnetoelastic anisotropy) in Ni dictate the easy magnetization direction. If the demagnetization field is high, it yields a high coercive field. This leads to the enhanced difficulty in moving domain walls and changing the direction of the magnetization in those domains, making it difficult to magnetize and demagnetize these domains.

Here we study the integration of VO₂ with Ni and closely monitor the electrical and structural transitions. The Ni morphology has been accurately adjusted to enhance the coercivity (3D growth) and provide pinned spins at the Ni/VO₂ interface. Then, this heterostructures has been compared with Ni flat films (2D growth) integrated with VO₂ to study the effect of spin engineering on the VO₂ metal-to-insulator transition. We have been able to prevent the structural transition of a thick VO₂ thin film by employing extrinsic spin pinning stimuli. Moreover, integration on silicon has been chosen since it enhances the possibility for the development of future infrared smart sensors, where the sensor and computational function can be embedded on a single chip. This quality combined with the structural pinning offers the potential of developing ultra-fast sensors which are more energy efficient.

9.2. Experimental

Ni/VO₂/YSZ/Si(001) epitaxial heterostructures were deposited using pulsed laser deposition (PLD)¹⁷⁻²⁰. Samples were prepared in a high vacuum, a multi-target deposition chamber (base pressure = 5×10^{-7} Torr). A KrF excimer laser ($\lambda = 248$ nm) was employed to ablate the c-YSZ (8 mol % Y₂O₃), VO₂ and Ni targets onto the Si substrate. Yttria-stabilized zirconia (YSZ) was chosen as a buffer layer between the Si substrate and the VO₂ film because of its excellent chemical stability on Si. The temperature during deposition was set to be 755°C and 540°C for c-YSZ and VO₂, respectively. The c-YSZ was deposited under oxygen partial pressure of 6.5×10^{-4} Torr. The VO₂ was deposited and cooled down in an oxygen partial pressure of 1.2×10^{-2} Torr. Once cooled down to the desired temperature, Ni films were then deposited under vacuum condition. Two different temperatures were chosen for the Ni deposition in order to produce both Volmer-Weber (3D or island) and Frank-van der Merwe (2D) growth. The 3D Ni samples were deposited at 280°C, whereas the 2D layer Ni samples were deposited at 150°C. The energy of the laser was set to 3-3.4 Jcm⁻², 2-3 J.cm⁻², and 2-3 J.cm⁻² for Ni, VO₂, and c-YSZ, respectively. The laser was used at 5 Hz frequency for depositing all the layers.

X-ray diffraction (XRD) θ - 2θ and ϕ -scans were performed, using a Rigaku X-ray diffractometer with a Cu K α source ($\lambda = 1.5418$ Å), to verify the quality of the films. Temperature-dependent XRD patterns of the different Ni/VO₂ thin films were collected during the heating and cooling cycles using a PANalytical Empyrean. A JEOL 2010 high-resolution, field emission transmission electron microscope (HR-TEM) and selected-area-electron diffraction (SAED) provided confirmation of the Ni growth mode as well as crystallinity. The FEI Titan 80-300 probe aberration-corrected scanning transmission electron microscope (STEM) operated at 200 kV was employed to collect atomic resolution HAADF images with the resolution limit of 0.07 nm, and

electron energy loss spectra (EELS) with an energy resolution of the electron source as high as 0.15 eV²¹. The electrical measurements were collected using a Quantum Design physical property measurement system (PPMS). Magnetic hysteresis measurements were then performed on the Ni/VO₂ heterostructures using a Quantum Design superconducting quantum interference device (SQUID) magnetometer over a temperature range of 4 K to 400 K while sweeping a magnetic field of ± 1000 Oe²². The magnetic moment vs temperature measurements were collected with and without the presence of a 200 Oe magnetic field.

9.3. Results and discussion

The Ni has been grown in two different growth modes, two-dimensional (2D) and three-dimensional (3D), on the VO₂/c-YSZ/Si heterostructures as shown in TEM micrographs in Figure 9.1a and b. X-ray diffraction (XRD) θ - 2θ -scan (out of plane) and ϕ -scan (in-plane) of both 3D and 2D Ni on the VO₂/c-YSZ/Si heterostructures depict the epitaxial nature of all the layers (Figure 9.1c, d, e, and f).

For 2D-Ni//c-YSZ/VO₂/Si heterostructures, the out-of-plane relationship was established to be Ni(002)/M₁-VO₂(020)/c-YSZ(111)/Si(100). For the 3D-Ni//c-YSZ/VO₂/Si heterostructures, however, after deposition of the Ni layer, the 2θ position of the VO₂ out-of-plane peak moves toward (002)M₂-VO₂. This leads to the out-of-plane relationship of Ni(002)/M₂-VO₂(002)/c-YSZ(111)/Si(100). The monoclinic nature of the VO₂ films was further confirmed by phi-scan symmetry information. In strain-free crystals, the transition from high-temperature rutile (R) phase ($a = b = 0.455$ nm and $c = 0.285$ nm) occurs directly into low-temperature monoclinic M₁ phase ($a = 0.575$ nm; $b = 0.453$ nm; $c = 0.538$ nm, $\beta = 122.60$). However, in the presence of internal and external stimuli, the formation of a transient monoclinic (C2/m) phase M₂ ($a = 0.906$ nm, $b = 0.580$ nm, $c = 0.425$ nm, $\beta = 91.80$) which is an intermediate of M₁ and R phases, often broadens

the transition characteristics²³. After deposition and cooling down to room temperature of the 3D-Ni, it appears that the M₂ phase may be stabilized.

Using the $\theta - 2\theta$ results, the 2θ and the $d_{(020)}$ -spacing values for the VO₂ in the 2D-Ni/VO₂ heterostructures are seen to equal 39.96° and 2.2561Å, respectively. The experimental values were compared to the standard values (M₁-VO₂ $d_{(020)} = 2.2585\text{Å}$) and the out-of-plane strain within the VO₂ film was calculated to be -0.11%; indicating that there is a very small compressive strain, and that the island VO₂ film is near full relaxation in the out-of-plane growth direction. For the 3D-Ni/VO₂ heterostructures, the 2θ and the $d_{(002)}$ -spacing values equals 39.56° and 2.2753Å, respectively. The standard values (M₂-VO₂ $d_{(002)} = 2.2616\text{Å}$) were compared to the experimental data and the out-of-plane strain within the VO₂ film was calculated to be 0.60%, indicating that there is a very small tensile strain. The Ni peak appears at 2θ of 44.60 and 44.64 for 2D and 3D growth, respectively. When compared to the literature (Ni $d_{(111)} = 2.034\text{Å}$), the residual out-of-plane strain for the 2D and 3D grown Ni films is -0.23% and -%0.32, respectively, indicating that the Ni films are near full relaxation in the out-of-plane orientation where they contain only a small compressive strain.

From the phi-scan, the epitaxial relationship for 2D-Ni/VO₂/c-YSZ/Si heterostructures can be written as:

$$(\bar{2}11) \text{ Ni} \parallel (10\bar{1}) \text{ R-VO}_2 \parallel (100) \text{ M}_1\text{-VO}_2 \parallel (010) \text{ c-YSZ} \parallel (010) \text{ Si}$$

$$(\bar{1}01) \text{ Ni} \parallel (502) \text{ R-VO}_2 \parallel (407) \text{ M}_1\text{-VO}_2 \parallel (100) \text{ c-YSZ} \parallel (100) \text{ Si}$$

$$(111) \text{ Ni} \parallel (010) \text{ R-VO}_2 \parallel (010) \text{ M}_1\text{-VO}_2 \parallel (001) \text{ c-YSZ} \parallel (001) \text{ Si}$$

The Si(202) and YSZ(202) reflections coincide, each showing sharp 4-fold symmetry (4 peaks) and there is no in-plane rotation between them. This lack of rotational shift confirms the cube on cube growth of c-YSZ on Si (100). The VO₂ (011) reflection has an angular separation of

32° from the c-YSZ (202) and Si (202) reflections. This separation and presence of eight peaks indicate a two-fold symmetry in the (011) reflection with four possible alignments of the VO₂ and c-YSZ unit cells. The twelve peaks for Ni can be interpreted as four in-plane domains of three-fold symmetry (3 peaks) with 120° separation. The four domains are at a 30° rotation with respect to each other and represent two sets of twins. Twinning in FCC metals such as Ni, is quite common, especially along the [111] direction, which in this case is the out of plane growth direction^{24,25}. The Phi-scan exhibits eight sharp peaks for M₁-VO₂ at 32° angular separation from YSZ (101) reflections. The eight stronger peaks correspond to two-fold symmetry of (011) reflections and four equally probable in-plane arrangements.

From the phi-scan the epitaxial relationship for 3D-Ni/VO₂/c-YSZ/Si heterostructures can be written as:

$$(\bar{1}01) \text{ Ni} \parallel (001) \text{ R-VO}_2 \parallel \sim (020) \text{ M}_2\text{-VO}_2 \parallel (010) \text{ c-YSZ} \parallel (010) \text{ Si}$$

$$(\bar{2}11) \text{ Ni} \parallel (100) \text{ R-VO}_2 \parallel \sim (200) \text{ M}_2\text{-VO}_2 \parallel (100) \text{ c-YSZ} \parallel (100) \text{ Si}$$

$$(111) \text{ Ni} \parallel (010) \text{ R-VO}_2 \parallel (001) \text{ M}_2\text{-VO}_2 \parallel (001) \text{ c-YSZ} \parallel (001) \text{ Si}$$

The phi-scan exhibits eight sharp peaks for M₂-VO₂ at 32° angular separation from c-YSZ (101) reflections. The eight peaks correspond to a two-fold symmetry of (20 $\bar{1}$) reflections and four equally probable in-plane arrangements.

Table 9.1. Crystallographic parameters used to collect the XRD ϕ -patterns through the Si (202), cubic YSZ (202), M₁-VO₂ (011), M₂-VO₂ (20 $\bar{1}$), and Ni (200) reflections represented in Figure 9.1.

	Ni (200)	M₁-VO₂ (011)	M₂-VO₂ (20$\bar{1}$)	c-YSZ (202)	Si (202)
2Θ (°)	51.84	27.79	27.39	50.08	47.304
Ψ (°)	54.73	44.40	44.01	45	45

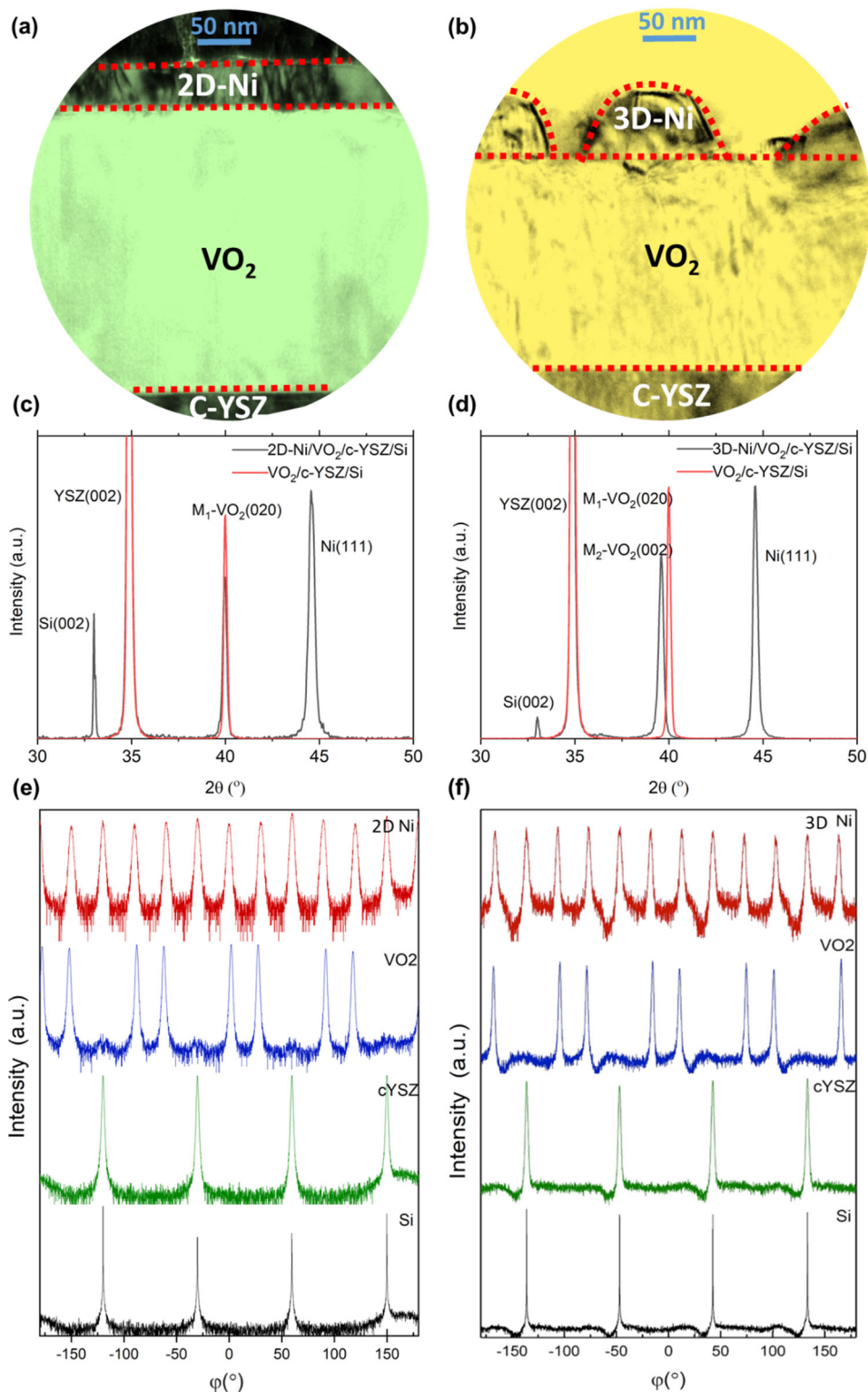


Figure 9.1. The cross-sectional low magnification TEM micrographs of Ni/VO₂ interface for (a) 2-D growth mode of Ni, and (b) 3-D growth mode of Ni. Θ - 2Θ XRD patterns of the VO₂/YSZ/Si thin film heterostructures before and after Ni deposition for (c) 2-D growth mode of Ni, and (d) 3-D growth mode of Ni. XRD ϕ -scans through the Si (202), cubic YSZ (202), M₁-VO₂ (011), M₂-VO₂ (20 $\bar{1}$), and Ni (200) reflections for (e) 2-D growth mode of Ni, and (f) 3-D growth mode of Ni.

To further investigate the structure of M_2 - VO_2 phase and the epitaxial relationship, the SAED pattern and the HAADF image belong to this zone-axis captured by STEM are depicted in Figure 9.2a. The SAED pattern confirms the M_2 structure for VO_2 and the provided epitaxial relationships. Figure 9.2b represents the 3D-Ni/ M_2 - VO_2 interface at a different zone-axis. There is an in-plane rotation for the VO_2 structure which was previously observed in phi-scan patterns as well. The in-plane rotation may occur to accommodate the misfit strain at the Ni/ VO_2 interface as the film transforms from rutile to M_2 phase at the growth temperature. In the inset of Figure 9.2 a and b, the schematic M_2 - VO_2 structures along with their coordinates have been provided.

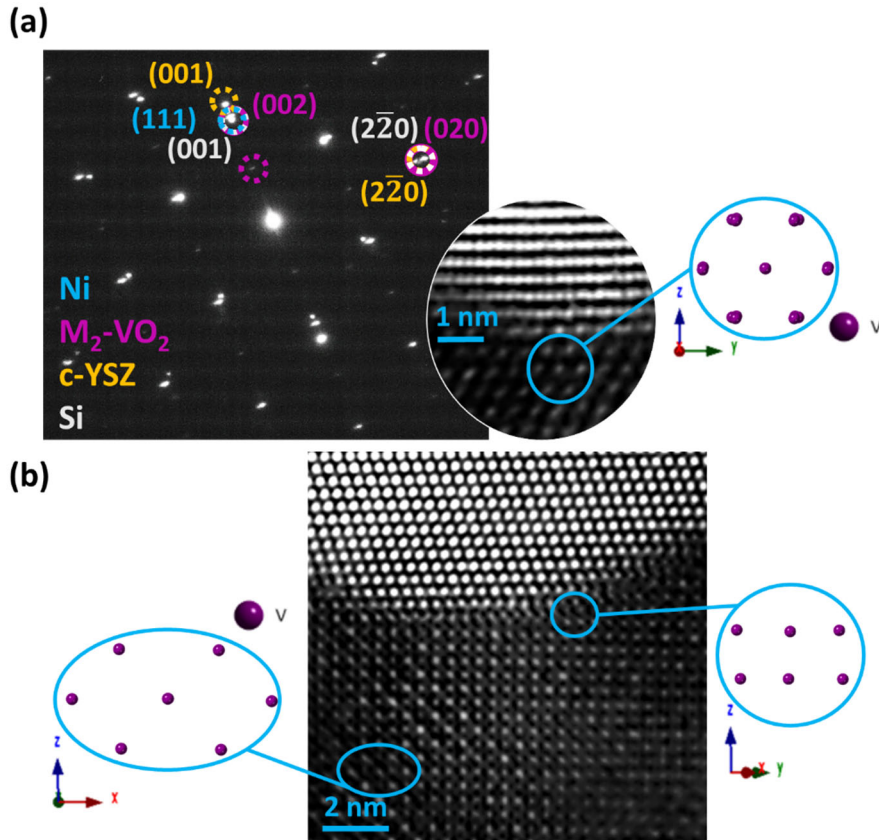


Figure 9.2. (a) The SAED pattern of 3D-Ni/ M_2 - VO_2 /c-YSZ/Si heterostructures belongs to the zone axis of $[110]$ Si, which showing the parallel alignment of $(\bar{2}11)3D-Ni/(100)M_2-VO_2/(110)c-YSZ/(110)Si$. The inset figure is a STEM-HAADF micrograph of Ni/ VO_2 interface and the schematic representation of M_2 - VO_2 belong to this zone-axis. (b) The STEM-HAADF micrograph of Ni/ VO_2 interfaces at the zone axis of $[110]$ Ni. The 60° in-plane rotation is observed for M_2 - VO_2 . The inset figure is the schematic representations of M_2 - VO_2 belong to two zone-axes of $[010]$ and $[\bar{1}10]$.

The V-V and V-O bonding characteristics in the pinned VO₂ thin films are analyzed by Raman spectroscopy and compared with the bulk VO₂ thin films as control samples in Figure 9.3a. The excitation laser beam (532 nm) spot size was ~1 μm; with the laser power restricted to 0.1 mW to avoid heat-induced phase transitions. The Raman spectra present in Figure 9.3a identifies the M₁ phase at room temperature for the bulk sample with sharp Raman peaks at 129, 196, 224, 308, 386, 498, and 614 cm⁻¹ belonging to A_g symmetry and 268, 340, and 445 cm⁻¹ for B_g symmetry²⁶⁻²⁸. The spectra are calibrated using the standard Si <100> vibrational peak at 520.6 cm⁻¹. The structural changes in strained VO₂ thin films with 2D and 3D Ni growth are analyzed by performing representative routine fits^{8,29} on V-V bonding states in Figure 9.3b and c. From Figure 9.3b, the high-frequency mode at ~645 cm⁻¹ (ω_{V-O}) is related to the reduced mass between the oxygen (O) and the vanadium (V) atoms, providing information relevant to V-O bonding states. Notably, in the case of 2D-Ni/VO₂, there is a shift in V-O peak from 615 cm⁻¹ to 640 cm⁻¹. Based on the spectral position of ω_{V-O} as a fingerprint for different VO₂ phases, the formation of M₂ phase of VO₂ is suggested in 3D-Ni/VO₂ films. This frequency shift may be closely related to a sensitive shift in phonon frequency associated with a structure distortion or symmetry change of V and O atoms in sub-lattices. Figure 9.3c shows that V-V mode is around 223 cm⁻¹ for 2D-Ni/VO₂, which is identified as an M₁ phase²⁸ at room temperature, changes to 219 cm⁻¹ for 3D-Ni/VO₂ films. The latter is due to a V-V mode associated with the rearrangement of V-V pairs in the M₂ phase³⁰⁻³². These prominent features explicitly reveal the stabilization of M₂ phase of VO₂ in the case of 3D grown Ni films on VO₂. These results are consistent with the X-ray diffraction and HAADF imaging studies, highlighting the stabilization of phase-pure epitaxial monoclinic M₂ film at room temperature. Notably, films under small compressive/tensile strain (< 1%) exhibit characteristic M₁ modes³². As the tensile strain increases, a redshift of ω_{V-O} occurs which is accompanied by the

emergence of an additional peak of lower frequency. The two peaks continue to split and shift until, at a critical strain value, there is an abrupt transition into the M_2 phase.

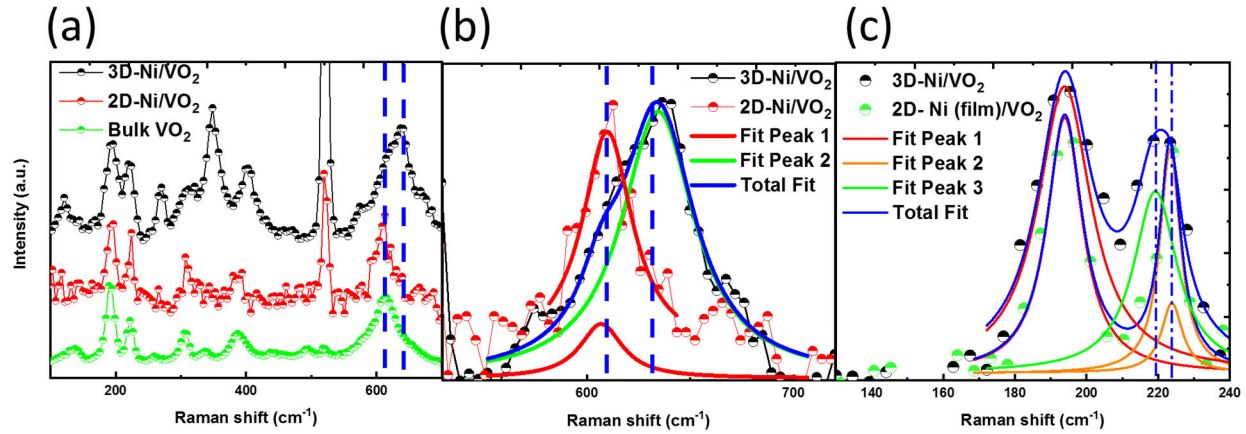


Figure 9.3. (a) Raman spectra for bulk VO₂ film, 2D and 3D-Ni/VO₂ films thin films. (b) Raman fitting for V-O bonding states in 2D and 3D-Ni/VO₂ thin films. (c) High-resolution Raman spectra for 2D and 3D-Ni/VO₂ films, highlighting the peak shift in V-V₂ peak as a result of M_2 phase formation.

To study the structural transition as a function of temperature in these two heterostructures, *in-situ* XRD has been employed. The 2D-Ni/VO₂ films show typical behavior of rutile to M_1 monoclinic transition in VO₂ structure as a function of temperature shown in Figure 9.4a. In 3D-Ni/VO₂ films, however, no structural transition is observed (Figure 9.4b). The M_2 -peak is stable across the whole temperature range of 300-370 K. The thermal expansion provides a small deviation in the peak position. These patterns clarify that the deposition of 3D-Ni has stabilized the M_2 phase of VO₂.

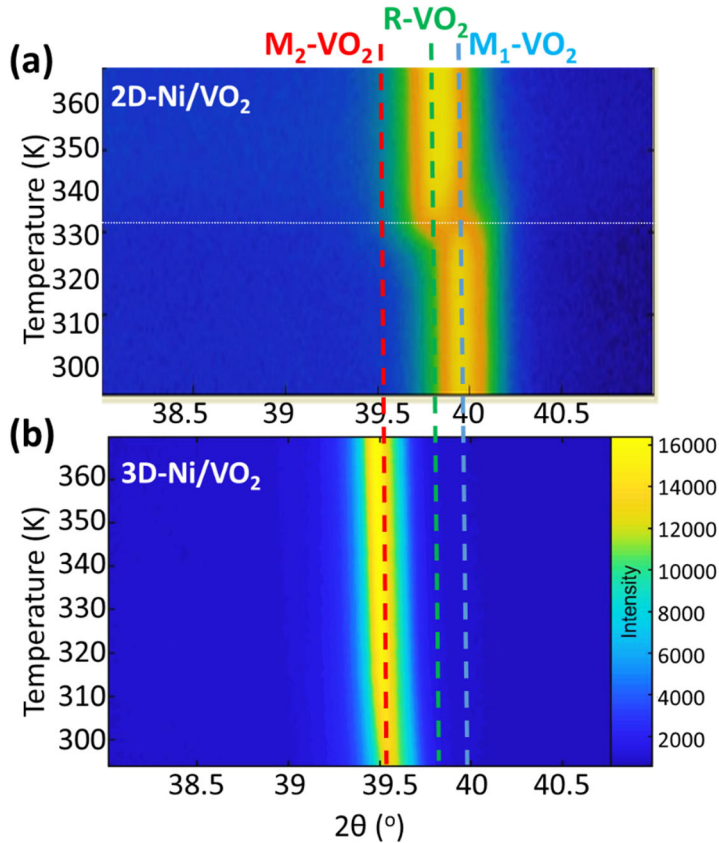


Figure 9.4. The in-situ XRD patterns as a function of temperature in (a) 2D-Ni/VO₂/c-YSZ/Si, and (b) 3D-Ni/VO₂/c-YSZ/Si heterostructures.

The electrical behavior of these films was also investigated to study the metal to insulator transition. Due to the parallel resistor configuration in these heterostructures, the electrical behavior of Ni dominates and most of the current pass through the Ni layer. However, the changes across the VO₂ transition is still detectable. Figure 9.5a shows the resistivity versus temperature plots for VO₂/c-YSZ/Si before and after depositing a very thin 2D layer of Ni. The presence of Ni squeezes the VO₂ hysteresis and as the Ni layer gets thicker, this effect becomes more prominent. Figure 9.5b depicts the resistivity vs temperature plot for 3D-Ni/VO₂ layers in a full temperature range of 4-370 K. It is observed that the electrical transition occurs in both 2D-Ni/VO₂ and 3D-Ni/VO₂. The presence of hysteresis between cooling and heating cycles and the reverse trend of resistivity for Ni around the VO₂ transition temperature indicate the electrical transition in 3D-

Ni/M₂-VO₂ films. We propose that the magnetic behavior of Ni plays a role in pinning of M₂ phase across the electrical transition in 3D-Ni/VO₂ films. Figure 9.5c represents the higher resolution of resistivity vs temperature plots at the presence of -1T, 0T, and +1T magnetic field. No difference is observed in the electrical transition of VO₂ in the presence of magnetic field and the plots are identical. Thus, the magnetic measurements were performed on both heterostructures. Figure 9.6a and b show magnetic moment (M) vs magnetic field (H) plots for 2D-Ni/VO₂ and 3D-Ni/VO₂, respectively, in zero fields cooled (ZFC) condition at different temperatures. Figure 9.6c and d represent M-H plots for 2D-Ni/VO₂ and 3D-Ni/VO₂, respectively, in the field-cooled (FC) condition (200Oe) at different temperatures. In the FC plots, the coercivity is enhanced at all temperatures. It is inferred that there is a magnetic ordering in VO₂ which is resisting ferromagnetic ordering in Ni. The FC plots also reveal the higher coercivity of 3D-Ni over 2D-Ni films. Figure 9.6e compares the coercivity vs temperature plots for these two samples where the coercivity of the 3D-Ni film is higher than the 2D-Ni film in all the temperatures. The shape anisotropy of a flat film induces high demagnetizing factor along the film normal and is almost negligible along the length of the film. This contribution favors easy magnetization along the in-plane axis^{33,34}. In contrast to 2D-films, where the in-plane magnetization does not lead to any demagnetization field for large film areas, a demagnetization field needs to be accounted for due to the in-plane magnetization of 3D-films, which yields a high coercive field^{35,36}. That means it is difficult to move the magnetic domain walls as changing the direction of the domain magnetization. Also, the coercivity can be increased by pinning of the domain walls. The residual strain at the 3D-Ni/VO₂ interface is slightly higher than 2D-Ni/VO₂ and further impede the domain wall motion and hence contribute to the coercivity. Thus, it is difficult to magnetize 3D-Ni to saturation and to demagnetize it back to zero magnetization. The increased coercivity generates stable spins that can

affect the VO₂ properties. It is evident that the behavior of 3D-Ni/VO₂ heterostructures differs seriously in the FC and ZFC conditions suggesting a strong interfacial reaction between VO₂ and 3D-Ni layers. Interestingly, it is shown that the M₂ phase of VO₂ has antiferromagnetic property³⁷. When a system consisting of ferromagnetic (FM)-antiferromagnetic (AFM) is cooled with the field (FC) through the Néel temperature of the AFM, exchange bias is induced which shows up as a shift in M vs H hysteresis loop along the magnetic field axis. This occurs due to exchange coupling leading to the pinning of the spins at the interface of FM/AFM. The inset plot at the top right corner of Figure 9.6e shows the exchange bias (H_{EB}) at different temperatures obtained from FC M- H plots for 2D and 3D-Ni/VO₂ films. H_{EB} is present in both samples, however, in 3D-Ni/VO₂ there is an enhancement around 350 K. Figure 9.6f depicts a peak in the second derivative plot of H_{EB} vs temperature. This peak is indicative of some magnetic transition. The exchange bias can also be monitored through magnetic moment behavior as a function of temperature in field-cooled and zero fields-cooled conditions as it is illustrated in Figure 9.7a. Below the Néel temperatures (T_N) AFM materials appear magnetically ordered with a zero net magnetic moment due to parallel and anti-parallel spins in a preferred direction. When they are joined to an FM, however, localized net moments are introduced that emanate from several sources. In AFM thin films with compensated interfacial spin planes, the balance between numbers of parallel and antiparallel spins is meddled at the surface, due to various sources such as misfit dislocations, surface steps, and surface roughness. As a result, localized net AFM moments are generated. Below the FM Curie temperature T_C but before the T_N of the AFM, the application of an applied field will couple the FM-AFM systems, the FM spins will align in the field direction, while the localized AFM spins will be coupled to the aligned FM spins. As the temperature is lowered through T_N, if the interfacial AFM spins are strongly coupled to the AFM lattice which is increased by magnetocrystalline

anisotropy, they will not be substantially rotated out of their alignment direction by the field applied at temperatures below T_N . But they can exert a strong torque on neighboring FM spins, tending to keep them aligned in the direction of the cooling field (a unidirectional anisotropy). This can cause a gap between field-cooled (FC) and zero fields-cooled (ZFC) magnetization plots as it is shown in Figure 9.7a³⁸. The derivative of the difference between moments in FC and ZFC plots vs temperature determines this blocking temperature as it is depicted in Figure 9.7b. This temperature interestingly is close to the metal-insulator transition in VO_2 .

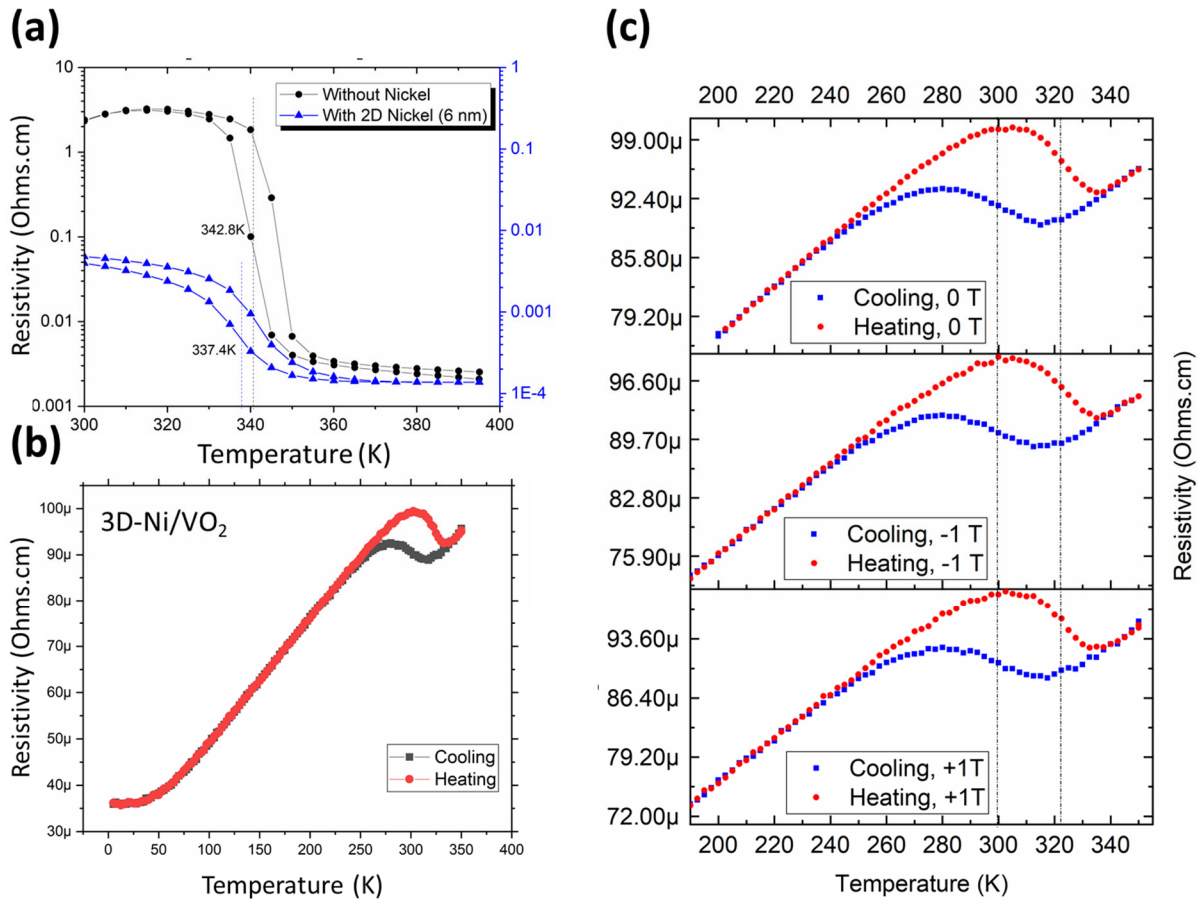


Figure 9.5. a) Resistivity vs temperature plots for $\text{VO}_2/\text{c-YSZ}/\text{Si}$ heterostructures before and after depositing a 6 nm 2D-Ni layer. b) The resistivity vs temperature plot for $3\text{D-Ni}/\text{VO}_2/\text{c-YSZ}/\text{Si}$ heterostructure in the temperature range of 4-370 K. c) Resistivity vs temperature plots in the presence of -1T, 0T, and +1T magnetic field for $3\text{D-Ni}/\text{VO}_2/\text{c-YSZ}/\text{Si}$ heterostructure.

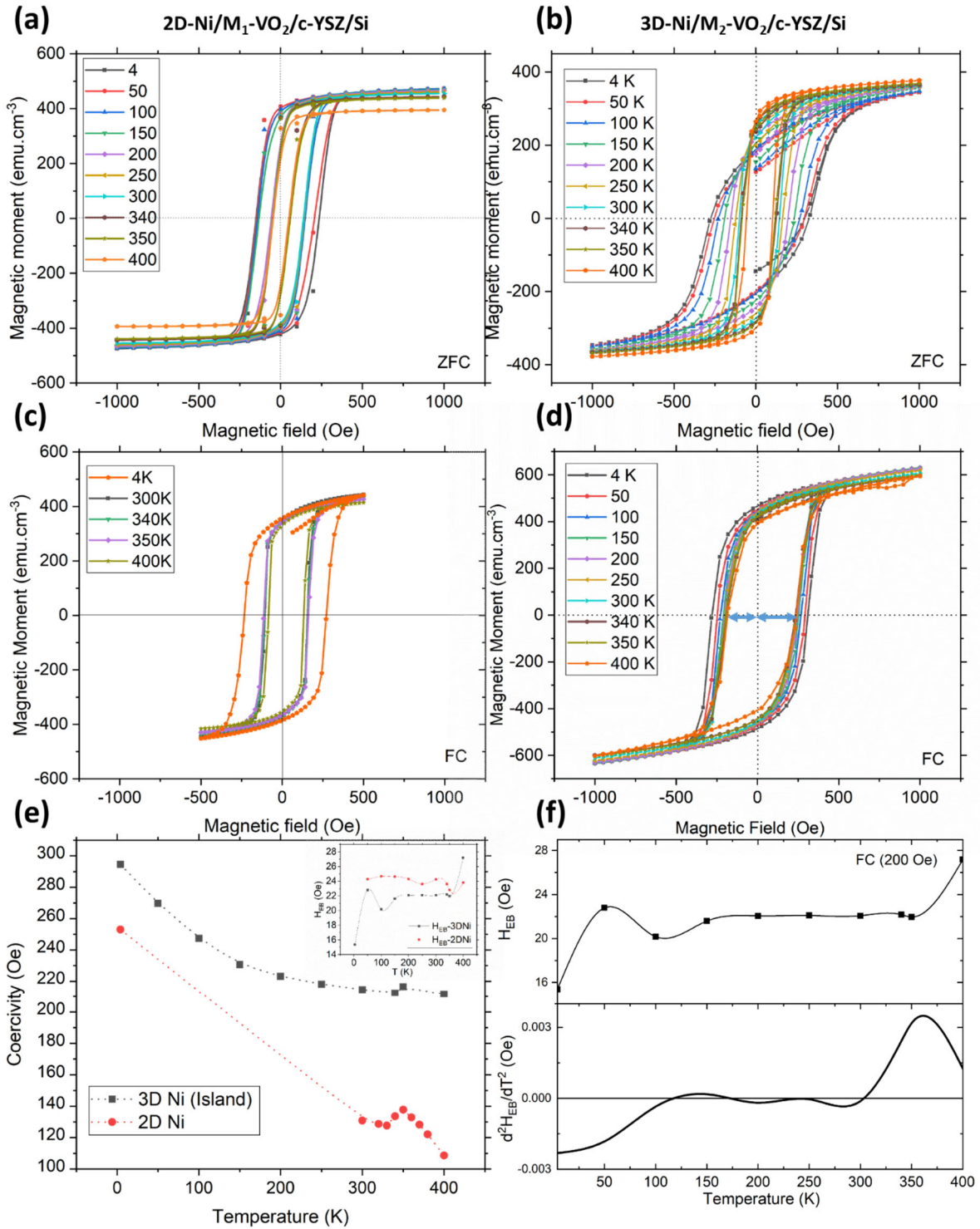


Figure 9.6. a, b) The zero fields-cooled (ZFC) magnetic moment measurements as a function of temperature for 2D-Ni/VO₂ and 3D-Ni/VO₂ films, respectively. c, d) The field-cooled (FC) magnetic moment measurements as a function of temperature for 2D-Ni/VO₂ and 3D-Ni/VO₂ films, respectively. e) The coercivity vs temperature plot for 2D-Ni/VO₂ and 3D-Ni/VO₂ films. The inset figure represents the exchange bias (H_{EB}) for 2D-Ni/VO₂ and 3D-Ni/VO₂ film. f) The H_{EB} and its second derivative with temperature for 3D-Ni/VO₂ films depict a peak around 350 K.

It is shown that in M_2 phase of VO_2 , the V-V pairing is not the only source of opening up the bandgap through the splitting of the $3d_{||}$ band but the antiferromagnetic spin ordering can lead to the same effect^{1,37}. It is theoretically proven that while the spin-splitting of the d_{xz} and d_{yz} states is rather small, the magnetic moment originates mainly from the local $d_{x^2-y^2}$ states. In M_2 phase, the dimerization of the V-V atoms in one chain causes splitting of the corresponding $d_{||}$ bands into bonding and antibonding branches, while in the other chain, the $d_{||}$ bands display spin-splitting and antiferromagnetic order³⁷. If the antiferromagnetic order is coupled with a ferromagnetic Ni with the high coercive field, which is the case for 3D-Ni films, it is possible to pin the M_2 structure across the metal-insulator transition, where above the T_N of the M_2 - VO_2 , the metallic property is achieved. Figure 9.6e shows the strong response of the coercive field to the VO_2 structural phase transition induced by strain in the 2D-Ni films^{13,14,16,39,40,41}. The 3D-Ni films' change of coercivity across the transition, however, is subtle due to the structural pinning. (As the coercivity gets enhanced in the FM, the coupling between FM and AFM is stronger and can pin the AFM structure.)

The magnetic entropy in isothermal and isobaric conditions, $\Delta S_m(T, H)$, can be expressed by Maxwell equation (See Appendix A) and used as a parameter sensitive to magnetic changes especially across the transition. By evaluation of $\Delta S_m(T, H)$ curves (Appendix A), the transition to antiferromagnetic state can be captured. The measurements need to be done under isothermal condition through multiple M-H plots for 2D and 3D-Ni/ VO_2 films. For each measurement, the exchange bias effect needs to be avoided as much as possible through zero field cooling for Maxwell the equation to be valid. In the case of 2D-Ni/ VO_2 , we observe three distinct peaks in the $-\Delta S_m(H, T)$ curves in Figure 9.7c. As the temperature is lowered, first, a positive peak ($T_1 \sim 370$ K) is observed followed by two negative peaks, $T_2 \sim 340$ K and $T_3 \sim 100$ K. The occurrence of the

positive peak (T_1) inferring a ferromagnetic ordering transition in VO_2 or at the interface of VO_2/Ni . As the temperature lowered, $-\Delta S_m$ becomes negative following by a peak appearance in the negative side. This peak is indicative of AFM ordering (exhibiting inverse magnetocaloric calorimetry effect, IMCE) which coincides with insulating behavior in VO_2 . The occurrence of the two peaks at T_2 and T_3 can be associated with the freezing of the area close to the interface and further away from it. The FM to AFM transition occurs as the structural transition happens in VO_2 structure. While, in the 3D-Ni/ VO_2 thin films there observed two minima in the negative side for $-\Delta S_m$ (in Figure 9.7d). first, a negative peak ($T_1 \sim 350$ K) is observed followed by another negative peak, $T_2 \sim 160$ K. There is no FM ordering observed and instead VO_2 goes directly to an AFM state. This AFM further stabilized around T_2 as the sample is cooled down. This behavior explains that metal-insulator transition in M_2 phase accompanied by AFM ordering in VO_2 . The presence of a strong coercive field promotes the AFM ordering through the coupling at the interface. In 2D-Ni/ VO_2 the transition between FM and AFM explains less coupling at the interface which allows the structural transition as well as magnetic transition.

For a ferromagnetic transition, the ΔS_m decreases and lattice entropy (ΔS_l) increases, due to the magnetic moment alignment. However, for an antiferromagnetic transition, ΔS_m increases and ΔS_l decreases. The ΔS_l is directly related to the temperature. The antiferromagnetic ordering in the M_2 phase and the enhanced exchange coupling by the coercive field at the interface of 3D-Ni/ VO_2 decreases the ΔS_l and prevents the structural transition.

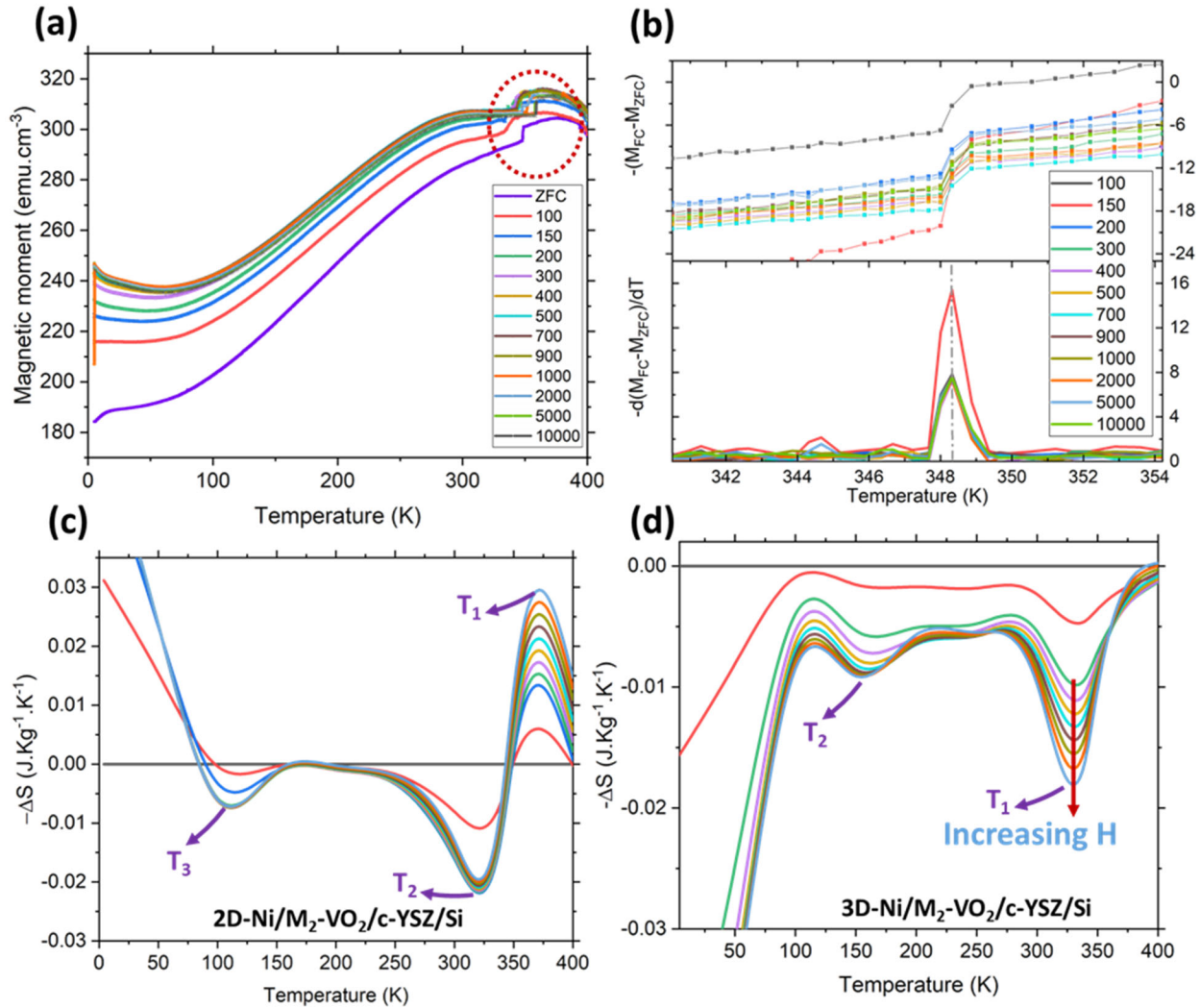


Figure 9.7. a) The Magnetic moment vs temperature plots at for zero fields-cooled (ZFC) and different field-cooled (FC) condition. The field unit is in Oe. b) The derivative of difference between FC and ZFC magnetization vs temperature illustrating a peak around 348K. c, d) The $-\Delta S_m$ (magnetization entropy) vs temperature for 2D-Ni/VO₂ and 3D-Ni/VO₂ films, respectively.

9.4. Conclusions

We successfully controlled and pinned the structural transition through stabilizing monoclinic M₂ phase of VO₂, while electronic and magnetic transition occurs across the transition temperature range. The manipulation is done by exploiting very stable spin of a high coercive field Ni layer on top of VO₂. The magnetization entropy was calculated and showed a PM to FM to AFM transition in case of 2D-Ni (flat Ni film). However, it showed a PM to AFM to AFM

transition in case of 3D-Ni/VO₂ (island Ni). The high coercivity in island Ni tends to couple with AFM better and pin the AFM M₂ phase of VO₂. This metal-insulator transition happens through AFM ordering in VO₂.

REFERENCES

1. Goodenough, J. B. The two components of the crystallographic transition in VO₂. *J. Solid State Chem.* **3**, 490–500 (1971).
2. Moatti, Adele, Sachan, Ritesh, Cooper, Valentino, Narayan, J. Electrical Transition in Isostructural VO₂ Thin-Film Heterostructures. *Sci. Rep.* **9**(1), 3009 (2019).
3. Ramanathan, S. Thin film metal-oxides. *Harvard Univ. Springer New York Dordr. Heidelb. London* (2010).
4. Mott, S. N. F. *Metal-insulator transition.* **26**, (London ; New York : Taylor & Francis, 1990).
5. Viswanath, B. & Ramanathan, S. Direct in situ observation of structural transition driven actuation in VO₂ utilizing electron transparent cantilevers. *Nanoscale* **5**, 7484–7492 (2013).
6. Zhou, Y., Ramanathan, S. Mott memory and neuromorphic devices. *P. IEEE.* **103**, 1289-1310 (2015).
7. Zhou, Y. & Ramanathan, S. Correlated Electron Materials and Field Effect Transistors for Logic: A Review. *Crit. Rev. Solid State Mater. Sci.* **38**, 286–317 (2013).
8. Moatti, A., Sachan, R., Gupta, S. & Narayan, J. Vacancy-Driven Robust Metallicity of Structurally Pinned Monoclinic Epitaxial VO₂ Thin Films. *ACS Appl. Mater. Inter.* **11**, 3547–3554 (2019).
9. Moatti, A., Sachan, R., Prater, J. & Narayan, J. Control of Structural and Electrical Transitions of VO₂ Thin Films. *ACS Appl. Mater. Inter.* **9**, 24298-24307 (2017).
10. Moatti, Adele, Sachan, Ritesh, Cooper, Valentino, Narayan, J. Electrical Transition in Isostructural VO₂ Thin-Film Heterostructures. *Sci. Rep.* **9**(1), 3009 (2019).
11. Eames, C. *et al.* Ionic transport in hybrid lead iodide perovskite solar cells. *Nat. Commun.* **6**, 7497 (2015).

12. Tao, Z. *et al.* Decoupling of Structural and Electronic Phase Transitions in VO₂. *Phys. Rev. Lett.* **109**, 166406 (2012).
13. Saerbeck, T., Venta, J. de la *et al.* Coupling of magnetism and structural phase transitions by interfacial strain. *J. Mater. Res.* **29**, 2353-2365 (2014).
14. Venta, J. D. La, Wang, S., Control of magnetism across metal to insulator transitions. *Appl. Phys. Lett.* **102**, 122404 (2013).
15. Abreu, E. *et al.* Ultrafast Electron-Lattice Coupling Dynamics in VO₂ and V₂O₃ Thin Films. *Phys. Rev. B.* **96**, 094309 (2017).
16. Finizio, S., Vafaei, M., *et al.* Control of the Magnetic Configuration of Ferromagnetic Nanostructures Across the Structural Phase Transition of Vanadium Dioxide. *IEEE Magn. Lett.* **7**, 6106604 (2016).
17. Moatti, A., Bayati, R. & Narayan, J. Epitaxial growth of rutile TiO₂ thin films by oxidation of TiN/Si{100} heterostructure. *Acta Mater.* **103**, 502-511 (2016).
18. Moatti, A., Sachan, R., Kumar, D., Narayan, J. Catalyst-assisted epitaxial growth of ferromagnetic TiO₂/TiN nanowires. *Acta Mater.* **167**, 112-120 (2019).
19. Moatti, A., Bayati, R., Singamaneni, S. R. & Narayan, J. Thin film bi-epitaxy and transition characteristics of TiO₂/TiN buffered VO₂ on Si(100) substrates. in *MRS Advances* **1**, 2635-2640 (2016).
20. Moatti, A. & Narayan, J. High-quality TiN/AlN thin film heterostructures on c-sapphire. *Acta Mater.* **145**, 134-141 (2018).
21. Moatti, A., Sachan, R., Prater, J. & Narayan, J. An optimized sample preparation approach for atomic resolution in situ studies of thin films. *Microsc. Res. Tech.* **81** (11), 1250-1256 (2018).

22. Moatti, A., Bayati, R., Singamaneni, S. & Narayan, J. Epitaxial integration of TiO₂ with Si (100) through a novel approach of oxidation of TiN/Si (100) epitaxial heterostructure. *MRS Adv.* **1**, 2629–2634 (2016).
23. Liu, M., Sternbach, A., Wagner, M., Slusar, T. & Kong, T. Phase transition in bulk single crystals and thin films of VO₂ by nano-infrared spectroscopy and imaging. *researchgate.net*
24. Reed, R. P. Deformation twinning in Ni and F.C.C. Fe-Ni alloys. *Philos. Mag.* **15**, 1051–1055 (1967).
25. Datta, A., Waghmare, U., Ramamurty, U. Density functional theory study on stacking faults and twinning in Ni nanofilms. *Scripta Mater.* **60**, 124-127 (2009).
26. Marini, C. *et al.* Optical properties of V_{1-x}Cr_xO₂ compounds under high pressure. *Phys. Rev. B.* **77**, 235111 (2008).
27. Kim, H.-T. *et al.* Hole-driven MIT theory, Mott transition in VO₂, MoBRiK device. *Phys. C Supercond.* **460**, 1076–1078 (2007).
28. Chen, L. *et al.* Tuning the phase transition temperature, electrical and optical properties of VO₂ by oxygen nonstoichiometry: insights from first-principles calculations. *RSC Adv.* **6**, 73070–73082 (2016).
29. Gupta, S. *et al.* Room-temperature ferromagnetism in epitaxial titanium nitride thin films. *Acta Mater.* **166**, 221-230 (2019).
30. Yang, H. W. *et al.* Unusual M₂-mediated metal-insulator transition in epitaxial VO₂ thin films on GaN substrates. *EPL (Europhysics Lett.)* **109**, 27004 (2015).
31. Chang, S.-J. *et al.* Probing the photothermally induced phase transitions in single-crystalline vanadium dioxide nanobeams. *Nanotechnology* **24**, 345701 (2013).

32. Atkin, J. M. *et al.* Strain and temperature dependence of the insulating phases of VO₂ near the metal-insulator transition. *Phys. Rev. B* **85**, 020101 (2012).
33. Bruno, P. Dipolar magnetic surface anisotropy in ferromagnetic thin films with interfacial roughness. *J. Appl. Phys.* **64**, 3153–3156 (1988).
34. Sander, D. The magnetic anisotropy and spin reorientation of nanostructures and nanoscale films. *J. Phys. Condens. Matter* **16**, R603–R636 (2004).
35. Palasantzas, G., Zhao, Y., Hosson, M., Wang, G. Roughness effects on magnetic properties of thin films. *Physica B*. **283**, 199-202 (2000).
36. Luo, Z.-Y. *et al.* Influence of Film Roughness on the Soft Magnetic Properties of Fe/Ni Multilayers. *Chinese Phys. Lett.* **29**, 127501 (2012).
37. Eyert, V. The metal-insulator transitions of VO₂: A band theoretical approach. *Ann. Phys.* **11**, 650–704 (2002).
38. Correa-Duarte, M., Salgueirino, V. Magnetic properties of nanowires guided by carbon nanotubes. (2010).
39. de la Venta, J. *et al.* Coercivity enhancement in V₂O₃/Ni bilayers driven by nanoscale phase coexistence. *Appl. Phys. Lett.* **104**, 062410 (2014).
40. Yang, Y. *et al.* Enabling magnetoelastic coupling in Ni/VO₂ heterostructure by structural phase transition. *J. Mater. Sci. Mater. Electron.* **29**, 2561–2567 (2018).
41. Foley, G., Singamaneni, S., Prater, J., Narayan, J., Control of Magnetic Coercivity in epitaxial Ni/VO₂/YSZ/Si(001) heterostructures by manipulation of Ni thin film growth modes. *MRS Adv.* **1** (50), 3409-3414 (2016).

APPENDICES

Appendix A

The Gibbs free energy, G , for any magnetic material can be written as:

$$G = U + pV - TS - MH \quad \text{Equation (9.1)}$$

Where U is the internal energy, V is the volume, p is the pressure, S is the total entropy, T is the temperature, M is the magnetization, and H is the magnetic field. If p and H are constant, the total entropy can be obtained as:

$$S(H, T, p) = -\left(\frac{\partial G}{\partial T}\right)_{H,p} \quad \text{Equation (9.2)}$$

The total entropy can be expressed in three forms of lattice entropy (ΔS_l), magnetic entropy (ΔS_m), and electronic entropy (ΔS_e). Then:

$$\Delta S(T, H, p) = \Delta S_l(T, H, p) + \Delta S_m(T, H, p) + \Delta S_e(T, H, p) \quad \text{Equation (9.3)}$$

If a magnetic field is applied, for a ferromagnet, the ΔS_m decreases and ΔS_l increases, due to the magnetic moment alignment parallel to the field direction. If the magnetic field is removed, the randomization increases ΔS_m and decreases ΔS_l . However, for an antiferromagnet, in the presence of the magnetic field, ΔS_m increases and ΔS_l decreases and vice versa. The ΔS_l is directly related to the temperature. For the entropy as a state function, we can write:

$$dS = \left(\frac{\partial S}{\partial T}\right)_{p,H} dT + \left(\frac{\partial S}{\partial p}\right)_{T,H} dp + \left(\frac{\partial S}{\partial H}\right)_{p,T} dH \quad \text{Equation (9.4)}$$

Under isothermal ($dp=0$) and isobaric ($dT=0$) conditions, only magnetic entropy remains, and it can be expressed through the Maxwell equation as:

$$\left(\frac{\partial S}{\partial H}\right)_T = \left(\frac{\partial S}{\partial T}\right)_H \quad \text{Equation (9.5)}$$

Since ΔS_m is a function of applied field, we will have:

$$\Delta S_m(T, H) = \int_0^{H_{Max}} \left(\frac{\partial M}{\partial T}\right)_H dH \quad \text{Equation (9.6)}$$

CHAPTER 10

10. Conclusions

VO₂ thin films were epitaxially grown on Si(001) and Al₂O₃(0001) substrates using pulsed deposition techniques. The effect of strain, defect, and spin engineering as a mean to affect electron-electron, electron-lattice, spin-spin, and spin-lattice interactions on structural and electrical transitions was investigated. Detailed microstructural investigations were performed by *in-situ* XRD, TEM, *in-situ* STEM (HAADF and EELS), and Raman spectroscopy techniques. Electrical properties of the samples were studied employing PPMS. EELS spectroscopy was employed to determine stoichiometry, valance state, and defect content. Magnetic properties were assessed through measuring isothermal M vs H plots and calculating entropy of magnetization.

The following briefly reviews the obtained results:

1. We integrated single crystalline rutile TiO₂ thin film with Si(100) through solid-state oxidation of TiN layer to be utilized as a buffer layer for VO₂. The first step of oxidation was established to be the diffusion of Ti atoms leaving Ti vacancies behind. It was indicated that the formation of these vacancies collapses the nitrogen octahedron. As a result, neighboring Ti bonds become weaker and more inclined to diffuse out. Thus, Ti vacancies get larger, forming small cuboids in which N₂ gas forms.

2. We have successfully integrated VO₂ thin film on Si through a buffer layer of TiO₂/TiN. The TiN was grown cube-on-cube on Si, and TiO₂ was oxidized epitaxially with [110] out-of-plane orientation. VO₂ was then deposited on TiO₂ with an out-of-plane direction parallel to [011]. The in-plane relationship established to be VO₂(110)/VO₂(010) || TiO₂(011) || TiN(112) || Si(112) based on transmission Kikuchi Diffraction. Metal to semiconductor transition was defined to be 350 K with 8 K hysteresis, according to resistance versus temperature measurements.

3. The (010)VO₂ epitaxial thin films were grown on a c-sapphire substrate via PLD. The epitaxial relationship was established to be sapphire(01 $\bar{1}$ 0) \parallel m-VO₂(001) and sapphire(01 $\bar{1}$ 0) \parallel m-VO₂(100). Our EELS spectroscopy results confirm different misfit strains in these two grains leading to the formation of V₂O₃ at one interface where there is higher misfit strain to accommodate that. The different misfit strain causes them to behave differently across the metal-insulator transition. The evidence provided the fact that the structural and electrical transition are separated due to the misfit strain.

4. It is argued that the velocity and temperature of the phase transformation are controlled by the thermodynamics and kinetics, where thermodynamics determines the feasibility and kinetics defines the rate of transformation. Unrelaxed strain in the film modifies the activation barrier for the structural transition and also defines the bandgap which affects the electrical transition. Our proposed model illustrates how strain might affect structural and electrical transitions differently and thereby creates a lag between these two transitions.

5. We capture an atomically sharp transition from a strained monoclinic to a relaxed tetragonal state of VO₂ thin films at a certain critical thickness (~15 nm) during the epitaxial growth on NiO/c-Al₂O₃ heterostructures. Below this critical thickness, the film pseudomorphically adopts a strained monoclinic phase even at the growth temperature. As it reaches to the critical thickness limit, the strained monoclinic transforms into a completely relaxed state with the formation of interfacial dislocations which subsequently glide into the film/substrate (VO₂/NiO) interface following DME paradigm through active slip systems of $\frac{1}{2}$ [0 $\bar{1}$ 1](011) and $\frac{1}{2}$ [10 $\bar{1}$](101).

6. Using STEM analysis, image processing, and strain analysis, we successfully depict the periodic formation of misfit dislocations, the strain centers, and the atomic rearrangement near dislocations cores in pseudomorphic phase of VO₂ below the critical thickness. Interestingly at the

vicinity of dislocation cores, for each dislocation, there is one atomic column missing to locally minimize the energy, which produces periodically positive and negative strain centers. This study provides us with the tool to obtain the desired structure of VO₂ and to manipulate and exploit the strain center at the dislocation core through external and internal stimuli leading to achievement of predictable properties.

7. We successfully demonstrated a sample preparation method for atomic resolution *in-situ* studies of thin film heterostructures, by combining mechanical wedge polishing and FIB lift-out approaches. We developed a soft-transfer method for transferring electron transparent thin film samples to the test stage by employing carbon nanotubes as an elastic connect. This eliminates the instrumental and user error introduced during the sample transfer on test stage brittle Si₃N₄ window and avoids the test stage failure.

8. Using *in-situ* STEM and *in-situ* XRD, we examined the electronic and structural property changes across the metal-insulator transition in VO₂ films which were grown pseudomorphically below the critical thickness where no strain releasing dislocations are formed for lattice relaxation. The results were compared with the above critical thickness grown thin films in VO₂/NiO/c-sapphire heterostructures which represent near-bulk behavior. It is successfully demonstrated that the bandgap decreases in pseudomorphic strained VO₂ in a way that structural transition is pinned, while electrical transition occurs.

9. DFT calculation was performed and the results show that the reduction in bandgap occurs by decreasing Δ_{V-V} through misfit strain in pseudomorphic strained VO₂ thin-film heterostructures. The bandgap manipulation is achieved through pinning of lattice degrees of freedom induced by strain.

10. We have achieved a stable metallic monoclinic phase of VO₂ by manipulating the electron-electron correlations through doping the system with oxygen vacancies in pseudomorphic strained VO₂ thin-films. These vacancies introduce electrons into the system which change the relative electron-electron interaction strength and as a result, modify the electronic properties of the VO₂ without any structural transition. In fact, the enhancement of free carrier concentration pushes the system to meet the Mott criterion and become metallic.

11. Above the critical thickness, we have shown the reversible behavior of turning off/on the electrical hysteresis by vacancy and oxygen doping in VO₂/NiO/c-sapphire heterostructures. This behavior can be exploited in non-volatile memory devices for neuromorphic applications.

12. We successfully controlled and pinned the structural transition through stabilizing monoclinic M₂ phase of VO₂ in Ni/VO₂/c-YSZ/Si heterostructures, while electronic and magnetic transition occurs across the temperature range. The manipulation is done by exploiting the robust spin in a high coercive field Ni layer on top of VO₂. The robust spin manipulates the spin-spin and spin-lattice interactions and eliminates the lattice degrees of freedom.

13. The coercivity in Ni in Ni/VO₂/c-YSZ/Si heterostructures was controlled by the kinetics of growth to provide 2D (flat film) or 3D (islands) growth modes. The magnetization entropy was calculated that showed a PM- FM-AFM transition during cooling in the case of 2D-Ni (flat Ni film). However, it showed a PM-AFM-AFM transition during cooling in the case of 3D-Ni/VO₂ (island Ni). The high coercivity of Ni islands tends to couple with AFM better and pin the AFM M₂ phase of VO₂. The metal-insulator transition happens through AFM ordering in VO₂.